QUANTIFYING HEAT TRANSFER EFFECTS OF A HIGH-SPEED, MULTI-STAGE, AXIAL RESEARCH COMPRESSOR

by

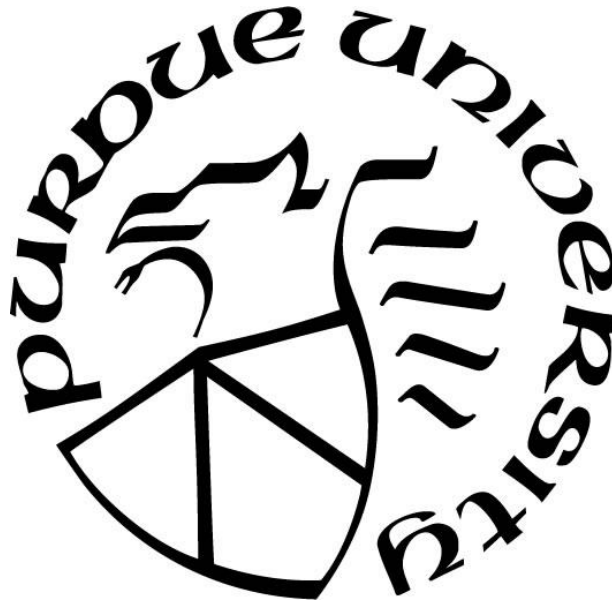**Nicholas J. Kormanik III**

A Dissertation

Submitted to the Faculty of Purdue University

In Partial Fulfillment of the Requirements for the degree of

Doctor of Philosophy

School of Mechanical Engineering

West Lafayette, Indiana

December 2021

THE PURDUE UNIVERSITY GRADUATE SCHOOL
STATEMENT OF COMMITTEE APPROVAL

Dr. Nicole Key, Chair

School of Mechanical Engineering

Dr. Carson Slabaugh

School of Aeronautics and Astronautics

Dr. Guillermo Paniagua

School of Mechanical Engineering

Dr. Aaron King

Rolls-Royce Corporation

Approved by:

Dr. Nicole Key

This work is dedicated to my family, friends,
and my two adoring redheads that helped me through it all,
Adeline and Jessica

ACKNOWLEDGMENTS

TABLE OF CONTENTS

LIST OF TABLES

9

LIST OF FIGURES

11

15

NOMENCLATURE, ABBREVIATIONS, & SYMBOLS

Nomenclature:

ρ	Density		[kg/m^3]
P	Power		[kW]
Re	Rotational Reynolds Number	$\dfrac{\rho \omega r^2}{\mu}$	[-]
X	Length of Knife Seal Surface		[m]
μ	Dynamic Viscosity		[N-s/m^2]
r_R	Knife Seal Tip Radius		[m]
r_o	Stator Well Outer Radius		[m]
r_i	Stator Well Inner Radius		[m]
ω	Rotational Speed		[rad/s]
$\dot{m}$	Leakage Flow Rate		[kg/s]
n	Number of Knife Seals		[-]
G_c	Dimensionless Rotor Stator Gap	c/r_o	[-]
Cp	Specific Heat Ratio		[J/kg-K]
a	Speed of Sound		[m/s]
M	Mach Number		[-]
$\dot{Q}$	Heat Rate		[kW]

Subscripts:

o	Stagnation value	AA	Area-Averaged
in	Inlet state	c	Corrected
out	Outlet state	isen	Isentropic
tip	Condition at the tip	tq	Torque-Based
poly	Polytropic	flow	Flow-Based
ad	Adiabatic		

Abbreviations:

P3S	Purdue 3-Stage
RANS	Reynolds-Averaged Navier-Stokes
URANS	Unsteady, Reynolds-Averaged Navier-Stokes
CFD	Computational Fluid Dynamics
1D	1-Dimensional
2D	2-Dimensional
3D	3-Dimensional
IGV	Inlet Guide Vane
R1	Rotor 1
R2	Rotor 2
R3	Rotor 3
S1	Stator 1
S2	Stator 2
S3	Stator 3
ADP	Aerodynamic Design Point
AIP	Aerodynamic Inlet Plane
TT	Time-Transformation
STT	Single-Sided Time-Transformation

ABSTRACT

A common assumption often made of dynamic compressors is that they are considered adiabatic, due to the fast-moving flow passing through the turbomachine and the small amount of any heat transfer relative to the large amount of work transferred to/from the flow. This research investigation combined the use of experimental measurements and computational simulations to take a deeper look into the implications that arise from applying this adiabatic assumption or neglecting heat transfer within a high-speed, multi-stage, axial compressor.

Preliminary testing of the Purdue 3-Stage (P3S) Axial Compressor Research Facility indicated the presence of heat transfer through stagnation temperature rises across stationary blade rows and higher than expected temperatures on the outside of the aluminum compressor casing, particularly in the front stages. Further experiments performed on the PAX200 compressor in the P3S facility involved a combination of surface temperatures, heat fluxes, and flow stagnation temperatures within the shrouded stator cavities and flowpath. These measurements confirmed that heat transfer was present throughout the stationary components (stators and casing) of the compressor and showed that they could noticeably affect the thermal flow properties within the compressor.

The influence of the heat transfer through these components was further explored through computational simulations, which showed the importance of incorporating conjugate heat transfer into the model and applying the correct thermal boundary conditions on the outside of the casing. Additionally, the effects on the spanwise temperature of the flow through increased spanwise mixing, convection, and different geometric and material properties of the casing were also explored. Overall, this investigation seeks to establish a correct thermal boundary condition and approach for validation of computational model. It also aims to reconcile the differences between computational models and experimental data by quantifying the impact that heat transfer has on isentropic efficiency for diabatic compressors.

1. INTRODUCTION

The gas-turbine industry has made significant strides throughout the last century to achieve high performance and reliability while providing the world with many solutions to provide power and propulsion in both land-based and air-based applications. However, as society has become more industrially advanced, environmentally conscious, and driven by cost/benefit analyses, engine manufacturers have been forced to also focus on improving environmental impact and cutting costs. One way in which this is accomplished is through the creation of more fuel-efficient engines, which use less fuel yet still maintain the same or greater performance. This requires optimizing and improving all aspects of the engine – from turbomachines to combustion to inlets/outlets – to better understand how current engine designs can be adapted to achieve higher efficiency. Even so, limits are being reached on how much efficiency can be recovered as the Brayton cycle associated with gas-turbine engines approaches Carnot limits, so every miniscule increase in efficiency significantly counts. For example, Wisler (1998) stated that an improvement of one point of efficiency in a high-pressure compressor can reduce the specific fuel consumption of an engine by 0.66%. As a result, aspects that were once considered negligible in understanding and evaluating the performance of a gas-turbine engine, such as heat transfer effects in the compressor section, are becoming increasingly important to designers who aim to achieve small gains in efficiency.

1.1 Research Motivation

In the case of turbomachines in a gas-turbine engine, there remain a few key areas for improvement in terms of increasing the engine efficiency. Machines with lower aspect ratios, or those with shorter blade heights relative to their axial length, have been developed to help save on the more traditional ways to improve fuel consumption and efficiency in air-based gas-turbine engines, such as decreasing size and weight of the engine. However, this reduction brings about new challenges with aerodynamics as the gap between the blade tip and the casing wall, referred to as the tip clearance, does not quite scale in the same way. Additionally, with the reduction in blade height, the tip and hub regions (referred to as endwalls) become much closer together.

With this growing trend toward smaller engine cores, the reduced aspect ratio begins to play more of a significant role on influencing the behavior of flows in the spanwise direction. More specifically, a lower aspect ratio forces the boundary layer flows in the endwall regions to interact more with the primary throughflow than with past compressor designs that incorporated a larger aspect ratio. This can create a spanwise mixing effect through a few different mechanisms: turbulent diffusion and secondary flows. Turbulent diffusion refers to the natural diffusion or spreading of the flow properties due to turbulent eddies that are inherent to the turbomachinery environment. Secondary flows are the weaker cross-flows (those that are not associated with the primary throughflow) observed in turbomachinery that are often a result of the blade geometry and endwalls, as shown in Figure 1.1. This mixing effect can cause an alteration in the flow from an ideal, efficient path through the compressor and can, thus, cause a negative impact on efficiency through induced blockage, leakages, or flow separation. More specifically, with enhanced mixing in these low aspect ratio machines with closer endwalls, heat transfer effects can become more evident and amplified as heat is carried more efficiently from the thermal boundary layer in the endwall regions to different locations throughout the span, affecting the overall flow properties.
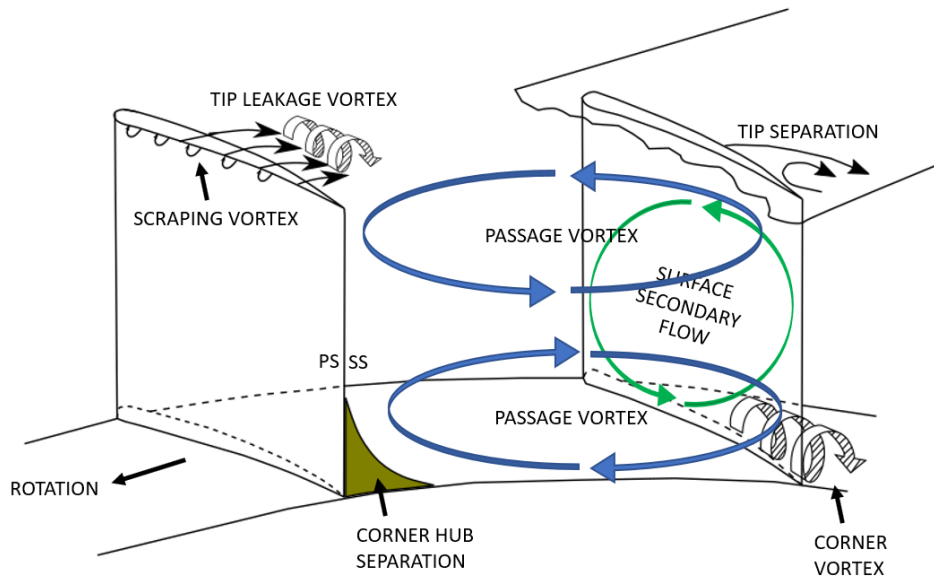
Figure 1.1. Secondary flows found in the flow path of a compressor.

The mechanisms responsible for the mixing or redistribution of flow properties such as pressure/temperature, and thus loss, in the spanwise direction have been well-researched and

established over time. However, they are still not entirely predictable using computational fluid dynamics (CFD) or standard throughflow codes, proving the value in experimental data to validate computational models. Additionally, most of the literature on heat transfer in compressors is focused on turbines and turbochargers, while the literature on spanwise mixing only focuses on low-speed compressors/cascades at common loading conditions. Few studies include high-speed, multi-stage compressor environments with complex three-dimensional geometry, which are more representative of modern-day gas-turbine engine operation. Additionally, many attempts have been made to pair experimental and computational data to achieve better understanding of spanwise mixing flow phenomena by employing computational methods in the 2D domain, but only 3D RANS CFD has come close to resolving the flow features completely.

From a more local point-of-view, the Purdue 3-Stage Facility has traditionally exhibited an increase in total temperature across stator rows. With no work being input into the flow across a stator, the stagnation temperature rise must be associated with a heat transfer phenomenon. It was hypothesized that spanwise mixing from heat sources such as windage in the stator cavities, and preheating effects from downstream blade rows conducting through the stator blades and the casing were causing this event to occur. This trend is true for both the original P3S compressor (PAX100) and enhanced by the temperatures involved with the newest compressor design (PAX200). If this is the case, an adiabatic condition, typically assumed in computational models which use experimental data for validation, are incorrectly describing the flow. As a result, the heat transfer must be characterized to effectively describe the actual boundary conditions that should be applied to the system. Similarly, utilizing the isentropic (adiabatic and reversible) efficiency to describe a non-adiabatic, or "diabatic," compressor needs to be reconsidered.

To better understand what is occurring in the Purdue 3-Stage Facility (and more generally, high-speed, multistage axial compressors), this investigation involved computational simulations and experiments on the PAX200 compressor to determine and quantify the ways in which heat transfer can affect the compressor properties and performance. Using a combination of CFD and experimental research, along with enhanced spanwise mixing effects, the performance discrepancies between the simulations and experimental compressor were reconciled and the influence of heat transfer effects on the flow were better understood.

While this investigation will primarily lead to improved understanding of the flow physics and thermal characterization of the P3S facility, there are also many benefits to the turbomachinery

community. The community is continuously looking at validation of these tools and improvements of their designs, which can only be achieved through careful comparison to experimental results. This research also fills a void in the literature by offering a wholistic and comprehensive approach to understanding the effects of heat transfer on compressor performance instead of assuming it negligible. Furthermore, the P3S facility features high-speed, low aspect ratio, multi-stage compressor designs, which are less common in the open literature. It is anticipated that this research will offer a deeper understanding of quantifying the heat transfer and effect of spanwise mixing in this complex geometric environment associated with more modern-day, engine-representative designs.

1.2   Literature Review

This research investigation draws upon a few different sources to establish what has already been done in the areas of heat transfer, spanwise mixing, and efficiency corrections as they relate to turbomachines and, more specifically, compressors. While much research has been done on turbochargers and turbines and low-speed compressors, there is a large void in applying these concepts to the compressors in modern-day, low aspect ratio, gas-turbine engines used in aviation and power generation applications.

1.2.1   Heat Transfer in Turbomachinery

From its most basic thermodynamic derivation, the gas-turbine engine finds its roots in the Brayton cycle. The Brayton cycle originated from the analysis of a piston engine with each piston stroke creating a compression/expansion process for the working fluid and the combustion occurring at a constant pressure process. This cycle, shown in Figure 1.2, is also directly applicable to gas-turbine engines. A compressor is used to increase the working fluid to a high pressure, fuel is added and ignited through a constant pressure process in a combustor, and the resulting energy is extracted through a turbine. In the final stage of the process, the working fluid is either exhausted to atmosphere, designated an "open" cycle, or if it is cooled, it would result in a "closed" cycle.
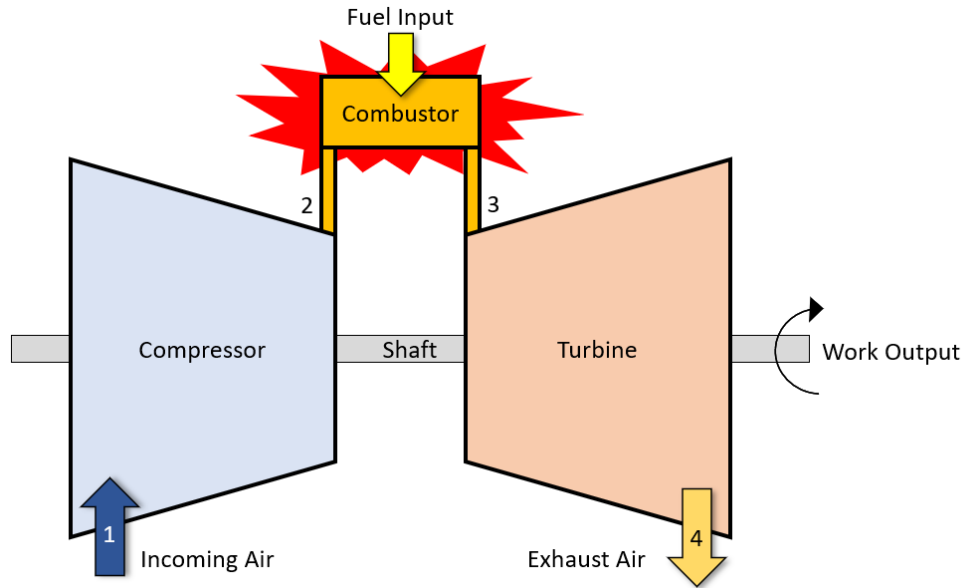
Figure 1.2. Brayton Cycle analysis for gas-turbine engine applications (open-form).

In the thermodynamic analysis of the gas-turbine engine, several assumptions are applied to each stage of the process to create an "ideal" Brayton cycle, or one that requires the least amount of energy input for the most amount of energy output. The ideal Brayton cycle follows a path of isentropic (adiabatic and reversible) compression and expansion within the turbomachinery components.

Turbomachines are typically deemed "adiabatic" because it is assumed that no heat transfer occurs between the flow and the surfaces of the flow path. This is due to the fast-moving flow passing through the machine and the small amount of any heat transfer relative to the large amount of work transferred to/from the flow. The opposite of this term, "diabatic," refers to flows in which heat transfer can occur, typically due to any large temperature gradients. This can involve any of the primary heat transfer methods: conduction, convection, and/or radiation.

As shown from a temperature and entropy standpoint in Figure 1.3, applying the isentropic (adiabatic and reversible) assumptions to the ideal Brayton cycle means that no heat transfer takes place between the flow and the environment and that no losses are present (entropy remains constant). For the turbine, this results in the maximum work output possible from the expansion process. For the compressor, this results in the minimum work input required to complete the compression process. In the actual Brayton cycle, it is expected that there will be irreversible losses

that take place. However, the assumption of adiabatic flow is often still applied, and the heat transfer is considered negligible since the relative amount of mass flow is quite large compared to the surfaces within the turbomachine where heat transfer can occur.
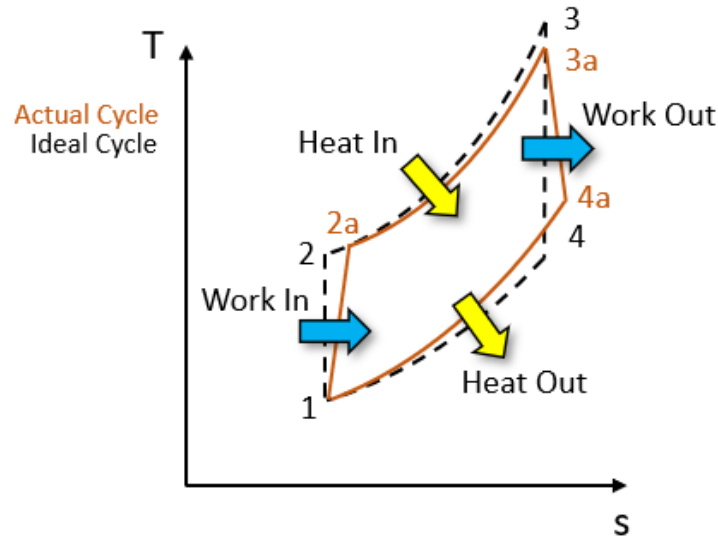
Figure 1.3. T-s diagram for ideal and actual Brayton Cycle.

Contrary to these adiabatic assumptions that are made to simplify the analysis of the real Brayton cycle, heat transfer is actually a very important topic in turbomachinery, with the most prominent research addressing the concerns associated with turbine blading downstream of the combustor. As the overall efficiency of the gas-turbine engine can be improved through achieving higher temperatures and energy in the combustor, it is imperative that the downstream blade rows are cooled enough to survive the extreme environment. Thus, much research has been performed in the areas of impingement and film cooling of turbine blades both experimentally and computationally.

While compressors are not necessarily subjected to the same extreme temperatures that plague the turbine within a gas-turbine engine, there are many other aspects of heat transfer that can be observed within a compressor environment. This includes reheating effects with multi-stage or closely coupled machines, heat generation from frictional windage, and heat soak as components reach a steady-state equilibrium. Typically, these heat transfer effects generally

contribute to a decreased performance or efficiency through producing an additional temperature rise compared to the ideal, adiabatic case (Dixon, 2005).

One area where heat transfer has been shown to affect the overall performance of a compressor is primarily in turbocharger or micro-turbomachinery applications through a reheating or preheating effect. Due to the close coupling of the compressor and turbine within a turbocharger, heat is lost from the turbine stage resulting in an artificially high apparent efficiency for the turbine. This lost heat travels to the compressor, resulting in an artificially low apparent efficiency for the compressor. In a stand-alone compressor, this same trend is found to a smaller extent as heat is conducted from downstream stages through the endwalls and surfaces that the primary flow interacts with as it moves toward upstream stages, causing a similar preheating effect.

In the open literature, turbochargers (Lüddecke et al., 2014 and Schinnerl et al., 2018) at low to mid-speeds can exhibit significant heat transfer effects that affect performance. This is because at low pressure ratios and mass flow rates, the resulting enthalpy increase/decrease in the compressor and turbine are relatively small compared to the heat transfer that occurs between the components, which leads to a deviation in the compressor and turbine matching and efficiency performance map characterization.

A study by Sirakov and Casey (2013) investigated this heat transfer effect on turbocharger performance in detail and found that heat transfer did not influence the overall pressure ratio characteristic of the turbocharger. However, it did have a significant effect on efficiency as the heat transfer was incorrectly attributed to work transfer under the standard adiabatic assumption, particularly at low speeds, pressure ratios, or mass flows. They implemented a water-cooling channel into the turbocharger to look at the relationship between heat transfer and performance and developed a guideline to correct turbocharger performance maps to adiabatic conditions using the difference between apparent and real work coefficients. Their method was derived by considering that heat transfer caused more impact on temperature rise at lower mass flow rates and expressed the difference between apparent and real work as,

$$\lambda_{apparent} - \lambda = \frac{\dot{Q}}{\rho_{o,in} a_{o,in}^3 D_{out}^2} \frac{1}{\phi_{o,in} M_{tip,out}^2}.$$ [1]

The denominator of this equation is proportional to the power absorbed by the compressor and assumes that the heat transfer rate is constant across the performance map. It also assumes that

the compression process happens adiabatically with heat transfer applied before or after the actual process. This preserves the shape of the velocity triangles, and keeps the density, Reynolds number, and Mach number unchanged – a common assumption when dealing with heat transfer analyses in compressors. Overall, they showed that from a modeling perspective, when adiabatic boundary conditions are commonly and incorrectly assumed, this can lead to issues with matching stages and can skew the accuracy of correlations used to quantify and understand purely aerodynamic loss mechanisms. Furthermore, it can negatively skew the end-user's perspective on the performance of the turbocharger at low speeds, since the heat transfer from the combustion process and turbine are still just as prominent at these less extreme conditions.

Another important heat transfer consideration for evaluating experimental performance in turbochargers is the concept of thermal heat-soak or heat loss within the system. This refers to the time spent waiting for everything to reach thermal equilibrium and is not just important in turbochargers but also in isolated, research compressors as shown in a study by Smith et al. (2019). They compared performance efficiency of a single-stage, shrouded impeller using measurements from both a torque meter and from the flow. The efficiency from the torque meter was isolated from any thermal effects of the facility and, thus, was a good comparison of the immediate performance of the compressor. Meanwhile, the flow-based efficiency took much longer to reach a steady-state condition due to the thermal heat soak of the facility. Additionally, there was an offset between the torque-based efficiency and flow-based efficiency – an indication of how much overall heat loss was evident in the compressor (on the order of 0.5-1°C). Significant wait times were required to ensure thermal equilibrium had been reached before data acquisition could take place.

Overall, heat generation can manifest within a compressor in a few different ways. First, many axial compressors in aviation applications commonly use shrouded stators for a few different reasons. They can be useful in easily mitigating the more high-risk negative impacts on efficiency of tip-leakage flows that are present with cantilevered stator designs and can be more structurally advantageous by dampening vibrational modes. They can also achieve a tighter clearance than cantilevered stators since any rubs that occur between the shrouds and the rotor drum do not directly impact the primary flow path.

However, these benefits of shrouded stators come at the cost of large temperature rises within the stator wells and cavity regions. With shrouded stators, as shown in Figure 1.4, air from

the primary flow path is drawn into the cavity by the pressure difference between upstream and downstream of the stator. This leakage flow phenomenon can affect the aerodynamics of the primary flow and can generate heat from friction through the process. As the flow descends into the rear cavity, the flow is partially trapped as it redirects itself, resulting in windage and heat generation before passing through the knife seal clearance where further heat generation takes place through a throttling process. Finally, the air is partially trapped in the front cavity before rejoining the primary flow path. There are many ways to predict and account for this heat generation using standard windage formulae incorporating geometry and mass flow estimations.
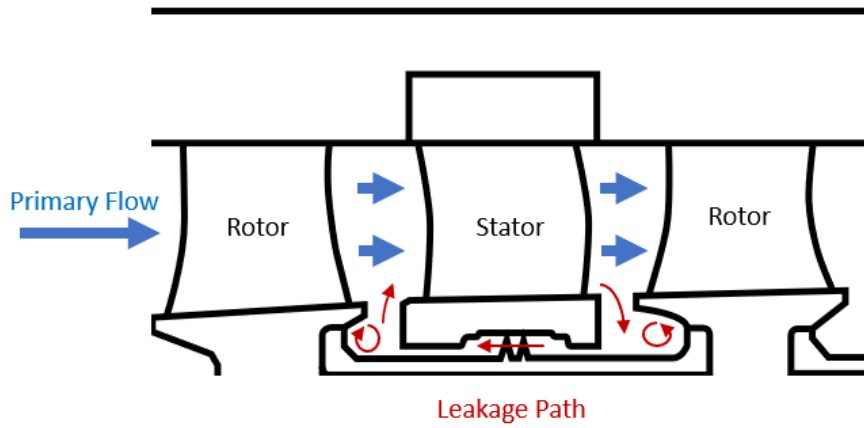
Figure 1.4. Typical leakage path for a shrouded compressor stator.

For example, Millward & Edwards (1996) concluded that windage heating/power across the knife seals, shown in Figure 1.5, of a shrouded stator is directly influenced by the mass flow rate going through the leakage path. They developed a simple correlation for windage power produced in plain lined labyrinth seals using experimental data that was accurate to within +/- 25%,

$$P = C_{ms}\pi X\rho\omega^3 r_R^4. \tag{2}$$

In their windage heating equation, C_{ms} is the seal moment coefficient and C_w is the flow number expressed as,

$$C_{ms} = 0.06 \left(\frac{C_w}{Re_R}\right)^{0.55} n^{-0.65}, \tag{3}$$

$$C_w = \frac{\dot{m}}{\mu r_R}.$$ [4]
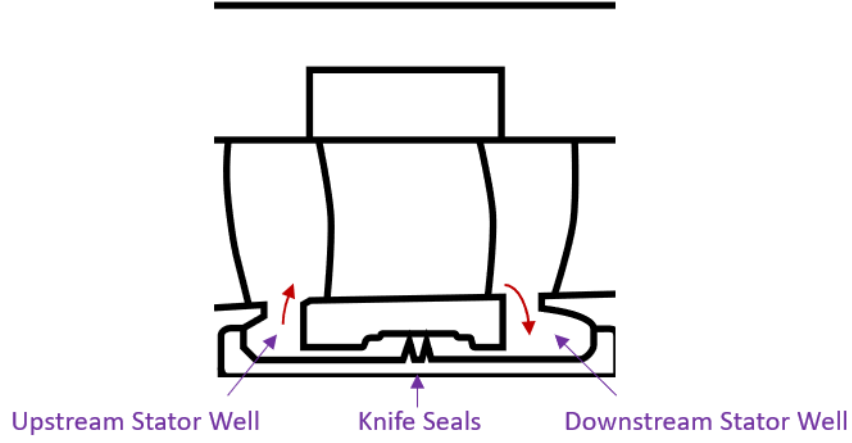
Figure 1.5. Terminology for shrouded stator region of a compressor.

Bayley & Childs (1994) developed a similar concept for stator wells, which they also found to be highly dependent on the mass flow rate in the leakage path. The power associated with windage in the wells was expressed,

$$P = 0.5\, C_m \left(\frac{Cw_w}{0.4 G_C Re_o}\right)^{0.3} \rho \omega^3 [r_o^5 - r_i^5]$$ [5]

where, C_m is the moment coefficient and Cw_w is the entrainment flow coefficient expressed as,

$$C_m = 0.04\, Re_o^{-0.2},$$ [6]

$$Cw_w = 0.22 Re_o^{0.8}\left[1 - \left(\frac{r_i}{r_o}\right)^{2.6}\right].$$ [7]

This power corresponds to a temperature rise within the stator wells, based on the leakage flow rate and specific heat ratio,

$$\Delta T = \frac{P}{C_p \dot{m}}.$$ [8]

28

In their investigation, Bayley & Childs also found that upstream stator wells were hottest with large gaps between rotor and stator and a low leakage flow rate. For the downstream stator wells, the stator wells were hottest at low leakage flow rates for a similar rotor-stator axial gap.

Lewis (2002), applied these correlations to quantify the temperature rise in the stator wells of an aeroengine using metal surface thermocouples on both the rotational and stationary parts of the cavities. He used these metal surface thermocouples and stagnation temperatures taken inside each well to calculate the steady-state and transient heat flux into the blade row and drum during compressor operation. He found good agreement between the correlations and experimental data, and the windage generation varied from 5 to 17kW per stage, with 50% generated in the downstream stator well, 30% across the knife seal, and 20% in the upstream stator well.

As discussed previously with respect to turbochargers, another way in which heat transfer can affect the flow in a compressor is through the blade and the endwalls. A study by Liu et al. (2017) focused on placing cooling channels inside of the stator blades and endwalls to try to boost aerodynamic performance. This was done both experimentally and using conjugate heat transfer CFD analyses. They were able to decrease the temperature through the stator by 1.4 to 2.9K, resulting in a lower entropy at the outlet and a slight increase in pressure. The cooling not only decreased the flow temperature but also decreased the separation and friction loss by increasing the Reynolds shear stress at the endwalls and re-energizing the flow.

Some additional ways in which heat transfer effects have been investigated on compressors include the use of steady and unsteady instrumentation on the rotating reference frame and investigating phenomena like buoyancy-induced flows within the compressor rotor drum (Owen et al., 2018). Another heat transfer effect on compressors involves compressor stability, particularly from a transient analysis perspective, through thermal growth of the casing and rotors (and thus tip clearances) and change in stall margin due to the influence of heat transfer on stage matching and boundary layer development (Kiss and Spakovsky, 2018). These topics are outside the scope of this investigation due to lack of high-frequency instrumentation in the rotational reference frame but will be included as a recommendation to future work in capturing temperature and heat flux measurements in the Purdue 3-Stage Facility through an upcoming slip ring upgrade.

While all the different heat sources identified in this section can be considered as causing unexpected heat and temperature discrepancies, they do not completely describe how the heat can

be transferred within the flow passage. Particularly in the case of low aspect ratio compressors, the concept of spanwise mixing offers additional insight into how stagnation temperature and other flow properties are redistributed throughout the flow path of a compressor.

1.2.2 Enhanced Spanwise Mixing and Influence of Eddy Viscosity

Spanwise mixing refers to the redistribution of mass, momentum, or energy across the span (hub to tip) of the turbomachine flow path. This results in the mixing of subsequent thermodynamic properties like pressure and temperature, as well as any derived quantities such as loss/entropy and efficiency. Typically, as most losses occur near the blade root and blade tip due to inherent loss mechanisms like tip leakage flow and hub flow separation, spanwise mixing can carry the generated entropy from the endwalls of each blade toward the midspan region and vice versa. This mixing process can render a blade design ineffective if the strategy that was used to diffuse the flow assumed a different radial distribution of flow properties that was not predicted correctly.

In a multi-stage environment, these effects of spanwise mixing and generated losses can stack up and propagate through downstream stages in the endwall regions. This is counterproductive to stage matching which is a crucial part of the design process in turbomachinery. Overall, each compressor is designed to a specific operating condition, where it will spend much of its operational life, based on a desired pressure ratio and incoming mass flow rate. This overall performance metric for the turbomachine is achieved from the performance of each individual stage (rotor-stator combination), which heavily relies on how well each stage is matched to the other. In the compressor design cycle, the rotational speed, blade angles and solidity (blade spacing) are chosen in such a way to accept a certain inlet condition, based on expected velocities, blockage, etc. of upstream stages. If a designed blade row does not perform as intended, velocity components could become altered, causing downstream stages to become mismatched. These downstream stages then operate at an off-design condition, which can compound across stages, creating a detrimental, unintended effect on major performance metrics such as pressure ratio, mass flow rate, stall margin, and overall efficiency for the stage and for the entire machine.

Introduction to Aspect Ratio

       Aspect ratio, the ratio of the blade height (span) to blade length (chord), shown in Figure 1.6, plays a crucial role in the development of spanwise mixing. Turbomachines of the past typically employed a high aspect ratio design (greater than 4) which resulted in very efficient designs that are still in use today (Wennerstrom, 1990). The idea behind this design trend was that with a fixed rotational speed and loading, if the blade height was increased and blade length was decreased, a shorter and lighter design could be produced.
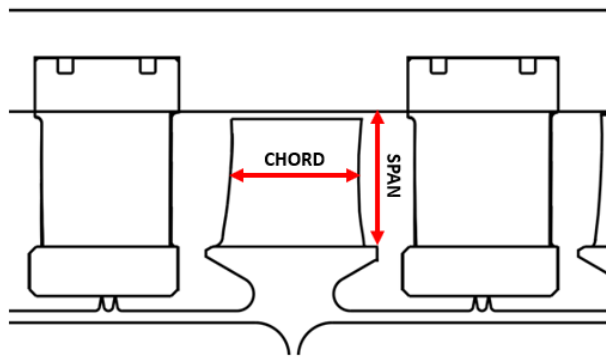
Figure 1.6. Blade aspect ratio in an axial compressor.

       An additional advantage with designing the blades in this way was that aerodynamic considerations could be greatly simplified by neglecting three-dimensional effects. This was especially useful in the computational methods that were used to predict aerodynamic performance to a high degree of accuracy with minimal effort. However, this simplicity came at the cost of needing to better address structural considerations as the longer blades associated with these early designs became highly susceptible to large blade deflections and high cycle fatigue failures. The longer blades also resulted in limited operating range through decreased stall margin, causing the turbomachine to encounter flow separation close to the intended design condition.

       To address these structural and operational concerns associated with high aspect ratios, turbomachinery designers began to experiment with lower aspect ratios to see what they could achieve in terms of aerodynamic performance. They began slowly working towards low aspect ratio (classified as less than 2.0) designs through shortening the blade height and lengthening the blade chord. While this would create a longer turbomachinery section, the circumferential diameter would be much smaller, still allowing for an overall smaller and lighter engine. Many studies

throughout the 1950's like Standahar and Geye (1955), Kussoy and Bachkin (1958), Young (1958), and Swan (1958) showed that with intermediate aspect ratios (between 2 and 4), there appeared to be a large increase in pressure rise at stall and in the stall margin itself, with a slight increase in efficiency. However, as the endwalls were now close enough together to affect one another, this design change resulted in the need for a better understanding of the aerodynamics to discover why these performance metrics were improving.

Significance and Impact of Aspect Ratio on Modeling

While the impact of spanwise mixing has been known to affect turbomachinery performance, its presence was far less significant with the higher aspect ratio blading used in the decades before the 1960s. Since that time, a gradual trend has occurred toward reducing the size and weight of aircraft-based gas-turbine engines to make them lighter, while increasing their bypass ratio. The bypass ratio is a ratio of the mass flow rate going through the bypass section of the engine, which contributes primarily to the thrust, to that going through the core, which is used to power auxiliary systems. In reducing the size of the engine core, a larger volume of air can bypass the core, leading to improved, propulsive efficiency of the engine. To achieve this, a move toward lower aspect ratios was made with little consideration at the time for how the internal aerodynamics of the engine would be affected. Somewhat unexpectedly, early multi-stage designs with low aspect ratio blading performed better than expected, as they were less susceptible to mismatching of incidence angles and maintained repeating stage conditions.

To better understand the aerodynamics involved with turbomachinery designs, two-dimensional, throughflow codes, established as an integral part of the design process, were not able to accurately predict the flow through the lower aspect ratio blading. Throughflow codes were initially created and developed to numerically predict and compare experimental results to cut cost and time in the engine development process, particularly for the embedded turbomachinery elements. These 2D codes were treated as inviscid, meaning that the bulk of the flow was treated as having no viscosity and thus, no resulting shear layers. However, to get accurate predictions, it was necessary to include losses from viscous effects in regions surrounding the bulk flow and consider the effects of secondary flows. The typical approach to accounting for these secondary flows and the resulting losses involved using correlations derived from experimental data to predict

how far downstream flows would mix out and what shape the spanwise profile would take (Cumpsty, 1989).

Typical losses observed in turbomachinery are generally characterized into 2 different categories based on viscous effects that are present in the flow: profile losses based on blade row parameters, and endwall losses which consider geometric considerations and loading effects (tip clearance, aspect ratio, loading condition, etc.). Profile losses are a result of boundary layer interaction on blade surfaces, their separation, and dissipation within the wake.

Due to the nature of building and implementing these loss correlations, 2D throughflow models, discussed in the following section, were originally only used to analyze peak loading/design conditions or lower throttling positions. They incorporated an overestimated profile loss and underestimated endwall loss to achieve a reasonable pressure distribution that could come close to matching experimental results. However, this estimation in loss also resulted in a highly inaccurate temperature distribution across the spanwise direction, indicating that throughflow codes were not able to completely resolve the loss distribution throughout the spanwise direction.

After examining the flow field more closely, experimental results for low aspect ratio blading did not match quite as well with previously developed codes, models, and predictions. With the endwalls much closer together on lower aspect ratio blades, stronger secondary flows were likely the culprit behind the difference between experimental and numerical results. Thus, the tracking of secondary flows became more significant and the generally accepted assumption that flow did not exchange mass or momentum in the spanwise direction began to break down. While many studies were performed on secondary flows and their impact on turbomachinery throughout the 1950s (Carter, 1946; Dean, 1954; Hawthorne, 1955), the general theory was not fully applied to practical 2D throughflow codes and applications until much later.

Inception of Spanwise Mixing

Initial spanwise mixing ideas began in the early 1940's. Through a study (Howell, 1945) on the axial velocity progression through a six-stage compressor, spanwise profiles of axial velocity were collected at different axial and radial locations throughout the compressor. The spanwise profiles became gradually less uniform throughout each stage which indicated the presence of loss in certain regions (calculated as 2% near the endwalls, 4% due to profile loss, and 4% for secondary flows – based on a compressor with 90% efficiency) and seemed to mix out

throughout downstream stages. For example, while there was a large difference between the endwalls and mid-span in the spanwise velocity profiles in the first few stages, after the fourth stage, there was little to no variation. The ability to achieve this repeating spanwise profile condition after a few stages suggested that some sort of redistribution of entropy occurred throughout the spanwise direction to prevent any further buildup and progression of loss. The results of this study launched an investigation into what mechanism was causing this redistribution of velocity and how other information (temperature, pressure, efficiency) migrate between mid-span and the endwalls.

The development of 2D throughflow models emerged as a tool that could be useful in explaining this phenomenon. Additional inputs were still required to help tie these models to physical experiments to achieve acceptable predictions of the flow behavior. With the highly complex flows observed in turbomachinery designs, empirically derived approximations based on existing experimental data were traditionally used as initial inputs and relied upon to provide an estimate for the associated losses. However, these approximations can sometimes lead to unsatisfactory results when applied to a broad range of turbomachinery designs, as the blade geometry and aerodynamics involved can differ significantly, requiring the need for a vast array of experimental data or a versatile enough approximation to account for many different designs.

As a result of early investigations (Tipton, 1968 and Hearsey, 1975), industry and academia started to research spanwise flow migration. During the late 1980s, there were three primary experimental contributors to the discussion on what specific mechanisms could drive the inception of spanwise mixing: Adkins/Smith of General Electric, Gallimore/Cumpsty of Rolls-Royce, and Wisler/Okiishi of General Electric and Iowa State. Throughout the 1960s, tests on a multi-stage axial compressor at General Electric were exhibiting different stagnation temperature and pressure profiles than were predicted. Furthermore, contrary to typical designs, a higher loss coefficient was observed near the mid-passage, which was unexpected since the endwalls generate most of the loss. Spanwise mixing was thought to be the culprit as higher loading conditions and lower aspect ratio blading were used in this compressor design than was previously traditional at that time. Adkins and Smith (1982) deduced that the hotter fluid located closer to the endwalls was slowly carried to mid-span throughout the later stages of the turbomachine via secondary flows. Using experimental data and their hypothesis, Adkins and Smith developed a method to calculate

the magnitude and effect of secondary flows on the performance of this multi-stage compressor to improve throughflow calculations and account for spanwise redistributions.

By closely examining each of the secondary flows that would affect the flow in the spanwise direction (tip leakage flows, boundary layer interactions, hub/tip separation, etc.), empirical models were derived to determine how quickly the secondary flows would convect both axially and in the spanwise direction. Endwall losses were characterized through tip clearance, blade, aspect ratio, and loading condition parameters (Smith, 1970), and profile losses (Koch and Smith, 1976) were characterized by blade shape and cascade parameters (solidity, blade thickness, velocity triangles, Mach and Reynolds numbers, etc.). The method correctly accounted for spanwise mixing on a few tested compressor designs. Many of the discrepancies in flow properties between the experimental and computational data were definitively driven by secondary flows. This was especially the case in the rear stages of the compressor, as the observed mixing became more complex and affected the entire span, particularly with respect to temperature.

Another important study by Gallimore and Cumpsty (1986), approached spanwise mixing from a different perspective and offered a counterargument to the theory that fluid migration was solely driven by secondary flows. Other experimental studies (Wagner et al., 1985 and Dring et al., 1979) showed significant amounts of spanwise mixing still occurred in the turbomachines that they tested but with little to no secondary flow contributions present. These studies concluded that more of a random, diffusion-like process was causing high loss to spread in the radial direction via boundary layer growth or diffusion.

While the results were similar for both compressor designs that were tested, losses spread in more of a random and diffusion-based fashion rather than the more predictable, deterministic fashion due to secondary flows, as suggested by Adkins and Smith. The observed levels of mixing were significantly evident through the entire span, which helped to stress the importance of needing to account for the spanwise mixing in throughflow codes. To better explain how turbulence was affecting the flow, further investigations into the various sources within the flow (wakes, unsteadiness, tip leakage flows, etc.) were carried out - all of which were thought to contribute to spanwise mixing.

Through this experimental work on two different compressor designs, Gallimore and Cumpsty dismissed the secondary flow theory and reasoned that secondary flows were not nearly as dominant as turbulent diffusion in the role of spanwise mixing. Their own model was produced

to develop a mixing coefficient based on stage geometry, loss, and loading condition, which helped to improve throughflow calculations (Gallimore, 1986). Their spanwise mixing model incorporated a solely turbulent diffusion process with no influence from secondary flows and focused losses more toward the endwall regions than traditional throughflow calculations. The model also helped to accurately reconcile differences between previous computational models and experimental data, particularly in terms of calculating more accurate compressor efficiencies.

With two conflicting arguments as to which was the most dominant mechanism of spanwise mixing – Gallimore and Cumpsty with turbulent diffusion, and Smith and Adkins with secondary flows – a third investigation was completed by Wisler, et al. (1987) to try to resolve the two opposing theories. They arrived at a few important conclusions. First, they discovered that both turbulent diffusion and secondary flows were equally important contributors to spanwise mixing, but their relative dominance was dependent on several different factors. From a purely spatial perspective, in the endwall region and near the blade surface specifically, secondary flows were highly dominant and produced a spanwise mixing effect that was generally at least equal to, if not more than, that of turbulent diffusion. However, in the freestream region, turbulent diffusion was overwhelmingly dominant. In terms of circumferential location, secondary flows generally carried flow inward from the endwall region toward the freestream flow, except for the rotor suction-side wakes, where the flow was diffused outward in the opposite direction.

Secondly, while these two mechanisms both strengthened with higher loading, their relative importance differed with loading condition, blade geometry, and compressor design. For example, from Adkins and Smith's hypothesis, at design point conditions, turbulent diffusion in the freestream region was much lower than at the endwalls, where secondary flow effects dominated significantly. However, with increased loading, the freestream was less distinguishable, creating a highly random and diffusive process across the blade span, supporting the original observations of Gallimore and Cumpsty.

Thus, the investigation by Wisler, Bauer, and Okiishi concluded that it was necessary to incorporate both secondary flows and turbulent diffusion as spanwise mixing mechanisms into a throughflow model to accurately describe the nature of flow occurring within a multi-stage turbomachine. Based on their observations, in general, lower momentum fluid located throughout the endwall region convected toward the freestream primarily through secondary flows, with a slight influence from turbulent diffusion in the freestream region. Then, as the convected flow

entered the rotor, it was spread circumferentially through a turbulent diffusion process. Meanwhile, in addition to circumferential movement, the low-momentum flow within the suction side rotor wake was spread outward, toward the endwalls, where it then encountered the downstream stator and repeated the process. Their results validated and settled the debate between the different hypotheses and verified that both were equally important in understanding and describing the phenomenon of spanwise mixing.

Computational Fluid Dynamics Developments for Spanwise Mixing

As mentioned previously, with the introduction of any new turbomachinery design, some form of a two-dimensional throughflow code is typically used to predict the aerodynamics associated with multiple blade rows. This 2D code offers an important compromise between the substantial amount of time and monetary resources required to perform a 3D CFD calculation and the overly simplistic, yet necessary, 1D approach. The 2D throughflow code accounts for both the meridional plane (radial/axial direction) and the blade-to-blade plane (axial/circumferential direction). This extra dimension allows for important characteristics to be considered such as velocity triangles and annulus geometry, which can both contribute to variation of the flow in the spanwise direction. Other, more complex flow phenomena like secondary flows, centrifugal forces, and boundary layer cross flows are also important to the 2D throughflow code and models are continuously evolving to better account for these aerodynamic effects. As a result, many attempts were made in the early 1990's to reconcile the turbulent diffusion and secondary flow mechanisms into a single 2D throughflow code that could adequately predict spanwise mixing.

Overall, even though each throughflow code developed during this time frame was created in a different way or modeled after different phenomenon, they were all able to reasonably match the experimental data that they were being compared to, indicating that spanwise mixing is the result of many different mechanisms and that employing any mechanism is a vast improvement over not employing any mechanism. However, with the 3D complexity of the flows involved in spanwise mixing and its effects, models that more accurately incorporated the true geometry and physics of the flow-field environment would be the most reliable for contributing to the development of new engine designs (Wennerstrom, 1991).

De Ruyck and Hirsch (1988) were one of the first to enhance the traditional computational method at the time, which considered separate 2D flows (those in the circumferential and

meridional directions) through superimposing additional secondary effects, often based off experimental data correlations, to account for those not covered by the original flow structures. Radial velocities associated with secondary flows were calculated using a throughflow computation on the primary flow and effects from various secondary flow sources (non-free vortex, endwall boundary layers, profile boundary layers, and wakes) were slowly superimposed onto the solution using continuity, passage-averaged vorticity, and transport equations. As a result, turbulent diffusion was the only required empirical value for their throughflow code to run effectively. In comparing the computational results to experimental data from a linear cascade and a rotor, it was deduced that turbulent diffusion was important, but secondary flow-driven mixing was more significant in the presence of untwisted blading (where free vortices were non-existent) and high loading (greater than 54° incidence) scenarios. Spanwise mixing only became detectable when radial flow velocities exceeded about 5% of freestream velocities, and that turbulent diffusion was most prominent in regions with viscous layers and wakes.

While Li and Chen (1992) worked to develop their own 2D throughflow model to adequately consolidate the different kinds of spanwise mixing mechanisms for a cheaper and less-time consuming prediction tool. A basic equation system was developed which could account for molecular motion, turbulent diffusion, and secondary flows in the form of circumferential non-uniformities for low-speed turbomachinery. By incorporating the two main forms of spanwise mixing (turbulent diffusion and secondary flows) into a single set of equations, better agreement with experimental results were achieved than the original codes of Gallimore/Cumpsty and Adkins/Smith. Any form of over-mixing or under-mixing could significantly affect radial temperature and pressure profiles. However, while Li and Chen believed that their model had the potential to accurately account for spanwise mixing in multi-stage transonic and supersonic compressors, an appropriate model was still necessary to obtain reasonable mixing coefficients for their code to be successful.

At the same time, Dring (1992) also worked on comparing mixing coefficients between the secondary flow model of Adkins/Smith and turbulent diffusion model of Gallimore/Cumpsty and applied them to different loading conditions. Additionally, his study focused on examining the role of spanwise mixing on the pressure forces and change in momentum on the blades using the two different models. While the turbulent diffusion model resulted in higher levels of mixing compared to the secondary flow model, higher loading conditions caused an opposite effect, particularly near

the hub region. Additionally, the existence of an axial mixing coefficient was established, as radial velocities seemed to decay with axial distance, and the hub corner separation strongly impacted radial mixing.

Another theoretical model (Imanari, 1994) was created to better observe the role of turbulent diffusion in spanwise mixing by looking at the periodic incoming wakes deviating from the repeated stage condition (used in Gallimore and Cumpsty's analyses) and adopting a purely theoretical approach (rather than using empirical data like De Ruyck and Hirsch). An investigation on spanwise mixing in a single stage compressor design without an IGV successfully predicted spanwise mixing coefficients across the stator with good agreement to the results of De Ruyck. Blade wakes impacted the tip clearance vortex or boundary layers in the endwall regions, which in turn, affected the spanwise mixing near the tip region, especially with increased tip clearance.

While most computational and experimental studies only focused on few loading conditions, Leylek and Wisler (1991) wanted to observe how several loading conditions could affect the relative dominance of the mechanisms involved with spanwise mixing and attempted to back up their work with 3D RANS computations. Similar to their predecessors, an ethylene gas-tracer, 3D hot-wire anemometry, and traditional pressure instrumentation were used to investigate the development of spanwise and passage-wise flows and diffusion level over different loading conditions. While both secondary flows and turbulent diffusion were equally important to explaining the occurrence of spanwise mixing, loading condition and geometric configurations significantly affected their relative dominance. Specifically, secondary flows were found in specific areas throughout the passage (endwall regions, blade surfaces) while turbulent diffusion could be found everywhere. Three-dimensional RANS computations that were performed had success in accounting for the off-design conditions that were tested, adding confidence, and reinforcing the effectiveness of this CFD code to predicting spanwise mixing effectively. This was an important development as 3D computational models seemed to be the only capable tool of combining the two different mechanisms in an accurate and predictable way.

Through this research in computational predictions of spanwise mixing, it was ultimately concluded that 3D RANS calculations would be essential to the compressor design process to determine the mechanisms for spanwise mixing and to adequately predict their effects on performance. Additionally, unsteady 3D URANS models offered the best resolution in resolving experimental data compared to steady RANS models (Goto et al., 2019). Through accurately

predicting and accounting for flow properties in the spanwise direction, individual compressor stages could be matched more successfully leading to better overall performance. With the complexity and resources involved in producing steady and unsteady 3D RANS computational models, many engine companies already had constructed their own proprietary models as part of their engine development process and began to individually look for ways to adapt their individual 2D through-flow codes to try to resolve what they believed to be the most important aspects of spanwise mixing.

A few recent studies (Cozzi et al., 2019 and Cozzi et al., 2018) brought this topic back to light for the purpose of fine-tuning steady 3D RANS simulations to better match the results from unsteady RANS simulations or experimental measurements. They noticed that unsteady RANS CFD was not typically a part of the current industrial standard in a typical engine design cycle due to computational cost, effort, and time. Steady CFD was more widely used, which employed mixing planes between blade rows. With the large influence of tip clearance in rear compressor stages with low aspect ratios, the vorticity was being washed out between blade rows through the mixing plane averaging technique. As a result, this technique was vastly underpredicting the radial mixing observed in steady RANS simulations compared to unsteady simulation and experimental results. To account for this, they developed a method to tune the steady RANS model to better reflect the correct vorticity levels that were originally washed out. This was achieved by enhancing the turbulent diffusion through applying different factors of eddy viscosity on the steady model to improve the diffusion of properties throughout the spanwise direction. When compared to unsteady RANS results and experimental data, they achieved much closer efficiency, pressure ratio and radial profile predictions using the modified steady RANS simulation.

1.2.3 Efficiency Basics and Overview

The fundamental premise behind calculating the efficiency of a turbomachine, and more specifically a compressor, comes from taking the ratio of different work/power values (Borgnakke & Sonntag, 2019). For instance, the specific work required to achieve a given total pressure ratio during the compression process of an ideal machine, compared to that of the specific work required of the actual machine to achieve the same total pressure ratio,

$$\eta = \frac{\int_1^x v_o \, dp_o}{\dot{W}_{actual}} = \frac{\dot{W}_{ideal}}{\dot{W}_{actual}}. \tag{9}$$

The actual work is more straight-forward since it is taken directly from the experimental measurements of the machine through shaft power (torque-based) or enthalpy change (aerodynamic-based) of the flow. However, this also means that these actual power values inherently include any aerodynamic, mechanical, and thermal losses. On the other hand, several types of efficiency arise depending on the different assumptions and characteristics that are given to the ideal machine, which is often hard to characterize. The most common ideal machines follow an isentropic process, an isothermal process, or a polytropic process, as shown in the h-s diagram in Figure 1.7.
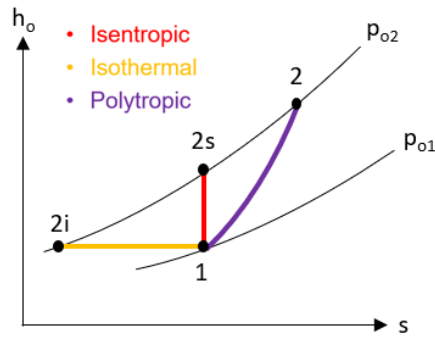
Figure 1.7. H-s diagram for an ideal compression process.

Isothermal Efficiency

With isothermal efficiency, the ideal compressor operates at a constant temperature from state 1 to 2i, where the work is either input slowly enough that it remains at equilibrium with its surroundings, (fully diabatic and heat transfer goes into environment or reservoir), or the volume of the gas can decrease to compensate for the increased pressure. This type of process is more common for positive displacement compressors and is not very applicable to dynamic compressors due to the speed at which the flow is compressed. As a result, isothermal efficiency is not covered in this research investigation.

Isentropic Efficiency: Flow-Based Approach

Isentropic efficiency is one of the most traditional ways to measure aerodynamic performance, and the ideal machine work is considered both adiabatic and reversible, following a line of constant entropy from state 1 to 2s. Thermodynamically, this represents the absolute minimum amount of work that could be input into the compressor to achieve the desired total pressure ratio. This is because with an adiabatic assumption, no heat transfer takes place, and with a reversible assumption, no losses occur in the ideal machine. Thus, isentropic efficiency only indicates the irreversible losses associated with the aerodynamics involved with compressing the flow and is described by relating the enthalpy rise between the constant entropy exit state and real entropy exit state for the same stagnation pressure rise,

$$\eta_{isen} = \frac{\dot{W}_{ideal}}{\dot{W}_{actual}} = \frac{h_{o2,s} - h_{o1}}{h_{o2} - h_{o1}}. \qquad [10]$$

This equation is valid for a real gas, but with the further assumption that little temperature variation takes place across the compressor, the ideal work can be simplified to resemble a perfect gas. This means that the specific heat is constant (calorically perfect) and the gas is thermally perfect. With these assumptions, the isentropic efficiency simplifies to the traditional formula for isentropic efficiency for a perfect gas,

$$\eta_{isen} = \frac{\dot{W}_{ideal}}{\dot{W}_{actual}} = \frac{\left(\frac{P_{o2}}{P_{o1}}\right)^{\frac{\gamma-1}{\gamma}} - 1}{\frac{T_{o2}}{T_{o1}} - 1}. \qquad [11]$$

However, Lou et al. (2014) showed that using this perfect gas assumption often overestimates the compressor efficiency while the real gas model results in a more accurate efficiency. This discrepancy grows with increased pressure ratio. Therefore, this study focuses on the use of a real gas analysis in evaluation of the computational and experimental data.

While the traditional isentropic efficiency equation is commonly used throughout industry, an isentropic compressor process is fundamentally based on removing the heat transfer terms from the first and second law of thermodynamics. One of the common flaws in this assumption is that if a compressor is not adiabatic, it should not be compared to a compressor that is – it should be

compared to a compressor that is diabatic as there is no way to recover the heat loss/gain that occurs. As discussed in Section 1.2.1, heat transfer often leads to a decrease in efficiency as it manifests in additional temperature rise and can cause a preheating effect within the system.

In a study by Casey and Fesich (2010), they noted that with diabatic flows, the measured enthalpy and temperature rise overestimate the actual work input and needs to be removed when comparing to an adiabatic machine. One common way in which this is achieved is to simply subtract any measurable heat transfer from the actual work,

$$\eta_{isen,1-2s} = \frac{h_{o2,s} - h_{o1}}{(h_{o2} - h_{o1}) - q_{12}}.$$

[12]

This correction helps to address the difference between the adiabatic nature of an isentropic ideal compressor and a real, diabatic compressor. However, while the result better represents the actual efficiency of the compressor, it is often difficult to characterize the heat transfer effects of the entire process. A common way to address this is by assuming that the diabatic compression process between states 1 and 2 is broken up into smaller parts, as shown in Figure 1.8. Only heat transfer takes place between states 1 and 1'. Adiabatic and irreversible compression takes place from states 1' to 2', and heat transfer occurs between states 2' and 2.
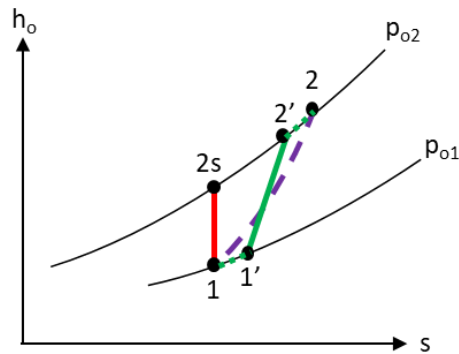
Figure 1.8. H-s diagram comparing the actual compression process (1-2) to a piecewise compression/heat transfer approach (via 1-1', 1'-2', and 2-2').

While this method is more correct, it still relates an "adiabatic," irreversible machine to one that is both adiabatic and reversible. As a result, the most correct method to correctly characterize the ideal machine would be to compare to one that also follows an irreversible process,

43

but with the isentropic temperature change solely related to the actual work input of an isentropic process. In other words, the ideal machine would be one that still included losses but to the most efficient extent possible. This ideal compression process is shown in Figure 1.9, through states 1 to 2qs, where the process from 1 to 2s is the traditional isentropic compression process, and the process from 1 to 2 is the actual compression process.
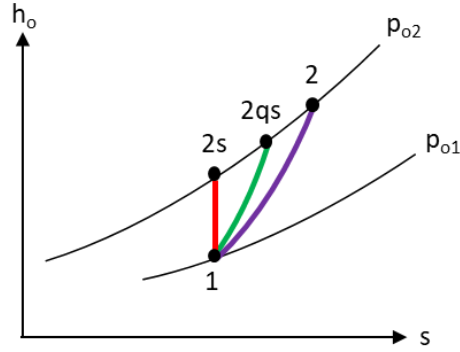
Figure 1.9. H-s diagram comparing an ideal isentropic compression process (1-2s), an ideal diabatic and irreversible process (1-2qs), and the actual compression process (1-2)

This ideal process is described through the following equation,

$$\eta_{isen,1-2qs} = \frac{\int_1^{2qs} v_o dp_o}{(h_{o2} - h_{o1}) - q_{12}}. \tag{13}$$

While this would be the most appropriate way to correct efficiency, there is inherent difficulty in integrating along the path from 1 to 2qs, so the path from 1 to 2s is generally still used to describe the ideal process in terms of isentropic efficiency. Polytropic efficiency, discussed in the next section, addresses this discrepancy, and attempts to get closer to describing the ideal process that occurs from 1 to 2qs.

Isentropic Efficiency: Torque-Based Approach

Another approach to isentropic efficiency involves using a torque-based approach instead of the aerodynamic-based enthalpy rise. Shaft power is usually easy to measure and is calculated from measured shaft torque and speed. It is typically a more direct indication of actual power used

to produce the desired compression as it includes all the frictional losses (windage and bearing or facility losses) associated with the compressor. These losses that are characterized through a combination of correlations or through running a bladeless compressor and establishing a "tare" torque associated with operation within the facility.

A relationship between the aerodynamic-based and torque-based work exists (Hall, 2011) through correcting the shaft work with frictional losses and the aerodynamic enthalpy rise with heat transfer,

$$\dot{W}_{shaft,\ measured} - \dot{W}_{friction} = \dot{m}(h_{o2} - h_{o1}) \begin{cases} + Q_{removed} \\ - Q_{added} \end{cases}.$$
[14]

While the torque-based isentropic efficiency is independent of direct heat transfer effects, a small correction must be made to account for the entropy loss associated with heat transfer. This correction, initially developed for turbine performance by Atkins and Ainsworth (2012) and applied in studies by and Yasa et al. (2007) and Maesschalck et al. (2014), begins with the actual shaft work with any facility/windage losses subtracted, referred to as "indicated efficiency (η_q)."

Adapting their work for use in compressors, the compression process begins with the inlet to the rotor (state 1), where work from the rotor is put into the flow, resulting in an increase in pressure, temperature, and energy. In a multi-stage, non-adiabatic compressor, heat is input/output into the flow through the blade rows and end-walls from upstream/downstream influences. Between state 2, located at the exit of the rotor or inlet to the stator, and state 3, located at the exit of the stator passage, the flow decelerates as it is turned back toward the axial direction. This results in an increase in static pressure but decrease in total pressure due to aerodynamic losses. In the adiabatic case, no work is performed across the stator, so the total temperature remains constant. However, in the non-adiabatic case, heat transfer takes place between the metal surfaces and the flow, resulting in an increase/decrease in total temperature. This is shown in Figure 1.10, and the h-s diagram for the stage, Figure 1.11.

Figure 1.10. Heat transfer input and work input for a compressor stage.

Figure 1.11. H-s diagram for an individual stage with heat transfer effects included.

As shown in Figure 1.11, the work associated with the adiabatic compression process is comprised of both the isentropic shaft work and the irreversible work:

$$\dot{w}_{ad} = \dot{w}_{s,isen} + \dot{w}_{irr}. \qquad [15]$$

This results in the isentropic efficiency expression,
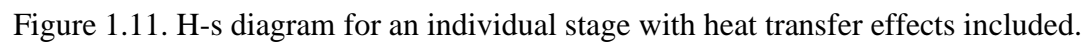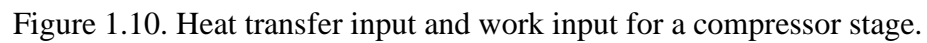
$$\eta_{isen} = \frac{\dot{w}_{s,isen}}{\dot{w}_{s,isen} + \dot{w}_{irr}} \qquad [16]$$

For the diabatic case, the difference between the rotor exit conditions for the adiabatic and diabatic states are unknown. Using an energy balance on the rotor control volume, the isentropic work becomes:

$$\dot{w}_{s,isen} = (\dot{w}_{s,ad} + \dot{q}_{1-2} + \dot{q}_{2-3}) - \dot{w}_{irr} - (h_{03,q} - h_{03,ad}), \qquad [17]$$

which leads to an expression for corrected torque-based efficiency for diabatic flows,

$$\frac{1}{\eta_{isen,corr}} = \frac{1}{\eta_{ad}} + \frac{\dot{Q}}{\dot{W}_{s,is}} - \frac{\Delta\dot{H}}{\dot{W}_{s,isen}}. \qquad [18]$$

The $\Delta\dot{H}$ term is included to correct for the difference in entropy between the diabatic and adiabatic cases and can be estimated to great accuracy through the expression,

$$\Delta\dot{H} = \dot{m}T_{03}\left(\frac{\dot{q}_{rotor}}{\frac{1}{2}(T_{01}+T_{02})} + \frac{\dot{q}_{stator}}{T_{02}}\right). \qquad [19]$$

Polytropic Efficiency

Finally, polytropic efficiency compares the ideal work to that of a polytropic process (PV^n = constant), which more closely resembles the actual work of the compression cycle, particularly for compression with heat transfer. Specific values of n establish different heat transfer cases, with n = γ = Cp/Cv the closest to describing the real compression/expansion process. The polytropic efficiency is a ratio of the ideal, polytropic work to the actual work:

$$\eta_{poly} = \frac{\dot{W}_{ideal}}{\dot{W}_{actual}} = \frac{\dot{w}_p}{h_{out} - h_{in}} \qquad [20]$$

For a perfect gas, the specific heat ratio, γ, remains constant and results in a simplified form of the polytropic efficiency:

$$\eta_{poly} = \frac{\gamma - 1}{\gamma} \frac{\ln\left(\frac{p_{o,out}}{p_{oin}}\right)}{\ln\left(\frac{T_{o,out}}{T_{o,in}}\right)}. \qquad [21]$$

However, this relationship gets considerably more complicated for a real gas, which does not maintain a constant specific heat ratio and requires an iterative process to solve for polytropic efficiency. However, as shown in Casey (2007), if the actual fluid properties at the inlet and exit of the stage are known, a good estimation can be found using a small-scale polytropic process assumption. This is called an entropy-based polytropic efficiency.

$$\eta_{poly} = \frac{s_{1h} - s_{out}}{s_{1h} - s_{in}}. \qquad [22]$$

This efficiency uses a virtual state, shown in Figure 1.12, which is defined as the state that exists if work was input into the fluid but dissipated by losses so that no pressure rise occurs. In other words, the entropy property associated with the inlet pressure and exit enthalpy of the process: $s_{1h} = f(p_{o1}, h_2)$.
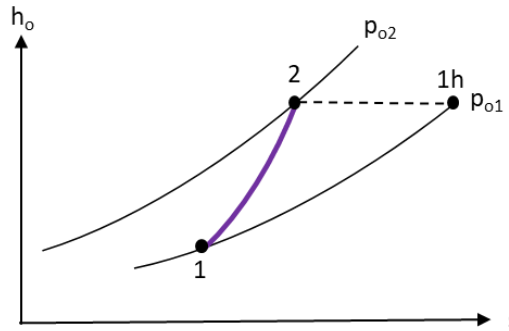
Figure 1.12. Virtual state used for polytropic efficiency analysis.

Finally, an analogous correction to isentropic efficiency can be made to produce a polytropic efficiency for adiabatic flow, which incorporates the difference in enthalpy rise coefficients discussed in Section 1.2.1 for turbocharger performance corrections,

$$\eta_{poly, ad} = \eta_p \frac{\lambda}{\lambda_{apparent}}. \tag{23}$$

1.3 Research Objectives

In a presentation by Cumpsty (2009), he discussed the lessons that had been learned across the years regarding 1D, 2D, and 3D flow and the role of CFD and experimental data in accurately predicting these flows. He noted that CFD has now transitioned to the point where 3D environments are now more accessible than ever, which is highly beneficial to recreating 3D flow phenomena and can help us to understand the complex flow physics in a reliable way. He also acknowledged that the most serious performance deficits observed today generally occur as a stage mismatch in the 1D flow analysis which is becoming increasingly difficult to meet as blades become more geometrically sophisticated. This desire to achieve high performance can sometimes push these metrics too far and cause deviations in 1D flow parameters that are detrimental to the overall design.

He also addressed the fact that while physical experiments still very much have a place in the design process as computational models for complex 3D flows are still evolving, they are now required to have more of a specific purpose to answer specific questions, particularly in the domain of high-speed, multi-stage turbomachinery. CFD and experiments must work together and be simultaneously presented in such a way that is targeted to understand and tackle a certain challenge. It is also increasingly important to supply a wholly inclusive and accurate geometry which considers annular shapes, blades, and any gaps or cavities to accurately capture the complexities that are trying to be understood today. This research investigation will follow his reasoning as it pairs both experimental and computational data to look at heat transfer effects on compressor performance of a high-speed, multi-stage compressor.

As shown in the literature, from the most basic analysis of the Brayton cycle, heat transfer is often assumed to be negligible when compared to the overall power input of the compressor and is completely valid when looking at the entire system in its most simplistic form. However, as engine developers are now striving for the smallest efficiency gains, what were once negligible thermal effects start to become more important. Even so, engine designers often use adiabatic boundary conditions for their computational models, which fail to include many phenomena that are evident in the literature, such as windage heating into the blade rows with shrouded stators,

preheating effects from downstream components, and environmental considerations. This adiabatic boundary condition is not necessarily chosen for its simplicity or ease in computational effort, but thermal boundary measurements are often not readily available from actual test cases. Thus, an objective of this research was to provide a comprehensive experimental dataset that maps the thermal boundary conditions within the stationary endwalls and blade rows within a compressor and compare it to an adiabatic boundary condition from CFD to observe the shortcomings that arise under this assumption. Other influences were also examined in the form of altering environmental, material, and geometric properties of the casing to explore their effects on compressor performance.

Additionally, throughflow codes and 2D computational models have inherent difficulty capturing the spanwise mixing of high-speed, multi-stage, low aspect ratio turbomachines, which can carry these thermal effects to unintended parts of the flow path. Another objective of this investigation was to computationally explore how thermal effects can propagate through the flow under enhanced spanwise mixing with the addition of turbulent diffusion for the purpose of tuning steady CFD models to better reflect the results measured in experiments. While previous studies have examined how enhancing spanwise mixing in steady CFD can help to better match experimental and unsteady CFD models, this study will focus on how the thermal effects from the endwalls propagate through the flowpath with different levels of spanwise mixing.

Finally, when comparing an adiabatic model to a real test facility, the use of adiabatic efficiency as a performance metric is not the most appropriate unless corrections are made to either the model or the experimental data to reconcile them both for comparison against the same ideal machine. This investigation provides guidelines for reconciling overall and interstage aeroengine compressor efficiency for heat transfer effects from the perspectives of aerodynamic-based enthalpy, torque-based shaft work, and polytropic efficiency. While elements of these have been applied to turbocharger applications, this is the first known application of these corrections to an axial compressor used for aviation or power generation applications.

Overall, this research offers an approach to understanding the impact of thermal effects on the interstage and overall aerodynamic performance of a high-speed, multi-stage, axial compressor. It not only provides a thermal boundary condition for validation of computational models, but it provides a better understanding of how different environmental, geometric, and material properties can affect the flow and performance of a compressor, along with how spanwise mixing can

enhance these effects. It also aims to reconcile the differences between computational models and experiment by quantifying the importance of boundary conditions and supplying ways to correct efficiency for heat transfer effects to better represent the ideal compressor to which the real compressor should be compared. Through providing this framework of quantifying how much heat transfer effects can affect the performance and efficiency of a multi-stage, high-speed compressor design, this work will offer a few insights into steps that gas-turbine engine companies can potentially take to improve their computational methodologies.

2. FACILITY OVERVIEW & METHODS

This research investigation took place at the Purdue 3-Stage (P3S) Axial Compressor Research Facility using the PAX200 compressor design. This section will fully describe the facility, its capabilities, and the compressor design that was used for this research. It will also provide a detailed overview of the recent upgrades that took place to prepare the facility for this study and highlight the experimental instrumentation, computational models, and techniques that were used to achieve the research objectives.

2.1 Facility Overview

The Purdue 3-Stage (P3S) Axial Compressor Research Facility, shown in Figure 2.1, features two axial compressors (denoted PAX100 and PAX200) that each resemble the rear stages of different Rolls-Royce high-pressure, compressor core designs. Used for jet-engine applications, the facility and compressors are geometrically scaled up in such a way that they still match operation-representative Mach numbers and Reynolds numbers. Each design features an aspect ratio less than 1.0 and with multiple stages and realistic flow conditions, the facility provides a unique environment to analyze stage interactions and flow effects to effectively validate computational design tools.

In the P3S facility, the three-stage compressor design under investigation is powered from the rear by an ABB 1,400 horsepower, alternating current motor and controlled manually from a control station outside of the test cell. Meanwhile, a liquid-cooled, variable frequency drive allows the motor to be kept within 0.01% of its intended programmable speed. Through a speed-increasing gearbox and a driveline featuring a torque meter and flexible disc couplings, the compressor can reach speeds up to approximately 8,250 RPM. The rotational speed is measured with an optical laser tachometer mounted over the high-speed output shaft on the gearbox, which also provides a once-per-revolution trigger to phase lock unsteady measurement systems to shaft position, allowing for tracking of individual rotor blades.
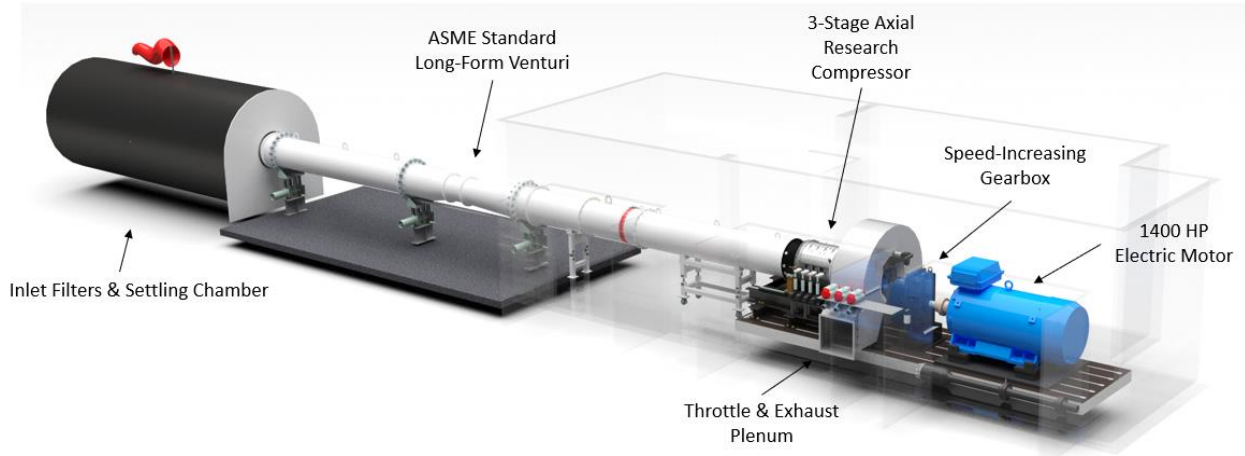
Figure 2.1. Overview of the Purdue 3-Stage Axial Research Facility.

Ambient air is drawn through a large settling chamber to isolate the incoming air from any crosswinds, and MERV 7 and MERV 8 filters are used to keep debris and particulates from entering the flow path. The incoming flow then passes through a reducing bell mouth, and aluminum flow straightening honeycomb before reaching an ASME standard long-form venturi mass flow meter. Three Rosemount 3051C high-accuracy pressure transmitters of different calibration ranges, paired with an upstream pitot-static probe, are used to measure stagnation pressure at the inlet and throat. These different calibration ranges (0-8 inches H2O and 0-11 inches and 0-13 inches H2O) were selected to cover the entire operating range of the compressor and ensure that the difference in pressure across the venturi is as accurate as possible, for different mass flow rates in the operating range.

Downstream of the venturi, the air then passes through an insulated circular duct section, 2 feet in diameter and 22 feet long, followed by a bullet-shaped nose cone located directly upstream of the compressor, shown in Figure 3.2. The nose cone contracts the flow area and directs the incoming flow to meet the inner diameter of the flow path, an annular area matching the blade height of the compressor. After passing through the compressor blading, the flow is exhausted through a sliding annulus throttle controlling the backpressure applied to the entire system. After passing through the throttle valve, the exhaust air exits the building back to ambient conditions through a scroll collector. Additional specifics associated with the layout of the facility and previous research can be found in Talalayev (2011), Kormanik (2017), and Kormanik et al. (2019).

For this facility, instrumentation may be inserted into several fixed positions around the circumference of the compressor casing. This includes total temperature/pressure rakes, hotwire/cross-film, steady/unsteady pressure probes and more. To account for the presence of stator wakes and potential fields, the stationary vane rows (IGV, S1, S2, and S3) are each circumferentially-indexable using linear actuators. Precision string potentiometers provide live feedback control of the stator positions, and the vane movements during each test are consistent for all vane rows to ensure no clocking effects are introduced. Three different aluminum casings (1.5%, 3%, and 4% of initial blade height) are available in the facility and are easily interchangeable to perform studies involving different tip clearance effects. The 1.5% casing was used for this study as it is the traditional baseline casing for both compressor designs. Furthermore, each casing features replaceable windows along the casing wall which can be used for optical access or over-rotor measurements including unsteady pressure and blade vibration.

2.1.1   PAX200 Compressor Design

This research investigation was performed on the PAX200 compressor series, shown in Figure 2.2. PAX200 is a Rolls-Royce compressor design with sophisticated, three-dimensional blade geometry, representative of an axial-centrifugal core design for use in modern-day Rolls-Royce engines. A "baseline" model (PAX200) was manufactured, consisting of a converging annulus, three rotor blade rows, three stator vane rows, and a variable IGV. A technology build was also designed and manufactured at the same time as the baseline model. The technology build features additional blade rows that can be interchanged with elements of the baseline model, including geometric features to mitigate loss associated with rotor tip leakage flow and improve stator diffusion and pressure recovery of the stage. The baseline blisk spacers incorporate knife-edge seals and can be replaced to allow for cantilevered stators to replace the original shrouded stator design for S1 and S2.
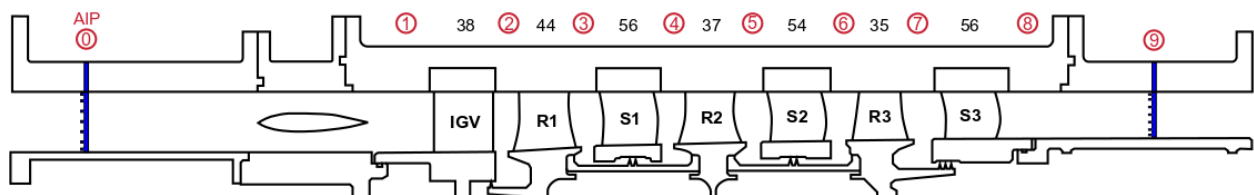
Figure 2.2. Compressor design layout and axial station nomenclature.

2.1.2 Structural Improvements

Before this investigation took place, a structural redesign occurred with the facility from 2018-2020 to accommodate the PAX200 compressor design. Compared to PAX100, the resulting higher power and thermal loads of PAX200 prompted significant upgrades of the structural components of the compressor test section. The only remaining components from the original facility at Iowa State University in the late 1980's were finally retired, and a complete redesign of the support mechanisms and driveline occurred. Florida Turbine Technologies, an engineering consultant, was contracted for the redesign and the new structural components are shown in Figure 2.3. These upgrades were necessary to add structural support and rigidity to the facility to accommodate the increased power and torque of the PAX200 compressor and maintain shaft alignment. The new support structure was also designed in such a way as to provide for mean line radial expansion to account for additional heat generation with the higher pressure ratios associated with the new compressor design.
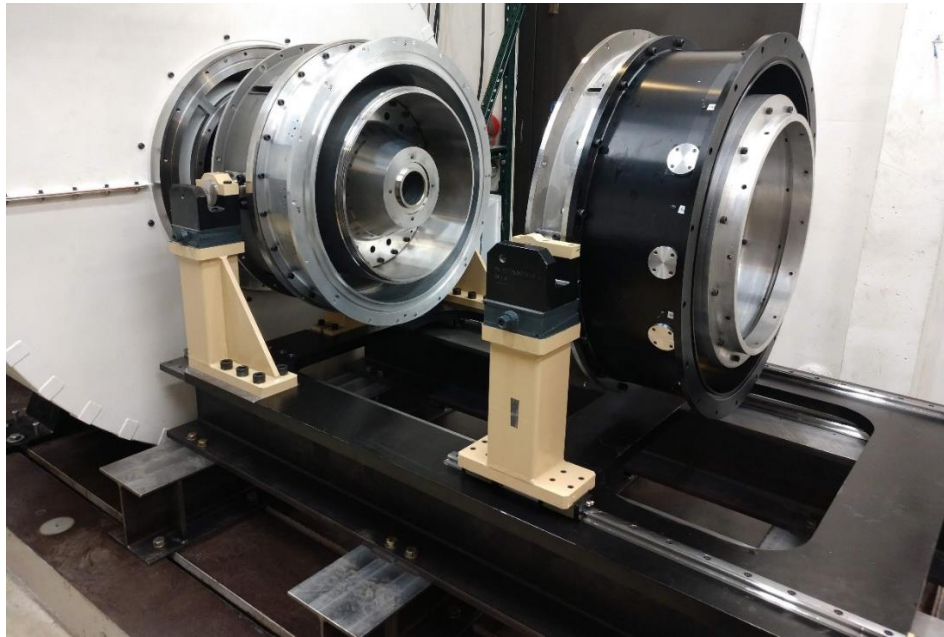
Figure 2.3. New structural supports added to the facility in 2020.

The primary elements of the new support structure included a large sliding plate set on top of the existing I-beam structure to ease with assembly and disassembly, and a front and aft frame to better support the compressor and maintain alignment with the higher power and speeds required

for the new compressor. The aft frame was fixed to the plate to provide a rigid datum, while the front frame was placed on sliding rails to allow for axial growth of the compressor casing. Both frames were supported from the side to maintain a mean line position and allowed for fine tuning of pitch, vertical, and horizontal alignment of each of the components. Finally, a centering strut ring was connected to the exhaust to ensure a uniform and centered exit flowpath and to support the cantilevering of the exhaust to the rear bulkhead. Previously, the exhaust was fixed to the floor, but during the redesign, the exhaust was moved to a cantilevered position to allow for radial expansion with temperature. The new support structure elements also incorporated extra instrumentation ports for static pressures and necessary routing ports through the struts for additional instrumentation capabilities with the implementation for a future slip ring.

The inlet ducting was retained from the existing facility, but adaptations were made to support thermal imbalances between outdoor and indoor temperatures for the purpose of achieving higher precision alignment during seasonal changes. Constant-spring pipe supports, shown in Figure 2.4, replaced the rigid inlet ducting supports located outside of the building to accommodate thermal movement in the vertical direction from frost heaving of the cement underneath the supports in the winter. The springs supports also feature sliding contacts between the legs and the ducting to accommodate thermal growth in the axial direction and any misalignment in the horizontal direction. A second filter was also added to the settling chamber to provide additional filtration with the higher mass flow rate of the new compressor design. The AIP inlet duct section was also replaced and designed in such a way that it could accommodate future inlet distortion studies with a screened inlet traverse.

Figure 2.4. Outdoor inlet section with addition of constant-spring support legs.

Inside the test cell, adjustable legs replaced the rigid legs on the existing inlet ducting pieces to address thermal growth in the vertical and horizontal directions. Finally, a decoupled inlet transition, achieved by a gap with a rubber seal ("rubber boot") was implemented into the removable inlet duct section to accommodate thermal growth in the axial direction. These elements are shown in Figure 2.5.

Figure 2.5. Adjustable leg supports for indoor inlet ducting and rubber transition for thermal growth in axial direction.

2.1.3 Driveline Improvements

To maintain accurate alignment of the driveline components with the higher power/torque requirements, new driveline components between the gearbox and compressor was installed in the facility. This included the introduction of a new support structure, designed by Torquemeters LTD and manufactured by Chesterfield and Engineering, flex couplings from Bibby Turboflex, and the installation of an ET2350 Torquemeter from Torquemeters LTD. These components replaced the existing components and bridge that were installed in 2016 (referred to in Kormanik, 2017) and are shown in Figure 2.6.

Figure 2.6. New driveline for the P3S facility consisting of flex couplings, torquemeter, and support structure.

To support the higher temperatures produced by the PAX200 compressor, the elements of the driveline were "hot" aligned to ensure that correct alignment would be achieved at high loading and speed conditions. This was done by deliberately misaligning the components in their cold state based on their estimated growth rates to ensure that they would thermally expand into their correct position. For example, after experimental tests showed that the gearbox was one of the hottest components in the driveline, the torquemeter shaft was aligned to be slightly higher than the gearbox shaft so that the gearbox could grow to match its vertical height. The compressor shaft

was then aligned to a vertical height 0.012" above the gearbox, but still below the torquemeter shaft. Meanwhile, the motor shaft alignment to the gearbox was kept in perfect alignment at cold conditions.

2.1.4   Additional Upgrades

With the major structural and driveline improvements to the facility, an opportunity presented itself to upgrade a few of the important auxiliary systems within the facility to improve measurement accuracy and ensure successful operation of the PAX200 compressor design. These upgrades included modifications to the orifice plate flow meter and S3 cavity to add versatility in altering the bleed flow from S3, minor instrumentation upgrades, and an upgrade to the throttle actuation system to achieve more even back pressuring of the facility at the compressor exit.

Orifice Plate & Stator Bleed Flow Modifications

With a new aft frame design as part of the structural upgrades to the facility, an important upgrade included the redesign of the bleed flow system carrying flow from the region under S3 to the orifice plate that measures the flow rate. Due to the shrouded stator design, a leakage path exists over the S3 knife seals as the flow tries to move from the high-pressure region of the main flow path to the lower pressure region around the bearing cavity, as shown in Figure 2.7. This upgrade involved a new rear plate for the aft frame, new instrumentation, and new selection of tubing and fixtures to carry the flow to the orifice plate (previously upgraded and discussed in Kormanik, 2017).
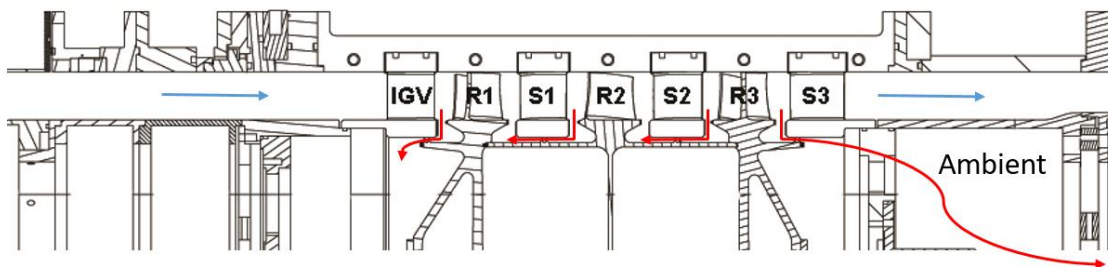
Figure 2.7. Secondary flow paths under blisk knife seals

Through original analyses performed in 2015 by Rolls-Royce and FTT on the design of the new compressor, a minimum flow rate of approximately 0.2 lbm/s was required to balance the effects of the flow choking upstream through the S3 knife seals of the final stage of the compressor and the forward acting thrust from the pressure build-up within the bearing cavity. Shown in Figure 2.8, modifications had been made to the existing plate for an effective exit area of 4.295 in^2 to achieve close to the desired mass flow rate for the bleed flow. Additionally, four holes were filled with an aluminum plug containing a thermocouple and a static pressure tap to monitor cavity pressure and temperature.
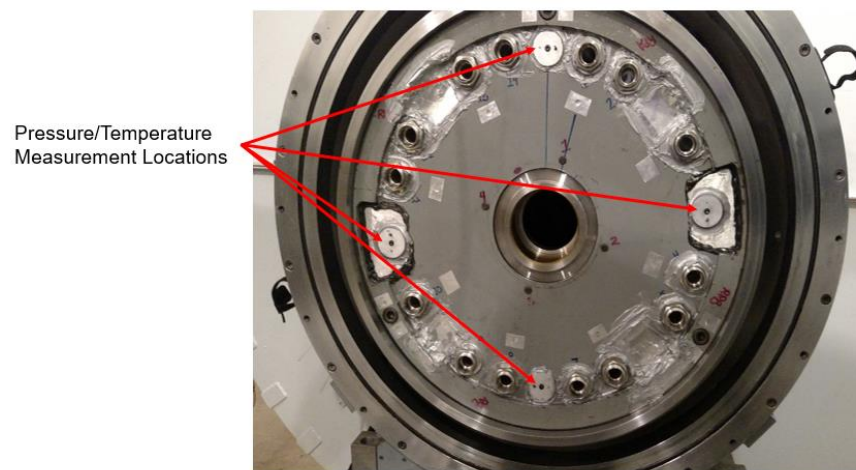
Figure 2.8. Original rear plate for S3 bleed flow before redesign with 14 asymmetric holes and 4 pressure/temperature measurement ports.

With the new redesign, this existing plate was replaced with a new manifold that would allow for a more uniform exit condition for the bleed flow and the ability to change the flow rate for future compressor designs and configurations. The new aft frame included 18 holes, spaced uniformly throughout the S3 cavity region at 0.8 inches in diameter, resulting in a maximum exit flow area of 9.048 in^2. An adapter plate/manifold was created that could attach to the aft frame and allow for customization of the 18 holes through a combination of restrictions, plugs, and openings for different mass flow rates to be achieved. As shown in Figure 2.9, fittings with stainless steel tubes were used to facilitate the transition between the manifold and any tubes or instrumentation. With the reduction in area due to the fittings and stainless-steel transition tubes used to carry the

bleed flow, 9 of the 18 holes were kept open while the remaining holes were filled with plugs or instrumentation to attain a similar bleed flow rate to the previous operation of PAX200.

Figure 2.9. Redesigned rear plate for S3 cavity bleed flow with 18 symmetrically placed holes and a variety of plugs and open ports.

From the stainless-steel transition tubes (1" OD and 0.870" ID) and Yor-Lok fittings, hose clamps were used to anchor hoses to the manifold. These hoses were then weaved around the driveline components to provide a flexible route to the existing orifice plate manifold. This flexible hose was made of EPDM rubber rather than the previously implemented polypropylene tubing. The hose was chosen primarily for its high flexibility, low pressure rating of 200psi, and ability to withstand temperatures up to 200°F.

The existing orifice plate was adapted to mimic the same features as the adapter manifold on the rear plate of the compressor. A new plate with 18 threaded holes for fittings or plugs and instrumentation was manufactured to directly replace the existing plate with welded fittings. Stainless-steel tubing was once again used to transition the orifice plate manifold to the rubber hose with hose clamps. This modified orifice flow meter manifold is shown in Figure 2.10.

Figure 2.10. Redesigned orifice flow meter manifold.

Finally, the existing instrumentation plugs from the old configuration were also adapted for the new bleed flow system. They were reconstructed out of 1" solid stainless-steel rod instead of the hollow tubing and installed in both the orifice plate manifold and S3 cavity manifold to monitor pressures and temperatures within the orifice plate manifold and S3 cavity. All other instrumentation remained the same for reading the pressure drop across the orifice plate itself.

Instrumentation Upgrades

With the new forward and aft frame designs, the existing velocity sensor mounting platforms were moved from directly next to the bearing housings to the outer wall of the frame due to accessibility concerns. With a greater need for accurate monitoring of any misalignment conditions and vibrations during operation, the existing CEC velocity sensors located on the gearbox, torquemeter platform, and front and rear frames were replaced with accelerometers. In addition to switching sensors, the mounting platforms for each of the frames were moved from the bearing housings to the outside of the casing at the locations specified in Figure 2.11. Two Industrial ICP HT622B01 single axis accelerometers with a frequency range up to 15 kHz were installed on each of the front and rear frames. Precision ICP tri-axial accelerometers with a frequency range up to 8 kHz were installed on the gearbox and torquemeter pedastal. The signal conditioning and acquisition is performed through an NI 9234 C Series Sound and Vibration Module connected through an NI 9185 cDAQ chassis.
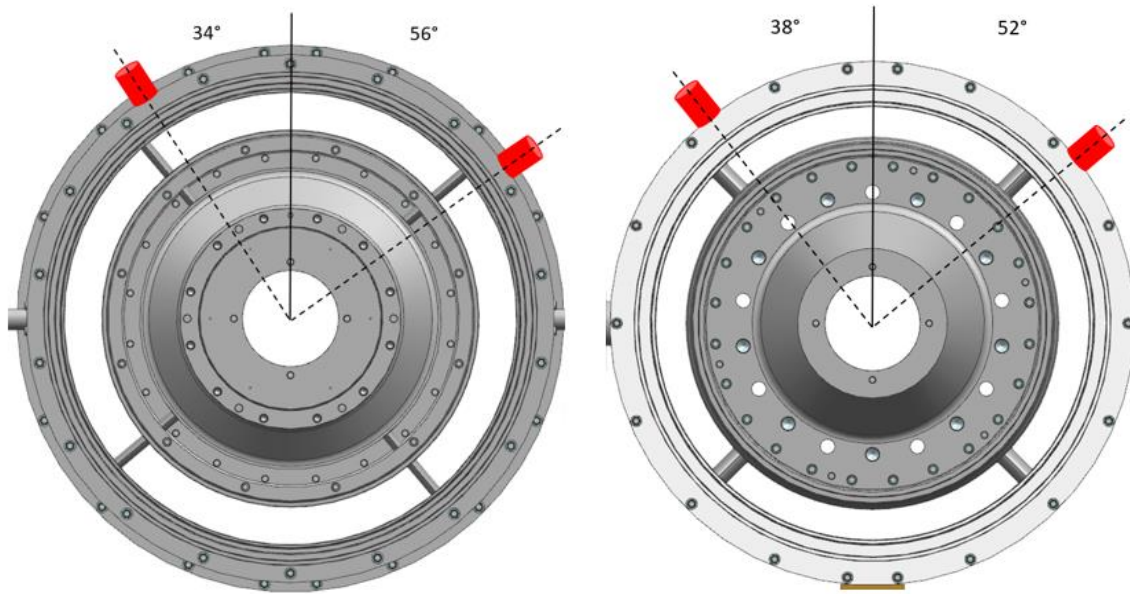
Figure 2.11. Accelerometer locations on forward frame (left) and rear frame (right).

Aside from the accelerometer upgrades, the only additional instrumentation upgrades involved the like-for-like replacement of the existing Omega HX94 thermo-hygrometer and United Sensor PAE-T-18-T-KL pitot-static probe used for calculation of mass flow rate and rotational speed. The humidity sensor was also moved from its outdoor location outside of the inlet ducting to inside the settling chamber of the facility to better reflect the actual humidity of the flow going through the compressor.

Throttle Upgrades

Another major upgrade to the facility involved the remodeling of the throttle actuation system, reinforcement of the throttle, and upgrades to positional feedback of the actuator. The existing throttle arrangement, Figure 2.12, featured a single point of contact on top of the sliding ring valve and two guide rails to help facilitate movement. With the higher mass flow rate and pressures associated with the PAX200 compressor, this arrangement was unable to maintain an even backpressure on the compressor in the facility.
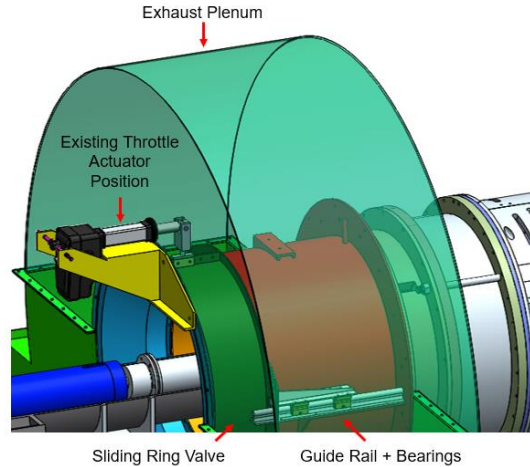
Figure 2.12. Existing throttle arrangement with one point of contact on top of the sliding ring valve, and two guide rails on each side.

With a single actuator originally acting as a primary point of contact on the sliding throttle valve, the sliding valve was found to slightly torque during operation when subjected to the loading of the compressor with high pressure/mass flow rate. The contact between the sliding valve and the rails facilitated this torque, as there was not enough rigidity in the sliding valve to form another stiff point of contact. In other words, the rails were enhancing the movement of the sliding valve under load, rather than acting as additional rigid points of contact.

While this typically still resulted in steady and consistent operation of the throttle, it created an uneven backpressure in the exhaust section, especially at higher loading conditions. To address this issue, more rigid points of contact were required. The original actuator was replaced with a Thomson Electrak HD actuator (HD24B026-0100SYN1FFSD) and two more identical actuators were added to the sliding ring valve. These actuators were selected due to their stroke range, load capability, and ability to sync and move all together, a new feature which was crucial to even back pressuring of the compressor.

For installation of the new actuators, new brackets were designed to attach to the outside of the exhaust plenum to support the actuators, similar to the existing design for the original actuator located at the top of the sliding valve. The existing bracket for this actuator was reused as the overall dimensions for the new actuators were identical. On the inside of the exhaust plenum, the piston side of the actuator was attached to the sliding ring valve with additional brackets that were designed to integrate with the existing hardware. These new brackets and the overall mounting

arrangement are shown in Figure 2.13. Finally, the sliding ring valve was stiffened using gussets welded to the outside of the ring to provide increased rigidity.
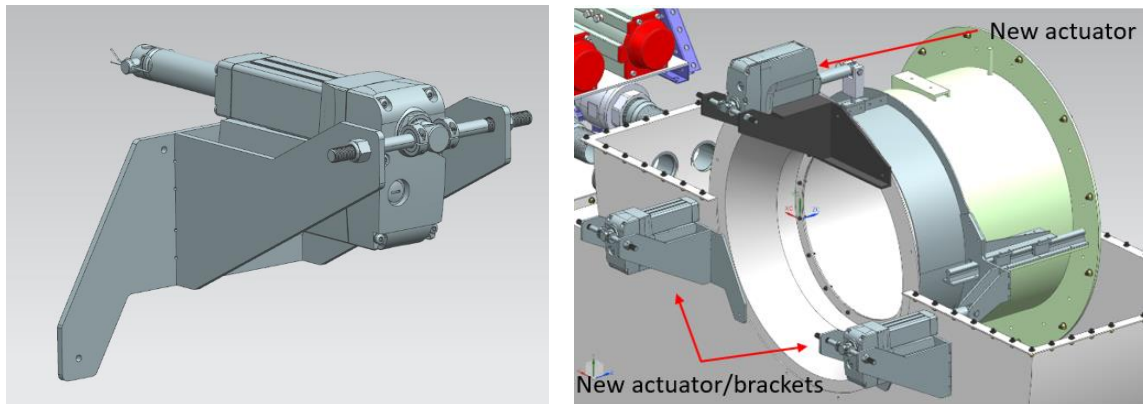
Figure 2.13. New actuator/bracket placement to provide more points of contact on sliding ring valve of throttle.

The addition of the two extra actuators to move the sliding throttle valve successfully achieved three rigid points of contact, which kept it from moving haphazardly during operation. However, to ensure that the movement of the sliding ring valve was uniform while loading the compressor and maintaining a loading condition, displacement sensors LVDT (Transtek 0245-00001 DC LVDT) were installed at four circumferential locations. The sensor housings were anchored to brackets welded to the outside of the exhaust, as shown in Figure 2.14. The sensors featured a rod anchored to the sliding valve, that slid in and out of the housing as it moved open/closed. This movement of the rod correlated to a voltage which indicated how far in/out of the housing the rod had been displaced.
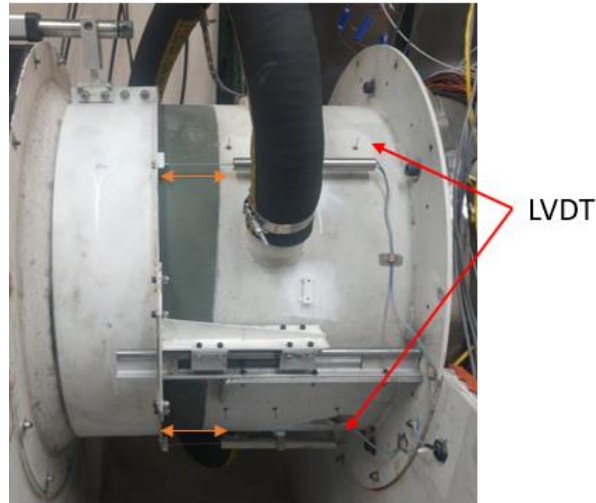
Figure 2.14. LVDT installation on to compressor exhaust section. Arrows indicate the axial displacement measured by the sensors.

The system was zeroed with the valve (throttle) fully closed to provide an indication of how open the throttle was at all times. The ability to measure the voltages of these 4 sensors during operation and keep track of their relative displacement guaranteed an even throttling of the compressor. In the case that the sensors showed that the sliding valve was not evenly back pressuring the compressor, the actuators were able to be taken out of their synchronized state and adjusted independently for fine tuning of the sliding valve. A summarized diagram for the circumferential locations of the throttle actuators and LVDT sensors is shown in Figure 2.15.
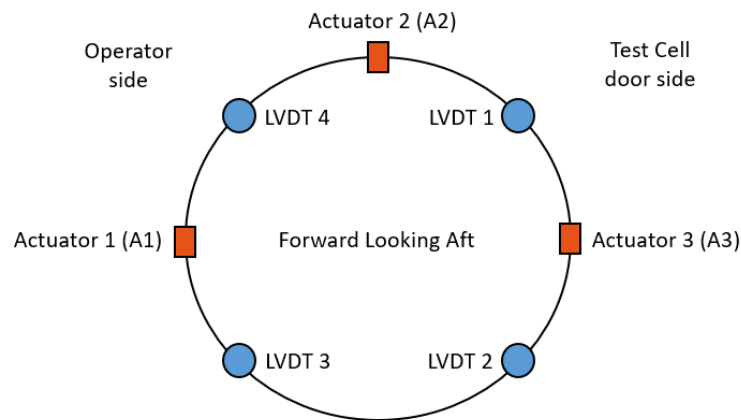
Figure 2.15. Throttle actuator placement around sliding ring valve. A1 and A3 are located near sliding valve rail locations.

In addition to physically adding new actuators to the throttling system, a complete overhaul was required on the electronics and controls to incorporate the new synchronization feature and upgraded on-board electronics for each actuator. A fail-safe was also incorporated into the throttle to ensure that it would always default to fully extend all three actuators (fully open the throttle). A visual representation of the final control board is shown in Figure 2.16.
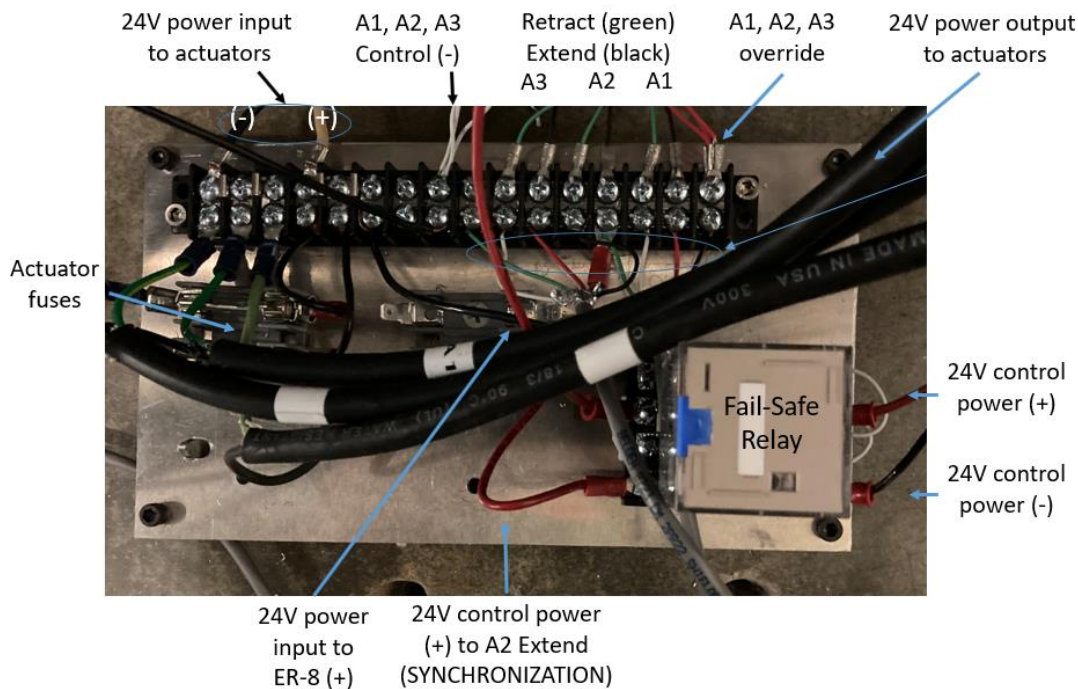
Figure 2.16. Visual representation of throttle actuation system.

The system works according to the wiring shown in Figure 2.17. Overall, two forms of power were supplied to the actuators and a central mechanical switch and fail-safe relay. A 24V power unit supplied all three actuators (A1, A2, and A3) and a separate 24V power unit supplied the electronic relay switch array (ER8) through a mechanical switch. Fuses were incorporated between these power units and the switches to protect the actuators from overcurrent.

To communicate with the actuators, a signal is sent directly from the computer to the actuators through the electronic relay switch, which toggles the extend, retract, or override feature on the actuators via their on-board electronics. The override feature takes the actuator out of synchronization mode and allows it to move independently of the other actuators. For the fail-safe

feature, when the emergency mechanical switch is engaged, power to the electronic relay is cut, closing the override switch on all the actuators, and forcing them to go into a synchronized mode. The master actuator (A2) is automatically placed into an extend state, triggering all three actuators to extend (open the throttle) simultaneously.
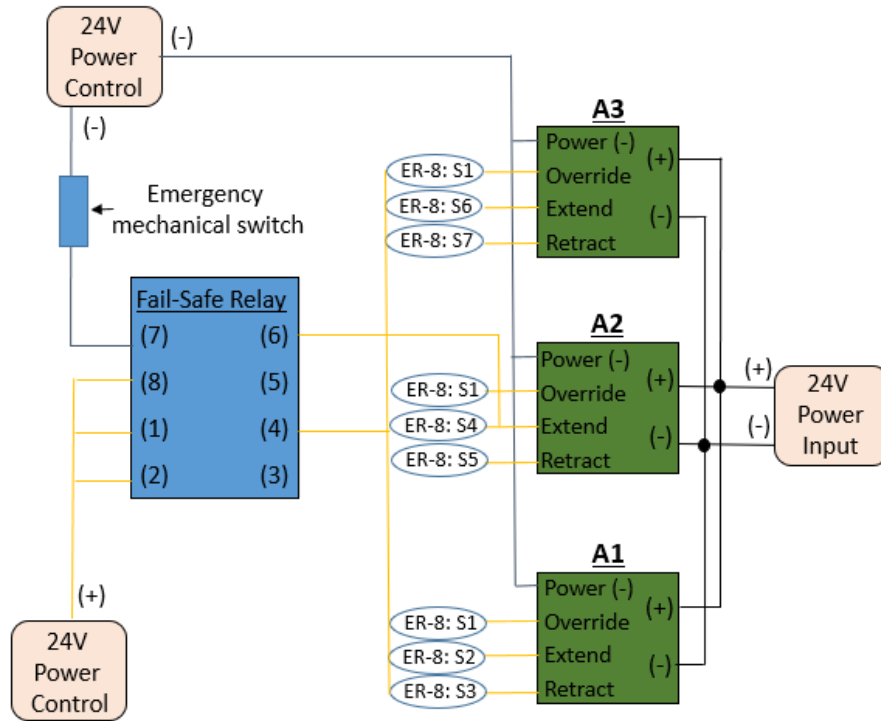
Figure 2.17. Wiring diagram for throttle actuation system.

Vane Actuation Modifications

      With the installation of the large sliding plate that was designed as part of the structural upgrades to the facility, the existing locations of the actuators had to be moved further away from the center of the compressor by about 5 inches. A redesign of the actuator rods used to connect the stator vane rows to the actuators was necessary due to the longer lever arm required. As a result, longer threaded rods were installed, and longer yokes, shown in Figure 2.18, were manufactured to help achieve a desirable stiffness to allow for efficient vane traversing.
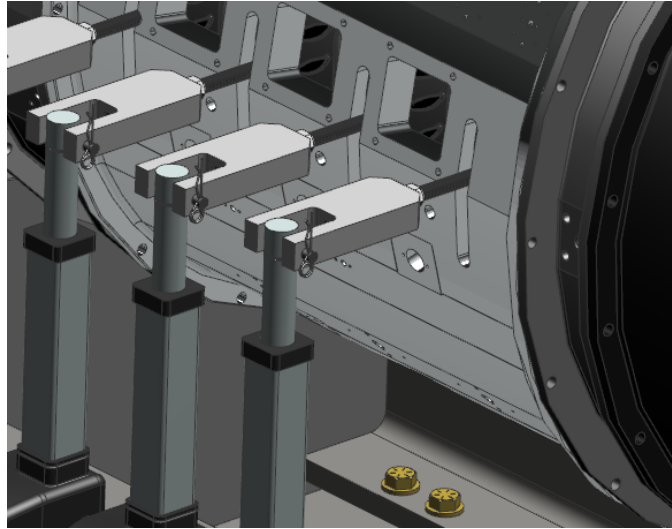
Figure 2.18. Extended yokes for stator vane actuation.

In addition to this physical upgrade to the vane actuation system, a complete overhaul was performed on the electronics and controls of the vane actuation system in a similar way to that of the throttle. The original actuators were retained, which required more complex wiring and control logic compared to the new actuator throttle actuators with their on-board electronics. However, a major simplification of the control board and switches for the vane actuators were still able to be achieved compared to Talalayev (2011). This vastly improved the efficiency of the system through removing redundant wiring and relay switches, which made the components and overall system a lot easier to follow, diagnose, and understand. Most importantly, it allowed all four blade rows to be traversed either independently (like before) or simultaneously (a new feature). With much of the time to complete a circumferential traverse in an experiment dedicated to moving each subsequent blade row, the ability to simultaneously traverse all four blade rows during operation greatly improved the time to take measurements across a full blade pitch. A visual representation of the final control board is shown in Figure 2.19.
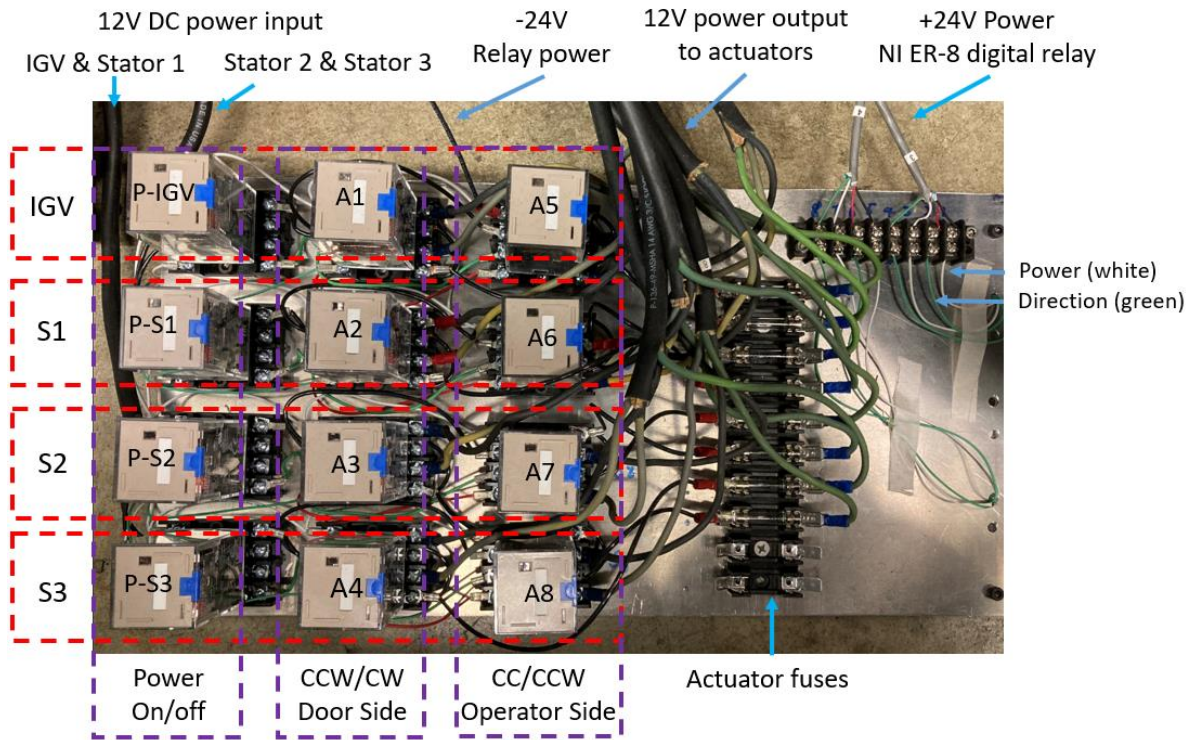
Figure 2.19. Visual representation of vane actuation system.

The system works according to the wiring shown in Figure 2.20 for the IGV blade row. Overall, two forms of power were supplied to the actuators in the single blade row through a central mechanical switch (denoted "P"). A 12V power unit supplied both actuators (A1 and A2) and a 24V power unit supplied the electronic relay switch. Fuses were incorporated between these power units and the switches to protect the actuators from overcurrent.

To communicate with the actuators, a signal is sent from the computer through the electronic relay switch, which triggers the mechanical switch to supply/cut-off power to the actuators. This switch triggers the start/stop motion of both actuators. The other two mechanical switches control the direction of the actuator, based on the signal from the electronic relay/computer. To rotate each vane row in one direction without the actuators moving against each other, the mechanical switches were wired opposite each other to provide a clockwise motion for one actuator and a counterclockwise motion for the other. This maintains consistent rotation of the blade row when needed. The same overall wiring procedure was repeated for each of the other blade rows.

70
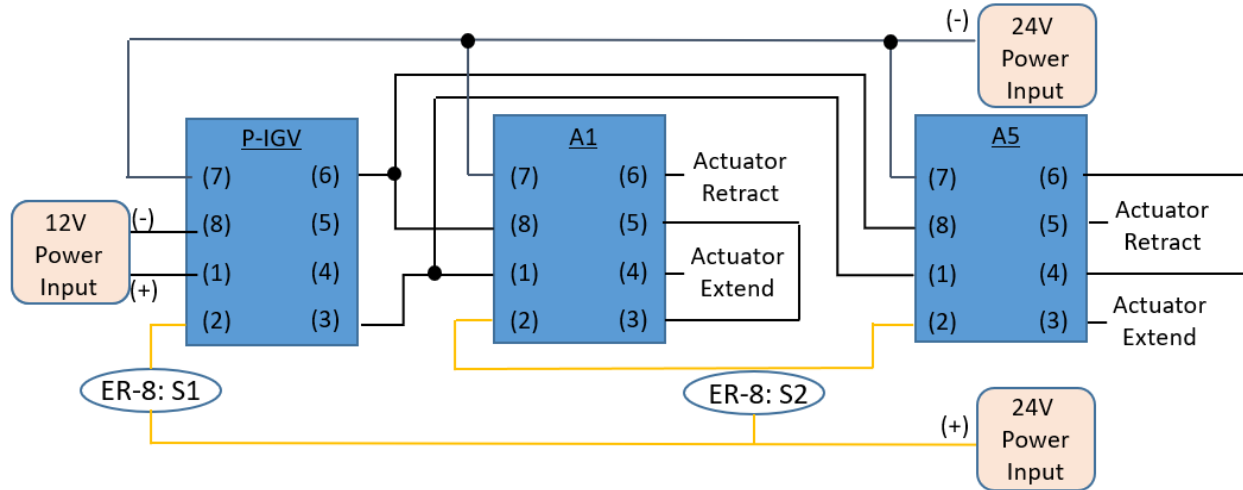
Figure 2.20. Wiring diagram for vane actuation system (specific to IGV).

2.2 Experimental Measurement Techniques

This research investigation relied upon the use of experimental methods and measurement techniques to acquire data relevant to understanding the PAX200 compressor performance and heat transfer characteristics that occur within the Purdue 3-Stage Axial Compressor Research Facility. Measurements taken from rakes at the inlet and exit planes of the compressor were used to set the loading condition and to keep flow conditions consistent between tests. Interstage rakes were used to establish the performance and flow characteristics at each axial station between blade rows. Thermocouple beads and heat flux gauges were attached to the metal surfaces to characterize thermal boundary conditions of the stationary components, and a stagnation temperature probe was used to capture the stagnation temperature in the stator wells. All these measurement techniques were crucial to characterizing the performance of the PAX200 compressor, establishing thermal boundary conditions for validation of computational models, and understanding the extent to which environmental effects can influence the heat transfer and performance of the system.

2.2.1 Performance Instrumentation and Measurements

To account for differing weather conditions associated with the density and gas properties of the unconditioned inlet air, an operating point was defined by correcting to a reference point known as standard-day conditions. Based on the properties of the air during the time of the experimental test, the rotational speed of the compressor and throttled mass flow rate were adjusted

71

accordingly to match standard-day conditions. A correction for humidity was also implemented so that comparable data can be collected year-round (Berdanier et al., 2015).

Measurements used for the correction to standard-day conditions were acquired at station 0, referred to as the Aerodynamic Interface Plane (AIP). A seven-element stagnation pressure rake and temperature rake were placed at this location, and the 50% mid-span measurements were used to calculate the required corrected speed and mass flow rate for the compressor to achieve the desired operating condition. For humidity measurements, an Omega HX94 thermo-hygrometer was located inside the settling chamber of the facility, near the inlet of the bellmouth. These measurements were used as inputs into the REFPROP thermodynamic equation program (Lemmon et al., 2013), which provides speed of sound and density values for the humid air mixture.

All data were acquired at the aerodynamic design point (ADP), shown in Figure 2.21, which is set by matching a value of Rc/Wc (ratio of total pressure ratio to corrected mass flow rate) based on the AIP (Station 0) and exit (Station 9) conditions of the compressor. This loading condition is achieved by slowly closing the sliding valve throttle located at the exit of the compressor to increase the back pressure and induce higher loading on the compressor, which lowers the mass flow rate and raises the pressure ratio. Establishing repeatability of this loading condition was imperative to keep consistent flow properties for taking detailed measurements in different tests. The ADP operating condition for the PAX200 compressor was determined as the optimal loading condition for which the compressor blading was designed. More details about this operating condition can be found in Kormanik (2017).
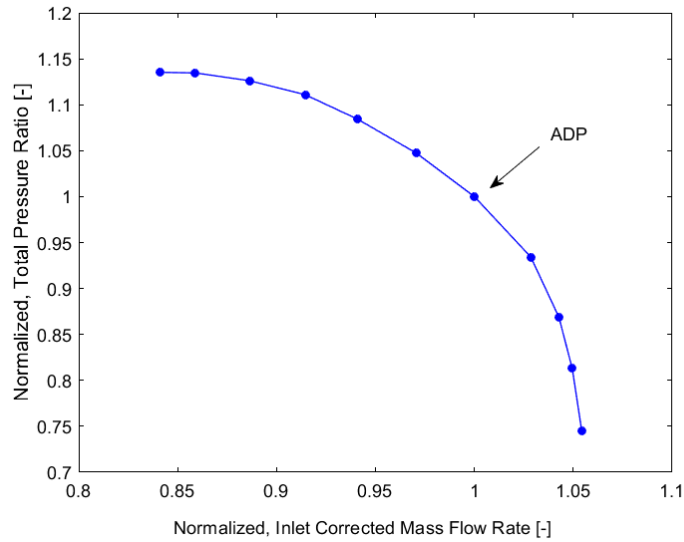
Figure 2.21. Compressor speedline for 100%, normalized to the ADP loading condition.

Overall and interstage performance of the PAX200 compressor design were characterized through a few basic steady measurement techniques. These techniques included total temperature and pressure rakes placed into the flow path and static pressure ports along the casing wall. At each axial location (between each blade row), seven-element stagnation pressure and temperature rakes were also placed in the flow path. Stator vanes were moved across a full vane passage based on the S2 blade count to acquire pitch-wise data, including wakes, at 20 different circumferential vane positions. Area-averaging and circumferential averaging were then used to characterize the loading condition based on one full vane passage on the speed line using the rakes at Station 0 and Station 9.

Additionally, four static pressure taps were distributed circumferentially at each axial location, except the AIP (where 13 are circumferentially distributed) and the exit plane (where 12 are circumferentially distributed). These static pressures give an indication of the potential field effects from downstream blade rows and circumferential flow uniformity throughout the compressor.

Measurements from the seven-element stagnation pressure rake at Station 9 were used in combination with the rake at the AIP to calculate the overall total pressure ratio and temperature ratios for the compressor. All the rakes capture flow properties at radial positions of 10%, 20%, 35%, 50%, 65%, 80%, and 90% span of the converging flowpath. Additionally, each rake was

73

aligned to the representative mean absolute flow angle and features Kiel heads which provide an angular acceptance range of ±30 degrees (verified by Aerodyn Engineering, the rake manufacturer). These rakes provide radial stagnation temperature and pressure profiles between each blade row and allow for the stagnation temperature and pressure field of each vane passage to be captured in detail.

All total and static pressures were measured with Scanivalve 3016 and 3217 Digital Sensor Array (DSA) pressure scanner modules. For maximum accuracy, each module was rated for a specific differential pressure range and chosen based on the pressures that would be encountered throughout the compressor (1 psid, 2.5 psid, 5 psid, or 15 psid). A barometric pressure sensor (Setra 270) was used to accurately measure the atmospheric reference pressure and actively re-zero the DSA modules during compressor operation. For temperature measurements, T-type thermocouples with special limits of error were used and scanned using a Keysight Technologies (Agilent) 34980A multiplex system.

2.2.2 Thermal Mapping of Metal Surfaces and Cavity Flows

While much of the temperature rise within the flow path comes from the work transmitted through the rotors, there is the potential for additional heat generation through the outer surfaces of the flow path. As discussed in Section 1.2.1, this could include influences such as stator well windage or conduction through the outer aluminum casing from the work input into the flow by downstream blade rows. The ability to quantify these heat transfer effects are crucial to establishing correct boundary conditions in CFD analyses and determining how much these secondary heat sources can impact the primary through-flow. These results were also relevant to quantify the potential amount of heat that could influence the primary flow via the transition of heat from metal surfaces to the boundary layers.

To quantify these heat transfer characteristics and boundary conditions, Fluxteq PHFS heat flux sensors and Omega SA1-T-SC adhesive-backed surface thermocouples were adhered to the stationary metal surfaces throughout the compressor flowpath in one vane passage. In total, this amounted to 42 surface thermocouples and 5 heat flux sensors, scattered throughout the flowpath, as shown in Figure 2.22. In addition to these measurements, inter-stage temperature rakes were placed in the flowpath at Stations 1, 2, and 4 to track any changes in flow properties.
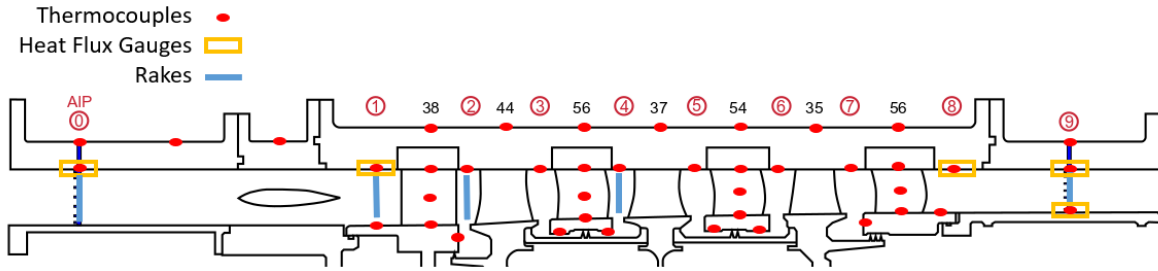
Figure 2.22. Distribution of metal surface thermocouples and heat flux sensors in flowpath.

The Fluxteq PHFS heat flux sensors were based on a differential-temperature thermopile design encapsulated with a Kapton polyimide material to measure the heat flux passing through the sensor surface. The response time was specified as 0.6 seconds, and they incorporated a T-type thermocouple within the sensor. The sensors were calibrated between a hot plate and a cold, water-cooled surface to provide results within 5% accuracy. The voltage output from the sensors was read through a National Instruments (NI) 9209 C-Series voltage input module through an NI cDAQ-9171 chassis and recorded using LabVIEW. The sensitivity of the sensor varies with temperature, so a sensitivity factor was established through the sensor calibration process. Then, it was applied to the data during postprocessing based on the temperature reading from the integrated thermocouple. This allowed for adjustment of the measurements for operating temperatures other than 25°C (the calibration temperature) for a temperature range from -50°C to 120°C.

A thermally conductive paste, OMEGATHERM 201, was used during calibration to reduce the thermal contact resistance between the sensor and the surface for enhanced accuracy of the calibration. When installed in the compressor, high-temperature, double-sided tape was used to adhere the sensor to the metal surface, as shown in Figure 2.23, and an adhesive tape was placed evenly over the sensor to ensure a uniform thermal resistance between the sensor and aluminum surface.
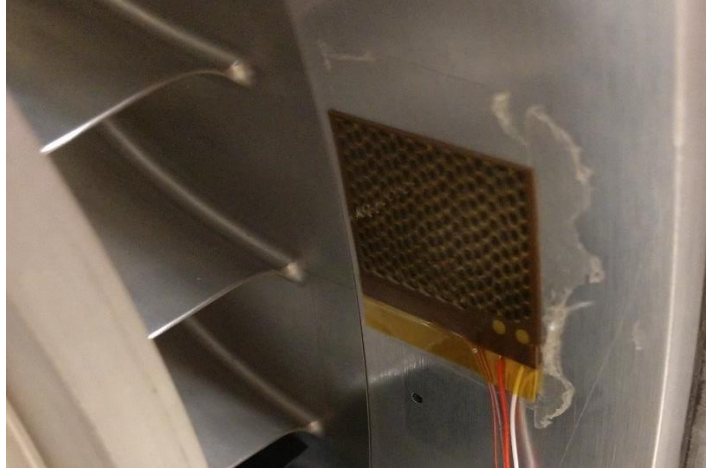
Figure 2.23. Heat flux sensor placed behind S3 on the inner wall of the aluminum casing.

T-type thermocouple beads were used in this investigation to measure the metal surface temperatures of the stator blade, hub, and shroud, as well as near the edge of each stator well throughout the flow path (Figure 2.24). The silicon-based self-adhesive pad was used to stick the thermocouple to the surface and aluminum tape was used to ensure that the thermocouple would not come loose during operation. Finally, a thin layer of M-Coat A polyurethane was applied to help blend the transition between the metal surface and the aluminum tape and to ensure the safety of the wires during operation. The thermocouples were rated for a temperature of 350°F and the polyurethane was rated for a temperature of 250°F. Overall, these temperature measurements were used to map the surface temperatures throughout the inner flow path during compressor operation. Several additional thermocouples were placed axially and circumferentially on the outside of the casing wall to characterize the influences of environmental convection and casing conduction. All data were acquired through the existing Keysight Technologies (Agilent) 34980A multiplex system at both transient (warm-up and cool-down operation) and steady-state conditions at the ADP.
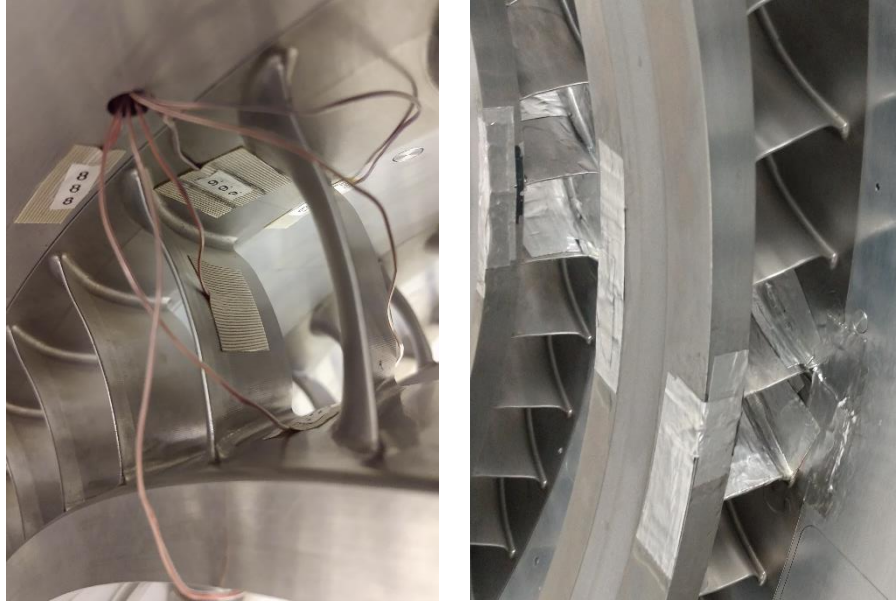
Figure 2.24. Thermocouples placed in the blade passage and on stator shroud.

A major benefit of the scaled-up geometry associated with the Purdue 3-Stage facility was the large axial gaps between blade rows. This allowed for instrumentation to easily fit inside the stator well and cavity regions, which was useful for characterizing the leakage flow temperature for comparison with the experimental metal surface temperatures and the computational simulations. With the assistance of a radial traverse system mounted to the outside of the casing wall, a single element, Kiel-head, stagnation temperature probe (T-type) was plunged into the flow path to measure the total temperature in the spanwise direction, including inside the stator wells. As was the case with stagnation pressure and temperature rakes during performance mapping, each probe was initially aligned to the absolute mean flow angle of the primary flow. However, once inside the stator well, the probe was rotated to cover a range of -80° to 80° with respect to the direction of rotation, in increments of 5°, as shown in Figure 2.25. This rotational sweep was performed to ensure that the probe would capture an accurate average flow temperature without precisely knowing the angle in which the leakage flow was entering or exiting the cavity/well. Each stator well's stagnation temperature field was characterized except for the cavity downstream of IGV due to geometric constraints.
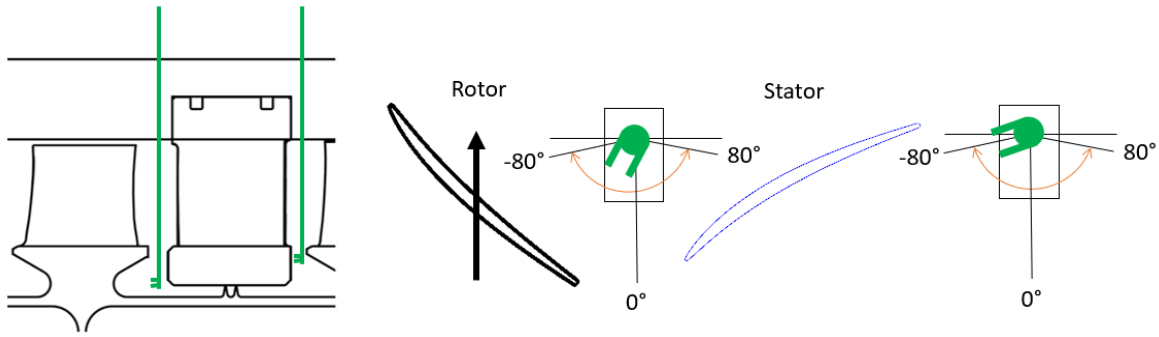
Figure 2.25. Probe orientation/location and rotational sweep in stator wells for upstream and downstream of each blade row.

2.2.3 Ambient Environment Characterization

A few other experimental studies were performed throughout this investigation to quantify the impact of different ambient and environmental conditions on the performance of the compressor during its operation. One study involved heating and cooling the casing during operation, as shown in Figure 2.26. For the cooled casing experiment, a blanket was made for the compressor out of two neoprene (outer layer) and cotton (inner layer) pouches. Right before operation, the pouches were filled with 40lbs of dry ice (-109°F sublimation temperature) and the compressor was quickly brought up to the ADP loading condition at 100% corrected speed, where it was left to idle until a steady-state condition was reached. Measurements from the metal surface thermocouples and stagnation temperature rakes were continuously acquired from start-up to shut down. After shut-down, the saddle bag was visually inspected to ensure that dry ice was remaining – an indication that the compressor was subjected to consistent cooling. Before the experiment was performed, care was taken to ensure that the instrumentation devices would be able to survive the extreme temperatures.

For the heated casing experiment, also shown in Figure 2.26, heat tape was wrapped circumferentially around the casing at the same axial location as the IGV and aluminum tape was used to hold it in place. Two layers of neoprene were wrapped around the front half of the casing to act as an insulator. The heat tape was cycled on and off from the control station in case of any undesired heat generation and toggled during operation to directly observe its effects. The compressor was brought up to the ADP loading condition at 100% corrected speed and left to idle until a steady-state condition was reached. Measurements from the metal surface thermocouples and stagnation temperature rakes were continuously acquired, with the heat tape turned on and

turned off several times with waiting periods in between before the compressor was brought to a stop.
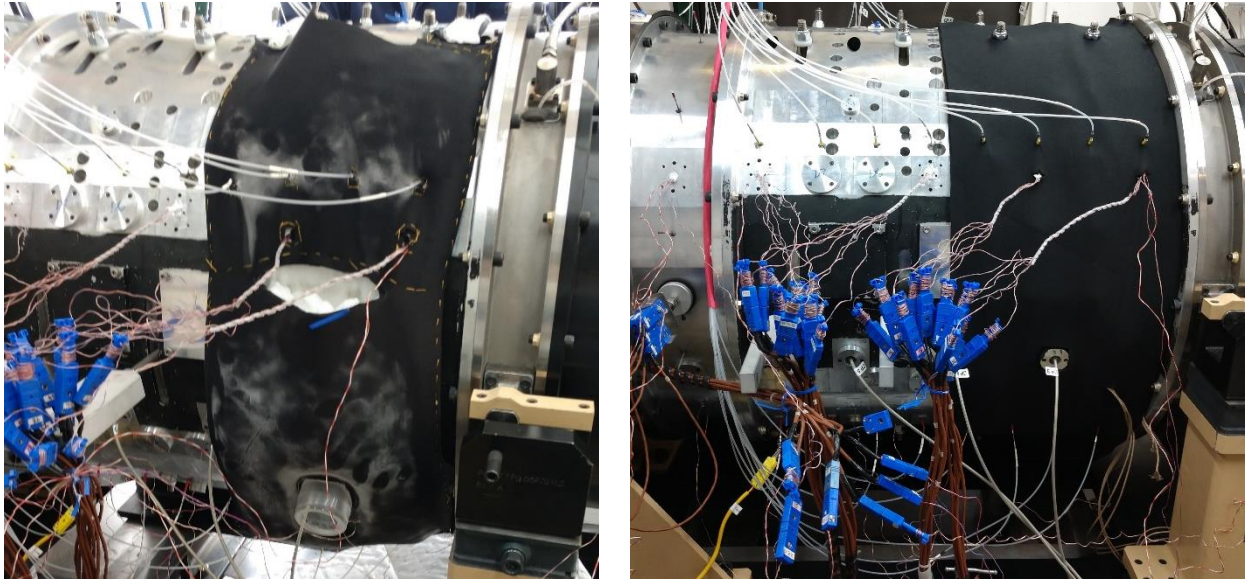
Figure 2.26. Attempts at cooling (left) and heating (right) the casing during compressor operation.

In addition to these heated and cooled casing experiments, two additional experiments were performed with the casing in its original, uninsulated state, to observe any effects from room temperature and convection during operation. Several thermocouples were placed throughout the room and circumferentially around the outside of the casing, as shown in Figure 2.27, to observe the impacts of running the compressor with two different ambient environments. First, with the traditional configuration of keeping the room temperature equivalent to the incoming flow temperature by keeping the test cell doors open and exposed to the outdoors. Second, with the configuration of keeping the room temperature significantly warmer than the incoming flow temperature by keeping the test cell doors closed and isolated from the outdoors. With each of these tests, a full 21-point circumferential traverse was performed at ADP at 100% corrected speed, and the resulting data were directly compared to one another.
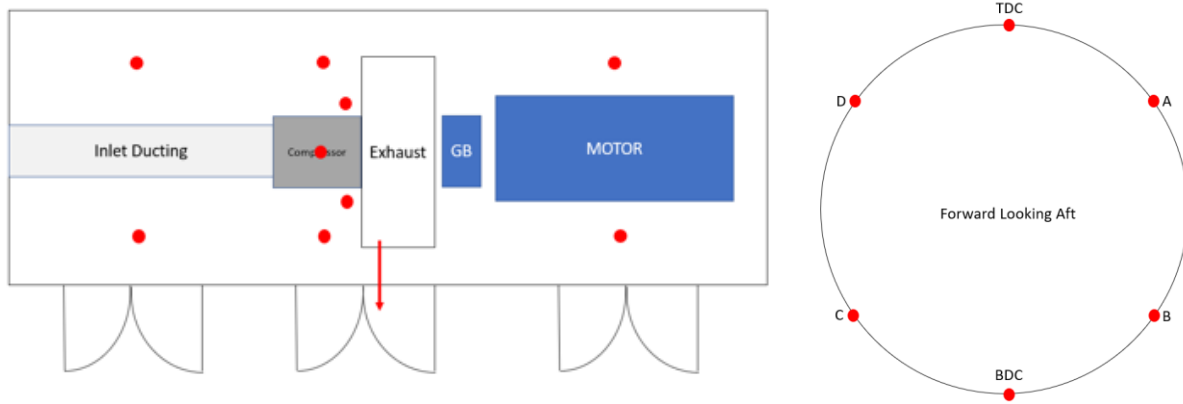
Figure 2.27. Thermal mapping diagram of the compressor outer casing and test cell during compressor operation.

2.3   Computational Techniques and Models

One of the most important and useful tools to aid this research investigation involved the use of computational fluid dynamics (CFD) to better understand the role of heat transfer within the P3S Facility and show how spanwise mixing can contribute to these effects. For this study, 3D parametric models of the PAX200 compressor geometry were constructed, which also included the cavity regions. A variety of computational simulations were performed using a combination of ANSYS CFX 19.1 and ANSYS 2020R1 as the CFD tools. Experimental data were used for establishing boundary conditions and for comparison with the computational results to help validate the computational models and explore the impact of heat transfer on the performance of the compressor.

ANSYS CFX is a commercially available tool, which is useful since it is accessible to all members of the turbomachinery community and encompasses a variety of turbomachinery and fluid dynamics applications. It incorporates the Navier-Stokes equations with a finite volume method solver. This means that the flow path is composed of discrete control volumes to which the Reynolds-averaged Navier-Stokes (RANS) equations can be numerically applied and solved using an iterative finite volume method to obtain mass, momentum, and energy properties. The solver is a vertex-centered computational tool and is commonly used in turbomachinery applications.

ANSYS TurboGrid is a package applied to CFX that can automatically generate grids composed of hexagonal meshes, a requirement of CFX. It incorporates the blade cross-sections,

hub geometry, and casing geometry to build a 3D geometric definition of the flow path. When paired with the built-in ANSYS meshing tool, these meshes can be better refined to capture details in specific regions that are of higher interest, like the boundary layer regions. However, many limitations still exist with the software in easily resolving complex blade geometries and flow features like the fillet regions where the blades connect to the endwalls and the cavities. Therefore, GridPro, an independent meshing program, was used as the meshing tool for all the fluid domains as it allowed for more customization in achieving high mesh quality of structured, orthogonal grids. Meanwhile, all the metal stationary components were meshed using the standard ANSYS meshing tool.

A variety of models and simulations were run to provide a diverse look at heat transfer effects within the P3S Facility. First, steady-state, and unsteady simulations were performed on the fluid domain of the PAX200 compressor while maintaining adiabatic thermal boundary conditions. Then, several different modifications were made to the models to better refine them and incorporate the thermal boundary conditions observed experimentally. Eventually these modifications led to the creation of a thermal structural model and a conjugate heat transfer model which explored the implementation of different geometric and material properties of the outer casing on the performance of the compressor, as well as changes to thermal boundary conditions, addition of environmental effects, and enhancement of spanwise mixing. All the computational results were compared to the experimental data taken in Section 2.2, with particular focus on the flow properties in the spanwise direction and the temperatures/heat rates of the stationary components.

This computational part of the investigation focused on refinement and adjustment of computational models to show the ways in which heat transfer can affect the thermal characteristics and performance of the compressor. It offered insights into how experimental data can be adapted to better relate to the computation results and provide a quantitative analysis as to how proper/improper thermal boundary conditions can affect results from the computational models. Furthermore, the use of comparing experimental data to CFD simulations verified the applicability and capabilities of ANSYS CFX in the validation of complex compressor design – an element that is very useful and cost effective to the turbomachine community.

2.3.1 Steady Model Development

First, a steady-state CFD model was developed that resembled a single circumferential passage of the annulus, as shown in Figure 2.28. The model began with the AIP (Station 0), where experimental stagnation pressure and temperature profiles were prescribed as the inlet boundary conditions. The mass-flow rate of the S3 bleed flow and static pressure at the primary flow exit plane (Station 9) were applied as the exit boundary conditions. This allowed for a constant flow rate through the bleed flow cavity, while allowing for a change in back pressure to achieve the correct operating condition for to ensure a matching flow characteristic.
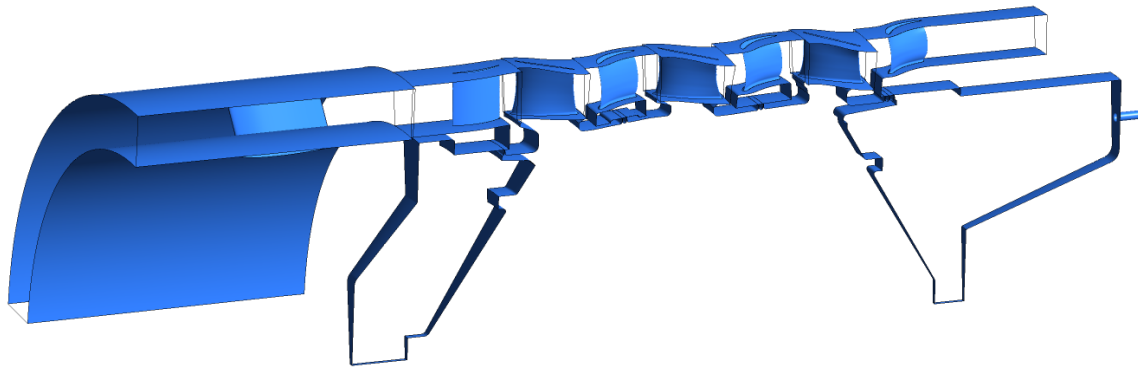
Figure 2.28. Steady-state computational model with fluid domains.

Mixing planes were used for each interface between blade rows and rotational periodicity interfaces were applied to the sides of each domain in the circumferential direction to maintain symmetry. Mixing planes are used to couple different domains, particularly between those that are rotating and stationary, through averaging the flow properties on both sides, while conserving mass, momentum and energy.

The total energy heat transfer model was used which includes high speed energy effects. including the viscous work term. No-slip velocity conditions were also imposed on the walls, and adiabatic heat transfer condition on the blades and endwalls were used for the initial runs. A rough wall characteristic was designated for all endwalls, with a sand grain roughness of 0.0007 inches for the aluminum casing, and 0.0002 inches based on inspections of the components.

While the ratio of total pressure to mass flow rate was used to set the loading condition, as done with the experimental data, the mass flow rate from the initial steady-state, SST, adiabatic

simulation was used as a baseline for all subsequent simulations to achieve the desired flow condition for direct comparison of results.

In addition to this baseline model, a few simulations were performed with an enhanced eddy viscosity, which was applied to the steady-state model in a similar fashion to Cozzi et al., 2019. Using the built-in calculation of eddy viscosity through CFX, the eddy viscosity of the steady-state simulation was increased by a factor of 1.1, 1.3, and 1.5 to observe how spanwise mixing would influence the radial profiles for stagnation temperature and pressure between blade rows to compare with unsteady and experimental results.

2.3.2   Unsteady Model Development

Once the steady-state simulation had been established, an unsteady model was created to better capture the realistic flow conditions of the compressor for improved comparison with experimental data. As with the steady-state model, SST was used as the turbulence model in combination with the total energy heat transfer model including the viscous work term. All other modeling properties were carried over from the steady-state simulation (no-slip condition, wall surface roughness, etc.). Due to constraints within the software with using mass flow rates for exit conditions, the S3 bleed flow cavity outlet was modified to a static pressure exit condition and fine-tuned during the simulation to the correct mass flow rate.

The unsteady model featured mixing planes for the front strut/ IGV, and IGV/R1 interfaces. A time transformation method was applied to the other interfaces between each blade row. This method is effective in improving solution accuracy with different blade pitches, especially compared to the more traditional profile transformation method. It applies periodic conditions in the circumferential direction that are phase-shifted with respect to time to try to address the uneven pitch count between blade rows.

With a multi-blade row simulation, ANSYS recommended using a combination of single-sided and regular time transformation methods at the interfaces between the domains to accurately convey information upstream and downstream. Regular time transformation (TT) transient interfaces were placed upstream of the rotors, while single-sided time transformation (STT) transient interfaces were placed downstream of each rotor. This modeling strategy, shown in Figure 2.29, was used to maintain the upstream blade wake thickness as it propagates downstream, which results in more accurate machine performance and losses.
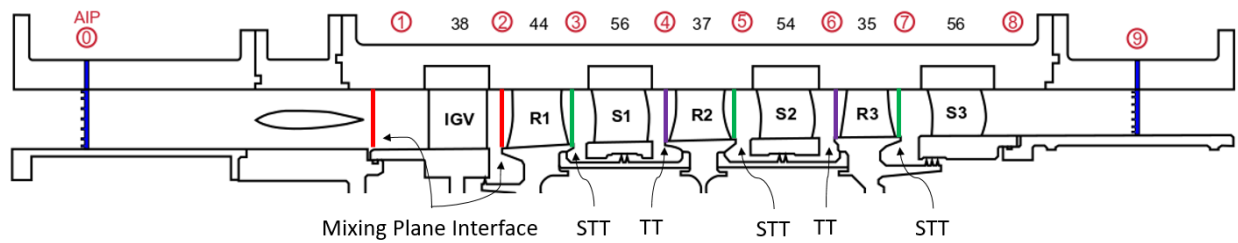
Figure 2.29. Interfaces between fluid domains in unsteady CFD model.

The time transformation transient blade-row method is only valid for compressible flows and for scenarios where the pitch ratio between adjacent blade rows is close to 1. Typically, the range of allowable pitch ratios for accurate solutions when using the time transformation method is between 0.6 to 1.5 (Giles, 1988), but this range becomes tighter with lower speeds and geometric features that extend toward the centerline of the turbomachine. Additional fluid domains for each blade row were added until acceptable pitch ratios were maintained for each interface between blade rows. This resulted in 3 fluid domains each for S1, S2, and S3, and 2 each for R1, R2, and R3. The resulting model is shown in Figure 2.30.

The unsteady simulation was initialized using the results from the steady-state simulation discussed in the previous section. First, however, the steady-state results were interpolated and duplicated across each extra domain that was not present in the steady-state model to provide an initial starting point for all domain elements in the model. In a similar way to the steady-state simulation, an adiabatic thermal boundary condition was applied to the endwalls of the model for direct comparison to the steady-state results, as well as experimental data.
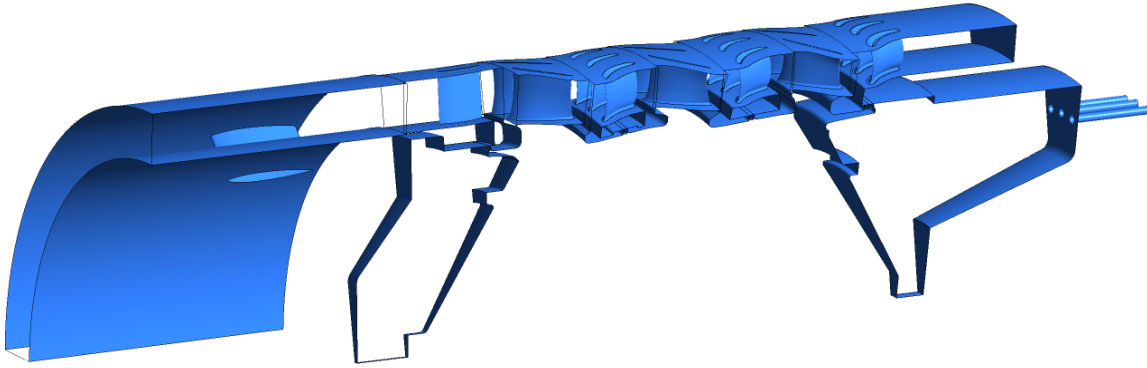
Figure 2.30. Unsteady, time transformation computational model featuring multiple passages to achieve correct pitch ratios.

2.3.3   Thermal Structural Model Development

Meanwhile, in addition to the fluid-based computational model, a structural model of the stationary metal components, shown in Figure 2.31, was created based on the facility geometry. Once the experimental performance and metal surface thermal mapping studies were performed (discussed in Section 2.2.1 and 2.2.2), the results were applied to the structural model to interpolate between measurements and build a complete map of the temperatures and heat fluxes within each component using a transient thermal analysis in ANSYS Workbench. This was accomplished using the experimentally measured flow temperatures at the 90% and 10% span points and applying them to the model. By adjusting the heat transfer coefficient on each surface through an iterative method, a complete thermal map was reproduced that mimicked the temperature results in the thermal mapping experiment. With the full thermal map of temperature of the stationary components of the compressor, an isothermal boundary condition was applied to the existing steady-state CFD model. This was done to observe how changing the endwall and blade temperatures to reflect the reality-based experiment would affect the flow properties and performance of the compressor.

Figure 2.31. Thermal model used for mapping temperatures and heat flux of all stationary metal components.

2.3.4 Conjugate Heat Transfer Model Development

With the development of a fluid-based model and a thermal structural model, a natural step was to fully combine the two models into one, creating a conjugate heat transfer model. Each stator and the entire shroud (encompassing the AIP inlet duct, forward frame, casing, and exit duct) were individually meshed using the ANSYS Meshing tool and then inserted into the existing steady-state model. Once the solid domains were added to the steady-state model in ANSYS CFX, fluid-solid interfaces were added between the surfaces and the fluid domains to achieve the desired coupled interactions. GGI (General Grid Interface) connections were used between the solid and fluid domains to account for the mismatch of the mesh elements and nodes between them. Finally, the same surface roughness values were added to the model for the endwalls and blades while maintaining a no-slip velocity condition at the wall.
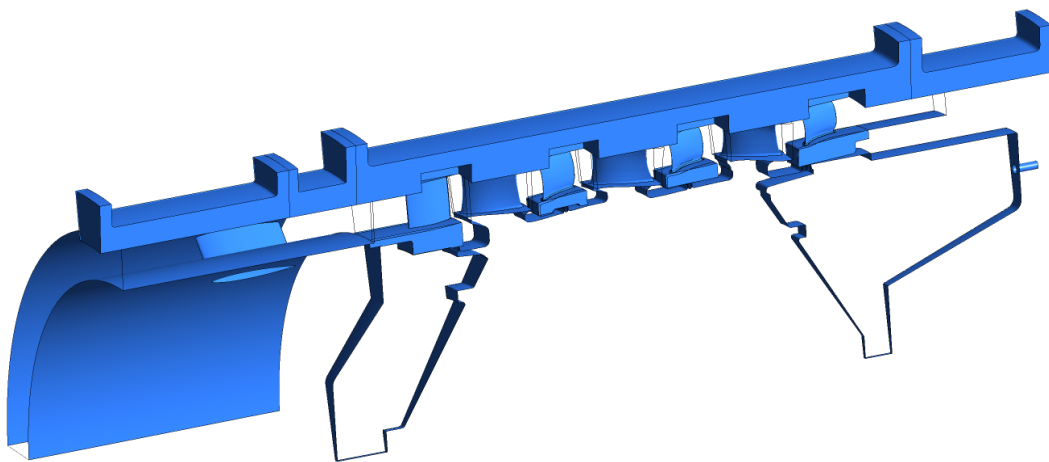
Figure 2.32. Conjugate heat transfer model with fluid domains and stationary metal components.

A few studies were performed using the conjugate heat transfer model to explore the effects of casing material properties, environmental ambient conditions (like the experimental study), and casing thickness on the compressor performance and temperature profiles. This was done in an effort to quantify the impact of heat transfer through the metal surfaces into the flow. Additionally, these simulations could help quantify the relative impact of each of these modifications and dictate future design or operation changes to the experimental compressor facility to achieve desirable performance. Finally, a similar eddy viscosity enhancement was applied to the model to observe how increased spanwise mixing would affect the properties in the radial direction.

Within the conjugate heat transfer model, the AIP inlet duct and exhaust duct were given the properties of 6061 aluminum, and the forward frame shroud and all stators were given the properties of 17-4 stainless steel. In the initial model, the casing of the compressor itself was given the properties of 6061 aluminum. These assigned material properties were representative of their physical components within the facility.

An additional study was performed with changing the material properties of the casing to observe its effect on the performance of the compressor. Besides the aluminum casing that was representative of the one used in the experimental facility, a 17-4 stainless steel casing and a plastic PFA (perfluoroalkoxy polymer) casing were both simulated. In this study, the other stationary metal components retained their original material properties, therefore only the material properties of the casing were altered.

Like the fluid-only model, an adiabatic boundary condition was initially applied to the outer wall of the casing and the surrounding elements (AIP inlet duct, forward frame, and rear frame). However, to better resemble a more realistic environment, a few studies were performed with adding convection to the outside of the casing to better understand the importance of choosing correct thermal boundary conditions for the outer wall of the casing. Two different diabatic boundary conditions applied to the outside of the casing were explored: The first involved an ambient room temperature at standard day conditions (59°F) with free convection of $1.76 \frac{BTU}{h-ft^2-°F}$ ($10 \frac{W}{m^2 K}$), simulating a physical environment with little or no breeze. The second involved an ambient room temperature at standard day conditions (59°F) with a forced convection of 17.6 $\frac{BTU}{h-ft^2-°F}$ ($100 \frac{W}{m^2 K}$), simulating a physical environment in which a lot of air is circulated around

the room/casing or a large temperature difference is produced between the outer wall of the casing and the room. These convection influences were performed for all three material selections of casing material (aluminum, stainless steel, and plastic).

The impact of different casing thicknesses on compressor performance were explored with the baseline experimental casing thickness of 1.5 inches, a reduced casing thickness of 0.5 inches, and an increased casing thickness of 2.5 inches, shown in Figure 2.33. Only the aluminum casing was used for this part of the investigation.
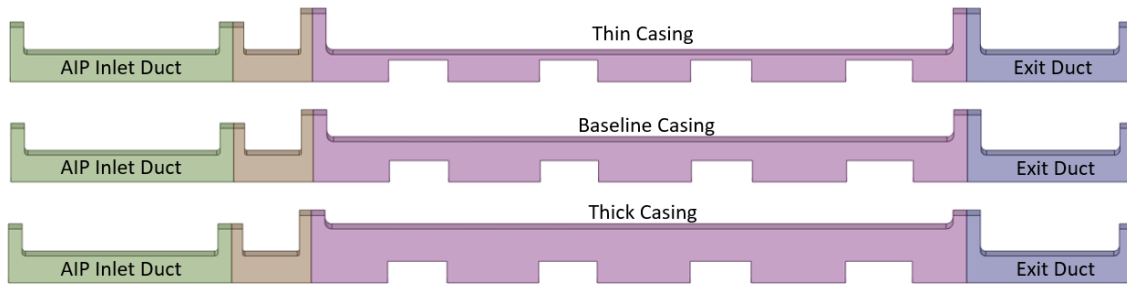
Figure 2.33. Geometric changes to casing for the conjugate heat transfer simulations.

Finally, an investigation on increased spanwise mixing through enhancing the eddy viscosity was performed, like that of the steady-state fluid-only model, to explore the impact of the metal surfaces on the radial properties of the flow. Once again, only the aluminum casing was used for this part of the investigation.

3. MEASUREMENTS OF SURFACE AND FLOW TEMPERATURES IN THE COMPRESSOR

Much of the motivation for this investigation arose from the unique observations associated with the experimental research on compressors in the P3S facility. These observations included an increase in total temperature across stator blade rows, a higher-than-expected total temperature ratio, and high temperatures on the outside of the aluminum casing in the front stages of the compressor. Further experimental testing of the PAX200 compressor was necessary to better understand the causes and quantify the effects of these thermal characteristics within the facility. While a few traditional and well-established experiments within the facility were used to characterize the overall performance of the compressor, much remained unknown about the temperatures and heat fluxes throughout the endwalls and cavities. These measurements were necessary to gain insights into how heat transferred throughout the stationary components and to characterize the proper thermal boundary conditions of the facility. During the experimental campaign, a great deal of knowledge was gained through plunging temperature probes in the cavity regions, acquiring surface temperatures and heat fluxes throughout the stator blades and casing, and applying different environmental factors to the outside of the casing. Overall, these experiments were useful in offering crucial insights into the heat transfer considerations that could affect the compressor performance, endwall temperatures, and/or interstage stagnation pressure and temperatures. Furthermore, these experiments also provided a unique and useful dataset to validate predictions from the computational model. As discussed in the next chapter, this validation of the computational model allowed for additional insights into how other thermal considerations could affect the compressor performance.

3.1 Baseline Radial Flow Profiles

First, using the seven-element rakes placed in between each blade row, radial stagnation temperature and pressure profiles were acquired across a 20-pt circumferential traverse spanning one stator passage. These circumferentially averaged profiles provided the average flow properties at each station in the compressor. The radial stagnation pressure profiles are shown in Figure 3.1, normalized by the area-averaged stagnation pressure for each respective station. A few

observations with these profiles indicated that a pressure deficit, most likely due to tip leakage flows near the tip behind each rotor and the turbulent boundary layer entering the inlet of the compressor, was redistributed lower in the flowpath as the air passed through each blade row. Furthermore, a hub deficit started to grow after the flow passed through S2. Both effects led to a pressure increase in the lower mid-span toward the exit of the compressor.
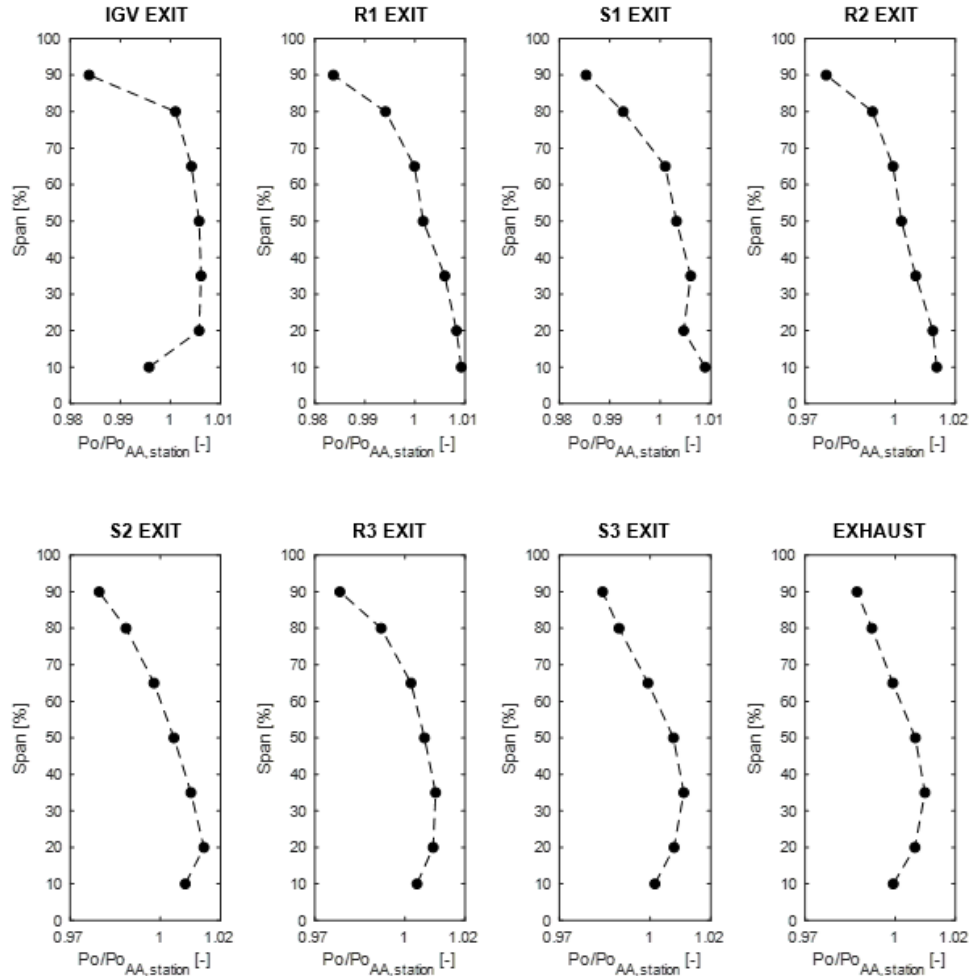
Figure 3.1. Experimentally measured radial stagnation pressure profiles between each blade row.

In the radial stagnation temperature profiles, Figure 3.2, there was a bigger distinction between the tip and hub portions of the temperature field. A high temperature at the tip showed potential influence from downstream heat conducted upstream through the casing, as well as the additional work put into the flow from the rotor to overcome the blockage at the tip. In the hub

region, the higher temperature, particularly in the front stages suggested that heat transfer was impacting the flow due to heat generation in the cavity regions. This was also theorized to be a contributing factor to the overall increase in temperature across each stationary blade row, shown in Table 3.1. One exception to this was the IGV, which turns the flow in the opposite direction as the stator blades to set up the flow, rather than increase the pressure of the compressor. Because of this flow expansion, the overall average temperature of the blade row decreased. However, the temperature near the tip increased due to potential downstream conduction through the casing. Finally, as the flow progressed toward the rear stage, it became more constant and uniform throughout the span, indicating that mixing had taken place.
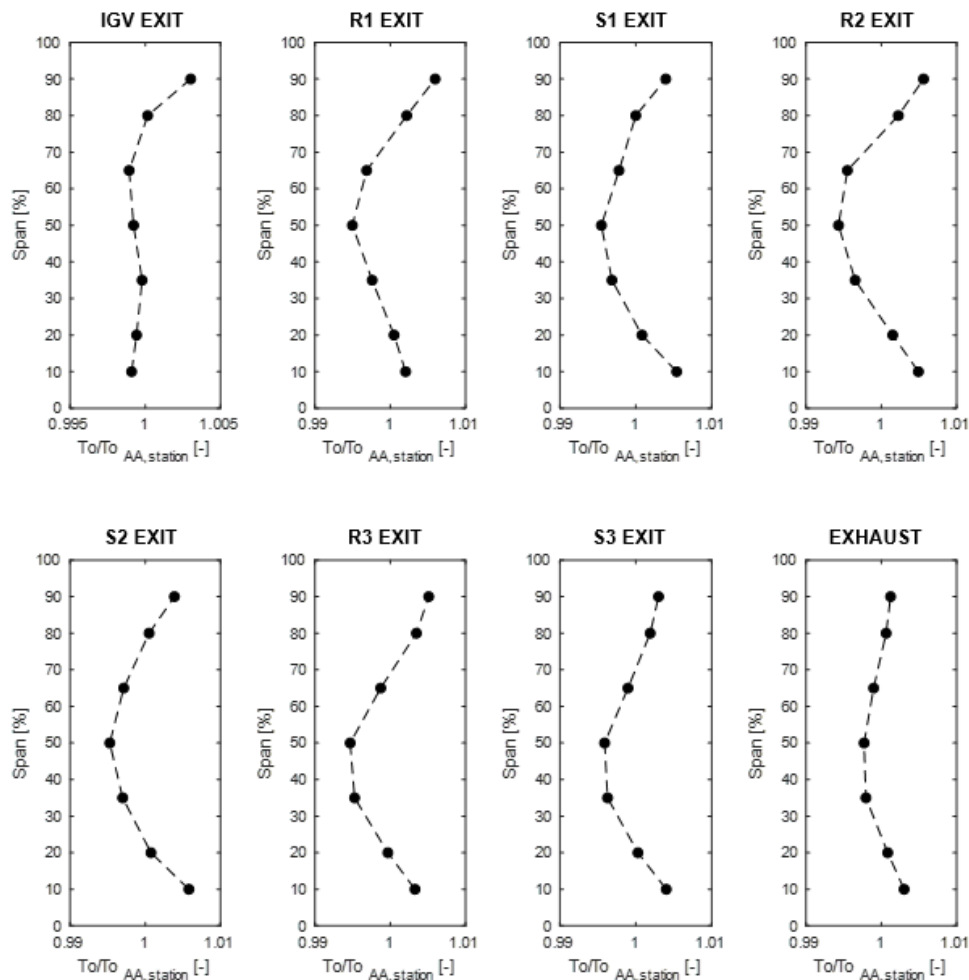
Figure 3.2. Experimentally measured radial stagnation temperature profiles between each blade row.

Table 3.1. Difference in area-averaged, stagnation temperature across stationary components, based on standard day conditions.

IGV Station 1 to 2	*S1* Station 3 to 4	*S2* Station 5 to 6	*S3* Station 7 to 8	*EXH* Station 8 to 9
-0.66°F	+1.90°F	+1.88°F	+1.33°F	+0.38°F

With the increase in temperatures across the stators in the PAX200 compressor, the radial stagnation temperature profiles showed the hottest regions of the flowpath were in the hub and tip regions. Mixing in each blade row was also considered to potentially contribute toward the heating of the flow through a heated fin interaction as the turbulent air passed through each stator row. Since rake measurements were restricted to 10%-90% span, more data were required to observe the endwall and cavity temperatures to better understand the heat transfer in these regions.

3.2   Cavity Flow and Endwall Characterization

With the high stagnation temperatures observed in the hub region of the experimentally measured radial profiles, the temperatures of the cavities were determined to be a good starting point at identifying potential heat sources that could be impacting the primary flow. As discussed in Chapter 2, to accurately capture these temperatures, traverses were performed with a single-element temperature probe in both the radial and rotational directions (relative to the probe). The probe was traversed radially through the primary flowpath at its absolute flow angle and then rotated +/- 80° with respect to the rotation of the rotor. In these experiments, 0° referred to the probe facing directly toward the rotation of the compressor to best capture the rotating cavity flow as it passed through the wells and knife seals.

Due to the axial location of the station 2 instrumentation port with respect to the downstream IGV stator well and its proximity to R1, the stagnation temperature characteristics of the IGV cavity were unable to be captured with the temperature probe. However, based on the observations made in literature and the comparison between the other cavities and the thermal mapping experiments (discussed in the next section), the temperature of the endwall was determined to be a reasonable estimate for the temperature of the stagnated flow in that cavity.

First, the stagnation temperatures of the downstream and upstream stator wells of S1 were examined. As shown in Figure 3.3, the stagnation temperature increased up to 15°F from the flow at 0% span, with the most significant temperature occurring with the probe oriented at around 70°

toward the downstream axial direction. (20° from the axial direction). This small spike in temperature was thought to indicate the direction of the flow coming out of the knife seal region directly under the stator, very close to the rotating drum.
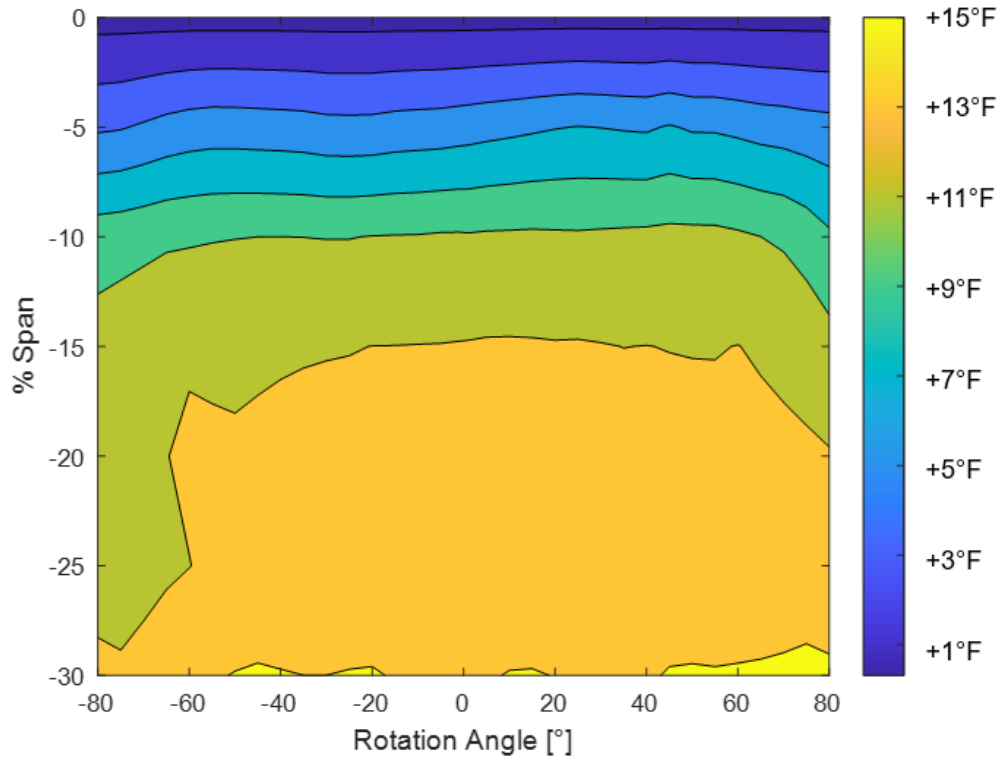
Figure 3.3. Stagnation temperature contour taken over a 160° rotation inside the upstream stator well of S1 (Station 3).

The downstream S1 well, shown in Figure 3.4, showed a similar trend, although with about half of the temperature gradient. The hottest flow occurred near the rotating drum, but small pockets of heat were observed at a 20° angle (toward downstream) and 40° angle (toward upstream) opposite the direction of rotation. These pockets could be the result of the flow recirculating within the cavity as it enters the well and redirects to go under the knife seals. The hottest temperatures near the drum occurred within the -60° to 40° range, (30° with respect to upstream axial direction to 50° with respect to the downstream axial direction). Overall, the difference between the hottest temperatures observed in the two wells, an indication of the temperature rise across the knife seal region, was equal to about 7°F. The recirculation and relatively large temperature increase between wells were thought to be the result of the S1 hub geometry. The S1 cavity region is the most unique

compared to the other stators, as it featured a radial contraction/expansion in area before passing over the knife seals, while the other stators had a constant radial area over the knife seals.
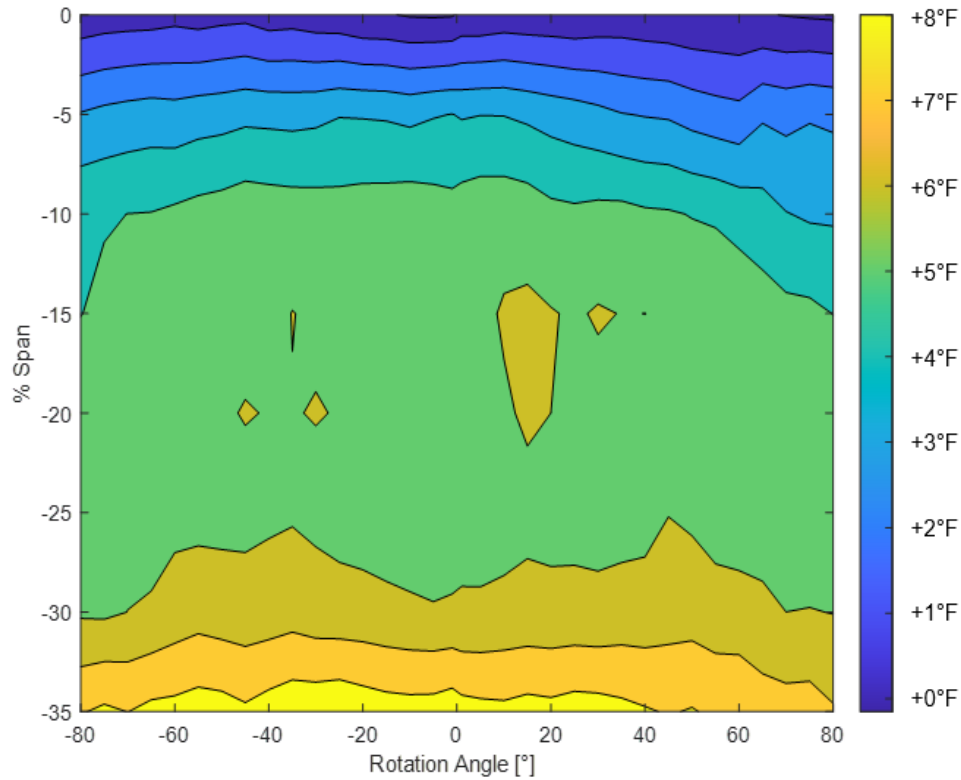
Figure 3.4. Stagnation temperature contour taken over a 160° rotation inside the downstream stator well of S1 (Station 4).

Next, the stagnation temperatures of the downstream and upstream stator wells of S2 were examined. Unfortunately, as shown in Figure 3.5, the temperature probe malfunctioned during the traverse and was only able to capture the full rotation up to -15% span. However, one full plunge was captured at a -35° rotation angle before the malfunction occurred. Much like the S1 upstream stator well, the S2 upstream stator well followed a similar trend, with an overall increase in temperature up to 16°F.
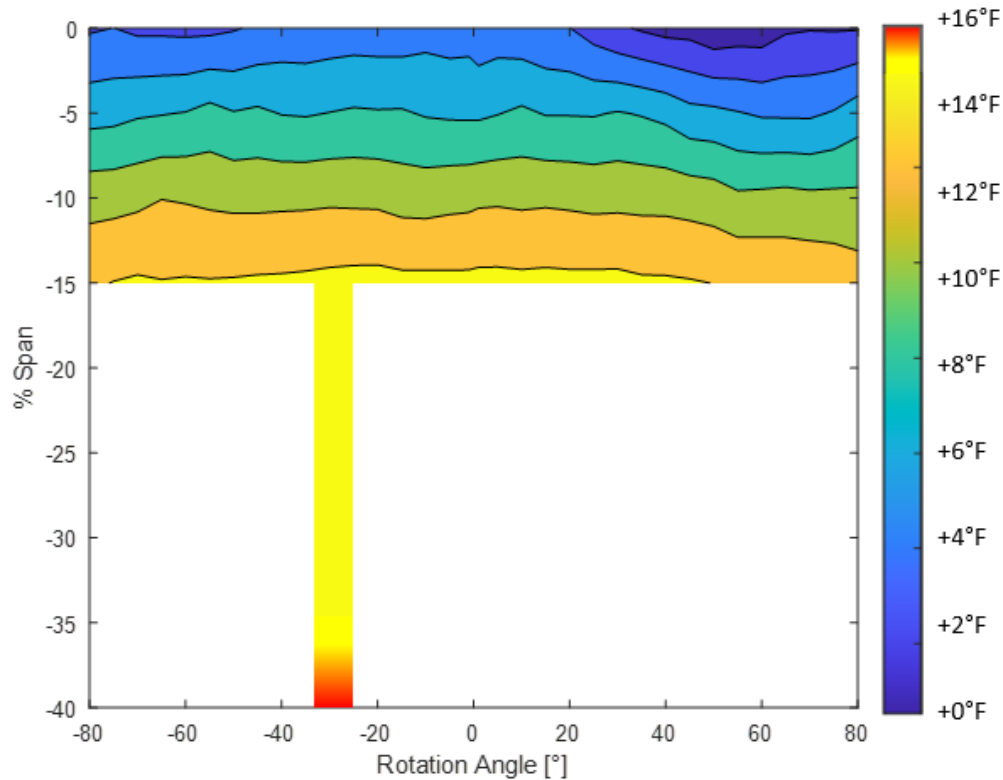
Figure 3.5. Stagnation temperature contour taken over a 160° rotation inside the upstream stator well of S2 (Station 5).

The downstream S2 well, shown in Figure 3.6, produced a similar trend to the previous cavity temperature contours with an overall increase in temperature up to 13°F. A small increase in temperature occurred at around -30° from the direction of rotation (60° rotation with respect to the upstream axial direction). The contour was much smoother compared to that of the S1 downstream well, most likely due to the difference in cavity geometry. Overall, the difference between the hottest temperatures observed in the two wells surrounding S2, was equal to at least a 3°F temperature rise across the knife seals.
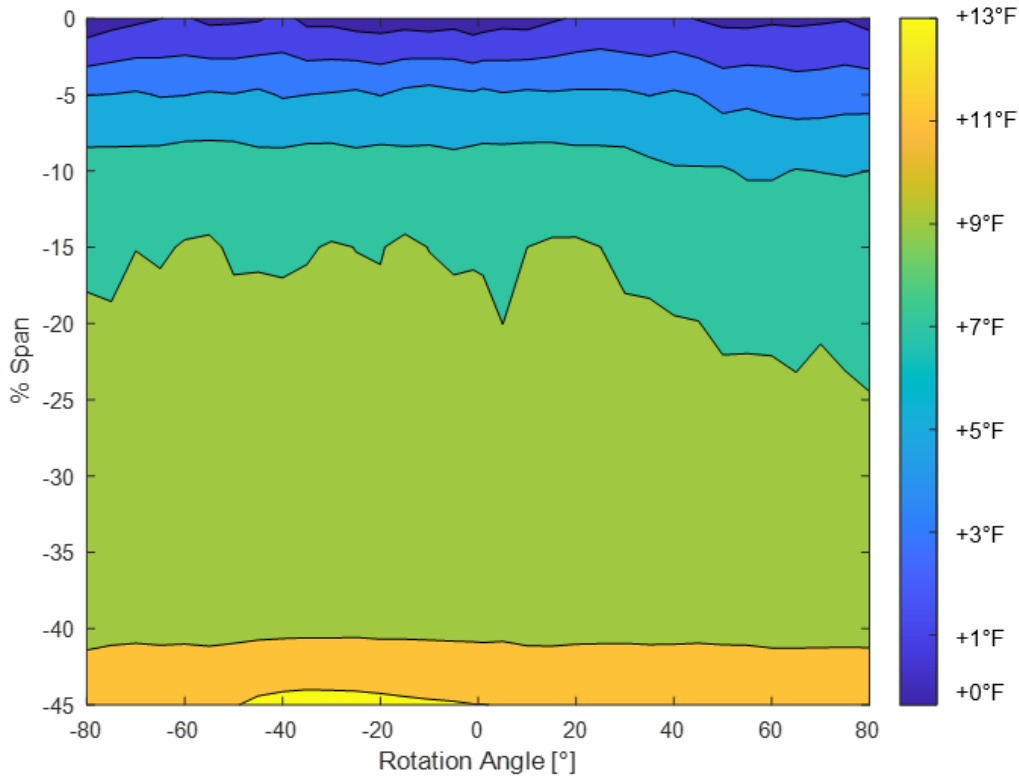
Figure 3.6. Stagnation temperature contour taken over a 160° rotation inside the downstream stator well of S2 (Station 6).

The stagnation temperature characteristic of the upstream S3 well, shown in Figure 3.7, was different due to the exit bleed flow passage. As described in Section 2.1.4, the flow in the compressor stage enters this upstream cavity and passes through the knife seals where it enters the region between the rotating drum and stationary bearing housing. The flow is then bled through a series of tubes back toward ambient conditions.

Two peaks of stagnation temperature were observed, with the largest peak occurring at a depth of about -20% of the span height into the cavity with a rotational angle of 20° from the direction of rotation (70° with respect to the downstream axial direction). A secondary peak was uniform across the lower third of the cavity, with the highest temperature near the same angle of rotation as the peak in the upper cavity. This phenomenon also suggests a recirculation of flow as the flow is forced to abruptly change direction as it tries to escape to the low-pressure conditions in the rear drum and bearing region of the compressor.
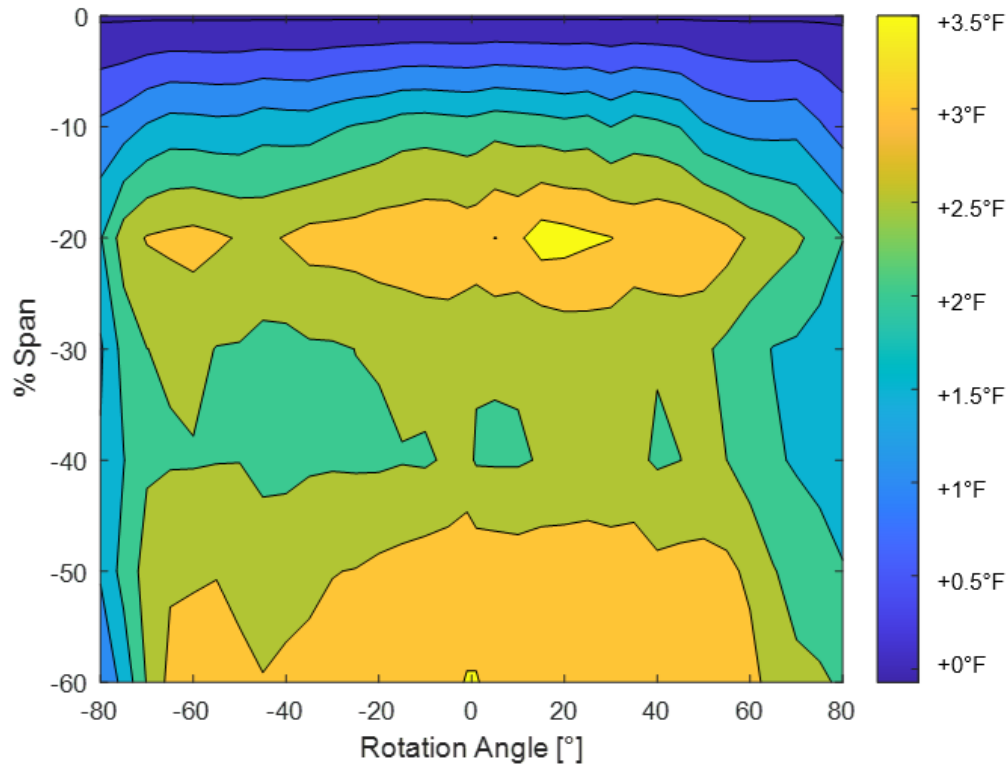
Figure 3.7. Stagnation temperature contour taken over a 160° rotation inside the upstream stator well of S3 (Station 7).

Overall, these stagnation temperature measurements provided a comprehensive look into the temperature rise within the stator wells of the PAX200 compressor. They also provided a qualitative look at the direction and potential flow interactions of the leakage flows going into and out of the cavity regions. Finally, they also proved useful in supplying a comprehensive boundary condition for the often hard-to-reach stator cavities and well regions. These results were crucial to the validation of computational models, that will be discussed in the next chapter.

In addition to the cavity flow measurements, the use of a temperature probe also allowed for characterization of the flow near the hub and shroud regions of the primary flowpath. Though the data were acquired at a fixed vane position, measurements from the probe were compared to the baseline experimental data for the entire span, as shown in Figure 3.8. Overall, the overlapping regions of the two measurement devices had very close alignment. Analysis of the upper region (90%-100% span) and lower region (0%-10% span) confirmed the influence of heat from the endwalls on the flowpath. In the upper region, there was a continual increase in temperature at each stator exit, particularly in the front half of the compressor (S1 exit). Conversely, there was a

gradual temperature decrease at the exit of each rotor, particularly with the rear stages (R3 exit). For the lower region of the flowpath, there was a consistent increase in temperature as the probe reached the endwall, with the most significant increase after each rotor exit. The profile of these stagnation temperature measurements reaffirmed the theory that the endwalls were the hottest parts of the flowpath and supported the need to quantify just how much heat could be entering the flowpath from the surrounding metal surfaces.
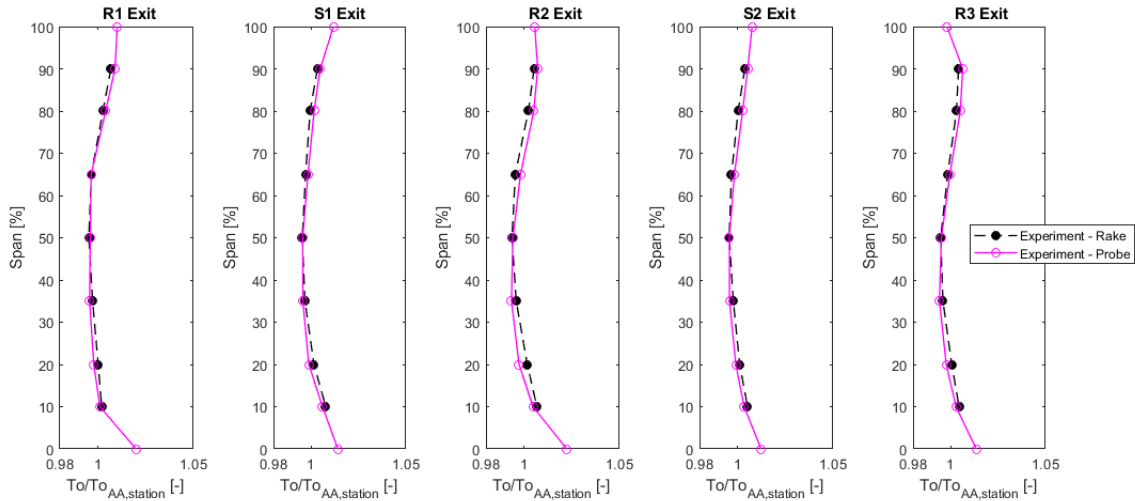
Figure 3.8. Stagnation temperature comparison between probe and rakes, taken at 50% vane passage.

3.3   Metal Surface Thermal Mapping

The stagnation temperatures of the air within the stator wells and cavities indicated a significant heat source coming from the endwalls of the primary flowpath. Therefore, it was important to better characterize these endwall temperatures and heat fluxes within the main flowpath to better understand the heat transfer throughout the compressor, particularly for the stationary reference frame. Many surface thermocouples were applied to the stator shrouds, hubs, blades, and cavity surfaces, as well as the inner and outer surfaces of the casing, to observe the relative temperature differences between components and the flow. Heat flux gauges were also installed at the front and rear part of the compressor casing to gather heat flux data needed to observe the flow of heat through the casing and for computational simulation comparisons. Each set of data in the following figures were produced by averaging the flow temperatures in each

region shown. For example, for Figure 3.8, the metal surface temperature measurements are shown with respect to $(T_{o1} + T_{o2} + T_{o3})/3$, with any temperatures above that average notated with a + (red) sign, and any temperatures below that average notated by a – (blue) sign.

The temperature measurements taken at the inlet duct, AIP, and IGV sections, shown in Figure 3.9, were all significantly higher than that of the average flowpath temperatures. Since the IGV blade provided a thermal barrier between the shroud and hub regions as the flow accelerated through the blade row and decreased in stagnation temperature, the only possible heat sources for this region of the compressor were conduction through the casing and heat generation in the cavity regions. With the magnitude of the temperature measurements, particularly on the exterior of the casing, these surface measurements indicated the presence of significant heat traveling through the casing from downstream stages to the front portion of the compressor. The results also showed the significance of the windage heating in the cavity regions and their potential thermal impact on the primary flow through the high temperatures located in the hub and cavity regions. Meanwhile, the hottest part of the flowpath was the cavity region of the IGV, as the front drum was considered a dead-head region where minimal flow traverses across the knife seals.
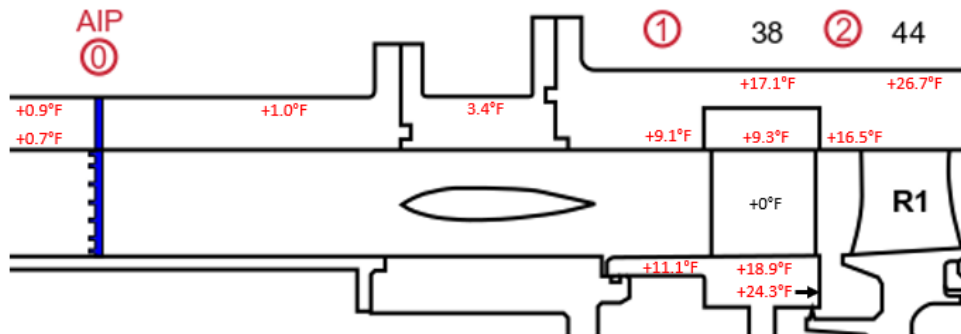
Figure 3.9. Temperature map of IGV surroundings, relative to the combined average flow temperature at Stations 0, 1, and 2.

As shown with the stationary components surrounding S1, Figure 3.10, the shroud of the flowpath was partially hotter than the average flowpath temperature, while the stator hub was significantly hotter. As shown in the results from the cavity plunges with the temperature probe, the upstream stator well was hotter than the downstream well. Furthermore, the stagnation temperatures from the probe tracked closely with these measured metal temperatures – within 2°F. With significant heat generation in the hub of the stator, this identified a key region in

99

which heat transfer could affect the overall temperature of the primary flow, particularly across the stator. As with the IGV, the blade temperature appeared to follow more closely with the flow than be influenced from the heat in the casing/stator shroud and hub.
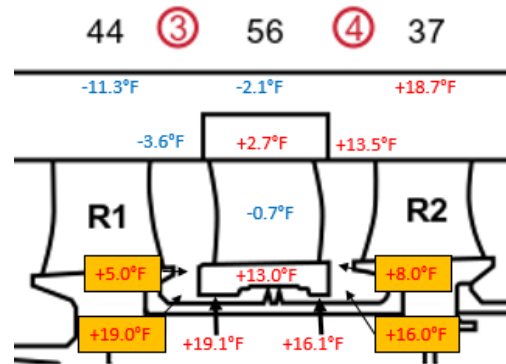
Figure 3.10. Temperature map of S1 surroundings, relative to the average flow temperature at Stations 3 and 4. Highlighted temperatures indicate stagnation temperature measurements of the flow from probe plunge.

A similar trend was observed with the components surrounding S2, shown in Figure 3.11. There was a similar increase in temperature between the cavity wells and the primary flow, with a slight deviation between the stagnation temperature and metal temperatures inside the cavity. As with the IGV and S1 blades, the S2 blade also acted isolated the heat between the shroud and hub.
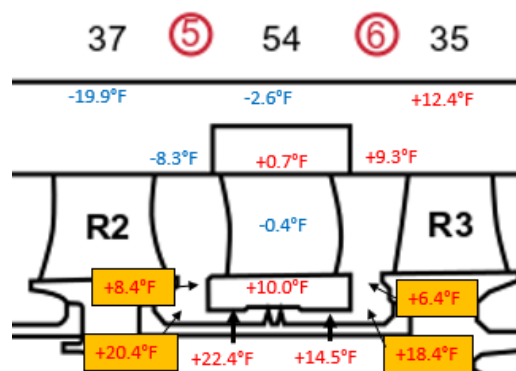
Figure 3.11. Temperature map of S2 surroundings, relative to the average flow temperature of Stations 5 and 6. Highlighted temperatures indicate stagnation temperature measurements of the flow from probe plunge.

100

Finally, with the rear components of the compressor, shown in Figure 3.12, the shroud temperature was actually cooler than that of the primary flow. The only significant heat source was in the S3 cavity with a slight increase in temperature before the flow passed through the rear knife seals into the rear drum/bearing region. As with the other parts of the compressor, the stagnation temperature measurements in the cavity region tracked closely with the metal surface temperatures, and the S3 blade was still cooler than that of the average flow temperature between stations 7, 8, and 9.
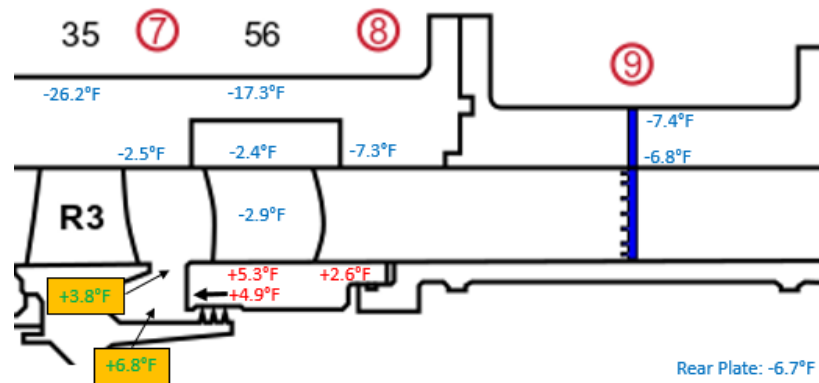
Figure 3.12. Temperature map of S3 surroundings, relative to the average flow temperature of Stations 7, 8, and 9. Boxed temperatures indicate stagnation temperature measurements of the flow from probe plunge.

In addition to the surface temperature measurements, heat flux gauges at select locations gave an indication as to the level of heat flux and direction of heat flow within the stationary components. Overall, as shown in Figure 3.13, a general trend of heat flowing out of the rear stages and into the casing was observed. Additionally, heat transfer from the casing into the front stages was observed. While these heat flux gauges did not cover the entire flow path, they confirmed some critical insights into the heat transfer characteristics at the front and rear of the compressor. As shown in previous studies on the facility, a linear trend of increasing temperature on the external surface of the casing established a conduction path from the rear of the casing to the front of the casing. The heat flux gauge measurements confirmed this overall conduction path.
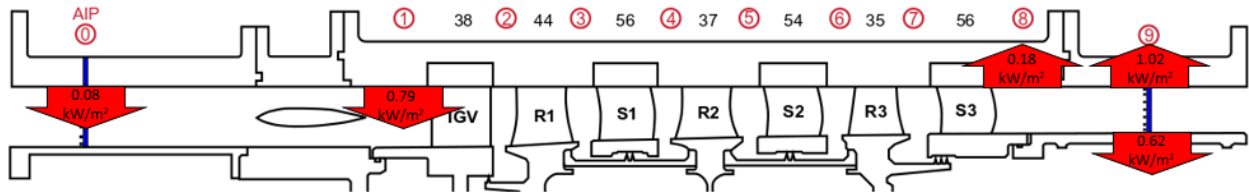
Figure 3.13. Heat flux gauge measurements for baseline casing.

Overall, these surface temperatures and heat fluxes, combined with the stagnation temperatures taken in the cavities, provided a substantial thermal map of the compressor to identify the various sources of heat within the compressor. With an average stagnation temperature increases across stators, the interaction of these heat sources with the primary flow were the only way in which this phenomenon could occur within the facility. A previous theory included the possible consideration of the shaft bearings as a potential heat source, but the results from the heat flux gauges also ruled this out. These thermal measurements also provided a valuable dataset that could be used to check the thermal boundary conditions applied to the computational simulations, which was a crucial element of this research investigation.

3.4   Environmental Effects on Stagnation Temperature Radial Profiles in the Flow-Field

To directly measure the impact that the ambient environment has on the stagnation temperatures in the flow-field and surface measurements of the compressor. First, an experiment was performed to change the convective heat transfer on the outside of the casing and track the corresponding metal and flow temperature changes. This particular experiment was performed using a circumferentially averaged data point and offered a direct quantitative evaluation of convective effects on the primary flow. Next, a few attempts were made to significantly cool and heat the casing of the compressor to try to achieve a large decrease/increase in temperature or heat transfer through the casing. While the results of these tests were primarily qualitative due to the inability to traverse the vanes a full blade passage to characterize a complete data point, they still provided valuable insights into the level of impact these changes in boundary conditions could have on the primary flow.

3.4.1 Convection Effects on Compressor Temperature Radial Profiles

First, different changes were made to the P3S facility and test cell by applying different ambient conditions to better understand the effect of convective heat transfer on the compressor. While these tests did not include changes to the heat transfer coefficient in the facility, in Newton's Law of Cooling, they take advantage of changing the difference in temperature between the control volume of the compressor and the environment. A full circumferential traverse point was obtained for this experiment to gain a more quantitative understanding as to how convection effects could influence the performance of the compressor.

The test cell was instrumented with a variety of thermocouples in the form of exposed, hanging beads at different locations throughout the room, as shown in Figure 3.14. Two tests were run back-to-back. The first test had the test cell doors closed (except for the exhaust door), which provided a stagnant, heated air surrounding the compressor casing. The second test had the test cell doors open to the environment, providing a thorough mixing of outdoor air to provide a large temperature difference between the compressor casing and the ambient environment.
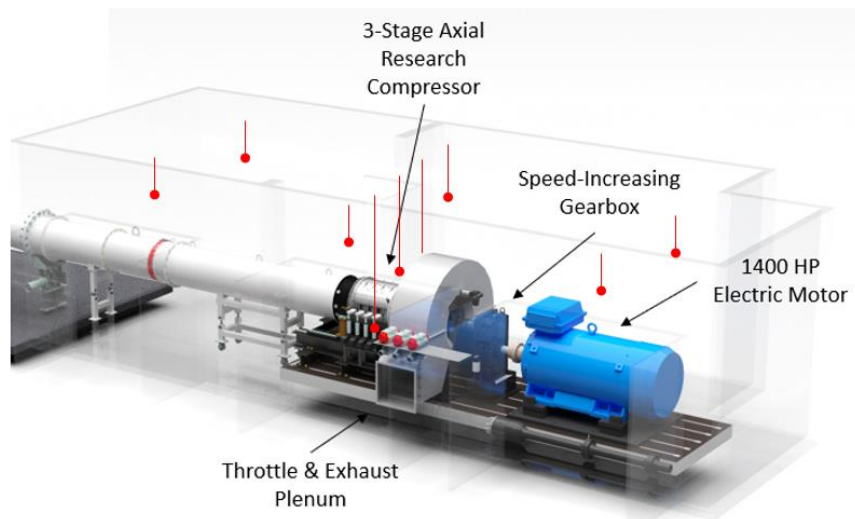
Figure 3.14. Hanging-bead, thermocouple locations throughout the test cell, used for monitoring ambient environment in the facility during operation.

For the hot environment, associated with the closed doors to the test cell, the hanging-bead thermocouples were measured during the traversed design point after a pseudo steady-state condition had been reached. The heat generation produced by the motor increases the room

temperature throughout the experiment, so the measurements varied by about 5° throughout the test. An overall difference between the outdoor ambient (compressor inlet) temperature and the measured test cell temperature is shown in Figure 3.15. On average, the room temperature was about 80-90°F above the inlet air entering the compressor. The hottest temperature was observed near the motor and the lowest temperature was recorded in the opposite corner of the room.
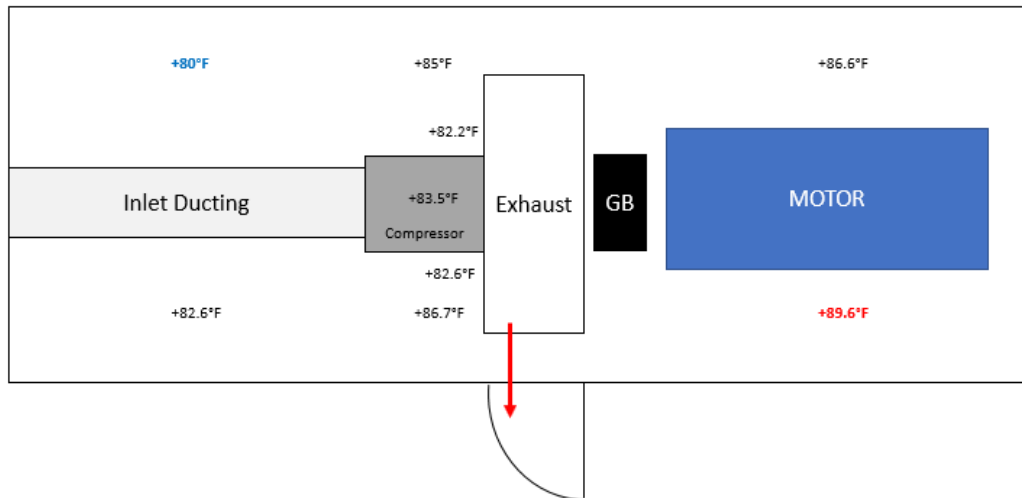
Figure 3.15. Temperature of the test cell with respect to the outdoor ambient (compressor inlet) air for the hot environment with test cell doors closed,

For the cold environment, associated with all the doors to the test cell open, the hanging-bead thermocouples were measured during the traversed design point after a steady-state condition had been reached. An overall difference between the ambient (inlet) temperature and the measured test cell temperature is shown in Figure 3.16. On average, the room temperature was much closer to the ambient temperature, though still about 30-50°F above the inlet air entering the compressor. The highest temperature occurred on the exhaust outlet side of the compressor, while the lowest temperature occurred on the opposing side of the compressor.
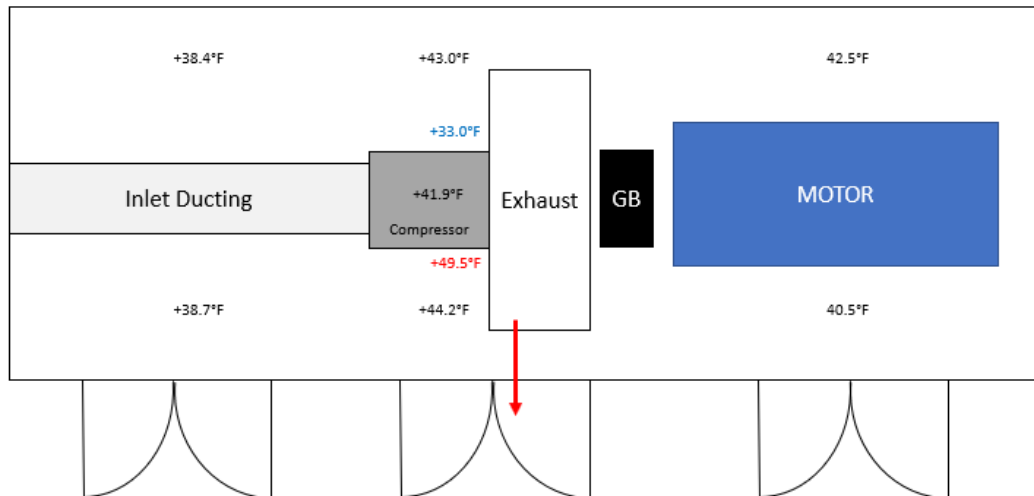
Figure 3.16. Temperature of the test cell with respect to the outdoor ambient (compressor inlet) air for the cold environment with test cell doors open,

With significant temperature and, thus, convection conditions between the two tests, the external surface temperature over S3 decreased about 4°F between the hot and cold test cell conditions. The radial stagnation temperature profiles were also compared between the two experiments at Stations 8 (S3 exit) and 9 (exhaust). As shown in Figure 3.17, while the profiles remained very similar through much of the flowpath, there was a slight difference in the very tip of the radial stagnation temperature profile (0.3°F). The hot test cell produced a slight increase in temperature near the shroud. From a performance standpoint, this resulted in a decrease in efficiency of about 0.25pts, indicating that keeping a convective condition in the facility induces a higher heat loss from the compressor which noticeably impacts the efficiency calculation.
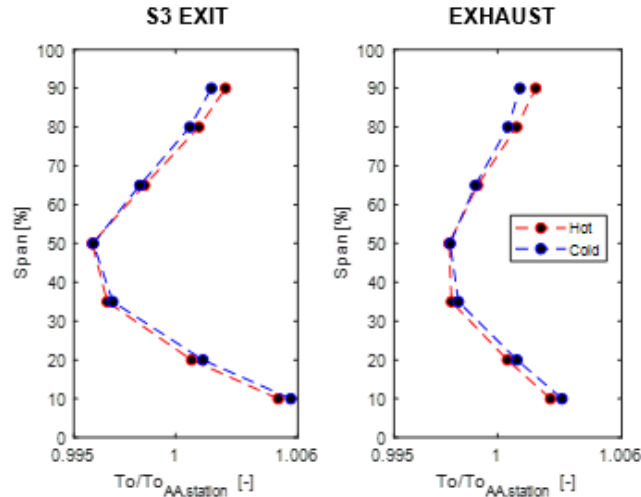
Figure 3.17. Difference in stagnation temperature profiles at Station 9 between hot and cold room environments.

A final observation that was made between the two experimental conditions was with the circumferential thermocouples placed around the outside wall of the compressor casing. As shown in Table 3.2, a relatively small variation (up to 6°F) was observed between the circumferential measurements taken over each blade row. While these variations at each blade row, could be a result of slightly different axial placement of the thermocouple beads, their position did not change between tests. Overall, a general trend was observed that the front of the compressor had an overall larger variation in temperature with the hot condition, signifying that the hot room had a more direct influence on the colder air at the inlet of the compressor. Conversely, the back of the compressor had a larger variation in temperature with the cold condition, signifying that the cold room had a bigger influence on the hotter exhaust flow at the outlet of the compressor.

Table 3.2. Circumferential variation in temperatures between environmental conditions.

	IGV	R1	S1	R2	S2	R3	S3
Hot	2.7°F	3.0°F	4.3°F	3.0°F	6.0°F	3.2°F	3.5°F
Cold	2.0°F	1.8°F	4.7°F	2.4°F	6.4°F	4.2°F	4.2°F
Difference	0.7°F	1.2°F	0.4°F	0.6°F	0.4°F	1.0°F	1.3°F

3.4.2 Effects of a Cold Compressor Casing on Temperature Radial Profiles

Next, it was desirable to produce a more extreme case of heating and cooling on a focused section of the compressor where qualitative observations could be made into discovering how sensitive the outside of the casing might be to ambient, environmental effects. The first of these experiments involved applying a pouch of dry ice to the outside of the casing around the entire circumference on only the front half of the compressor. Similar surface thermocouple measurements were used to characterize the temperature difference between the baseline results and those with the cold pack applied, as shown in Figure 3.18. For this part of the compressor, which was directly exposed to the dry ice, there was a global decrease of about 2-3°F among the stationary components as a result of the cooling attempt, particularly around the IGV.
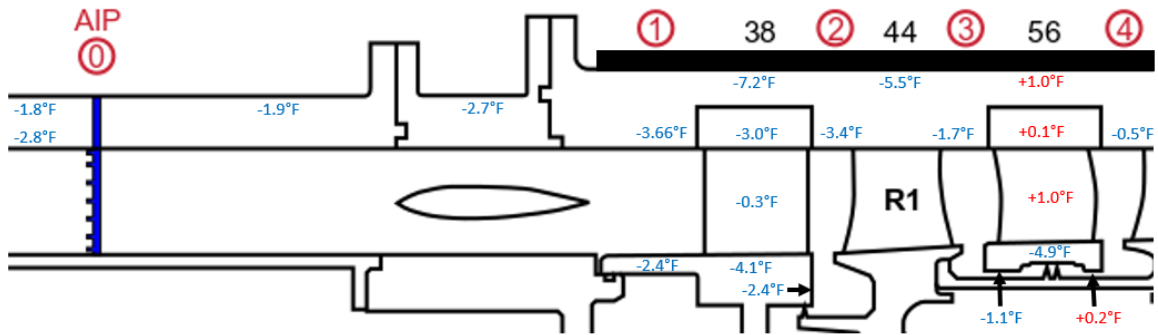
Figure 3.18. Temperature difference in stationary metal temperatures relative to baseline compressor casing (Section 3.3) for cooled compressor casing scenario. Cooling applied to Stations 1-4.

With the rear part of the compressor, Figure 3.19, which was not exposed to the dry ice blanket, there was a higher overall metal surface temperature observed with the stationary components at the inner flow path. With the dry ice located in the front half of the compressor, the outer neoprene layer of the blanket insulated the compressor from the ambient environment, allowing all the thermal energy to go into the sublimation of the dry ice. Acting as an insulator, trapping the heat in the rear half of the casing more than it would under normal operation.
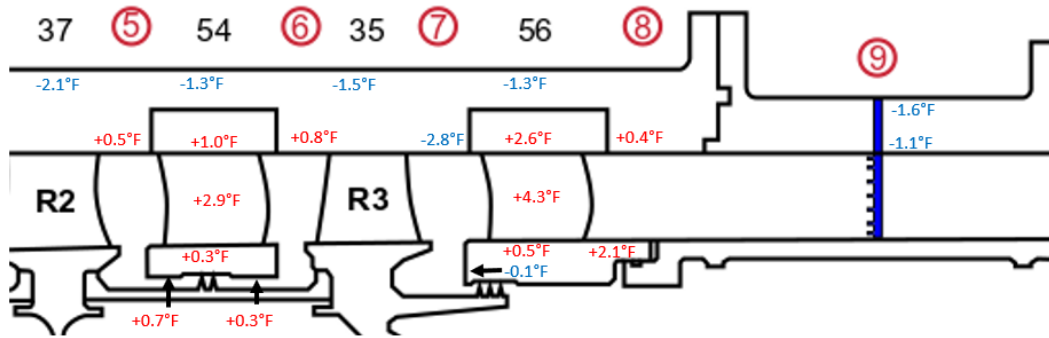
Figure 3.19. Temperature difference in stationary metal temperatures relative to baseline compressor casing (Section 3.3) for cooled compressor casing scenario.

This was also evident in the heat fluxes, shown in Figure 3.20, which showed an increase in heat flux (+0.22 kW/m^2) in the Station 8 region between the flow path and the casing compared to the baseline condition. The results also showed little change between the other heat flux measurements, signifying that while the cooled casing scenario decreased the temperature of the inner surface temperatures slightly, they were still significantly warmer than the flow.
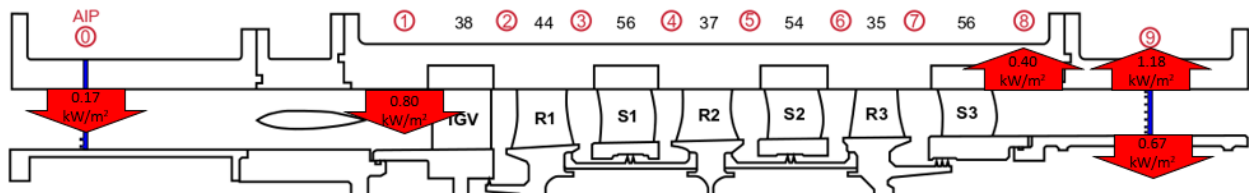
Figure 3.20. Heat flux gauge measurements for cooled casing scenario.

From a performance standpoint, the efficiency between the baseline and the cooled casing resulted in an approximate efficiency decrease of 0.8pts, which was unexpected. However, this was most likely due to the additional adhesive material applied to the thermocouples in the flowpath to keep them attached to the metal surfaces between the baseline and cooled casing runs. For reference, the addition of the thermocouples into the flowpath already decreased the efficiency by about 1.3pts from the baseline condition with the clean flowpath. Overall, the results showed that while the dry ice was somewhat effective at cooling the casing, especially on the outside surface, it was not enough to overcome the heat generation within the compressor.

3.4.3 Effects of a Heated Compressor Casing on Temperature Radial Profiles

A similar approach was taken with the second experiment, which involved heating the outside of the front half of the casing using a combination of heat tape and neoprene insulation. Similar surface thermocouple measurements were used to characterize the temperature difference between the baseline results and those with the heat tape applied, as shown in Figure 3.21. For this part of the compressor, which was directly exposed to the heat tape and neoprene insulation, there was a global increase of about 3-5°F among the stationary components due to the heating attempt, particularly around the IGV.
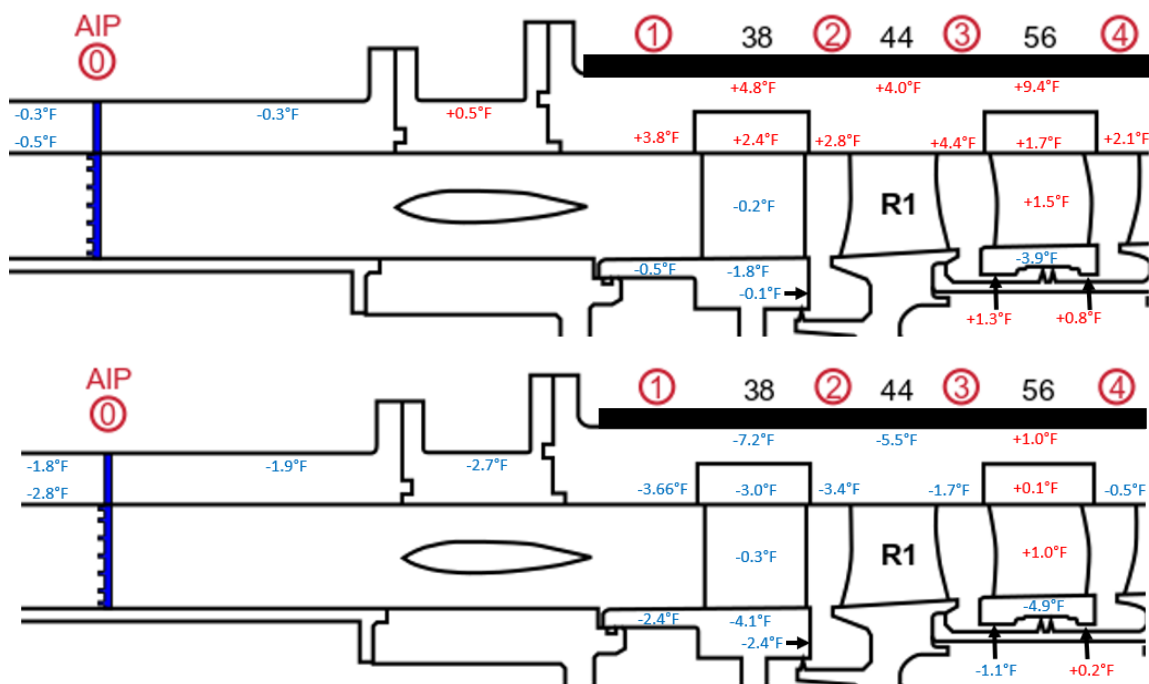
Figure 3.21. Temperature difference in stationary metal temperatures relative to baseline compressor casing for heated compressor casing scenario (top). Heat/insulation applied to Stations 1-4. Cooled casing scenario included for reference (bottom).

With the rear part of the compressor, Figure 3.22, which was not exposed to the heat tape, there was a much higher overall metal surface temperature observed with the stationary components at the inner flow path. While the heat tape was heating the front half of the compressor, the neoprene layer was also acting as an insulator, keeping heat in the rear half of the casing more than it would under normal operation. Combined with the impact of the heat tape, this effect also resulted in a global increase of about 3-5°F, like the front half of the compressor.
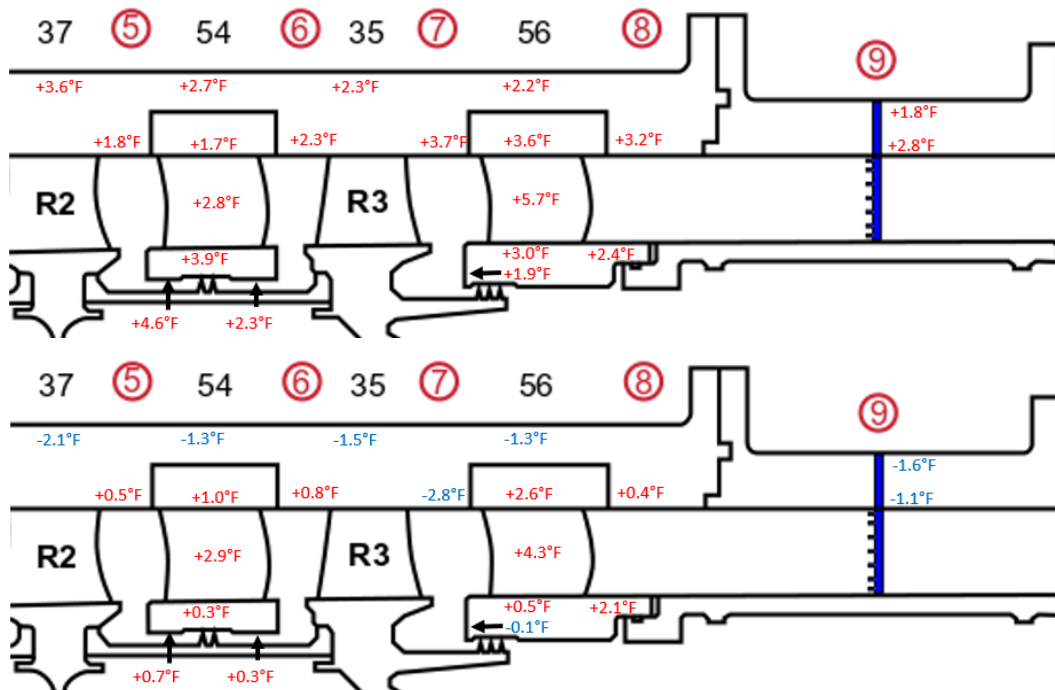
Figure 3.22. Temperature difference in stationary metal temperatures relative to baseline compressor casing for heated compressor casing scenario (top). Cooled casing scenario included for reference (bottom).

This was also evident in the heat fluxes, shown in Figure 3.23 and Table 3.3, which showed a reversal in heat flux in the Station 8 region between the flow path and the casing compared to the baseline condition. This was attributed to the shroud temperature now being greater than that of the flow temperature. The results also showed little change between the other heat flux measurements. Overall, these results showed that that heating the casing had a more significant impact on the overall metal surface temperature map of the compressor, as well as the direction of heat flow within the casing, particularly in the rear stages.
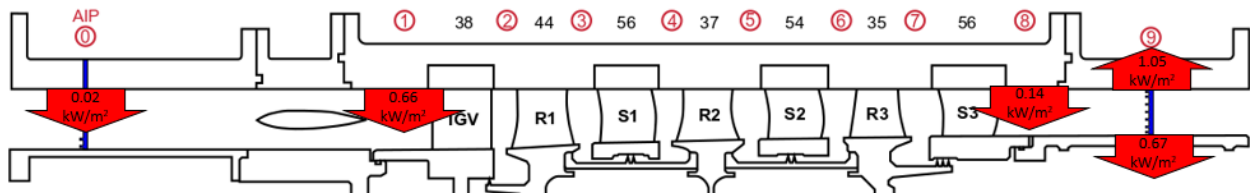
Figure 3.23. Heat flux gauge measurements for heated casing scenario.

Table 3.3. Heat flux comparison between baseline, cooled, and heated casing experiments.

	Station 0 Shroud	Station 1 Shroud	Station 8 Shroud	Station 9 (shroud)	Station 9 (hub)
Baseline Condition	0.08 kW/m^2 (into flow)	0.79 kW/m^2 (into flow)	0.18 kW/m^2 (out of flow)	1.02 kW/m^2 (out of flow)	0.62 kW/m^2 (out of flow)
Cooled Casing	0.17 kW/m^2 (into flow)	0.8 kW/m^2 (into flow)	0.4 kW/m^2 (out of flow)	1.18 kW/m^2 (out of flow)	0.67 kW/m^2 (out of flow)
Heated Casing	0.02 kW/m^2 (into flow)	0.66 kW/m^2 (into flow)	0.14 kW/m^2 (into flow)	1.05 kW/m^2 (out of flow)	0.67 kW/m^2 (out of flow)

In comparing the baseline case with these two extremes – cooling the compressor with dry ice and heating the compressor with heat tape – a few comparisons were made. From a performance standpoint, the efficiency between the baseline and the heated casing resulted in an overall approximate decrease of 1.7pts (additional decrease of 0.9pts compared to the cooled casing) between Stations 0-9. This was more expected as the compressor was not only heating the front half of the compressor but also insulating it, resulting in an overall increase in temperature throughout the whole compressor.

In summary, throughout the experimental tests performed on the PAX200 compressor in this chapter, an increase in stagnation temperature across the stators was always observed. Through experimental testing of the temperatures of the stationary components within the facility and the heat flux through the casing, potential heat sources were identified that could contribute to this temperature increase. Cavity plunges and surface thermocouples in the cavity regions gave a clear indication to the significance of windage heating and its impact on heating the entire hub of the shrouded stator. The plunges also showed that the measured stagnation temperature within each stator well closely matched that of the nearby metal surface. Finally, surface thermocouple and heat flux measurements, paired with heat applied to the casing and varying convection effects, gave an indication as to how much heat transfer could influence the measurements typically used to calculate compressor performance.

Overall, these experimental results proved that the behavior of the stationary components within the P3S facility were far from adiabatic, particularly with respect to the casing. As a result, with computational models often employing an adiabatic condition, it is necessary for them to take heat transfer into account if a match between experimental data and computational results is to be achieved. This dataset provided a comprehensive thermal map of the compressor, offering a more correct boundary condition to that of the experiment that could be used for computational

validation of the facility. Furthermore, the exact level of heat transfer was found to be highly sensitive to the ambient conditions within the experimental facility, which change quite often due to the different seasons and weather conditions in which the compressor is operated. Crucial insights were observed into how ambient and environmental conditions could be further explored computationally. Additional simulations would quickly and more easily provide a better idea as what conditions would be the most ideal for compressor operation. They could also give an indication as to how much the measurements used to calculate performance could be affected by applying different boundary conditions. All these computational considerations will be addressed throughout the next chapter.

4. MODELING CONSIDERATIONS FOR AEROTHERMAL PREDICTIONS

Computational simulations were performed using ANSYS CFX to better understand the heat transfer throughout the stationary components of the compressor. The simulations were particularly useful in comparing the different possible considerations that could impact the thermal characteristics of the compressor. These considerations included the use of different boundary conditions (adiabatic, isothermal, and diabatic), the implementation of conjugate heat transfer to the fluid model, and alteration of geometric and material properties of the compressor casing. Furthermore, the influence of enhanced mixing within the compressor to address spanwise stagnation temperature discrepancies between experimental and computational results was investigated. The results from these simulations were not only used for validation, but they also offer insights into which considerations have the most impact on compressor performance measurements and interstage pressure and temperature.

4.1 Adiabatic Boundary Conditions

First, as with most computational models, an adiabatic boundary condition was applied to the compressor to provide a baseline comparison between the experimental results and all subsequent simulations that were performed. Steady and unsteady models were developed using ANSYS CFX to compare radial flow profiles at each of the stations in the compressor flowpath corresponding to the experimental rake locations. The steady and unsteady models both involved the use of an adiabatic thermal boundary condition for all blade and endwall surfaces in both the rotating and stationary reference frames. The same ADP operating condition that was tested during the experimental testing campaign was applied to the steady and unsteady simulations. The resulting mass flow rate from the adiabatic steady simulation was then used to set the loading condition for all subsequent steady and unsteady simulations. All performance metrics (TPR, TTR, efficiency, etc.) were normalized by and compared to the performance metrics of this adiabatic, steady simulation case. Furthermore, the results from the simulations and the experimental data were normalized by the area-average flow property at each station.

113

As shown in Figure 4.1, the computational models were largely successful in predicting the measured radial stagnation pressure profiles. The steady and unsteady models had similar profiles and aligned very well with the lower half of the flowpath. However, a discrepancy was evident in the upper half of the flowpath, especially at the 80% span position, as both models struggled to capture the shape of the experimental pressure profile.

Figure 4.1. Comparison of interstage stagnation pressure profiles between experimental data and adiabatic versions of steady and unsteady fluid-only models, normalized with respect to the area-averaged value at each station.

As shown in Figure 4.2, there was a much larger discrepancy with the prediction of the radial stagnation temperature profiles. As with the pressure profiles, the computational models adequately predicted the overall trend of the temperature profiles, particularly with the unsteady simulation near the hub. In the tip region, there was a significant difference between the results from the computational models and the experimental results. The unsteady model had more success in predicting the tip temperature in the rear stages while the steady simulation was more successful in predicting the tip temperature in the front half of the compressor. Furthermore, the unsteady model was better at predicting the temperature in the mid-span region, which was most likely due to the removal of mixing planes that were used throughout the steady model. A consequence of the mixing planes is the averaging of properties between domains, which includes the vorticity of the flow. With time transformation interfaces between blade rows, the unsteady model is more accurate in carrying the vorticity through the flowpath, which allows more mixing to occur.

In comparing the overall performance metrics between cases (Table 4.1), the efficiency of the unsteady model is much higher than that of the steady model. This is due to the large overall decrease in total temperature ratio across the machine – a result of the higher fidelity unsteady model. With a very close match between the total pressure ratio and mass flow rate of the experimental data, the efficiency struggles to reach that of the adiabatic steady or unsteady cases. The relatively high total temperature ratio was a major contributor to this difference.
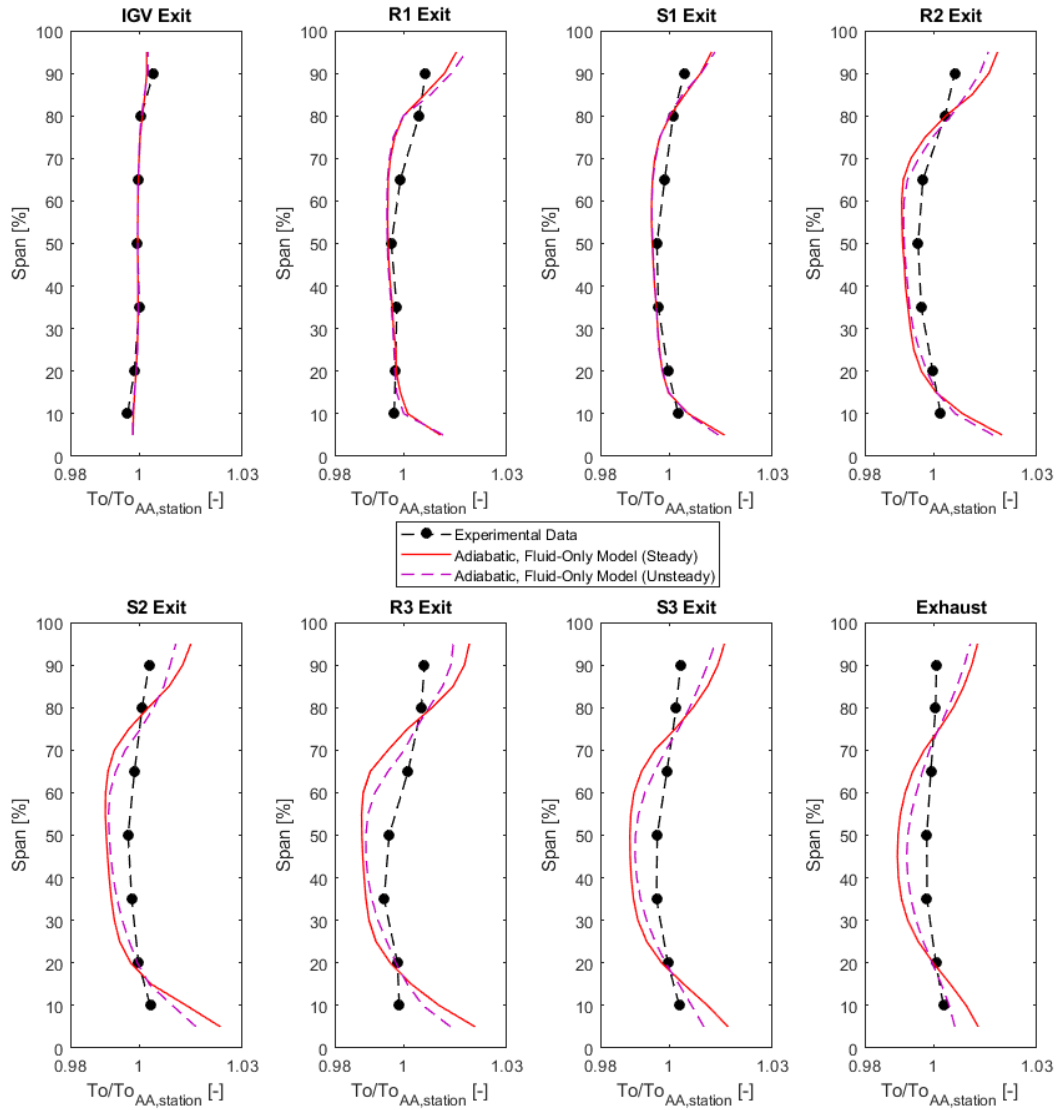
Figure 4.2. Comparison of interstage stagnation temperature profiles between experimental data and adiabatic versions of steady and unsteady fluid-only models, normalized with respect to the area-averaged value at each station.

Table 4.1. Performance metric comparison between experimental results and adiabatic steady and unsteady, fluid-only models, normalized with respect to the adiabatic, fluid-only model.

	TPR [-]	$\dot{m}_c$ [-]	$\frac{R_c}{W_c}$[-]	TTR [-]	$\Delta\eta_{is}$ [pts]
Experimental Data	0.995	0.994	1.001	0.999	-0.441
Adiabatic, Fluid-Only Model (steady)	1	1	1	1	-
Adiabatic, Fluid-Only Model (unsteady)	0.995	0.996	1.000	0.996	+1.194

Overall, the tip region was consistently off in both pressure and temperature. The stagnation temperatures in the tip region of the simulations suggested that the temperatures of the stationary components could provide insight into why such a large discrepancy would exist between the experimental and computation data. While an adiabatic boundary condition was a useful starting point for the simulations, the results in Chapter 3 showed that the heat transfer effects are measurable and thus, relaxing the adiabatic assumption is explored in the following section.

4.2   Implementation of the Isothermal Boundary Condition

There were significant differences between the temperature values of the endwall temperatures of the adiabatic steady and unsteady simulations to that of the experimentally measured endwall temperatures. As shown in Figure 4.3 and Figure 4.4, there was about a 10°F difference in the S3 domains between the steady and unsteady cases and an even greater difference in the cavity regions. When compared to the thermal model of the PAX200 compressor, derived from the experimental data and shown in Figure 4.5, this temperature discrepancy was about 20°F in the cavities and exhaust region. This comparison was made through assessing the difference between the interpolated metal surface temperatures coming from the thermal model based on the experimental measurements, with that of the domain boundaries of the CFD model. Cavities were included in both models for direct comparison between experimental and computational results.
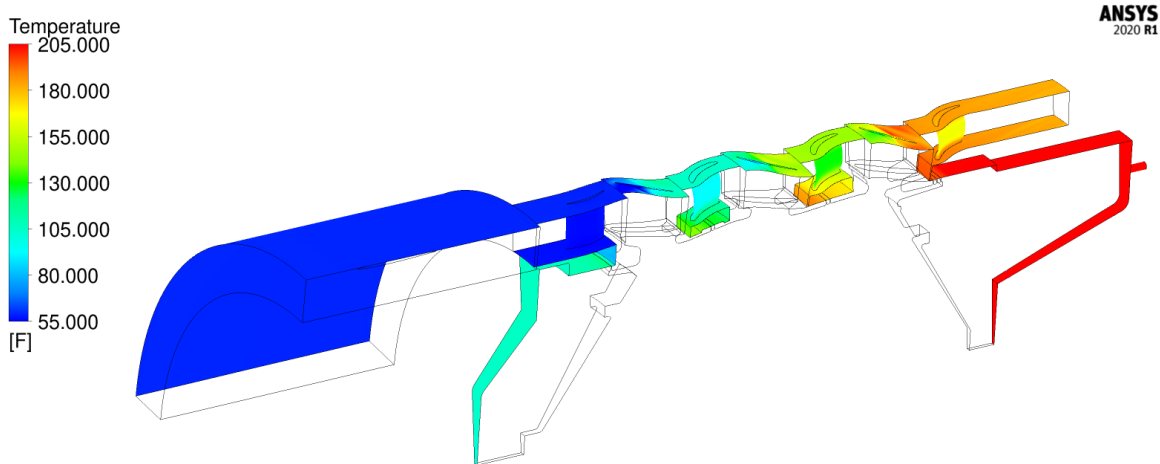
Figure 4.3. Stationary frame endwall temperatures for the steady simulation case with an adiabatic thermal boundary condition.

117
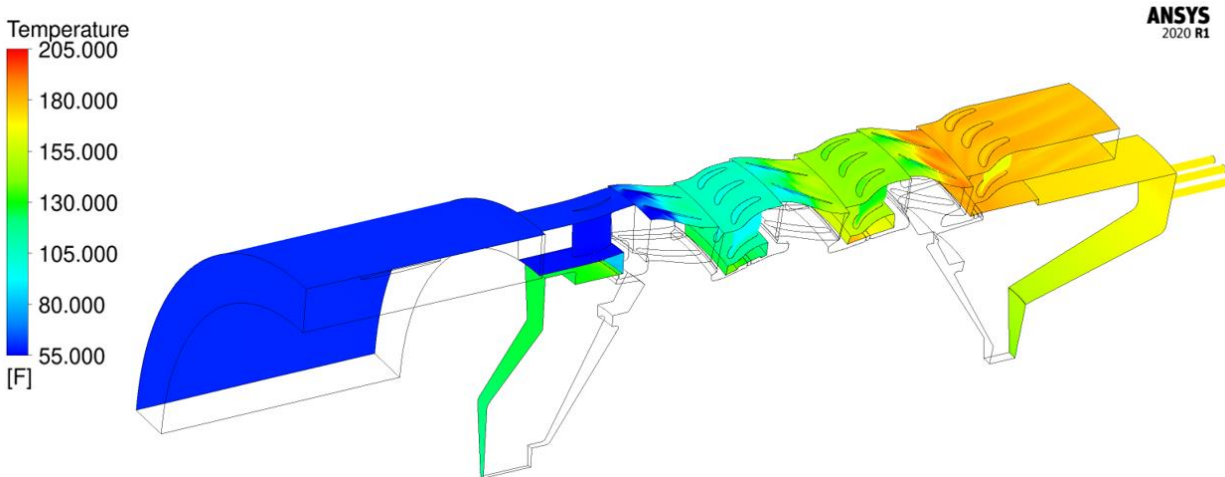
Figure 4.4. Stationary frame endwall temperatures for the unsteady simulation case with an adiabatic thermal boundary condition.
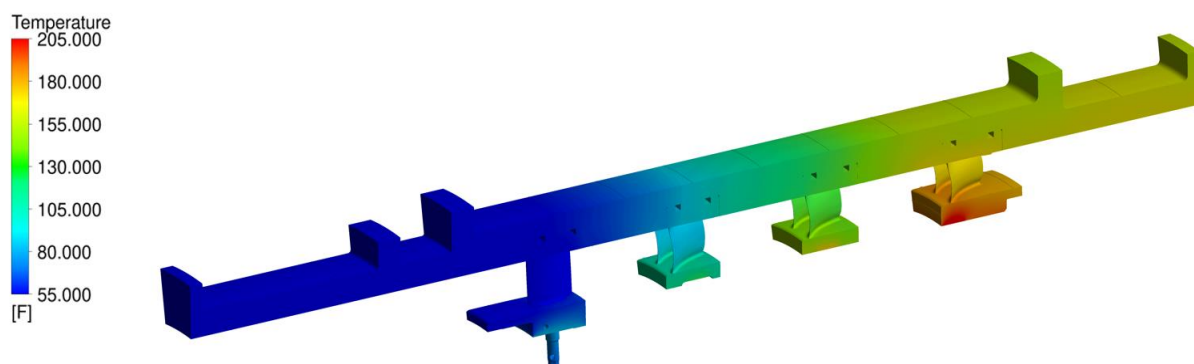
Figure 4.5. Stationary frame endwall temperatures derived from the experimental measurements.

To help reconcile the differences between the stationary endwall temperatures between the adiabatic simulations and the experimental data, the boundary condition in the computational model was changed from adiabatic to isothermal. Interpolation between the surface thermocouple measurements taken from the experimental testing was used in the thermal structural model to produce a thermal map of all stationary components associated with the P3S facility. Through taking the temperatures at the same mesh points in the computational model, this thermal map was input into the CFD models as an isothermal boundary condition.

The change in the thermal boundary condition did not have any impact on the interstage stagnation pressure profiles (Figure 4.6). This is a similar trend to what was observed in the turbocharger literature discussed in Section 1.2.1, with heat transfer not affecting overall pressure ratio of the compressor in a turbocharger.
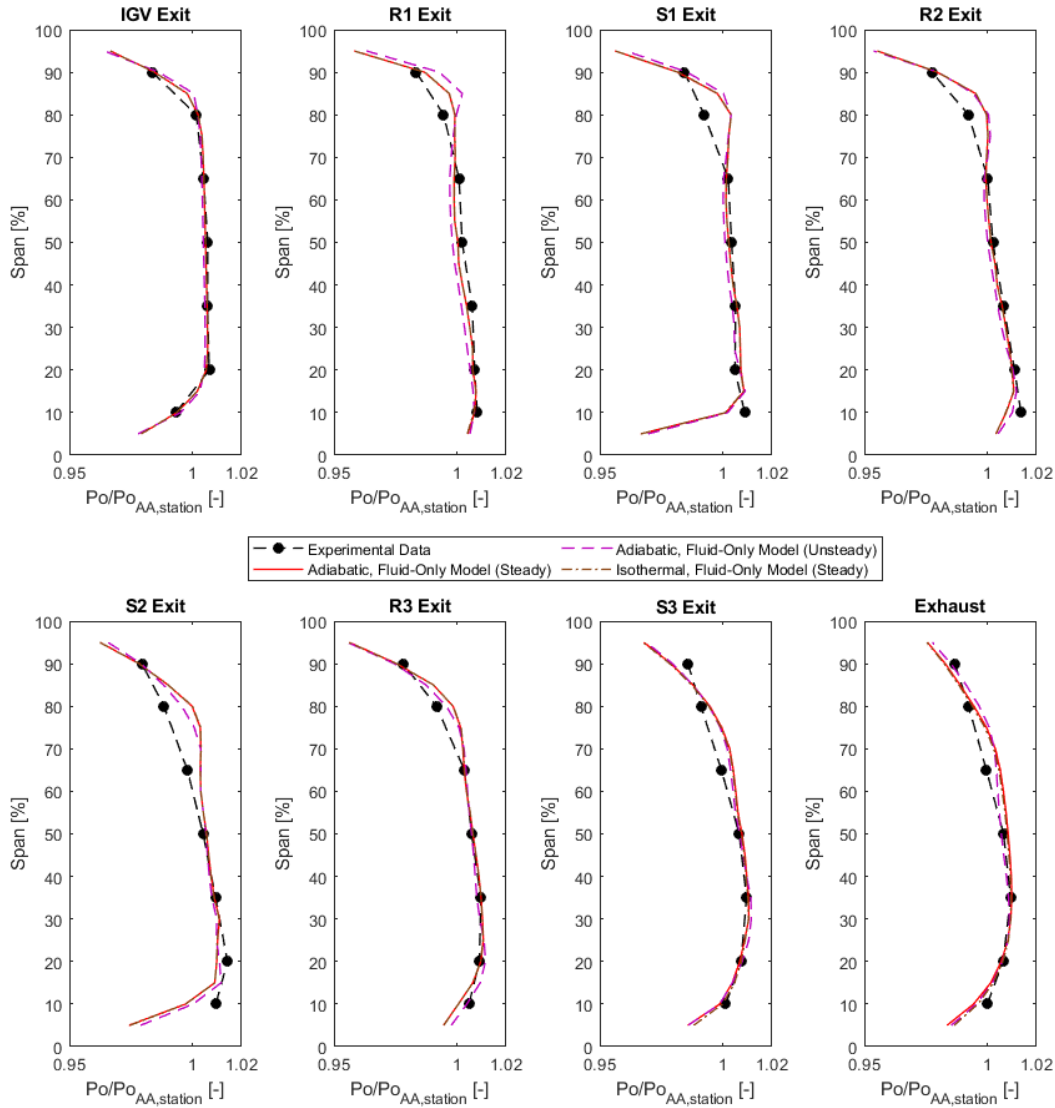
Figure 4.6. Comparison of interstage stagnation pressure profiles between experimental data and adiabatic steady and unsteady, fluid-only models with an isothermal, steady model, normalized with respect to the area-averaged value at each station.

The interstage stagnation temperature profiles in Figure 4.7, show an interesting result with the tip region of the isothermal simulation. The temperatures still follow the adiabatic steady model

119

throughout most of the flowpath except for the tip region where, as anticipated, the shape of the profile moved closer to that of the experimental data. However, with the overall performance metrics (Table 4.2), the resulting total temperature ratio and pressure ratio for the isothermal model were very similar to the steady, adiabatic model, but with much improved efficiency. Since the adiabatic system contained less irreversibilities than that of an isothermal system, an increased overall efficiency for the simulation with an isothermal boundary condition did not seem feasible.
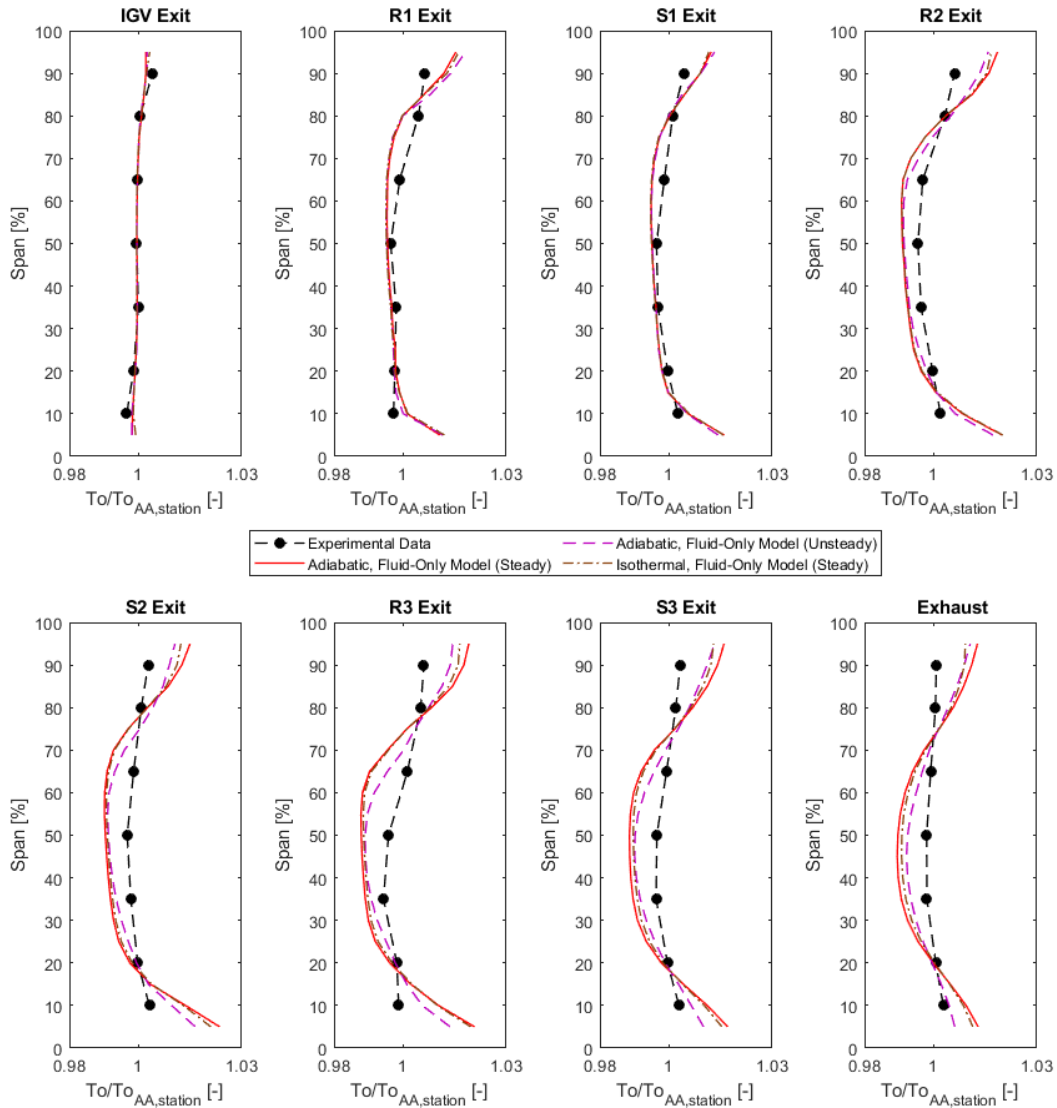
Figure 4.7. Comparison of interstage stagnation temperature profiles between experimental data and adiabatic steady and unsteady, fluid-only models with an isothermal, steady model, normalized with respect to the area-averaged value at each station.

Table 4.2. Performance metric comparison between experimental results, adiabatic steady and unsteady, fluid-only models, and isothermal, steady model, normalized with respect to the adiabatic, fluid-only model.

	TPR [-]	$\dot{m}_c$ [-]	$\frac{R_c}{W_c}$[-]	TTR [-]	$\Delta\eta_{is}$ [pts]
Experimental Data	0.995	0.994	1.001	0.999	-0.441
Adiabatic, Fluid-Only Model (steady)	1	1	1	1	-
Adiabatic, Fluid-Only Model (unsteady)	0.995	0.996	1.000	0.996	+1.194
Isothermal, Fluid-Only Model (steady)	1.001	1	1.001	0.999	+0.632

A comparison of the heat flux taken during the experimental testing and the isothermal simulation shows that the flow of heat was opposite in the isothermal model compared to that of the experiment. Forcing the endwalls in the model to match the experimentally acquired surface temperatures through an isothermal boundary condition was artificially cooling the flow in the rear stages of the compressor, resulting in a higher overall efficiency. This was not what the heat flux gages showed in the experimental results, as the flowpath was determined to be the hottest part of the compressor. This fact required a heat flux from the flow and into the casing for the rear blade rows of the compressor, and into the flow from the casing for the front blade rows of the compressor. Thus, the isothermal boundary condition was inadequate in capturing the correct heat transfer of the system due to the solid components missing in the model.

4.3   Coupling Solid and Fluid Domains Through Conjugate Heat Transfer

After observing that the isothermal boundary condition was producing an increase in performance due to artificial cooling of the flow, a coupled analysis incorporating the solid and fluid interaction between components was developed. A conjugate heat transfer model was developed which incorporated the actual stainless steel stator blades and the metal components that would have an influence on the tip region of the compressor: the aluminum AIP inlet, the stainless-steel forward and aft frames, and the aluminum casing. While a solid-fluid interface was applied to all fluid domains interacting with solid components, an adiabatic boundary condition was initially applied to the outer wall of each solid component, where it would interact with the ambient environment of the test cell. The same surface roughness was applied to the interfaces between the domains. This change in boundary conditions/interfaces is shown in Figure 4.8.
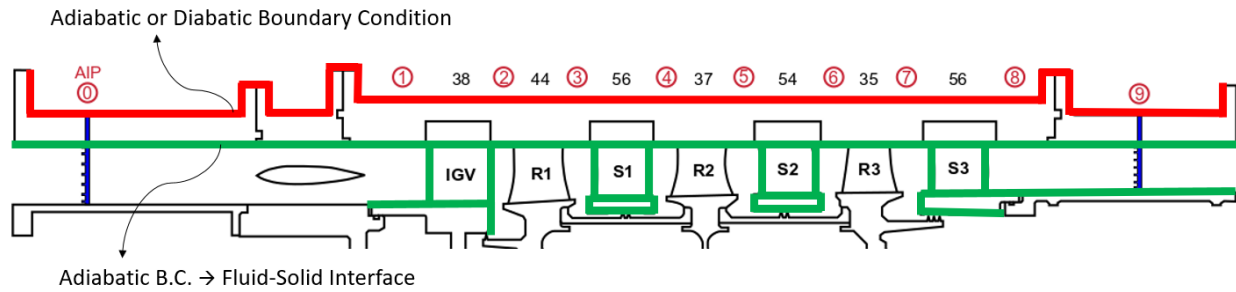
Figure 4.8. Change in boundary conditions/interfaces between fluid-only and CHT model.

As shown in Figure 4.9, unlike with the isothermal model, the addition of the solid components to the computational model produced a difference in the interstage stagnation pressure distributions between the fluid-only and conjugate heat transfer simulations. With the conjugate heat transfer model, there was more pressure loss near the upper half of the flowpath, while the bottom half experienced a gain in pressure. This is a result of the solid components imposing a Rayleigh flow condition onto the fluid. As the temperature is increased due to the system coupling, the pressure near the tip decreases (since the flow is subsonic). This shift in pressure at the top causes a loss in pressure that is compensated with an increase in pressure in the lower region of the blade span.
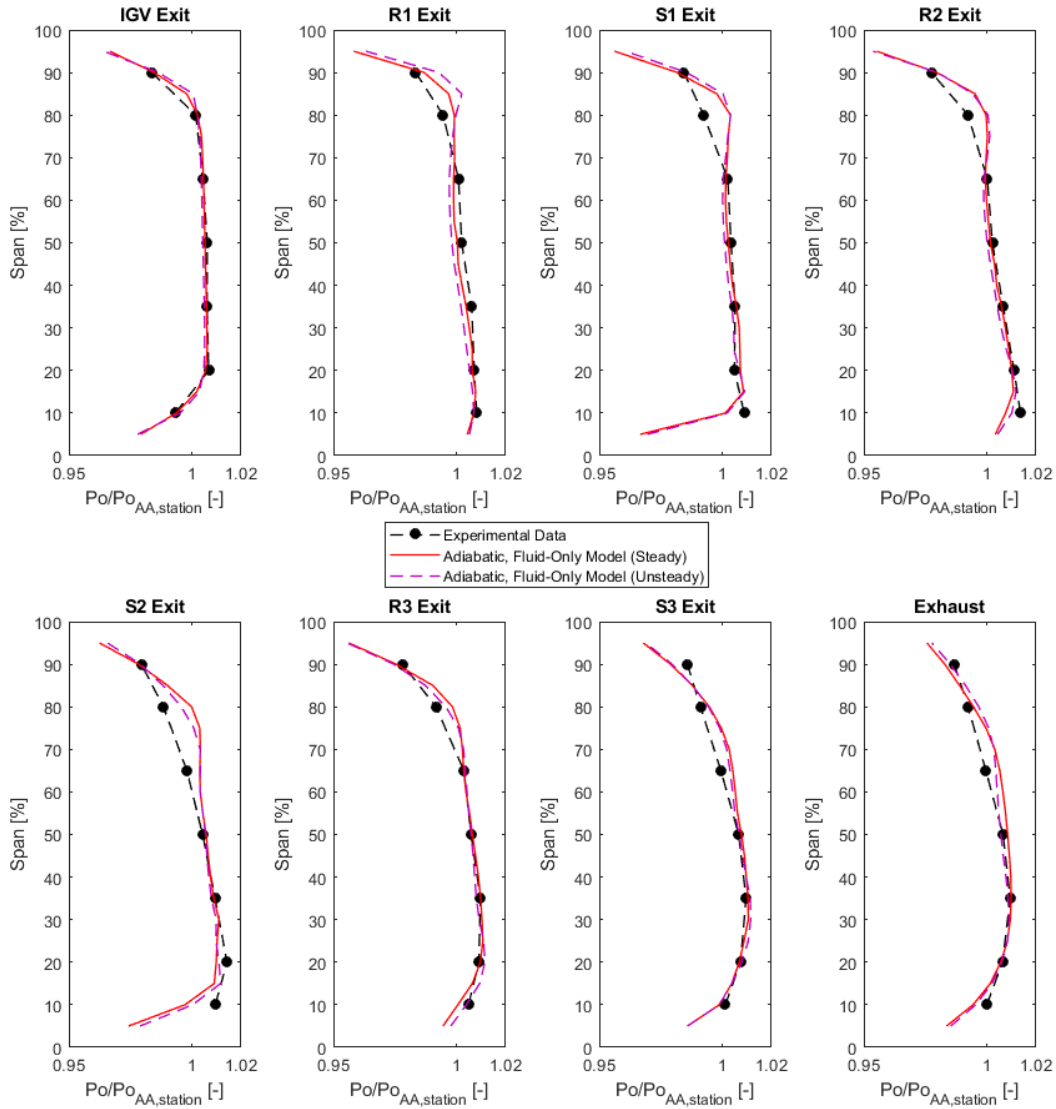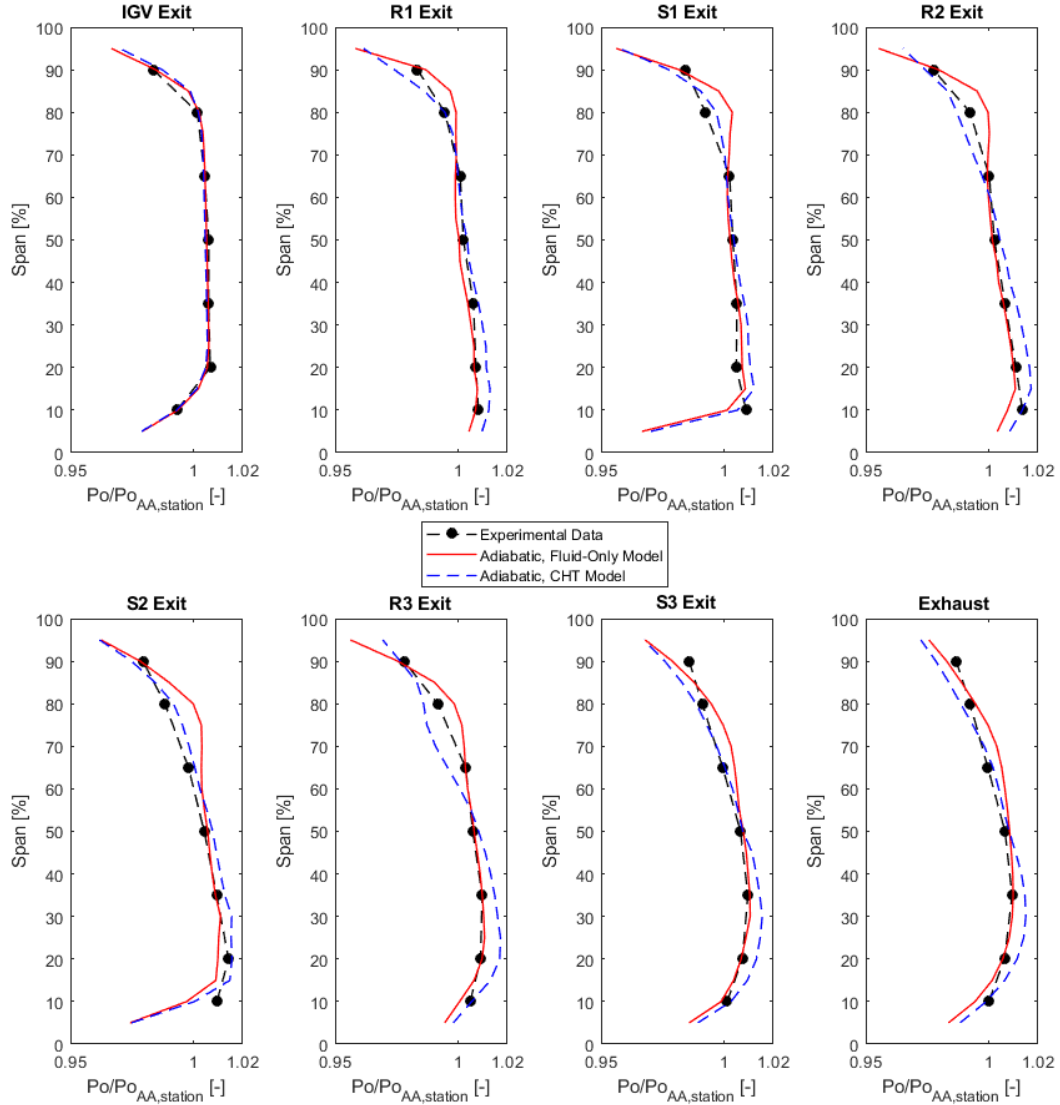
Figure 4.9. Comparison of interstage stagnation pressure profiles between experimental data and adiabatic versions of fluid-only and conjugate heat transfer models, normalized with respect to the area-averaged value at each station.

With the stagnation temperature profiles, shown in Figure 4.10, the addition of the solid components to the computational model produced a subtle difference between the fluid-only and conjugate heat transfer simulations. The major difference was in the profiles near the tip region, which did not match as well to the experimental data with the conjugate heat transfer model. This was attributed to the addition of the solid components and the adiabatic boundary condition on the outer wall, additional heat was stored in the system in the stationary components. The addition of the solid components affected the midspan region as well, with a slight decrease in temperature as

the heat was drawn toward the tip region due to the thermal conductivity of the aluminum casing. This combination of conditions led to an increase in stagnation temperature in the tip region.
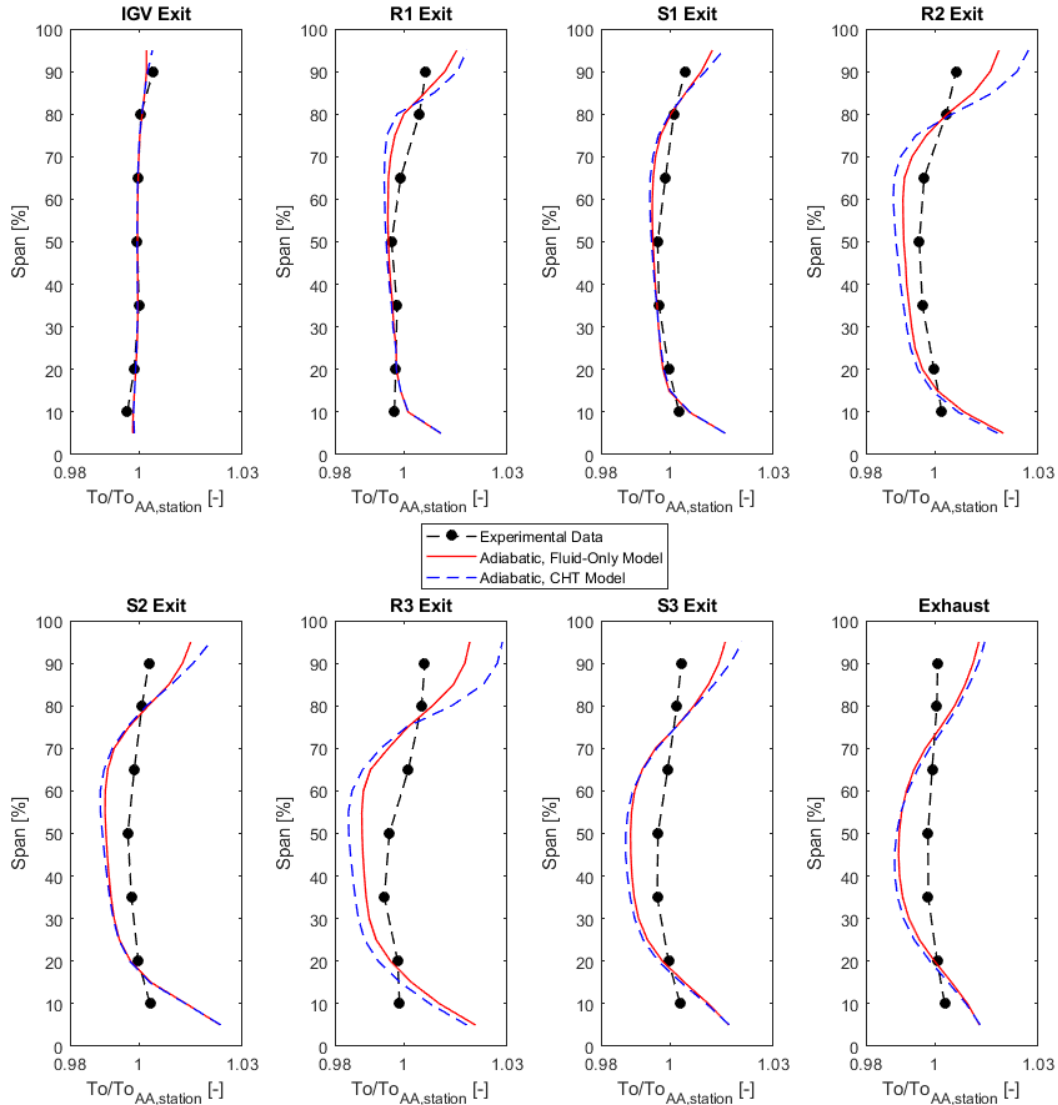
Figure 4.10. Comparison of interstage stagnation temperature profiles between experimental data and adiabatic versions of fluid-only and conjugate heat transfer models, normalized with respect to the area-averaged value at each station.

As shown in Table 4.3, adding the solid components to the fluid model dropped the efficiency of the compressor by about 1.29pts, a relatively large amount. This was a result of the extra heat stored in the system through the aluminum components, with a drop in pressure due to the fluid-solid interaction. The heat flux direction matched that of the experimental data, adding

confidence that the conjugate heat transfer model was more accurately representing the thermal characteristics of the compressor compared to the incorrect isothermal model. This was also confirmed through an analysis of the surface temperatures in the CHT model, shown in Figure 4.11. These temperatures were much closer to those measured in the experiment, with a deviation at the shroud to within 5°F. However, while the IGV and S1 cavities predicted the surface temperatures of the experiment very well, the S2 and S3 cavities were still predicted to be over by up to 15°F. This was most likely due to the rotating reference frame remaining adiabatic, not allowing any heat transfer to take place into the drum, resulting in an overprediction of temperature.

Table 4.3. Performance metric comparison between adiabatic fluid-only and CHT cases, normalized with respect to the adiabatic, fluid-only model.

	TPR [-]	$\dot{m}_c$ [-]	$\frac{R_c}{W_c}$ [-]	TTR [-]	$\Delta\eta_{is}$ [pts]
Adiabatic, Fluid-Only Model	1	1	1	1	-
Adiabatic, CHT Model	0.981	1	0.981	0.997	- 1.285
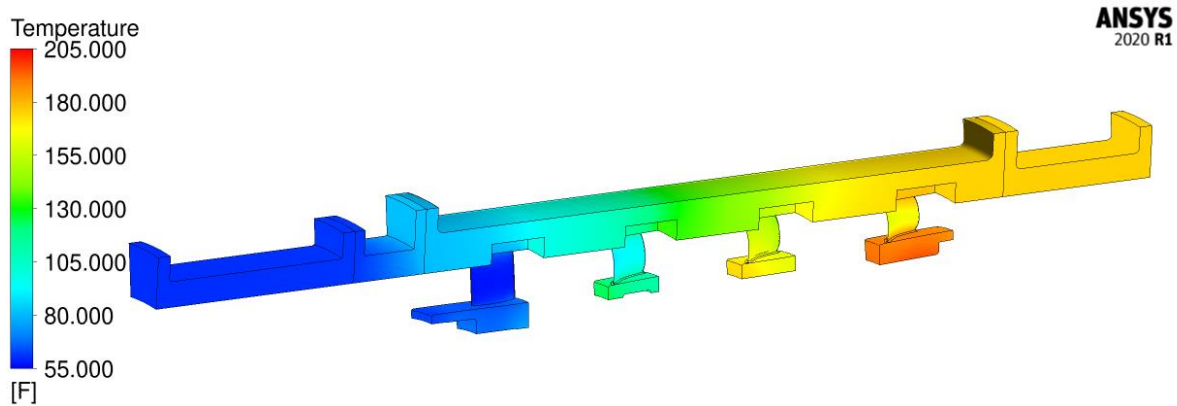
Figure 4.11. Static temperatures of the stationary components from the adiabatic, CHT model.

4.4   Convection Effects on Compressor Temperature Radial Profiles and Efficiency

The adiabatic, CHT model correctly predicted the heat flow trends throughout the stationary components, yet the model still did not predict the tip region measured in the experiment. While running the PAX200 compressor, the outer wall of the compressor casing was not insulated due to instrumentation constraints, and numerous fans were typically used throughout the test cell

during operation creating a convective environment. Therefore, through removing the adiabatic thermal boundary condition on the outside of the casing, different convective conditions could be applied to the outer wall of the casing to gather insight into how ambient conditions surrounding the facility could affect the interstage flow characteristics.

First, the CHT simulation was adapted so that the outer wall of the casing was no longer adiabatic but subjected to two different ambient conditions: one simulating an environment with similar casing temperature or stagnant air (natural convection), and another simulating an environment with a large temperature difference between the casing and ambient air (forced convection). In comparing the adiabatic and diabatic CHT cases (Figure 4.12), there was virtually no change in radial stagnation pressure profile between any of the cases, similar to the introduction of the isothermal condition compared to the adiabatic, fluid-only model in Section 4.2.

However, there was a noticeable change in the radial stagnation temperature profiles, shown in Figure 4.13, particularly near the tip of the downstream blade rows. With higher convection, the heat from the fluid near the inner endwall of the flow path was drawn more efficiently away from the flow and into the casing, particularly in the third stage of the compressor and to a lesser extent in the first stage. This trend was also evident in the experimental data. The actual environment of the test cell would be a lower convection coefficient near the front of the compressor and a higher convection coefficient toward the back of the compressor due to temperature differences between ambient air and the compressor casing.

As shown through the normalized performance metrics in Table 4.4, there was a large increase in isentropic efficiency between the adiabatic and diabatic CHT cases. This was confirmed in the overall TPR and TTR change between the cases. While the TPR remained constant through an increase in convection, the TTR of the compressor dropped with higher external convection. This is due to more heat being carried from the tip region and lost to the environment during operation. Additionally, the higher convection contributed to a slightly more mixed out stagnation temperature profile in the third stage of the compressor. Overall, the high convection case recovered much of the efficiency loss that was produced through adding the solid components to the model, though it remained lower than the adiabatic, fluid-only simulation by about 0.4pts.
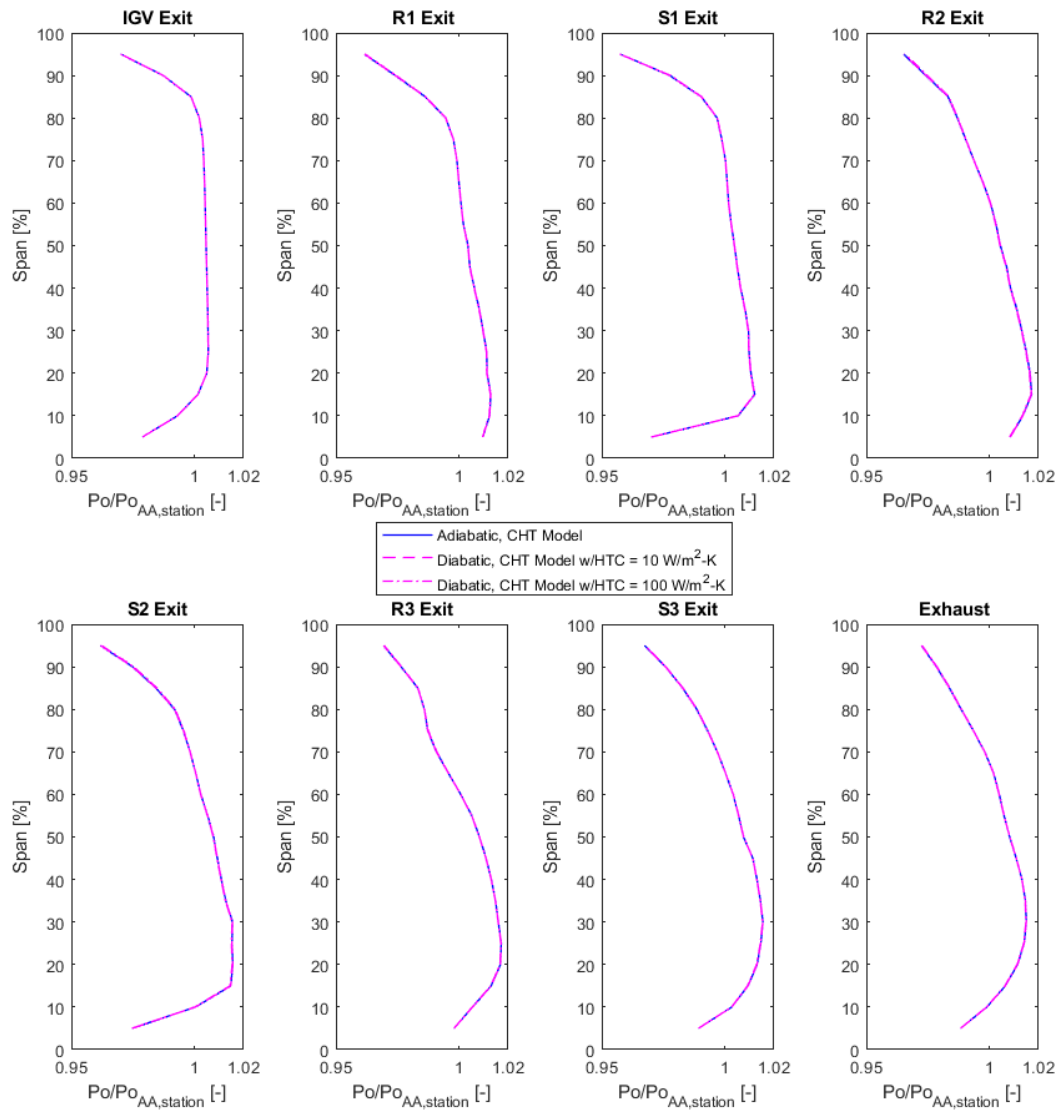
Figure 4.12. Comparison of interstage stagnation pressure profiles between adiabatic, low-convection, and high-convection CHT models, normalized with respect to the area-averaged value at each station.
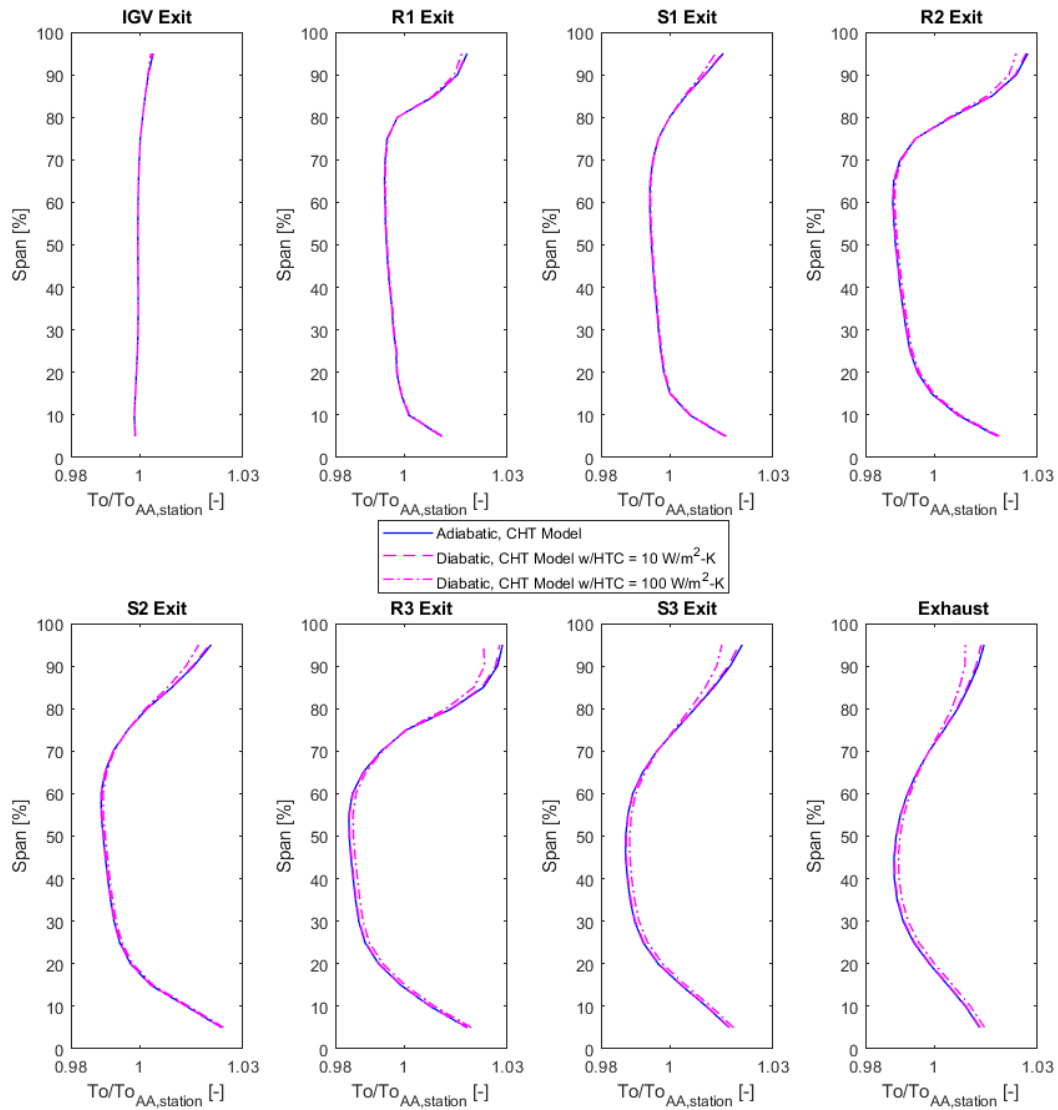
Figure 4.13. Comparison of interstage stagnation temperature profiles between adiabatic, low-convection, and high-convection CHT models, normalized with respect to the area-averaged value at each station.

Table 4.4. Performance metric comparison between adiabatic and diabatic CHT cases for two levels of convection, normalized with respect to the adiabatic, fluid-only model.

	TPR [-]	$\dot{m}_c$ [-]	$\frac{R_c}{W_c}$[-]	TTR [-]	$\Delta\eta_{is}$ [pts]
Adiabatic, Fluid-Only Model	1	1	1	1	-
Adiabatic, CHT Model	0.981	1	0.981	0.997	- 1.285
Diabatic, CHT Model w/CC = 10 W/m²-K	0.981	1	0.981	0.996	-1.146
Diabatic, CHT Model w/CC = 100 W/m²-K	0.982	1	0.983	0.995	-0.377

The predicted static temperatures of the stationary components from the high convection, diabatic simulation were compared to the experimental surface temperatures that were measured during testing (Figure 4.14). While the front half of the compressor tracked closely with the experimental data, the rear endwall of the compressor was significantly underpredicting the temperature of the rear stage by about 15°F. Additionally, the cavity temperatures of S2 and S3 were similarly overpredicted compared to the adiabatic case, indicating that the ambient environment surrounding the compressor did not affect the cavity regions.

However, the low convection model (convection coefficient = 10 W/m²K) tracked quite well with the experimental data in terms of the rear stage endwalls, with an overprediction up to 3°F. This verification in endwall temperatures indicated that typical operation of the P3S facility more closely resembled that of a low convection environment, than that of a high convection one. It also confirmed that ambient environment had little to no effect on the cavity temperatures. Thus, the adiabatic thermal boundary condition on the rotating components was likely the cause for the overprediction of the cavity temperatures in the rear stage of the computational model.
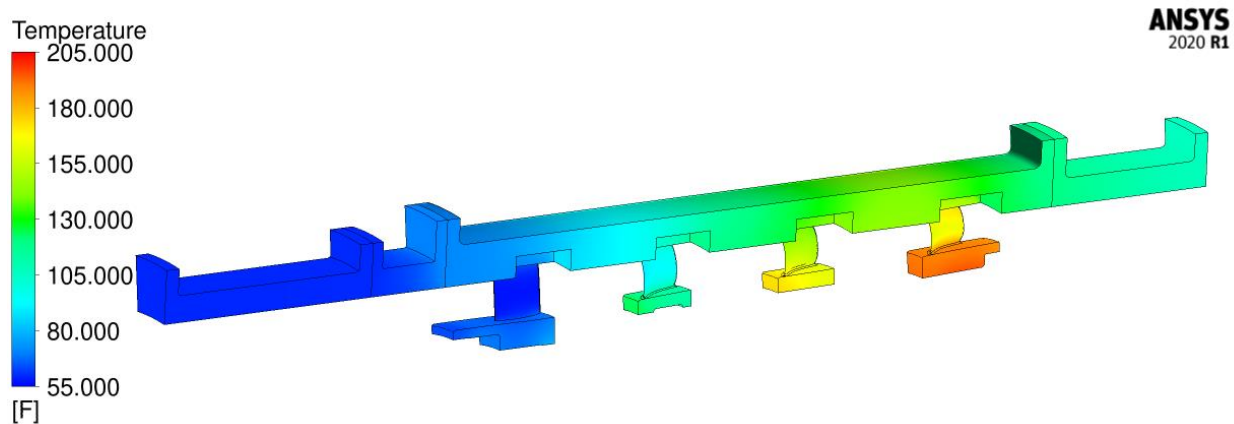
Figure 4.14. Static temperatures of the stationary components from the high convection (diabatic), CHT model.

4.5   Geometric and Material Effects

Since it was shown that the ambient environment effects produced a significant impact on the flow in the tip region of the compressor, it was hypothesized that the casing material and thickness could produce additional effects. In a real gas-turbine engine, the casing would not be as thick as that of the P3S facility, which requires a specific thickness to remain structurally robust with the presence of many instrumentation ports. Thus, the geometry and material choices of the casing were modified in the computational model to assess their effects on the flow-field.

First, the geometric properties of the casing were changed within the CHT model. Three different thicknesses were compared: the original thickness ("baseline"), a thickness that was twice as thick as the baseline condition ("thick"), and a thickness that was half that of the baseline condition ("thin"). For the first round of simulations, an adiabatic thermal boundary condition was applied to the outer wall of the casing between the solid and the ambient environment to discern any differences between the different thicknesses before a more correct, diabatic condition was introduced to the outside of the casing.

In comparing the three thicknesses, a few trends were observed. As shown in the radial stagnation pressure profiles in Figure 4.15, there was no variation in radial stagnation pressure. This was somewhat expected as there was no change in interface condition between the solid and fluid, and from previous simulations and literature, heat transfer did not alter the pressure profiles. With the radial stagnation temperature profiles, Figure 4.16, there was also no variation between the cases. This was due to the heat still trapped within the facility from the adiabatic condition, regardless of the amount of metal in the structural and stationary components. Furthermore, these simulations confirmed that any further differences between the thickness of the casing would be a direct result of relaxing the adiabatic assumption on the model.
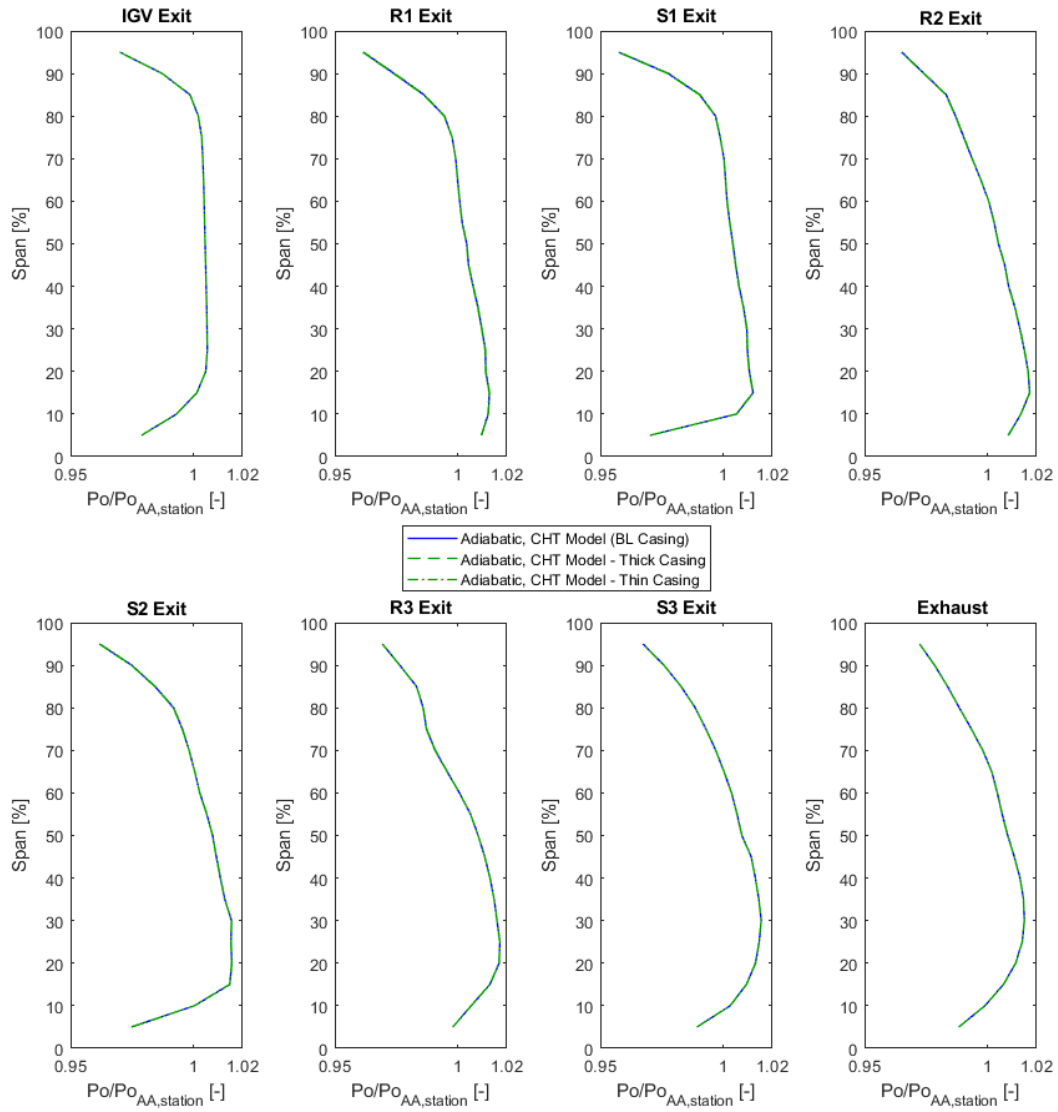
Figure 4.15. Comparison of interstage stagnation pressure profiles between adiabatic CHT models of various casing thicknesses, normalized with respect to the area-averaged value at each station.
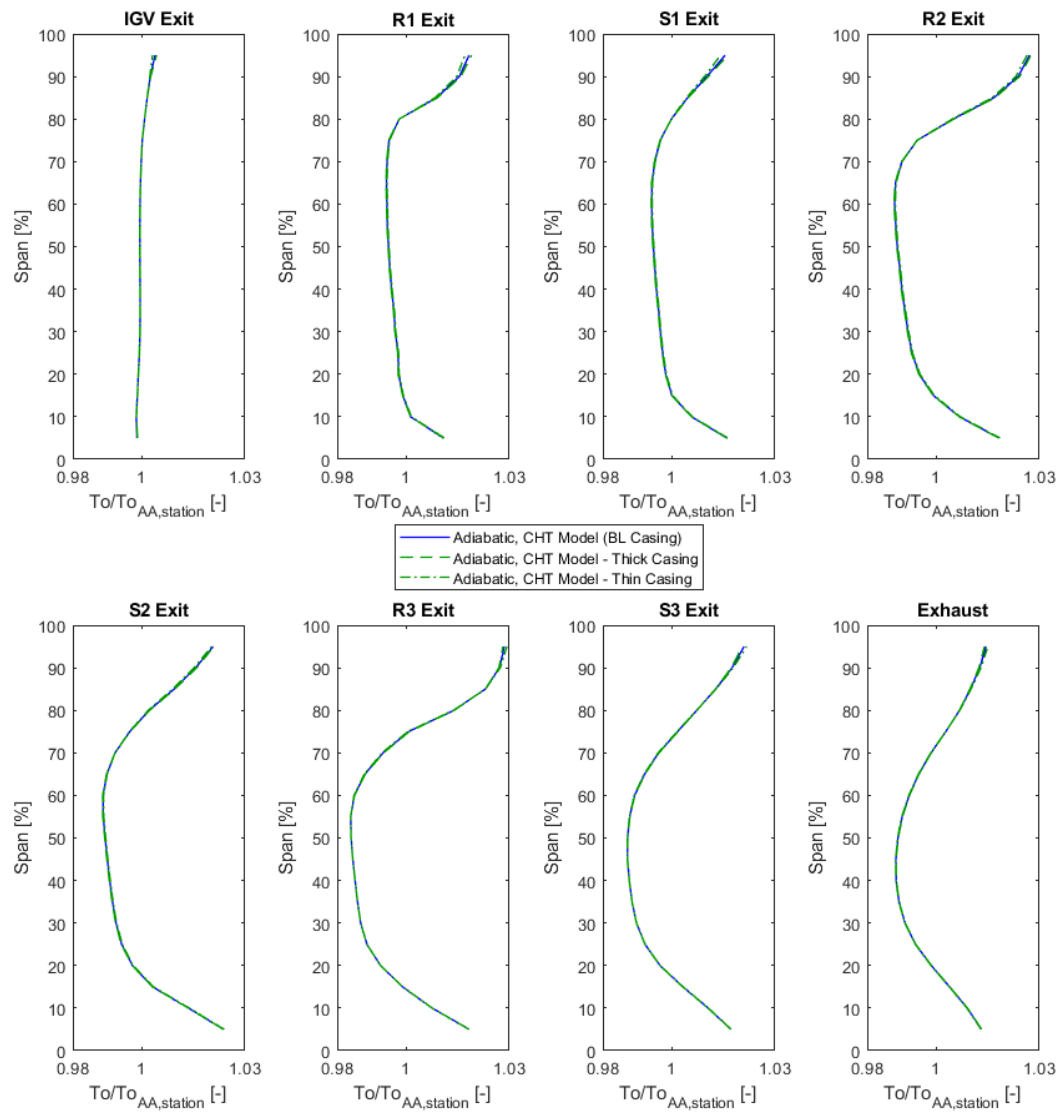
Figure 4.16. Comparison of interstage stagnation temperature profiles between adiabatic CHT models of various casing thicknesses, normalized with respect to the area-averaged value at each station.

In terms of performance metrics, as shown in Table 4.5, there was little to no variation in efficiency (about 0.04pts) between the different casing thicknesses for the adiabatic CHT simulations. This comparison confirmed that in an adiabatic environment, to which most computational analyses are compared, the thickness of the casing is irrelevant as the amount of heat transfer in the casing has a negligible effect on the performance of the compressor.

Table 4.5. Performance metric comparison between adiabatic CHT cases for different casing thicknesses, normalized with respect to the adiabatic, fluid-only model.

	TPR [-]	$\dot{m}_c$ [-]	$\frac{R_c}{W_c}$[-]	TTR [-]	$\Delta\eta_{is}$ [pts]
Adiabatic, Fluid-Only Model	1	1	1	1	-
Adiabatic, CHT Model (baseline casing)	0.981	1	0.981	0.997	-1.285
Adiabatic, CHT Model (thin casing)	0.982	1	0.981	0.997	-1.304
Adiabatic, CHT Model (thick casing)	0.981	1	0.982	0.996	-1.265

Next, the adiabatic condition was relaxed to include that of a highly convective, diabatic environment. A convection coefficient of 100 W/m^{2}K was applied to the outer surface of the casing and additional simulations were performed to observe how the different casing thicknesses affected the flow conditions and performance with a diabatic boundary condition.

As shown in Figure 4.17 and Figure 4.18, this diabatic condition resulted in very little variation, if any, in the radial stagnation pressure and temperature profiles between the cases. However, as shown in Table 4.6, the efficiency significantly improved with the diabatic model, as shown in Section 4.4. However, the variation (about 0.08pts) between the different casing thicknesses for the high convection CHT simulations doubled compared to that of the adiabatic CHT simulations. This relatively small change in efficiency indicated that while approximately the same amount of heat was drawn out of the flow, a greater amount of it was transferred to the ambient environment under the diabatic condition with the thinner casing, compared to the thicker casing, resulting in a slightly better performance.

Overall, the simulations and analysis performed with the different casing thicknesses showed that while different casing geometry provided a slight impact to the performance of a compressor, it was negligible compared to measurement capabilities. Therefore, operating the PAX200 with a thick compressor casing would cause a negligible change in the flow properties, compared to that of other environmental factors in the facility, such as convection.

Figure 4.17. Comparison of interstage stagnation pressure profiles between high convection (diabatic) CHT models of various casing thicknesses, normalized with respect to the area-averaged value at each station.
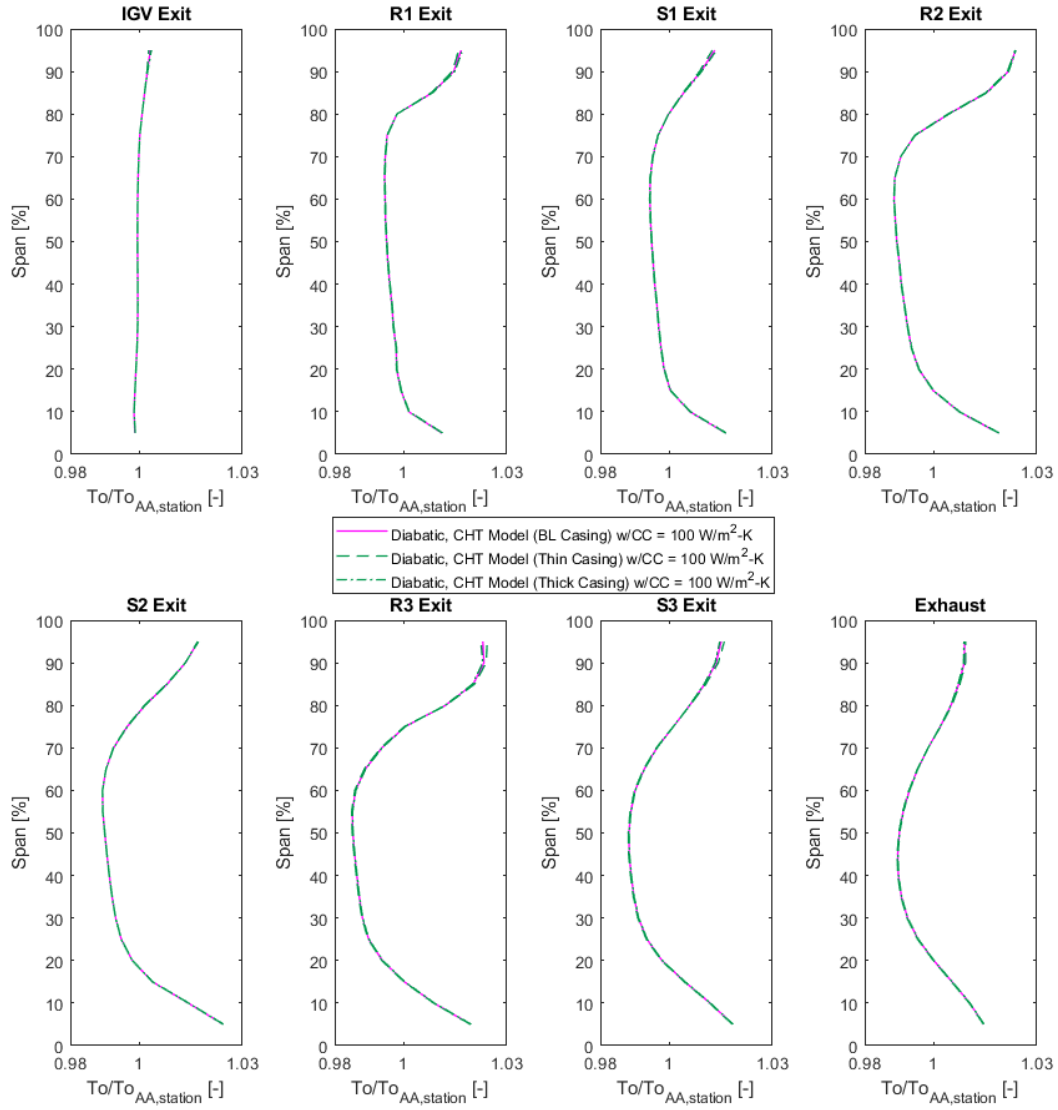
Figure 4.18. Comparison of interstage stagnation temperature profiles between high convection, (diabatic) CHT models of various casing thicknesses, normalized with respect to the area-averaged value at each station.

Table 4.6. Performance metric comparison between high convection (diabatic) CHT cases for different casing thicknesses, normalized with respect to the adiabatic, fluid-only model.

	TPR [-]	$\dot{m}_c$ [-]	$\frac{R_c}{W_c}$[-]	TTR [-]	$\Delta\eta_{is}$ [pts]
Adiabatic, Fluid-Only Model	1	1	1	1	-
Diabatic, CHT Model (baseline casing)	0.982	1	0.983	0.995	-0.377
Diabatic, CHT Model (thin casing)	0.982	1	0.982	0.995	-0.443
Diabatic, CHT Model (thick casing)	0.982	1	0.982	0.995	-0.367

In addition to examining the casing thickness in the P3S facility, the casing material was also considered. In the front half of the compressor, the inner shroud of the casing experienced relatively higher temperatures than that of the flow – an indication that heat transfer from downstream stages was conducting upstream within the aluminum casing. Since different materials have different thermal conductivities, different materials were applied to the computational model for the casing to explore how the thermal characteristics of the compressor would be affected. As with the simulations on different casing thicknesses, an adiabatic boundary condition was initially applied to the outer wall of the casing to create a baseline for when that assumption would be relaxed. Three different materials were examined in the computational CHT model: the original aluminum casing, a stainless-steel version, and a plastic, Perfluoroalkoxy alkanes (PFA) version.

While the radial stagnation pressure profiles, shown in Figure 4.19 were once again unchanged, there was a difference in the radial stagnation temperature profiles, shown in Figure 4.20. As anticipated, with the newly introduced materials (stainless steel and PFA plastic), which were less thermally conductive, the temperature at the tip was lower than that of the aluminum casing. This was particularly evident in the front half of the compressor, upstream of S1. After passing through R3, the temperature at the tip became slightly hotter than the aluminum casing. With the lower thermal conductivity, the heat flow throughout the system is more resistant to traveling upstream, which was also confirmed in the surface temperature results in the front half of the compressor, which aligned closer to that of the flow temperature. However, with the adiabatic condition, the same amount of relative heat is stored within the solid components.
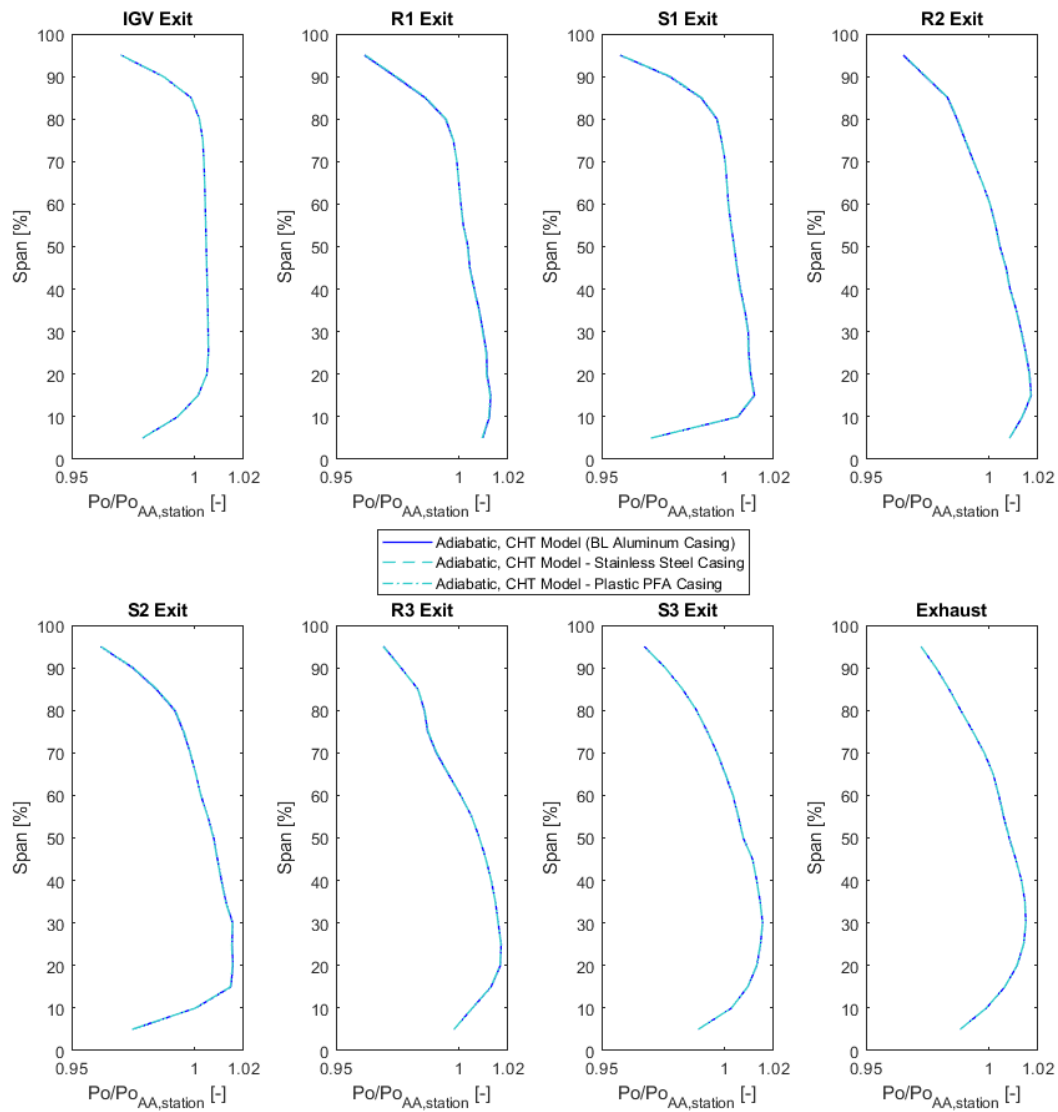
Figure 4.19. Comparison of interstage stagnation pressure profiles between adiabatic CHT models of various casing materials, normalized with respect to the area-averaged value at each station.
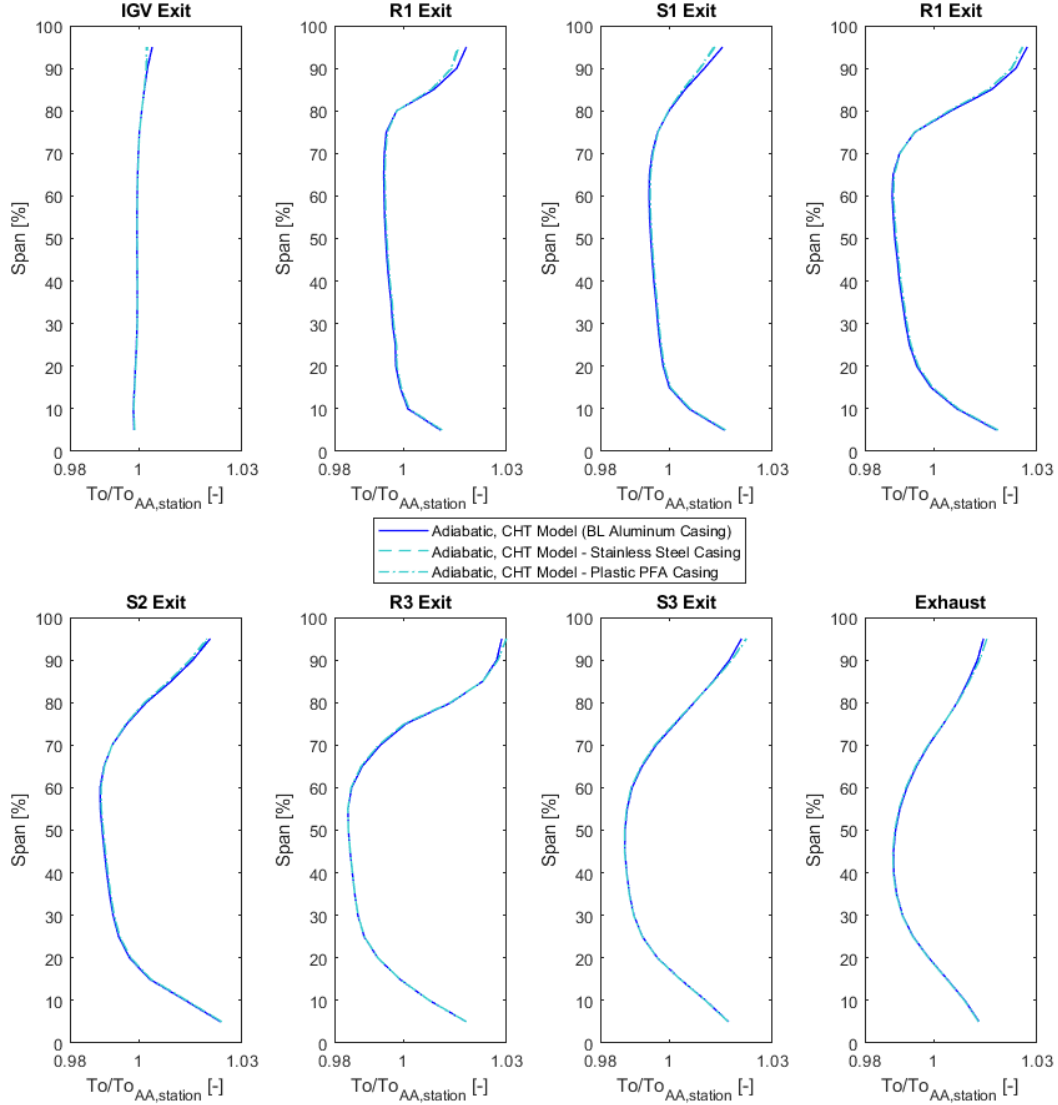
Figure 4.20. Comparison of interstage stagnation temperature profiles between adiabatic CHT models of various casing materials, normalized with respect to the area-averaged value at each station.

From a performance perspective, as shown in Table 4.7, this heat storage manifested in a similar efficiency variation (about 0.04pts) with changing material properties of the casing, compared to changing the casing thickness for the adiabatic CHT model. Overall, this comparison showed that with an adiabatic condition, the material of the casing again did not have a significant effect on performance, although it did slightly impact the surface temperature of the inner endwalls of the flowpath. It also provided a baseline comparison to the diabatic results to assess the influence of the external environment on the thermal characteristics of the compressor.

Table 4.7. Performance metric comparison between adiabatic CHT cases for different casing materials, normalized with respect to the adiabatic, fluid-only model.

	TPR [-]	$\dot{m}_c$ [-]	$\frac{R_c}{W_c}$[-]	TTR [-]	$\Delta\eta_{is}$ [pts]
Adiabatic, Fluid-Only Model	1	1	1	1	-
Adiabatic, CHT Model (aluminum casing)	0.981	1	0.981	0.997	-1.285
Adiabatic, CHT Model (stainless steel casing)	0.982	1	0.982	0.997	-1.322
Adiabatic, CHT Model (plastic casing)	0.982	1	0.982	0.997	-1.309

In a similar fashion to that of the casing thickness analysis, the adiabatic boundary condition on the outer wall of the casing was relaxed to include that of a highly convective, diabatic environment. A convection coefficient of 100 W/m^{2}K was applied to the outer surface of the casing for different casing materials.

As shown in Table 4.8, contrary to the adiabatic CHT simulations, there was a large change in efficiency (about 0.75pts) between the different casing materials for the high convection CHT simulations. This was not evident in the radial stagnation pressure profiles, shown in Figure 4.21, as once again there was negligible variation between the different material simulations. However, this large change was more obvious in the radial temperature profiles, shown in Figure 4.22. The same trend was observed as the adiabatic case but to a much larger extent. Like the adiabatic CHT model, with the newly introduced materials (stainless steel and PFA plastic), the temperature at the tip was lower than the aluminum casing, particularly in the front half of the compressor and upstream of S1. After passing through R2, an earlier point compared to the adiabatic simulations, the temperature at the tip became slightly hotter than the aluminum casing and increased with each successive stage.

The overall performance and radial stagnation temperature trends indicated an enhanced effect of the material selection with a diabatic boundary condition. The materials with lower thermal conductivity prohibited the heat from traveling both upstream, yet also to the ambient environment. This was especially true with the plastic version of the casing as it acted most like an insulator, trapping all the heat within the fluid-solid system, resulting in the worst efficiency. Because the aluminum casing had a higher thermal conductivity, it facilitated the heat transfer between the flowpath and ambient environment, effectively cooling the flow in the rear stages, which overcame the heat addition in the upper stages, resulting in the best efficiency.
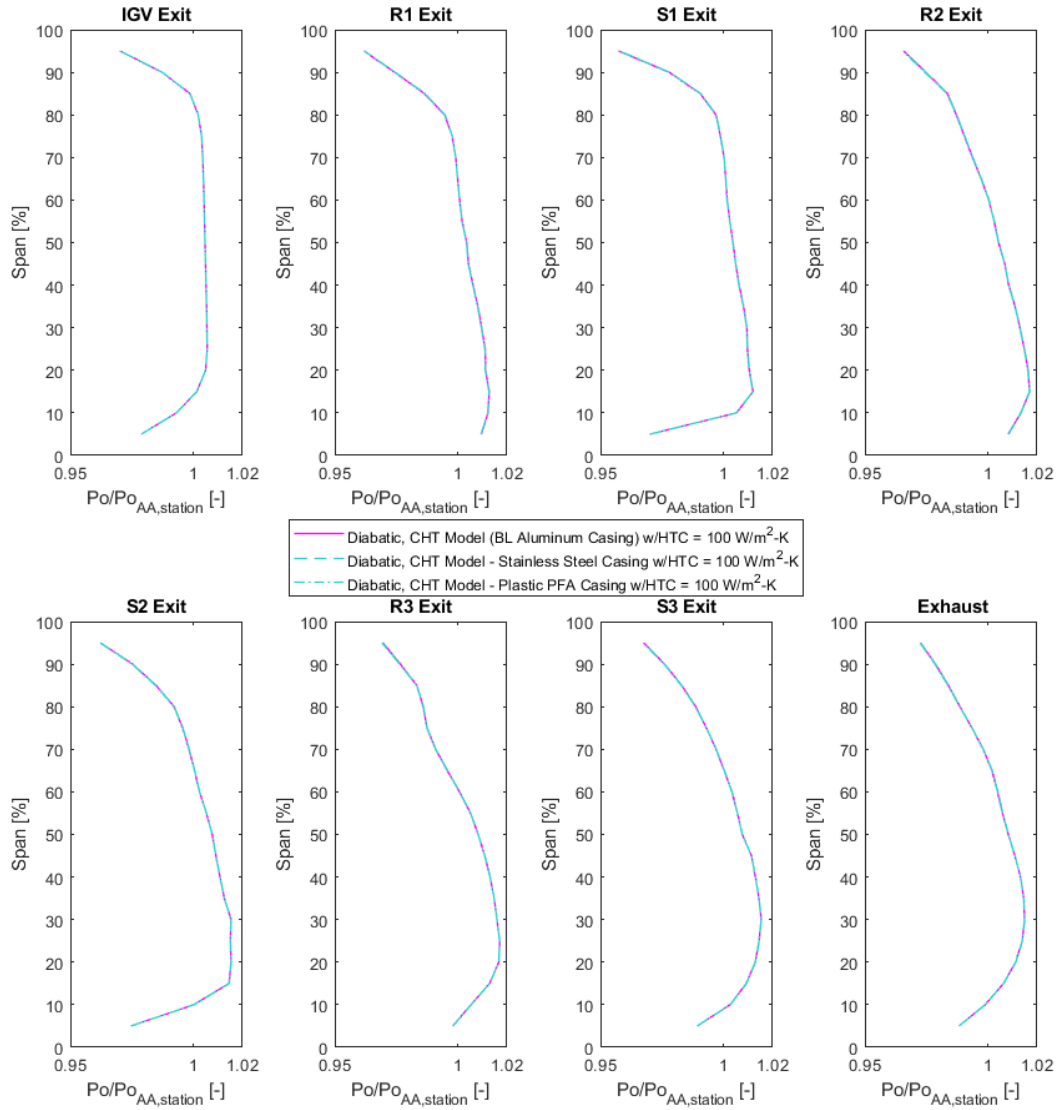
Figure 4.21. Comparison of interstage stagnation pressure profiles between high convection (diabatic) CHT models of various casing materials, normalized with respect to the area-averaged value at each station.
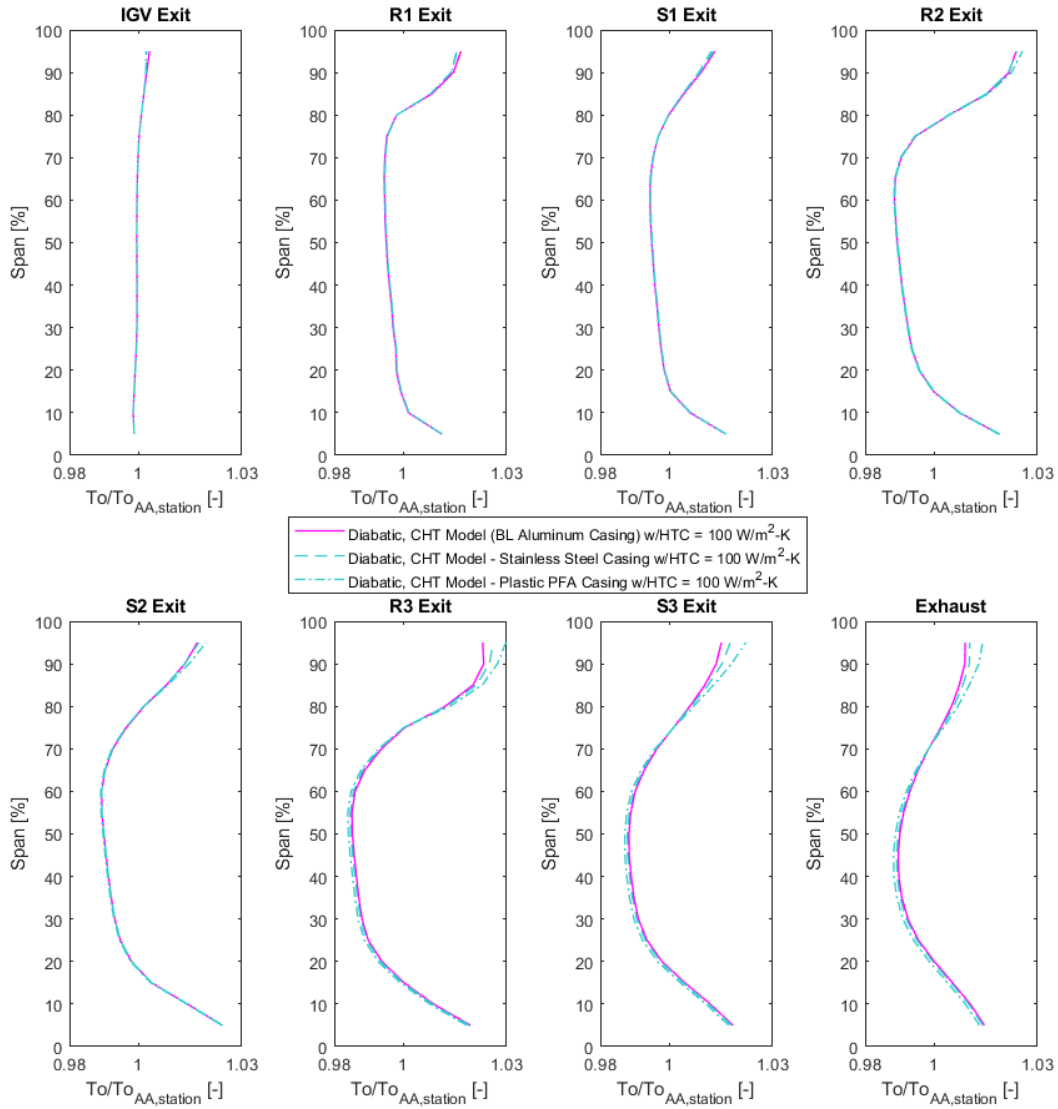
Figure 4.22. Comparison of interstage stagnation temperature profiles between high convection (diabatic) CHT models of various casing materials, normalized with respect to the area-averaged value at each station.
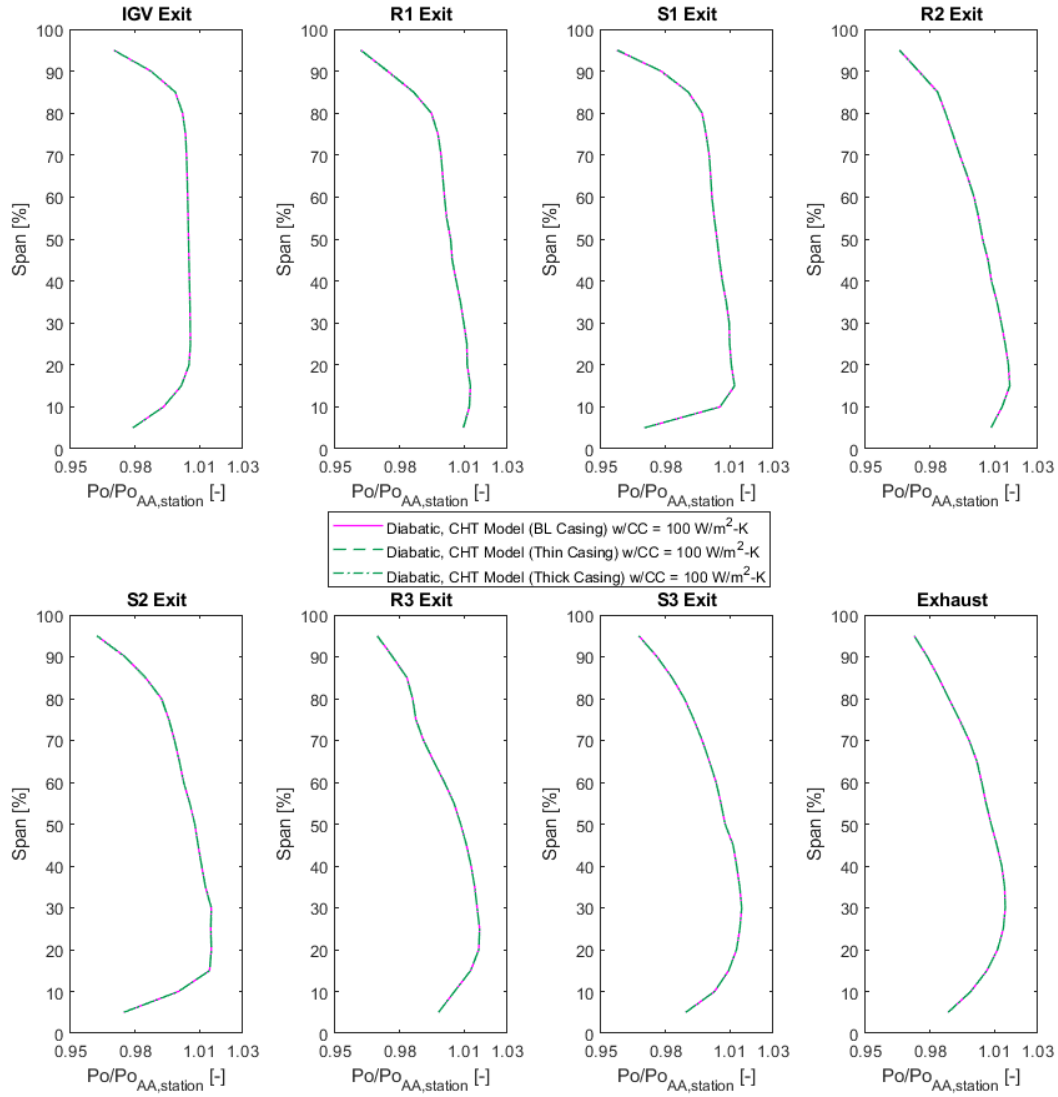
Table 4.8. Performance metric comparison between high convection (diabatic) CHT cases for different casing materials, normalized with respect to the adiabatic, fluid-only model.

	TPR [-]	$\dot{m}_c$ [-]	$\frac{R_c}{W_c}$[-]	TTR [-]	$\Delta\eta_{is}$ [pts]
Adiabatic, Fluid-Only Model	1	1	1	1	-
Diabatic, CHT Model (aluminum casing)	0.982	1	0.983	0.995	-0.377
Diabatic, CHT Model (stainless steel casing)	0.983	1	0.983	0.995	-0.572
Diabatic, CHT Model (plastic casing)	0.982	1	0.982	0.996	-1.112

With a diabatic condition, the more thermally conductive material transfers the heat from the flowpath to the ambient environment more efficiently, even at the cost of the heat flowing from downstream blade rows toward the front of the compressor. Meanwhile, the materials with lower thermal conductivity act more like an insulator, isolating upstream blade rows from the higher temperatures downstream, but at the cost of trapping the heat within the system.

4.6   Impacts of Enhanced Mixing with Increased Eddy Viscosity

While the high-convection, diabatic conjugate heat transfer model helped to resolve the radial stagnation temperature profile differences at the tip, this higher fidelity model still did not match the measured flow characteristics in the mid-span region. The measured temperature profile in the mid-span was much more mixed out – a result of losing eddy viscosity between the mixing planes. Therefore, a few simulations were performed to add more eddy viscosity into the flow, through enhancing the eddy viscosity by a factor of 1.1, 1.3 and 1.5 times that of the initial simulations.

Initially, the computational analysis was performed with the adiabatic, fluid-only model to achieve a good starting value and ensure that adequate levels of mixing were being introduced to the model. As shown in Figure 4.23, with increased mixing, the radial stagnation pressure matched much more closely at the tip, particularly behind each rotor at 80% span. This indicated that a large level of mixing might be occurring in this region experimentally, most likely due to tip leakage flows. However, the increased mixing strayed from the experimental data near the hub region. This was due to limitations in the ANSYS software which were only able to implement the enhanced eddy viscosity at a system wide level, rather than in particular regions or blade rows. Ideally, a system with increased mixing near the rotor tip and unchanged mixing toward the hub could be better in predicting the experimental data.

142
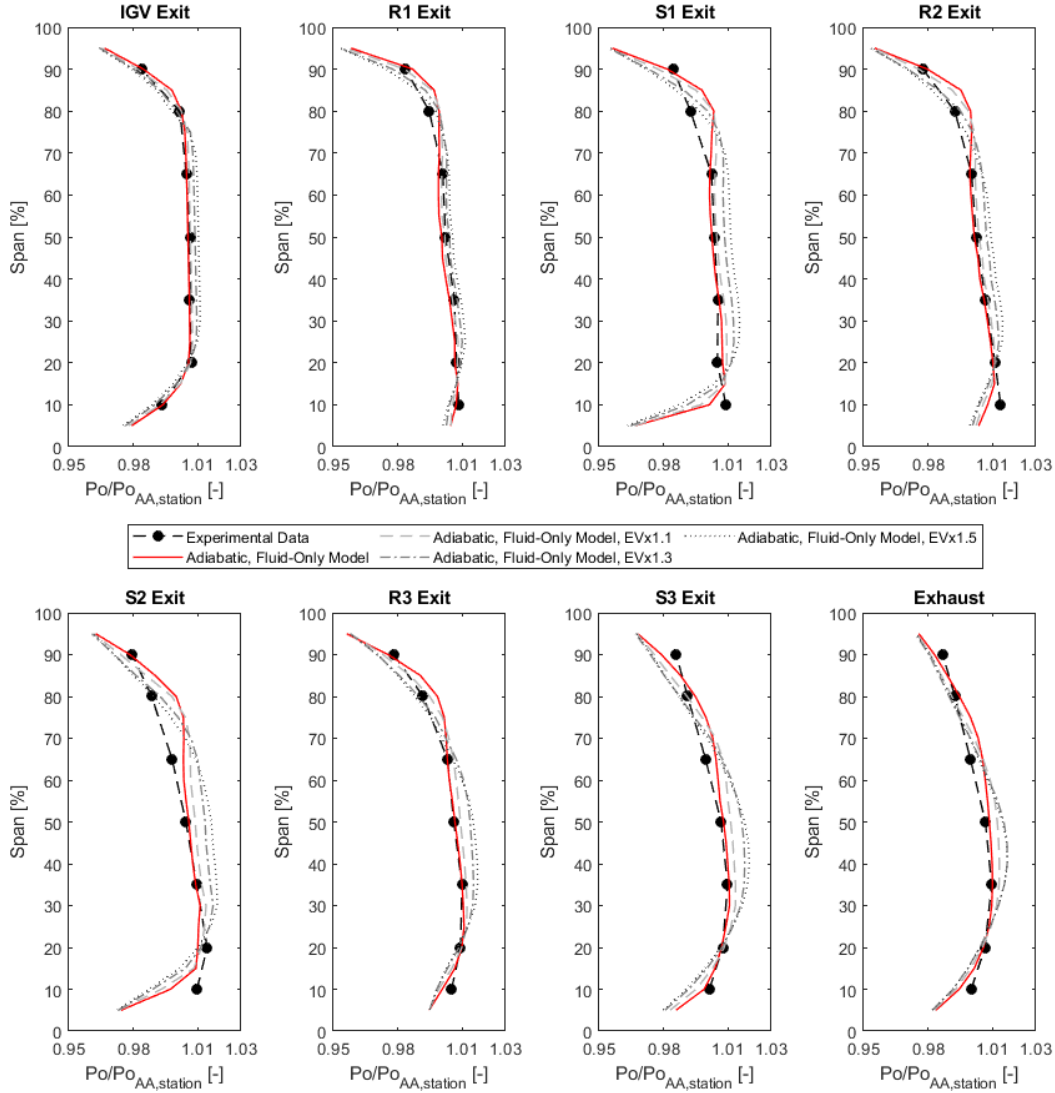
Figure 4.23. Comparison of interstage stagnation pressure profiles between experimental data and adiabatic, fluid-only cases with increasing eddy viscosity, normalized with respect to the area-averaged value at each station.

Another area where the lack of mixing was evident in the computational model was with the radial stagnation temperature profiles, shown in Figure 4.24. With increased eddy viscosity, the overall profile was much closer to the experimental data across the entire flowpath, particularly in the mid-span region after the stators and in the tip region for all stations. The hub profile also improved slightly, although only in the last stage of the compressor.
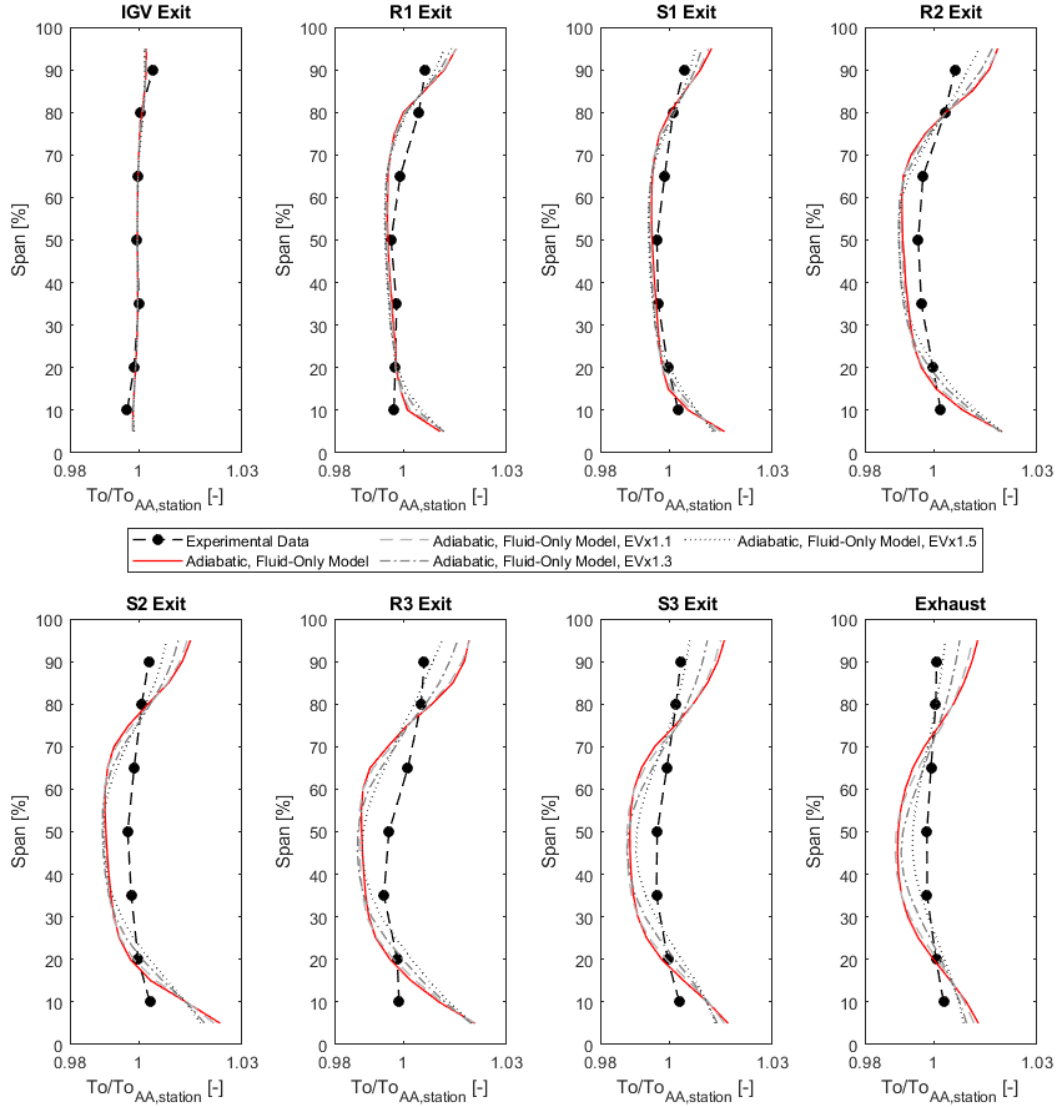
Figure 4.24. Comparison of interstage stagnation temperature profiles between experimental data and adiabatic, fluid-only cases with increasing eddy viscosity, normalized with respect to the area-averaged value at each station.

While this method of correcting the steady computational model through increasing the eddy viscosity showed effective results in better predicting the experimental data, it came at the cost of significantly reduced overall performance, as shown in Table 4.9. With the increased overall mixing, the pressure ratio and efficiency quickly drop, while temperature ratio only decreases slightly. Therefore, as discussed in Section 1.2.2, a tuning process was required to balance this tradeoff. Due to the artificial implementation of mixing into a steady model, it was therefore not possible to achieve both accurate radial mixing compared to that of the experiment,

144

as well as accurate performance metrics. However, the method still provided valuable insights and trends when compared to an unsteady simulation, at significantly reduced computational time and effort.

Table 4.9. Performance metric comparison between experimental data and adiabatic, fluid-only cases with increasing levels of eddy viscosity (EV), normalized with respect to the adiabatic, fluid-only model.

	TPR [-]	$\dot{m}_c$ [-]	$\frac{R_c}{W_c}$[-]	TTR [-]	$\Delta\eta_{is}$ [pts]
Experimental Data	0.995	0.994	1.001	0.999	-0.441
Adiabatic, Fluid-Only Model	1	1	1	1	-
Adiabatic, Fluid-Only Model (EVx1.1)	0.995	1	0.995	1.001	-1.286
Adiabatic, Fluid-Only Model (EVx1.3)	0.973	1	0.973	0.999	-3.871
Adiabatic, Fluid-Only Model (EVx1.5)	0.948	1	0.948	0.996	-6.146

To better reflect the true boundary conditions of the facility, the same simulation was performed with the conjugate heat transfer model. Simulations were performed with both an adiabatic outer wall applied to the compressor casing, as well as a highly convective, diabatic boundary condition applied to the external side of the compressor casing.

Similar to the previous results observed with the CHT model, the addition of the solid components achieved slightly better prediction of the experimental data profiles compared to that of the fluid-only model, especially at the hub. As shown in Figure 4.25, the radial stagnation pressure profiles between blade rows were off in the lower mid-span region – likely a limitation to the implementation of the mixing in the software and not including a diabatic thermal boundary condition or fluid-solid interfaces/solid domains for the rotating solid components. The tip region matched well in the rear stages. These pressure profiles were unchanged, as expected, with the diabatic model (Figure 4.26) as the heat transfer did not affect the pressure characteristic of the system.

As shown in Figure 4.27, the radial stagnation temperature predictions were much closer to that of the experiment, particularly in the rear stages of the compressor at the tip. With the diabatic condition, (Figure 4.28), the stagnation temperature at the tip was actually underpredicted, indicating that too much convection and mixing were applied to the system. Similar to the pressure profiles, the predictions miss in the hub region, which was likely a combination of overmixing, not including the fluid-solid interactions and solid domains for the rotating components in the CHT model, and an adiabatic condition applied to the rotating reference frame.
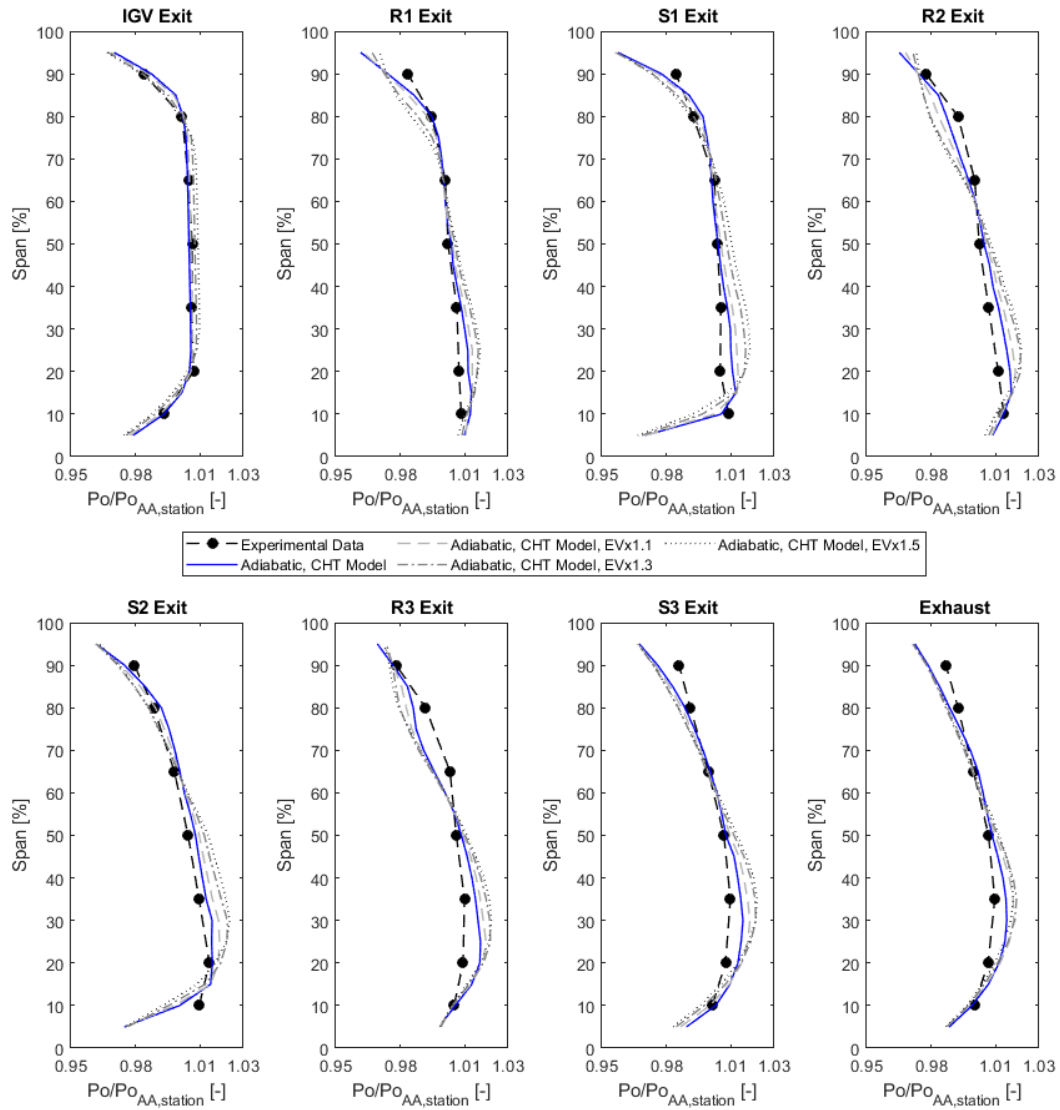
Figure 4.25. Comparison of interstage stagnation pressure profiles between experimental data and adiabatic CHT cases with increasing eddy viscosity, normalized with respect to the area-averaged value at each station.
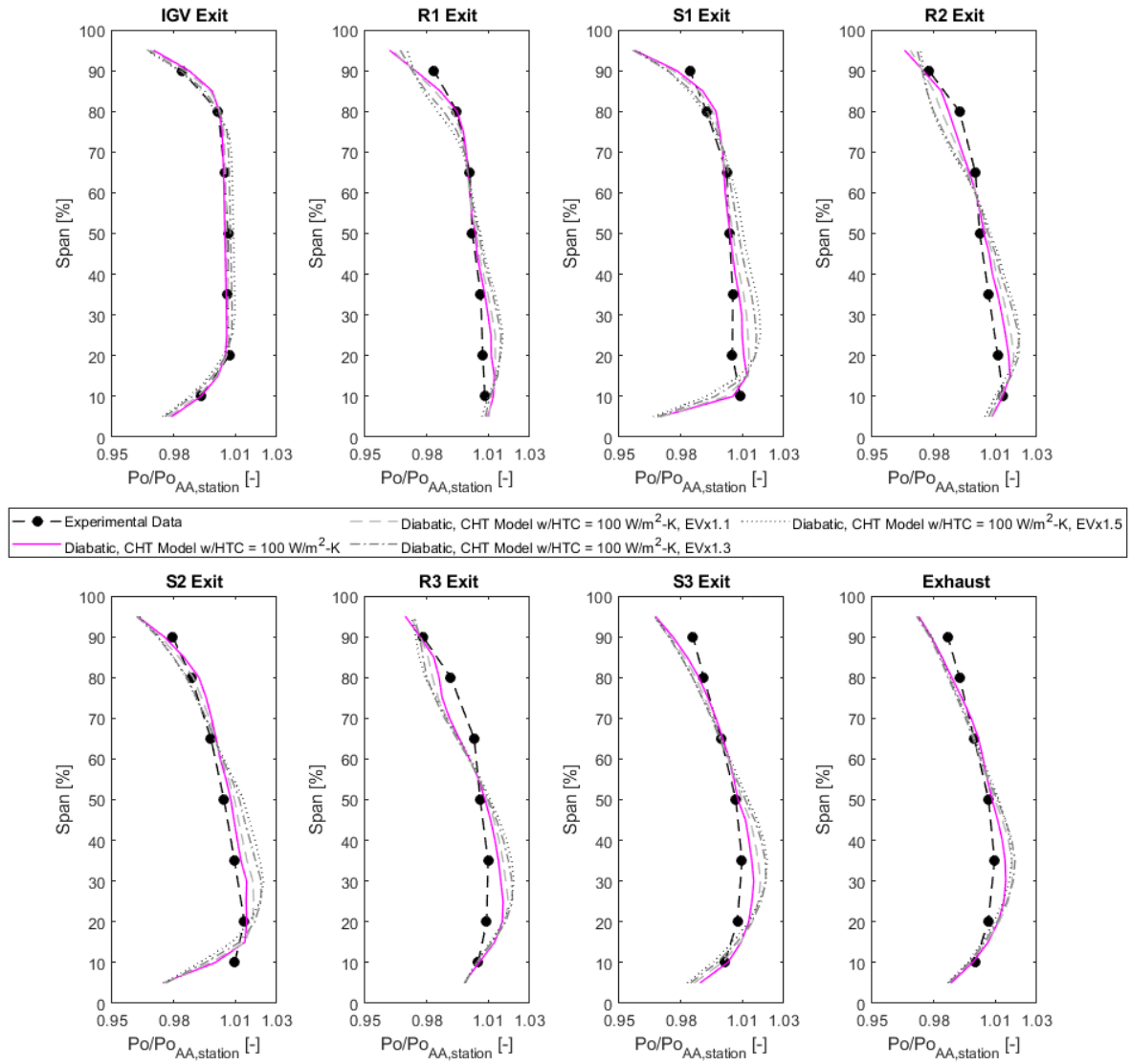
Figure 4.26. Comparison of interstage stagnation pressure profiles between experimental data and high convection (diabatic) CHT cases with increasing eddy viscosity, normalized with respect to the area-averaged value at each station.
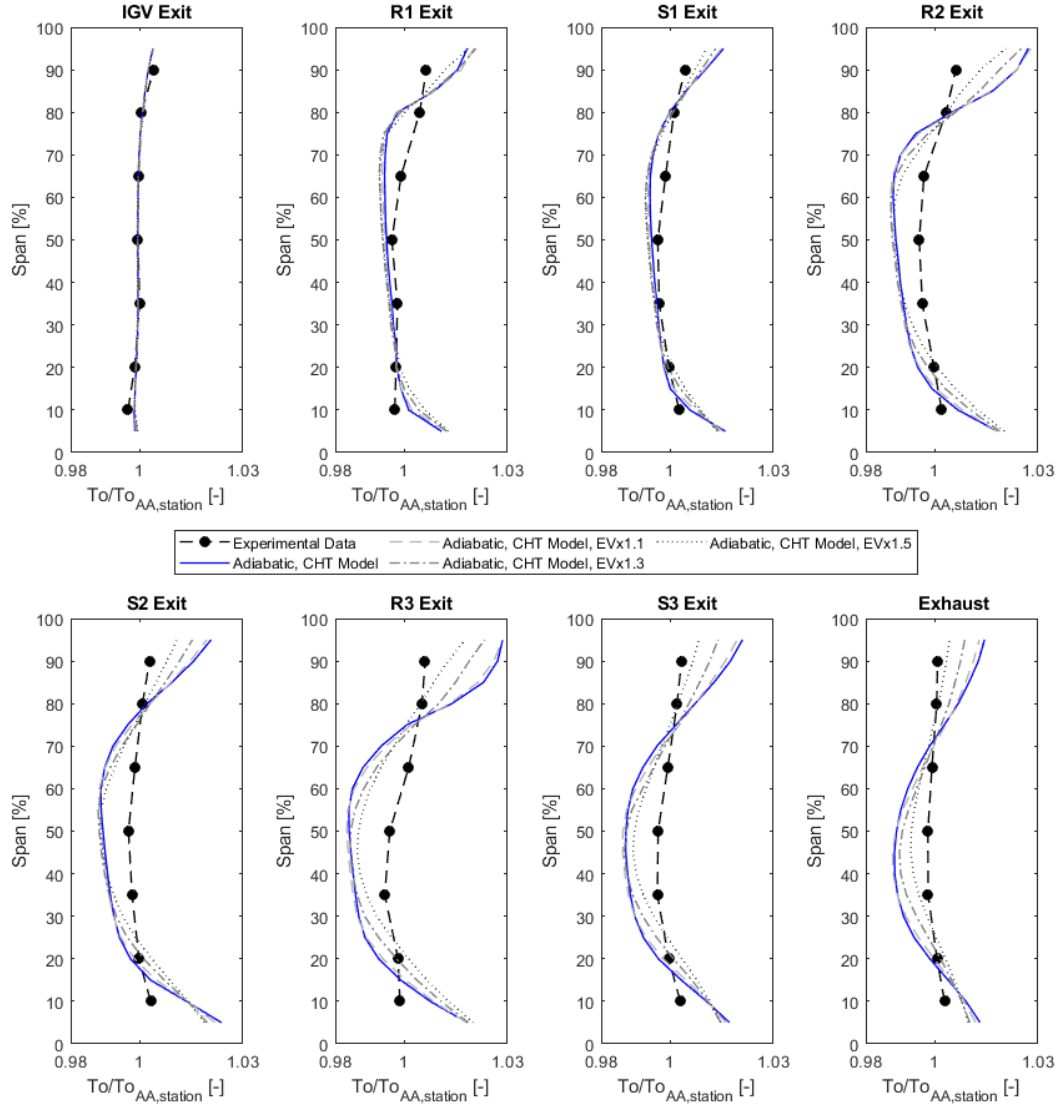
Figure 4.27. Comparison of interstage stagnation temperature profiles between experimental data and adiabatic CHT cases with increasing eddy viscosity, normalized with respect to the area-averaged value at each station.
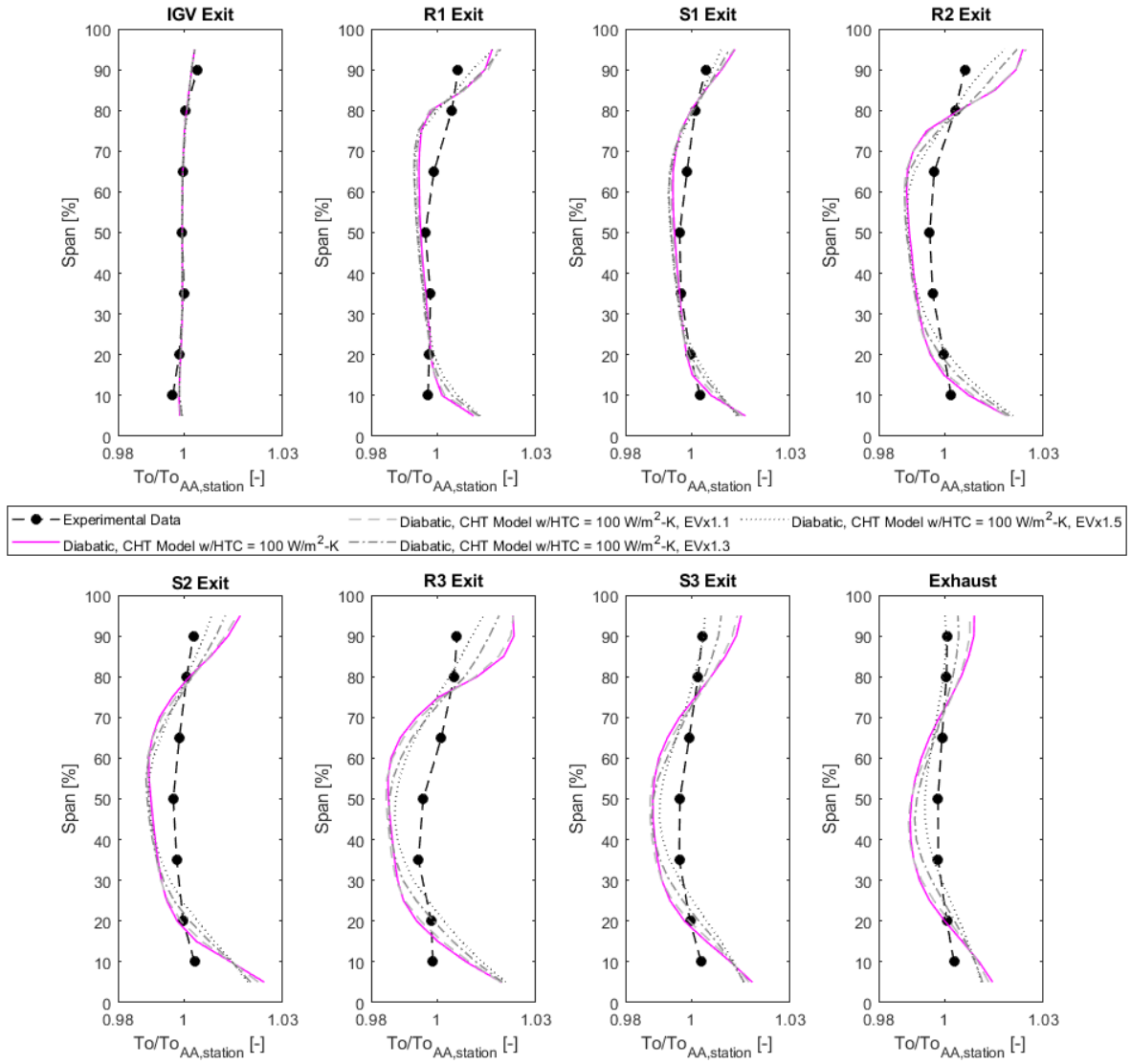
Figure 4.28. Comparison of interstage stagnation temperature profiles between experimental data and high convection (diabatic) CHT cases with increasing eddy viscosity, normalized with respect to the area-averaged value at each station.

The performance of both the adiabatic (Table 4.10) and diabatic (Table 4.11) CHT simulations followed the same trend as those without mixing in previous sections. The simulation with the adiabatic outer wall of the casing provided the worst efficiency, while the simulation with the highly convective case helped recover several points of efficiency, although still less than that of the adiabatic, fluid-only model.

Table 4.10. Performance metric comparison between experimental data and adiabatic CHT cases with increasing levels of eddy viscosity (EV), normalized with respect to the adiabatic, fluid-only model.

	TPR [-]	$\dot{m}_c$ [-]	$\frac{R_c}{W_c}$[-]	TTR [-]	$\Delta\eta_{is}$ [pts]
Experimental Data	0.995	0.994	1.001	0.999	-0.441
Adiabatic, CHT Model	1	1	1	1	-
Adiabatic, CHT Model (EVx1.1)	0.966	1	0.966	0.995	-3.102
Adiabatic, CHT Model (EVx1.3)	0.938	1	0.938	0.991	-5.781
Adiabatic, CHT Model (EVx1.5)	0.915	1	0.914	0.987	-7.979

Table 4.11. Performance metric comparison between experimental data and adiabatic fluid-only cases with increasing levels of eddy viscosity (EV), normalized with respect to the adiabatic, fluid-only model.

	TPR [-]	$\dot{m}_c$ [-]	$\frac{R_c}{W_c}$[-]	TTR [-]	$\Delta\eta_{is}$ [pts]
Experimental Data	0.995	0.994	1.001	0.999	-0.441
Diabatic, CHT Model (CC = 100 W/m²-K)	1	1	1	1	-
Diabatic, CHT Model (CC = 100 W/m²-K, EVx1.1)	0.967	1	0.967	0.994	-2.218
Diabatic, CHT Model (CC = 100 W/m²-K, EVx1.3)	0.939	1	0.939	0.990	-4.934
Diabatic, CHT Model (CC = 100 W/m²-K, EVx1.5)	0.916	1	0.916	0.986	-7.151

The highest mixing (EVx1.5) simulation was selected for each of the three models (adiabatic, fluid-only; adiabatic, CHT; and diabatic CHT) for a more direct comparison between them. In comparing the environmental boundary condition influences on the stagnation pressure profiles at each station, it was expected that no change would occur in pressures between the adiabatic and diabatic boundary conditions with the CHT model. This was affirmed in Figure 4.29, as the only impact on the shape of the pressure profile occurred between the fluid-only and conjugate heat transfer model, even with the enhanced mixing. As shown previously, the system-wide increase in eddy viscosity caused more significant differences in the hub regions in the front stages, as the flow was likely overmixed.
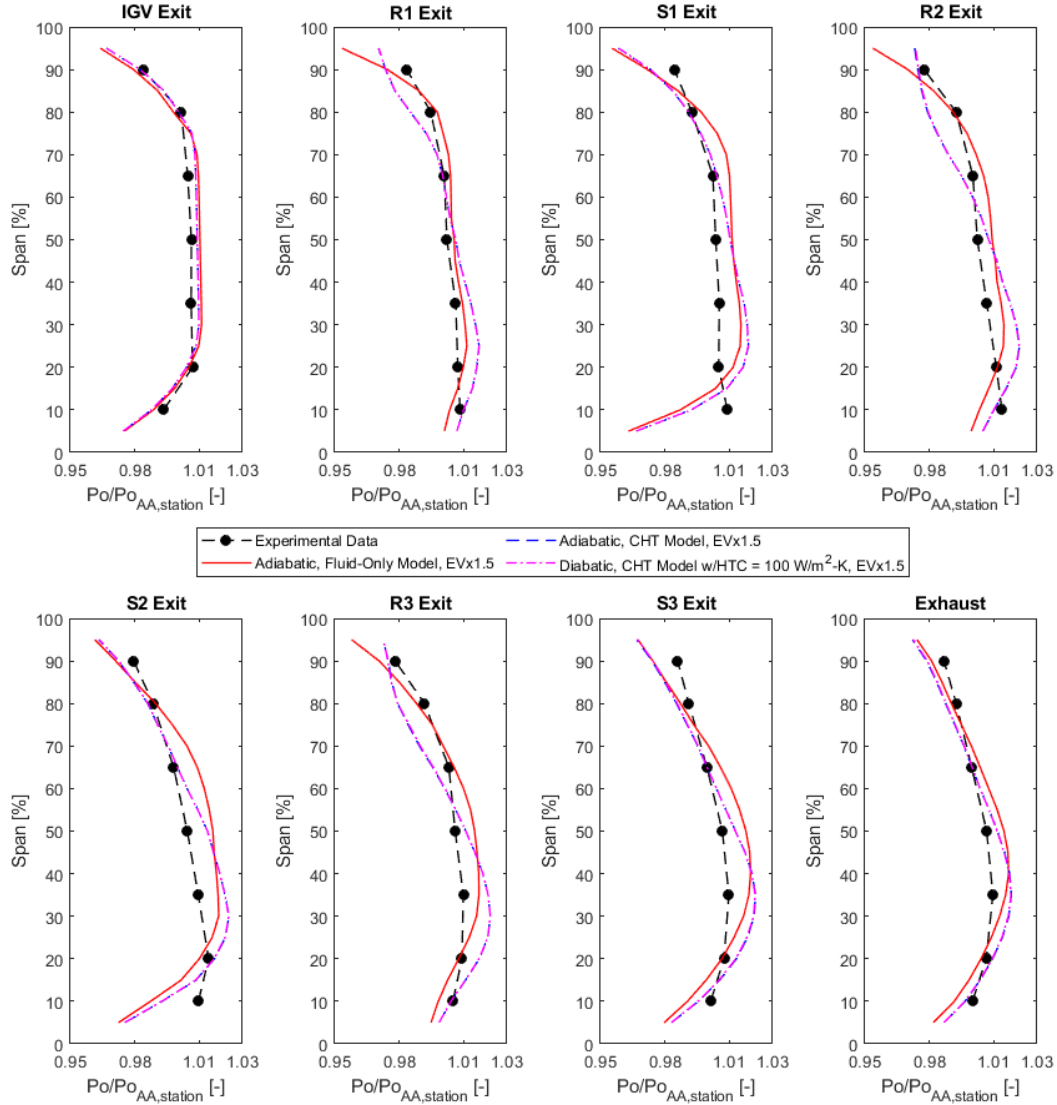
Figure 4.29. Comparison of interstage stagnation pressure profiles between experimental data and all adiabatic and diabatic simulations with eddy viscosity (EV) x 1.5, normalized with respect to the area-averaged value at each station.

In comparing the radial stagnation temperature profiles between the adiabatic fluid-only model and the adiabatic and diabatic CHT models with the experimental results, a bit more deviation took place between the cases. As shown in Figure 4.30, with equal levels of increased mixing across simulations, the diabatic CHT model achieved the best tip and mid-span predictions in the rear blade rows, while the adiabatic fluid-only model achieved a better mid-span prediction in the front blade rows. Overall, the models did not adequately capture the hub region, likely a result of overmixing from the system-wide increase of eddy viscosity, particularly with the cavity

flow interactions with the primary flow. The mixing in the hub would not be as prominent as the tip, which typically has high levels of turbulent diffusion associated with tip leakage flows. Another slight impact for this overprediction in temperature could also be a result of the adiabatic boundary conditions still applied to the rotating components and the solid components not being included in the system like the stationary reference frame.

From a performance perspective, in Table 4.12, the same trend was observed between all the cases compared to the previous sections throughout this chapter. The adiabatic, fluid-only model produced the highest efficiency since it only considered the fluid within the control volume of the system. The adiabatic, CHT model produced the lowest efficiency as it incorporated the heat transfer effects of both the solid and fluid domains within the control volume. Implementing a diabatic boundary condition helped to recover some of this efficiency as heat transfer was able to take place with the ambient environment, causing a reduction in temperature in the rear stages of the compressor. This concept is further reinforced by the fact that in most of the cases presented in this chapter, the total pressure ratio remains unchanged with a change in efficiency, suggesting the thermal characteristics and boundary condition selections are primarily responsible in affecting the compressor efficiency.
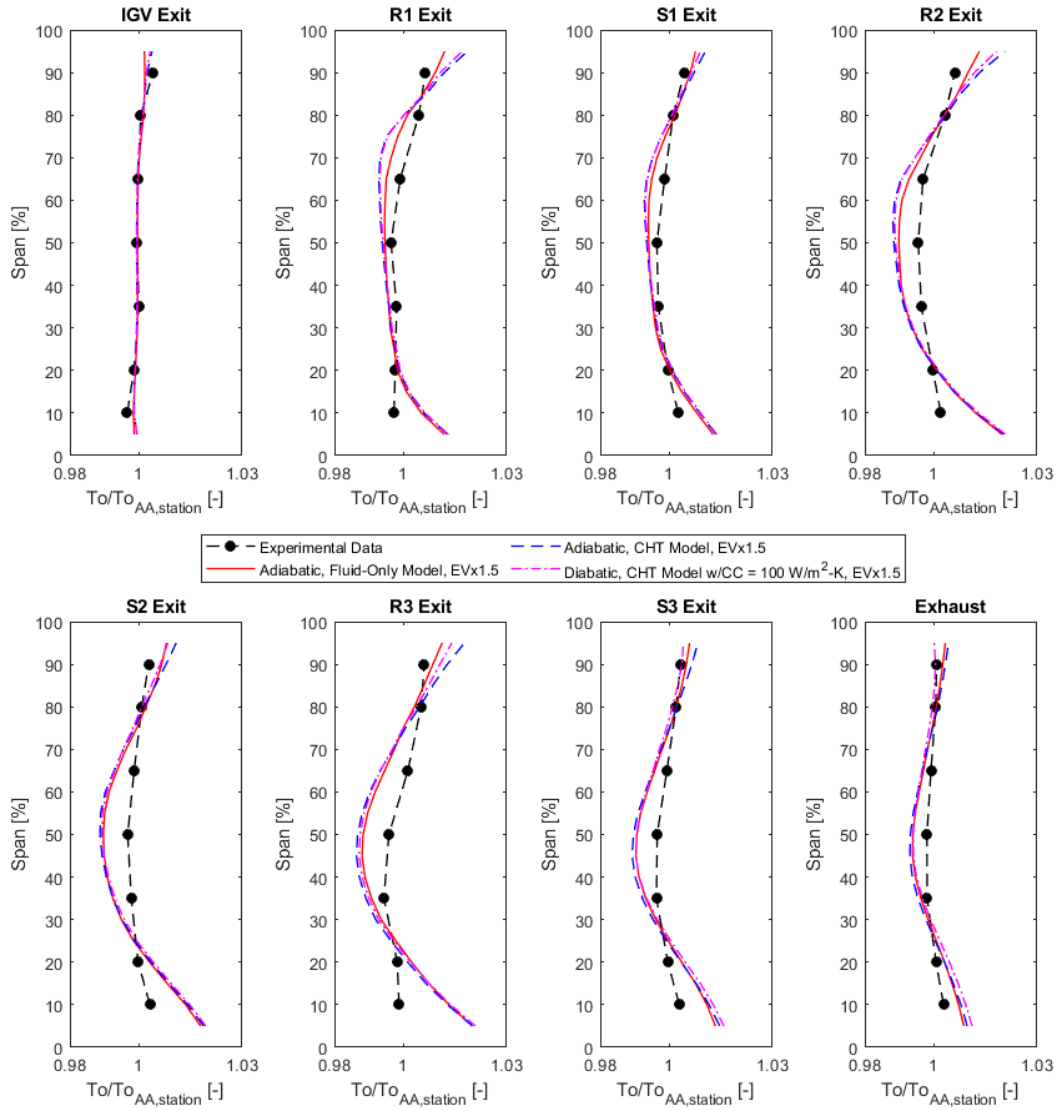
Figure 4.30. Comparison of interstage stagnation temperature profiles between experimental data and all adiabatic and diabatic simulations with eddy viscosity (EV) x 1.5, normalized with respect to the area-averaged value at each station.

Table 4.12. Performance metric comparison between experimental data and all adiabatic and diabatic simulations with eddy viscosity (EV) x 1.5, normalized with respect to the adiabatic, fluid-only model.

	TPR [-]	$\dot{m}_c$ [-]	$\frac{R_c}{W_c}$ [-]	TTR [-]	$\varDelta\eta_{is}$ [pts]
Experimental Data	0.995	0.994	1.001	0.999	-0.441
Adiabatic, Fluid-Only Model	1	1	1	1	-
Adiabatic, Fluid-Only Model (EVx1.5)	0.948	1	0.948	0.996	-6.146
Adiabatic, CHT Model (EVx1.5)	0.915	1	0.914	0.987	-7.979
Diabatic, CHT Model (CC = 100 W/m²-K, EVx1.5)	0.916	1	0.916	0.986	-7.151

In summary, the adiabatic, fluid-only model provided a good starting point for achieving reasonable computational results with minimal computational effort. Most engine development programs commonly implement an adiabatic boundary condition and rely on predicting the fine details in the flow, such as stagnation pressure and temperature profiles at each blade rows to understand the implications of any small design changes. However, for the PAX200 compressor, while the adiabatic model got close in predicting overall performance, it did not correctly predict the radial stagnation pressure and temperature profiles at each station, as well as the surface temperatures of the stationary components, compared to the experimental data taken in the P3S facility. This was particularly true in the tip region for both pressure and temperature, as well as the mid-span and hub regions for temperature. It was determined that much of this discrepancy was because the endwall and cavity temperatures associated with the adiabatic boundary condition were much different compared to those measured in the experimental tests.

The addition of the stationary components (stators and outer casing) to the fluid-only model, provided a system coupling between the fluid and solid domains. This conjugate heat transfer model had much better success at predicting the stagnation pressure profiles at the tip compared to the fluid-only model as well as the metal surface temperatures throughout the casing and stators. This was even true with maintaining an adiabatic boundary condition on the outside wall of the casing. However, the prediction of the stagnation temperature in the tip region only improved after creating a convection condition on the outer surface of the casing. The addition of a convective boundary condition on the outside of the casing also showed that the ambient environment of the facility can result in a significant impact on the thermal characteristics and efficiency of the compressor, with pressure remaining largely unaffected (as discussed in the literature).

Through exploring how material properties and geometric considerations could affect the thermal characteristics of the system, it was determined that with a diabatic condition, material

selection became much more significant as it can act as an insulator to the system or more efficiently draw heat away from the flowpath to the ambient environment.

Finally, to help account for the remaining discrepancies in radial stagnation pressure and temperature profiles, particularly in the mid-span region, simulations with increased mixing using an enhanced eddy viscosity approach were performed. Overall, this greatly improved the temperature predictions when compared to the experimental data in all regions of the flowpath. This enhanced eddy viscosity approach also aligned well with the nature of the unsteady simulation that was performed, which had closer radial profiles to that of the experimental results.

Overall, an examination of the relative impacts of conjugate heat transfer, boundary condition selection, material and geometry consideration, and mixing within a computational model, provided a better understanding of what thermal considerations were relevant or irrelevant to the PAX200 compressor and P3S facility. The introduction of a CHT model, with the addition of convection, and enhanced mixing were all necessary to achieve more accurate predictions of both the radial stagnation pressure and temperature between blade rows, as well as the metal surface temperatures of the stationary components. These computational considerations not only provided an understanding into how the current effects are observed throughout the P3S facility, but also provided some valuable insight into how using correct thermal characteristics and boundary conditions are essential to accurately predicting the flow field.

5. CORRECTING EXPERIMENTAL MEASUREMENTS AND EFFICIENCY FOR HEAT TRANSFER EFFECTS

As described in the previous chapters, the behavior of the P3S facility is far from adiabatic. Both the experimental and computational data showed that the performance of the compressor could be altered through its environment as well as by including the metal components within the control volume of the system. Because the PAX200 compressor is subjected to a non-adiabatic or diabatic condition, the use of an isentropic efficiency was not entirely correct. Discussed in Section 1.2.3, an isentropic efficiency compares the actual work input of a compressor to that of an isentropic (adiabatic and reversible) compressor. Therefore, a more correct assessment of the performance of a diabatic compressor is to compare it to one which is reversible and diabatic. This chapter uses a combination of the experimental and computational data acquired from the previous chapters and lays out a process for correcting the traditional isentropic efficiency to one that is both diabatic and reversible to better describe the true performance of the compression process. This is done not only from the perspective of an overall compressor performance but also that of correcting efficiency and temperature for individual stages.

5.1 Overall Compressor Experimental Efficiency Correction

This section will discuss ways in which the overall compressor isentropic efficiency could be corrected to that of a more realistic, non-isentropic environment – one that is irreversible and diabatic. To achieve this correction, elements of heat transfer and windage were calculated from experimental data and/or derived from the computational simulations and used to adjust the actual work input into the system to better relate to that of a reversible and adiabatic system. This was done from both torque-based (using shaft work) and flow-based (using aerodynamic work) perspectives.

5.1.1 Torque-Based Efficiency

As discussed in Section 1.2.3, a few corrections could be made to the isentropic efficiency equation when looking at the physical shaft work input into the compressor. Through adapting

Equation 14, a first correction was made to the equation by taking any windage (frictional work) into account and assuming an adiabatic system,

$$\eta_{isen,tq,c1} = \frac{h_{o2,s} - h_{o1}}{T\omega - windage} \qquad [24]$$

Using the empirical correlations, discussed in Section 1.2.1 for stator wells and knife seal windage, the friction generated in each of the shrouded cavity regions was calculated for the PAX200 compressor design and is shown in Table 5.1. The knife seal below the IGV shroud was not calculated due to the assumption that no flow passes through the knife seal due to the stagnant air located in the front disk region of the compressor, resulting in no windage across the knife seal. Each of these windage values were applied to the experimental results to produce a relative difference in efficiency for each of the stationary blade rows. This change (delta) in efficiency is the first adjustment, or correction, to the original efficiency value when including the given effect.

Table 5.1. Windage power generation from stator wells and knife seals for each stationary blade row, with relative impact on efficiency.

	IGV	S1	S2	S3
Stator Well Windage	0.454 kW	0.598 kW	0.838 kW	0.612 kW
Knife Seal Windage	-	0.415 kW	0.486 kW	0.816 kW
Total Windage	0.454 kW	1.013 kW	1.324 kW	1.428 kW
Δη	+0.05pts	+0.12pts	+0.15pts	+0.16pts

Using the same empirical correlations for the stator wells, which are derived from disks, the work from friction generated in the front and rear disks of the rotor drum were calculated and listed in Table 5.2. Based on the manufacturer information for the grease-packed rolling element bearings, the facility windage was estimated to be 0.5 kW. With the facility windage contributing less than 0.1pts in efficiency, additional windage from elements like the flex couplings and shaft in the driveline were assumed negligible. As before, this change (delta) in efficiency is the further adjustment to the original efficiency value when including the given effect.

Table 5.2. Windage power generation from front and rear disks and facility, with relative impact on efficiency.

	Front/Rear Disk	Facility
Windage	4.96 kW	0.5 kW
Δη	**+0.55pts**	**+0.06pts**

In using this first efficiency correction as the new initial isentropic efficiency, and adjusting it to meet an adiabatic assumption, minor heat transfer effects still needed to be addressed. While using the torque-based efficiency is useful due to its ability to neglect major heat transfer effects, a small correction to account for the entropy loss associated with any heat transfer in the system was still required. Through the application of Equations 18 and 19, a second corrected isentropic efficiency, $\eta_{is,tq,c2}$, was calculated, providing an additional efficiency adjustment, shown in Table 5.3. The heat rate values used in this calculation were found using heat transfer coefficients derived from CFX and applying them to the experimental data. This allowed for calculation of heat rates through the metal surfaces in the real compressor and will be discussed in more detail in the following section. This final change in efficiency is the final adjustment to the original efficiency value when including the given effect.

Table 5.3. Heat transfer correction values and relative impact on efficiency.

$\dot{Q}$	**-1.495 kW**
$\dot{\Delta H}$	**-1.570 kW**
Δη	**-0.05pts**

With two different efficiency corrections applied to the torque-based experimental results, a final, corrected value was obtained for the efficiency of the compressor. Using the windage and resulting heat transfer corrections, the original experimental, torque-based, isentropic efficiency was increased by 1.04pts to reflect that of an actual adiabatic compressor. These steps are summarized in Table 5.4.

Table 5.4. Summary table describing relative efficiency corrections and total impact on torque-based efficiency.

$\Delta\eta_{isen,tq} \rightarrow \Delta\eta_{isen,tq,c1}$ (windage correction)	$\Delta\eta_{is,tq,c1} \rightarrow \Delta\eta_{isen,tq,c2}$ (heat transfer correction)	Total $\Delta\eta_{is,ctot}$
+1.09pts	-0.05pts	+1.04pts

5.1.2 Flow-Based Efficiency

As discussed in Section 1.2.3 and in a similar fashion to the torque-based efficiency, a few corrections could also be made to the flow-based isentropic efficiency equation when looking at the aerodynamic work input into the compressor using the heat transfer associated with the stationary components in the compressor. First, an overall isentropic efficiency was calculated using the experimental flow properties measured at station 0 (AIP inlet) and station 9 (exhaust). This calculated efficiency followed the standard approach to isentropic efficiency, comparing the actual work to a reversible and adiabatic process. However, with the noticeably diabatic behavior of the compressor, the influences of heat transfer were removed from the actual work of the compressor to help make this comparison to an adiabatic system more correct. Through adapting Equation 12, a first correction was made to the equation by taking heat generation (assumed from frictional work in the stator shroud regions) into account, notated $\eta_{isen,flow,c1}$.

Using the same empirical correlations for stator wells and knife seal windage as the torque-based efficiency corrections and assuming that all frictional windage was converted to heat generation, the heat generation for each blade row that would interact with the primary flow was calculated. The knife seal below the IGV shroud was not calculated due to the assumption that no flow passes through the knife seal due to the stagnant air located in the front disk region of the compressor, resulting in no windage across the knife seal. The knife seal below S3 was also not calculated due to the assumption that all air passing through the knife seal exits the compressor through an alternate flowpath that does not directly impact the aerodynamic flow properties at Station 8 and Station 9. The same is also true of any facility and front/rear disk windage as they do not affect the primary flowpath. Each of these windage/heat generation values were applied to the experimental results using Equation 12 to produce a relative difference in efficiency for each of the stationary blade rows, shown in Table 5.5. Similar to the torque-based analysis, this change in efficiency is the first adjustment, or correction, to the original efficiency value when including the given effect.

Table 5.5. Windage power heat generation from stator wells and knife seals for each stationary blade row, with relative impact on efficiency.

	IGV	S1	S2	S3
Stator Well Heat Generation	0.454 kW	0.598 kW	0.838 kW	0.612 kW
Knife Seal Heat Generation	-	0.415 kW	0.486 kW	-
Total Heat Generation	0.454 kW	1.013 kW	1.324 kW	0.612 kW
$\Delta\eta_{isen,flow,c1}$	**+0.05pts**	**+0.12pts**	**+0.15pts**	**+0.07pts**

In addition to the heat generated due to windage, as shown with the experimental data through the hot inner wall metal temperatures measured at the front of the compressor and the heat flux gauges, a heat path was observed from downstream stages to the front stages of the compressor. To calculate the impact of this heat transfer on the primary flow within each stage, more details were required about the heat transfer interaction between the stators, casing wall, and the flow. With convective heat transfer coefficient information unknown but remaining consistent based on the turbulence levels presented in the flow, a convective heat transfer coefficient was derived from the computational simulations.

The heat transfer coefficient from ANSYS CFX is automatically calculated using the heat flux of the region under examination and the temperature difference between the first element of the mesh off the wall (wall adjacent temperature) and the wall temperature. Since experimental results were unable to capture the temperature this close to the metal surface, the CFX data needed to be translated to provide a meaningful convective coefficient that could be compared with the experiment.

To achieve this, an average heat flux, wall temperature, wall adjacent temperature, and surface heat transfer coefficient were first calculated and taken from ANSYS CFX for a specific section of the compressor (shroud, cavity, hub, blade). With results from the experimental data at 10%, 50% and 90% radial span, temperatures at the same spanwise locations were used in CFX to calculate convective heat transfer coefficients for the hub/cavity, blade, and shroud, respectively. This conversion provided a convective heat transfer coefficient that could be directly related to the experimental data. Then, using the experimental stagnation temperatures at the span points from the experimental data, the area of each section of the compressor, and the measured metal surface temperatures from the experimental data, a heat rate was able to be calculated for the experiment based on the experimental data.

This translation was repeated for each region of the compressor to establish a heat rate and overall heat flow for the compressor. The detailed results and heat flow paths are found in the Appendix. A summary for each blade row and section of the compressor can be found in Table 5.6, with a visual representation of the heat path shown in Figure 5.1.

Table 5.6. Summation of the heat transfer rate for each blade row based on the experimental data, using convective coefficients derived from ANSYS CFX.

	Inlet	IGV	R1	S1	R2	S2	R3	S3	Exhaust
Heat Rate [kW]	0.059 into flow	1.121 into flow	-0.294 out of flow	0.331 into flow	-0.812 out of flow	0.100 into flow	-1.034 out of flow	-0.495 out of flow	-0.473 out of flow
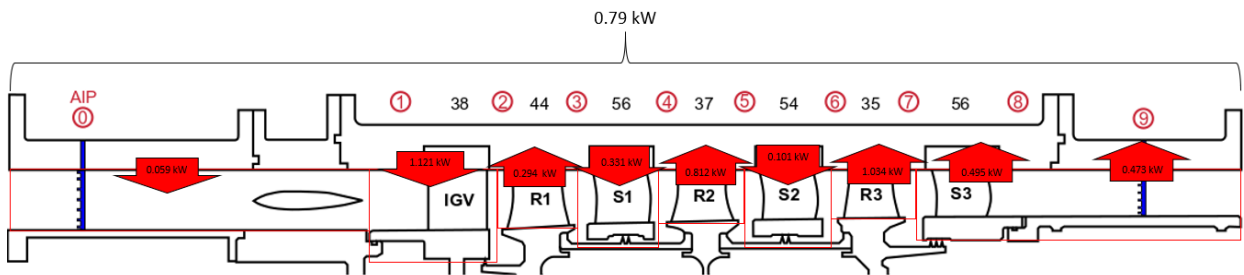
Figure 5.1. Heat flow path through the compressor, based on experimental data.

Comparing the heat flux/rates at the AIP shroud, shroud at the entrance to IGV, shroud at the exit to S3, and the shroud and hub of the exhaust, most of the values tracked closely with the heat flux gauge data obtained during experimental testing, as shown in Table 5.7. The AIP shroud matched almost exactly, while the results from CFX underpredicted the heat transfer into the IGV shroud. The results from CFX overpredicted the heat flux out of the S3 shroud and underpredicted the heat flux in the exhaust shroud, however by ignoring the distribution of the heat flux and treating them as a combined entity, the results align very closely with the heat flux gauge results. Finally, the results from CFX were significantly different for the exhaust hub, although this was most likely a result of the adiabatic condition applied to the disk region in the computational simulation.

Table 5.7. Heat flux comparison between experimental results from heat flux gauges and experimentally derived heat flux using CFX convection coefficient approach.

	AIP Shroud	IGV Shroud	S3 Shroud	Exhaust Shroud	Exhaust Hub
Experimentally Measured	+0.08 kW/m^2	+0.79 kW/m^2	-0.18 kW/m^2	-1.02 kW/m^2	-0.62 kW/m^2
Derived from CFX	+0.07 kW/m^2	+0.25 kW/m^2	-0.56 kW/m^2	-0.60 kW/m^2	+0.00 kW/m^2

Using the calculated experimental heat rates, the heat rate for each individual blade row was summarized into an overall heat rate for each stage, shown in Table 5.8. As expected, based on the heat flux gage data, heat addition was evident in the IGV and Stage 1 of the compressor, while heat removal was observed in Stage 3. As shown in the computational simulations, this is a result of the diabatic condition on the outside of the compressor casing which transfers heat through the casing from the flow to the ambient environment, and upstream through conduction.

Table 5.8. Heat rate for each stage of the compressor, based on experimental data.

	Full Compressor (Stations 0-9)	Casing Only Stations 1-8	Stage 1 (Stations 2-4)	Stage 2 (Stations 4-6)	Stage 3 (Stations 6-8)
Net Heat Rate [kW]	-1.495 (out of flow)	-1.081 (out of flow)	0.038 (into flow)	-0.711 (out of flow)	-1.529 (out of flow)

In a similar way to how the heat generation from the cavity regions was corrected for by subtracting it from the actual work (Equation 12), a second corrected isentropic efficiency, $\eta_{isen,flow,c2}$, was calculated using the heat rate calculated for the full compressor through the stationary components. This provided an additional efficiency adjustment. With two different efficiency corrections applied to the flow-based experimental results, a final, corrected value was obtained for the efficiency of the compressor. Using the windage/heat generation calculations accounting for the cavity regions with the heat flow calculations accounting for the heat transfer through the stationary reference frame, the original experimental, flow-based, isentropic efficiency was increased by 0.23 pts to reflect that of an actual adiabatic compressor. These steps are summarized in Table 5.9.

Table 5.9. Summary table describing relative efficiency corrections and total impact on flow-based efficiency.

$\Delta\eta_{isen,flow} \rightarrow \Delta\eta_{isen,flow,c1}$ (windage correction)	$\Delta\eta_{isen,flow,c1} \rightarrow \Delta\eta_{isen,flow,c2}$ (heat transfer correction)	Total $\Delta\eta_{isen,flow,ctot}$
+0.39pts	-0.16pts	+0.23pts

One issue that was not addressed with calculating these efficiency correction values was the impact of the heat transfer from/to the rotating reference frame. This could also have a significant effect on the heat transfer and efficiency of the compressor, specifically with respect to correctly capturing the heat flow in and out of the hub and cavity regions. This could lead to a further temperature increase which could impact efficiency as it is suspected that the drum of the compressor could also be hotter than the flow path.

5.2   Interstage Experimental Performance Correction

While torque-based efficiency is challenging to apply at an interstage level due to the inability to experimentally break down the shaft work into specific stages, flow-based efficiency, particularly on research compressors like PAX200, is often more easily attainable. This is because detailed flow measurements, at least in the P3S compressor facility, can be taken between each blade row. Therefore, in a similar fashion to correcting the overall compressor efficiency, looking at the heat transfer at an individual stage level can offer additional insights into the performance of each stage of the compressor. Finally, the heat transfer and temperature measurements taken between each stage provide a means to evaluating each stage temperature, particularly with respect to addressing the observed temperature increases across the stators of each stage.

5.2.1   Heat Transfer Correction

Through a very similar approach that was followed in the previous section, corrections could also be made on a stage level to the flow-based isentropic efficiency using the previous calculated heat rates and windage values. First, using the interstage rake values, an efficiency was calculated for each stage based on the isentropic (adiabatic and reversible) form of the equation. Stage 1 incorporated measurements from upstream of R1 to downstream of S1, stage 2 incorporated measurements from upstream of R2 to downstream of S2, and stage 3 used the measurements from upstream of R3 to downstream of S3. With the noticeably diabatic behavior of the compressor at each stage, the influences of heat transfer were removed from the actual work for each stage of the compressor to help make this comparison to an adiabatic system more correct.

Next, using the same windage values already calculated in Table 5.5, but looking at each individual stage, a first correction was made to the isentropic efficiency by taking heat generation

(assumed from frictional work in the stator shroud regions) into account, notated $\eta_{isen,flow,c1}$. Each of these windage/heat generation values were applied to the experimental results using Equation 12 to produce a relative difference in efficiency for each of the individual stages, shown in Table 5.10. This heat generation results in roughly 15-30°F increase of temperature across each shrouded stator, which corresponds to the measured temperature increases recorded in Chapter 3.

Table 5.10. Windage power heat generation from stator wells and knife seals for each stage, with relative impact on efficiency.

	Stage 1 (S1)	Stage 2 (S2)	Stage 3 (S3)
Stator Well Heat Generation	0.598 kW	0.838 kW	0.612 kW
Knife Seal Heat Generation	0.415 kW	0.486 kW	-
Total Heat Generation	1.013 kW	1.324 kW	0.612 kW
$\Delta\eta_{isen,flow,c1}$	**+0.33pts**	**+0.45pts**	**+0.2pts**

In a similar way to how the isentropic efficiency was corrected on a compressor-wide basis for the heat path through the stationary components in the compressor, a second corrected isentropic efficiency, $\eta_{isen,flow,c2}$, was calculated on a stage-basis using the heat rates calculated in Table 5.8. This provided an additional efficiency adjustment. With two different efficiency corrections applied to the flow-based experimental results, a final, corrected value was obtained for the efficiency of the compressor. Using the windage/heat generation calculations accounting for the cavity regions, with the heat flow calculations accounting for the heat transfer through the stationary reference frame into/out of the flow, the original experimental, flow-based, isentropic efficiency was increased by up to 0.34pts for Stage 1 due to the influx of heat into the stage. There was however a decrease of up to 0.30pts for Stage 2 and Stage 3 to reflect the loss of heat into the casing to reflect that of an actual adiabatic compressor. These steps are summarized in Table 5.11.

Table 5.11. Summary table describing relative efficiency corrections and total impact on flow-based efficiency for each individual stage.

Stage	$\Delta\eta_{isen,flow} \rightarrow \Delta\eta_{isen,flow,c1}$ (windage correction)	$\Delta\eta_{isen,flow,c1} \rightarrow \Delta\eta_{isen,flow,c2}$ (heat transfer correction)	Total $\Delta\eta_{isen,flow,ctot}$
1	**+0.33pts**	**+0.01pts**	**+0.34pts**
2	**+0.45pts**	**-0.24pts**	**+0.21pts**
3	**+0.2pts**	**-0.5pts**	**-0.30pts**

As discussed previously, one issue that was not addressed with calculating these efficiency correction values was the impact of the heat transfer from/to the rotating reference frame. This could also have a significant effect on the heat transfer and efficiency of the compressor, specifically with respect to the hub and cavity regions. This could lead to a further temperature increase which could impact efficiency as it is suspected that the drum of the compressor is also hotter than the flow path.

5.2.2   Temperature Rise Across Stators

One of the primary motivations behind this research was to investigate the temperature increase across the compressor stators observed during experimental testing. With the stationary vanes, no work is imparted into the passing air, it was theorized that this increase in temperature could be due to the many heat transfer phenomena discussed throughout this investigation.

To better understand how the boundary conditions of the compressor might affect this increase in temperature, the stagnation temperature results from the computational simulations and experimental were compared. The measurements from the experimental data taken with the stagnation rakes were area-averaged, and circumferentially averaged across one pitch, based on the S2 blade count. This resulted in capturing over 100% of the S1 and S3 pitches, which was corrected for during the circumferential averaging to ensure a representative average for that blade row. However, with the IGV featuring a low blade count, this resulted in an overly large pitch for the IGV allowing for only about 70% of the IGV pitch to be captured. From the computational simulations, the same radial span points were taken from a few of the boundary condition models discussed throughout Chapter 4, to create an equivalent area-averaged and circumferentially averaged value that could be directly compared with the experimental data. These results are shown in Table 5.12.

Looking at the inlet section (Stations 0-1), the closest correlation to the experimental data occurred with the CHT model, although it still slightly underpredicted the temperature rise. For the IGV (Stations 1-2), the experimental results showed a decrease in overall temperature, while the computational simulations all showed an increase in temperature. This discrepancy was thought to be a result of the experimental data only capturing about 70% of the vane passage, giving extra weight in the circumferential averaging of the data to the wake present in the flow.

On the other hand, the computational simulation included the entire vane passage and thus, a more wholistic average for the vane passage.

Overall, there was an increase in stagnation temperature across the stators for most of the simulations, especially for the IGV. This indicated that the temperature increase across the stators observed in the P3S facility was not an uncommon occurrence, at least not with the spanwise positions that were measured during experimental testing. For S1 (Stations 3-4) and S2 (Stations 5-6), the largest increase in temperature occurred with the simulations, which mirrored the experiment. However, the computational results did not predict quite as high of a temperature increase as the experimental results, with similar results between models, regardless of the boundary conditions. With S3 (Station 7-8) and the exhaust section (Station 8-9) of the compressor, most of the simulations predicted an overall decrease in temperature, contrary to the increase in temperature observed with the experimental results. However, the enhanced mixing case provided an increase in temperature, though relatively low compared to the experiment.

Table 5.12. Average temperature differences across each stationary section for experimental results and computational simulations.

	Inlet Station 0 to 1	IGV Station 1 to 2	S1 Station 3 to 4	S2 Station 5 to 6	S3 Station 7 to 8	Exhaust Station 8 to 9
Experiment	+0.20°F	-0.66°F	+1.90°F	+1.88°F	+1.33°F	+0.38°F
Steady, Adiabatic, Fluid-Only Model	0.00°F	+0.09°F	+0.23°F	+0.44°F	-0.04°F	0.00°F
Steady, Adiabatic, CHT Model	+0.05°F	+0.21°F	+0.28°F	+0.44°F	-0.05°F	0.00°F
Steady, Diabatic (HTC = 100 W/m²K), CHT Model	+0.05°F	+0.19°F	+0.23°F	+0.40°F	-0.23°F	-0.13°F
Steady, Adiabatic, CHT Model (EVx1.5)	+0.07°F	+0.25°F	+0.29°F	+0.42°F	+0.07°F	+0.01°F
Steady, Diabatic (HTC = 100 W/m²K), CHT Model (EVx1.5)	+0.05°F	+0.22°F	+0.27°F	+0.34°F	-0.16°F	-0.13°F

To gain a better understanding as to why the simulations underpredicted the overall temperature rise across the stators, further analysis was performed on a few of the computational models. Looking at each of the stators individually, the metal surface temperatures and stagnation flow temperatures were considered in the meridional view, as shown in Figure 5.2. In each of the temperature contours, it was shown that much of the temperature increase occurred in

the endwall regions, as that was generally the hottest part of the stator. This was also indicated in the results from the surface temperature mapping experiment. However, the bulk flow through the stator was much cooler compared to that of the experimental results. This was partly addressed with the enhanced mixing approach applied to the computational model in Section 4.6.
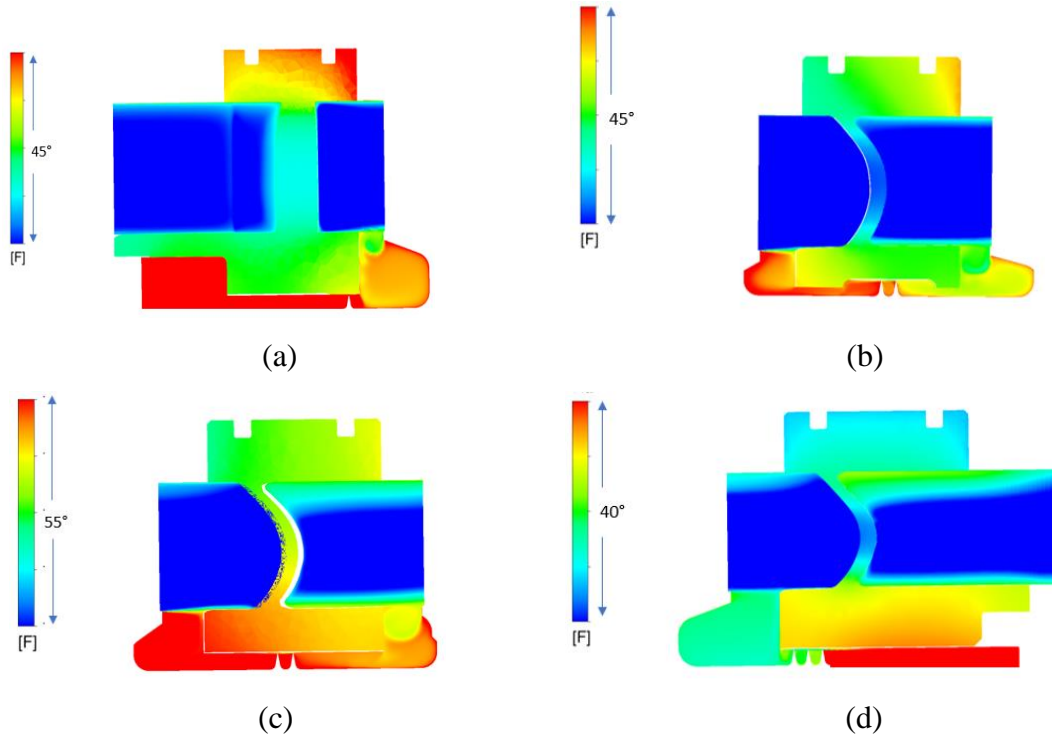
Figure 5.2. Axial view of IGV (a), S1 (b), S2 (c), and S3 (d) showing metal surface and stagnation air flow temperatures for the CHT, low convection (HTC = 10 W/m^2-K) case.

In addition to these temperature contours, the stagnation temperature profiles from the CFD simulations were compared to the experimental measurements acquired with the stagnation temperature probe, discussed in Section 3.2. These results are shown in Figure 5.3, highlighting the differences between the different boundary conditions in the CFD simulations. The adiabatic fluid-only model, adiabatic CHT model, and diabatic CHT model with enhanced mixing were all compared to the probe from 0% to 100% span.

Overall, these results showed that the conjugate heat transfer model simulations matched the experimental data much more closely, particularly in the tip region of the flowpath, when a diabatic condition was applied with enhanced mixing. However, all the computational models significantly missed the correct prediction of stagnation temperature at the hub compared to that

167

of experiment. The results from the diabatic, conjugate heat transfer model performed closest to that of the experiment but were still significantly off.
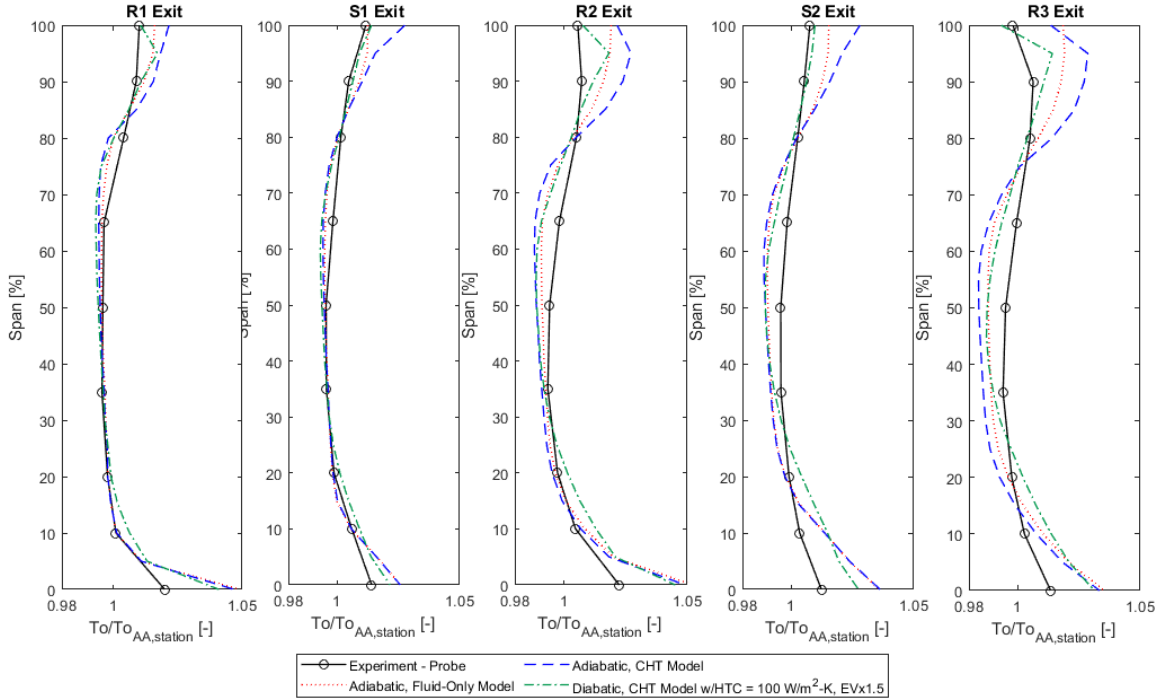
Figure 5.3. Full-span stagnation temperature comparison between experimental probe and CFD simulations.

Based on this observed relationship of the flow temperatures in the endwall regions, the temperature rise across the stators at the endwalls and midspan were tabulated, essentially removing the influence of the area-average process that was used in the previous analysis. The circumferential average was still maintained. These results provided a few additional insights into the temperature behavior across each blade row.

With the inlet section of the compressor, the experimental data showed a large temperature increase in the region closest to the shroud, which was unmatched by the computational model. However, all the simulations showed a slightly higher increase near the hub of the inlet section than the experimental data. The IGV results further promoted the influence of missing the IGV wake in the pitchwise acquisition of the experimental temperature data.

The simulation results all showed an increase in temperature across all span positions, apart from the adiabatic, fluid-only model and the adiabatic, CHT model with enhanced mixing, which

still had a negligible decrease in temperature compared to the experimental results. Through the evaluation of the S1 results, the only simulation that was able to sufficiently predict the experimental temperature increase across the stator was that of the enhanced mixing model. In that case, it overpredicted the temperature rise in the midspan region, but still underpredicted the increase in the hub and shroud temperatures. For S2 and S3, the enhanced mixing model also produced similar results to S1. However, for S3, the hub region was vastly underpredicted which could have been a result from not incorporating heat transfer in the rear drum area into the model. Finally, for the exhaust region, a blend of the adiabatic CHT model and the enhanced mixing model showed the most promise in successfully predicting the experimental temperature difference.

Table 5.13. Temperature differences across each stationary section by spanwise position for experimental results and computational simulations.

	Span Position	Inlet Station 0 to 1	IGV Station 1 to 2	S1 Station 3 to 4	S2 Station 5 to 6	S3 Station 7 to 8	Exhaust Station 8 to 9
Experiment	90%	+1.06°F	-0.41°F	+0.79°F	+0.86°F	0.00°F	-0.74°F
	50%	-0.13°F	-0.82°F	+2.17°F	+2.45°F	+2.10°F	+1.52°F
	10%	+0.02°F	-0.31°F	+3.76°F	+2.41°F	+1.80°F	-0.25°F
Steady, Adiabatic Fluid-Only Model	90%	+0.04°F	-0.05°F	-1.30°F	-1.60°F	-2.45°F	-2.04°F
	50%	+0.02°F	0.00°F	+0.01°F	+0.10°F	+0.22°F	+0.60°F
	10%	+0.13°F	-0.04°F	+2.69°F	+3.58°F	+0.27°F	-1.14°F
Steady, Adiabatic, CHT Model	90%	+0.03°F	+0.20°F	-2.73°F	-5.09°F	-7.52°F	-3.12°F
	50%	+0.02°F	+0.01°F	+0.06°F	+0.18°F	+0.57°F	+1.04°F
	10%	+0.13°F	+0.08°F	+2.66°F	+3.84°F	+0.48°F	-1.04°F
Steady, Diabatic (HTC = 100 W/m²K), CHT Model	90%	+0.02°F	+0.12°F	-2.84°F	-5.11°F	-7.62°F	-3.15°F
	50%	+0.02°F	+0.01°F	+0.05°F	+0.20°F	+0.48°F	+0.91°F
	10%	+0.13°F	+0.10°F	+2.67°F	+3.86°F	+0.45°F	-1.06°F
Steady, Adiabatic, CHT Model (EVx1.5)	90%	-0.15°F	-0.10°F	-1.34°F	-1.53°F	-2.46°F	-1.65°F
	50%	+0.13°F	-0.00°F	+0.05°F	+0.32°F	+1.25°F	+1.92°F
	10%	+0.15°F	-0.01°F	+1.95°F	+1.29°F	-1.62°F	-2.53°F
Steady, Diabatic (HTC = 100 W/m²K), CHT Model (EVx1.5)	90%	-0.09°F	+0.20°F	-2.06°F	-3.11°F	-4.96°F	-2.25°F
	50%	+0.03°F	+0.00°F	+0.09°F	+0.45°F	+1.30°F	+1.91°F
	10%	+0.14°F	+0.23°F	+1.90°F	+1.29°F	-1.20°F	-2.47°F

Overall, as hinted at and discussed in Chapter 4 and shown in the full-span profiles, incorporating enhanced mixing and adiabatic and diabatic boundary conditions into the model achieved a much closer result to that of the experiment. It effectively captured the correct stagnation temperature profile at each stage, as well as the temperature rise across each of the stationary sections within the compressor. This signified the correct boundary condition would be between an adiabatic boundary condition and one of high convection. Furthermore, the computational simulations indicated and confirmed that a temperature rise across the stators was

expected, even with no work provided to the flow by the stator. It is also expected that the heat transfer into/out of the rotating reference frame could contribute to changing the behavior of these computational simulations, much in the same way that adding the stationary components did.

6. CONCLUSIONS & RECOMMENDATIONS

Throughout this research investigation several conclusions were made on the heat transfer characteristics of the PAX200 compressor and P3S facility. The PAX200 compressor has a diabatic thermal boundary condition as verified by experimental measurements obtained on the stationary components. In addition to the surface temperatures that were acquired, the heat transfer characteristics of the compressor impacted the stagnation temperatures of the flow path, which have a large impact on the performance metrics, such as efficiency. Further analysis using computational simulations allowed for deeper exploration into the importance of using the correct boundary conditions in simulation and confirmed that a diabatic boundary condition was much more correct than an adiabatic condition. With a diabatic system in both experimental and computational simulations the idea of using isentropic efficiency, based on a reversible and adiabatic system, to characterize the flow was not entirely correct. Thus, using a combination of experimental and computational research, methods for correcting efficiency and the temperature increase across stators was developed and applied to the PAX200 experimental data.

6.1 Conclusions from Experimental Measurements of Surface and Flow Temperatures

With the experimental portion of this research investigation, several conclusions were made with respect to the effect of heat transfer on the stationary components of the PAX200 compressor and the stagnation temperature measurements in the flow path. Experimental measurements were crucial in understanding the initial effects of heat transfer within the facility and provided a means to characterize the thermal boundary conditions of the compressor.

Through baseline compressor mapping of the entire 100% corrected speed line, stagnation temperatures and pressures were taken throughout the flow field in both the radial and circumferential direction to characterize an ADP loading condition. Of most interest were the stagnation temperature radial profiles, which showed high temperatures near the endwalls. Apart from the IGV, this data also showed an increase in stagnation temperature (up to 2°F, on average) across the stator vanes, a phenomenon that was unexpected due to the inability of the stator to impart work into the flow.

To help assess the possible heat sources that could lead to this increase in temperature across the stators, stagnation temperature probes were plunged into the cavity regions to explore the temperature rise due to well windage and knife seal throttling. On average, the temperature in the cavity was found to increase up to 15°F within the wells, with a minimal increase (less than 5°F) across the knife seals themselves. Metal surface temperatures and heat fluxes were measured throughout the flow path of the compressor to provide an indication of how hot the stationary components were with respect to the flow during operation. These metal surface and flow temperatures also showed that the measured stagnation temperature within each stator well closely matched that of the nearby metal surface (to within 2-3°F), and that the hub region of each stator blade was significantly hotter than the flow path (between 10-20°F). Additionally, the heat flux gauges and external casing surface temperatures showed a path of heat conduction through the casing moving from the rear stages toward the front of the compressor.

Finally, a combination of circumferentially spaced surface thermocouples on the exterior of the casing, axially spaced surface thermocouples on the interior of the casing, stagnation flow temperatures, and heat flux measurements on the inside of the casing were used to explore various levels of heat transfer through convection. The outside of the compressor casing was exposed to different cold and hot ambient conditions, as well as a more extreme approach with applying dry ice and heat tape to the front-half of the casing. These experiments were used to give an indication as to how heat transfer could influence the measurements typically used to calculate compressor performance.

For example, heat transfer on the outside of the casing affects the flow inside the compressor through both temperature and efficiency, with a 0.3°F change in stagnation temperature at the tip of the exit resulting in about 0.25pt difference in efficiency. The higher heat transfer due to convection present on the outside of the casing produced a higher heat removal in the rear stage, resulting in lower tip temperature and higher efficiency. This also gave an indication as to how highly sensitive the flow in the compressor is to ambient conditions in the test cell and confirmed a diabatic thermal boundary condition was necessary to correctly describe the facility.

6.2   Conclusions from Computational Simulations and Boundary Condition Selection

With a basis for what temperatures and heat fluxes could be expected in the compressor, computational simulations were compared to the experimental data to support validation of the

model and better understand the heat transfer characteristics of the PAX200 compressor. A computational model was developed to provide insights into the extent to which the PAX200 compressor represented a diabatic system, the effect of heat transfer on the flow properties and performance metrics of the primary flow path, and the importance of choosing correct boundary conditions that describe the real compressor operation.

First, an adiabatic, fluid-only thermal boundary condition was implemented into the model and compared to the experimental data. The results showed that the adiabatic condition vastly underestimated the temperatures in the front half of the compressor, overestimated the temperatures in the rear half of the compressor, and missed on the prediction of the cavity temperatures. This prompted the implementation of an isothermal boundary condition based on a thermal model that was developed using the experimental surface temperatures. Unfortunately, the isothermal boundary condition altered the thermodynamics of the compressor and cooled the flow resulting in an unrealistic increase in performance.

With the isothermal and adiabatic boundary conditions inadequate for predicting the surface temperatures within the PAX200 compressor, a conjugate heat transfer approach was taken to couple the solid, stationary components of the compressor to the fluid domains to better resemble the thermal characteristics of the real compressor. The rotating reference frame maintained an adiabatic thermal boundary condition due to the lack of measurements on the rotating surfaces.

First, an adiabatic condition on the outside of the casing was simulated with the conjugate heat transfer model to observe its relationship to the initial adiabatic, fluid-only model. This resulted in an expected loss in efficiency (approximately 1.25pts) due to the expansion of the control volume of the system and the storage of the heat inside the casing, compared to the adiabatic, fluid-only model. Next, like what was performed in the experimental research performed on the compressor, the adiabatic assumption was relaxed, and different levels of convection on the outside of the casing were explored. Similar to what was achieved in experiment, higher levels of convection resulted in a slight decrease in the radial stagnation temperature at the tip in the rear stages, producing an overall increase in efficiency (up to 0.9pts), though still resulting in an efficiency lower than that of the adiabatic, fluid-only simulation.

Other considerations that were made to the computational model involved changing the thickness and material of the casing. These simulations resulted in no difference for the adiabatic

boundary condition applied to the external side of the casing, but slight differences were observed with a diabatic condition. For the different casing thicknesses, the thicker casing resulted in a slightly worse efficiency than the baseline casing, while the thinner casing resulted in a slightly higher efficiency. However, this range in efficiencies was within 0.1pts and deemed negligible compared to the influence of changing the convective conditions on the external side of the compressor.

In addition to different thicknesses, three materials for the casing were also examined: the aluminum baseline casing, a stainless-steel casing to match the stator material, and a plastic casing. While the adiabatic boundary condition resulted in no difference between materials, the diabatic condition produced vastly different results. The temperature at the tip of the rear stages increased with decreasing thermal conductivity of the materials under examination. This occurred because of the heat escaping through the casing with less resistance for the aluminum casing, compared to the plastic casing. In other words, the plastic casing produced more of an insulated, adiabatic condition for the compressor, while the aluminum casing was the most efficient at moving heat heat from the flow path through the casing to the ambient environment, effectively cooling the flowpath. The range in efficiency for the different material selections varied by about 0.7pts, a much more significant impact than the different casing thicknesses. In all the conjugate heat transfer simulations, the stagnation pressure profiles were not affected by any change in external thermal boundary conditions on the outside of the compressor.

Finally, while the other simulations focused on the overall temperature of the flow and the endwalls, the overall shape of the circumferentially averaged stagnation temperature profiles were examined through increases in eddy viscosity. This was done to make up for the washed-out vorticity between mixing planes in the steady simulations and show how enhanced mixing could better explain the radial profiles acquired through the experimental data. At the expense of the performance of the compressor (often up to 7pts in efficiency), the artificially higher eddy viscosity applied to the simulations resulted in a significantly improved radial temperature profile between the computational simulation and experimental results. This comparison was made between the adiabatic, fluid-only model, and the adiabatic and diabatic conjugate heat transfer models, with the diabatic, conjugate heat transfer model showing the best agreement between the experiment and simulation in terms of overall shape of the stagnation temperature throughout the flowpath, with some overpredictions in the hub regions. In terms of levels of convection, the lower convection

case produced better profile matches in the front half of the compressor, while the higher convection case produced better profile matches in the rear of the compressor.

6.3   Conclusions on Efficiency Corrections and Temperature Assessments

Through the computational and especially the experimental phases of this research investigation, the PAX200 compressor did not exhibit the behavior of an adiabatic system. Heat generation through the cavity regions and through the stationary components were evident, and a major heat path existed between the downstream stages and the upstream stages/ambient environment facilitated by the aluminum casing. While the traditional approach was to directly calculate the isentropic efficiency using the interstage and overall compressor measurements, this directly relates the system to one that is adiabatic and reversible which was not entirely correct.

Using correlations and flow properties to calculate the windage in each cavity region, corrections to the actual work of the compressor were accounted for to help remove the diabatic effects of the facility to make this comparison with an isentropic efficiency more correct. Furthermore, the computational model was used to establish a heat transfer convection coefficient that could be applied to the experimental surface and flow temperature data. These heat rates throughout the flow path were calculated to observe both the heat path through the system and through each individual blade row/stage. This heat rate was also applied to the efficiency calculation to produce a further correction to get the actual work closer to that of an adiabatic system. On a full compressor level, these corrections totaled an increase of approximately 0.55pts. On a stage level, these corrections provided up to a 0.34pt increase in the front stage to a -0.30pt decrease in the rear stage.

Finally, a deeper look into the temperature increase across each stator was taken through comparing both the area-averaged, and spanwise stagnation temperature increases across the stator. This was done both experimentally and with the computational simulations. The computational simulation that offered the highest correlation to that of the experimentally observed temperature increases was that of the enhanced mixing, which also offered the best prediction of spanwise temperature profile. Overall, the computational results also predicted an increase in stagnation temperature across the stators, which confirmed that this phenomenon was not an uncommon occurrence, at least with respect to PAX200, assuming a diabatic environment.

6.4   Recommendations for Future Research

Throughout this research investigation, many opportunities for future research studies became evident. However, due to time, resources, and monetary implications, these further areas of research ended up outside the scope of this research endeavor. However, they are still important to advancing knowledge and understanding of heat transfer within axial compressors and are included in this section for hope of future development.

The main purpose of this research was focused on building a better understanding of the thermodynamics and heat transfer elements of the compressor and identifying potential heat sources and their impact on the surface and flow temperature. A deeper look into the more specific aerodynamics of how this heat is mixed throughout the flowpath was briefly addressed but ultimately fell outside the scope of this investigation. This was particularly with respect to the interaction of the hot flow from the cavity wells and knife seals and their interaction with the primary flow. A study by Demargne & Longley (2000) starts to cover this as they investigate stator cavity flows and their impact on performance. Additionally, the PAX200 compressor has the ability to replace the S1 and S2 shrouded stators with cantilevered versions which provides a further potential to examine the impact the stator shrouds, wells, and knife seals play on the radial temperature profiles in the flowpath.

Much of this research investigation covered the impact of heat transfer within the stationary reference frame, particularly that of the compressor casing and stator vanes. However, much information is still unknown about the rotating reference frame, which incorporate the rotors, rotating cavity regions, and the front and rear disks of the compressor. The need for these measurements to further understand the heat transfer in the system is apparent, especially with the highest stagnation temperature rise in the flow occurring in the hub and cavity regions throughout this investigation.

A future upgrade to the facility will add a slip ring device to the compressor with the potential to transmit data between the rotating and stationary reference frames, allowing the ability to acquire temperature measurements on the rotor blade, drum, and cavity regions. This data acquisition capability will be very useful for extending this work and adding further knowledge and understanding to the heat transfer characteristics of the compressor that were not captured in this study. Additionally, in a similar fashion to what was done in this investigation, it will allow for comparisons with the current adiabatic thermal boundary condition for the rotating elements in

176

the computational model. The ability to make this comparison will verify if the adiabatic thermal boundary condition is adequate to correctly represent the rotating elements of the compressor, or if an isothermal boundary condition or conjugate heat transfer approach would be more applicable. The ability to evaluate the temperatures on the rotating reference frame would also be useful for better predicting the impact on temperature profiles and the heat transfer in the hub and cavity regions. This could help address some of the discrepancies observed with temperature increase across stators and offer an additional efficiency correction to truly reflect that of an adiabatic system. Furthermore, a look into buoyancy induced flows within the drum itself could be explored, similar to recent studies performed by Jackson, et al. (2021).

In terms of computational model recommendations, while this research investigation extensively focused on comparisons between experimental data and steady CFD simulations, it briefly introduced the unsteady model for the PAX200 compressor. Due to time constraints and complexity, an unsteady, conjugate heat transfer was unable to be developed. An unsteady, conjugate heat transfer model could help to further investigate the heat transfer effects on the flowpath and offer additional validation to the eddy viscosity alterations that were made to the steady CFD simulations performed throughout this study.

APPENDIX

This section includes all tabulated elements from the computational models and experimental facility to calculate the heat transfer rates expressed in Chapter 5. Figure A.1 shows the process that was used to translate the heat transfer coefficient from CFX, which is based on wall-adjacent temperature, to one based on 90% span as the reference temperature.
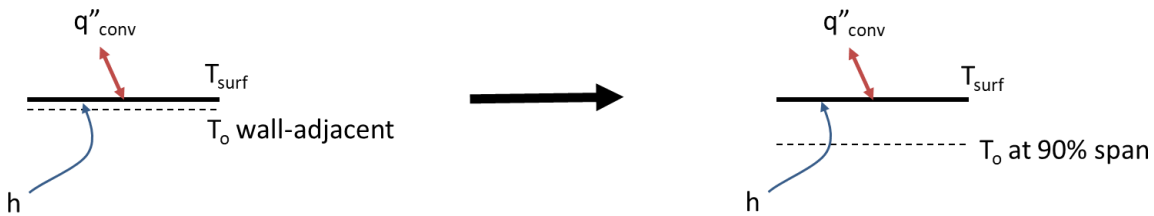
Figure A.1. Process to convert the reference temperature that is used to calculate the heat transfer coefficient in CFX to one that could be applied in experiment.

After recalculating the average heat transfer coefficient value to 90% span, it was then applied to the experimental data to recalculate an experimental heat flux and heat rate based on the measured wall temperature and surface area for each surface. The results are shown in Tables A.1-A.6, with the resulting heat flow path shown in Figures A.2-A.7.

Table A.1. Convection coefficient translation from computational simulation in CFX to experiment and corresponding heat rate for each section of IGV.

	IGV Blade	IGV Hub	IGV Shroud (Casing)	IGV Shroud (Stator)	IGV Cavity
Heat Flux (CFX) [BTU/s-ft^2]	0.0691	0.1587	0.3338	0.3338	-0.0744
HTC (CFX) [BTU/s-ft^2-°F]	0.3379	0.3367	0.2077	0.2077	0.3386
HTC (Experiment) [BTU/s-ft^2-°F]	0.0480	0.0220	0.0141	0.0194	0.0063
Area [ft^2]	2.112	1.744	1.170	1.137	0.395
Heat Rate [BTU/s]	0.0274	0.6100	0.1879	0.1743	0.0643
Heat Rate [kW]	0.0289 (into flow)	0.6435 (into flow)	0.1982 (into flow)	0.1839 (into flow)	0.0666 (into flow)
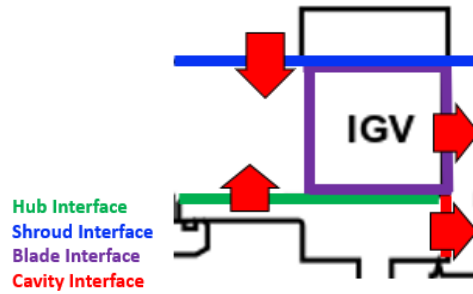
Figure A.2. Heat path for IGV based on experimental data and heat transfer coefficient from computational simulation in CFX.

Table A.2. Convection coefficient translation from computational simulation in CFX to experiment and corresponding heat rate for each section of S1.

	S1 Blade	S1 Hub	S1 Shroud (Casing)	S1 Shroud (Stator)	S1 Cavity
Heat Flux (CFX) [BTU/s-ft^2]	0.0980	-0.0173	0.0699	0.0699	-0.1100
HTC (CFX) [BTU/s-ft^2-°F]	0.3435	0.3396	0.2193	0.2193	0.3390
HTC (Experiment) [BTU/s-ft^2-°F]	0.0186	0.0038	0.0055	0.0069	0.0064
Area [ft^2]	2.84	0.951	0.529	1.115	1.325
Heat Rate [BTU/s]	0.1317	0.0436	0.0081	0.0036	0.1270
Heat Rate [kW]	0.1390	0.0460	0.0085	0.0038	0.1340

Hub Interface
Shroud Interface
Blade Interface
Cavity Interface
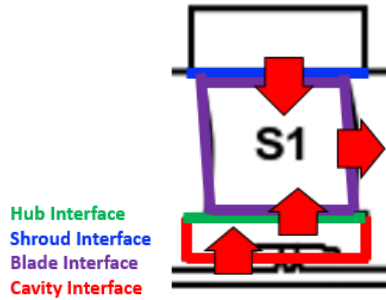
Figure A.3. Heat path for S1 based on experimental data and heat transfer coefficient from computational simulation in CFX.

Table A.3. Convection coefficient translation from computational simulation in CFX to experiment and corresponding heat rate for each section of S2.

|	S2 Blade	S2 Hub	S2 Shroud (Casing)	S2 Shroud (Stator)	S2 Cavity
Heat Flux (CFX) [BTU/s-ft^2]	0.0174	0.1137	-0.0663	-0.0664	-0.0978
HTC (CFX) [BTU/s-ft^2-°F]	0.3450	0.3391	0.2263	0.2263	0.3390
HTC (Experiment) [BTU/s-ft^2-°F]	0.0007	0.0047	0.0167	0.0156	0.0041
Area [ft^2]	2.54	1.04	0.611	1.17	1.471
Heat Rate [BTU/s]	0.0060	0.0387	-0.0157	-0.0236	0.0900
Heat Rate [kW]	0.0063	0.0408	-0.0166	-0.0249	0.0949
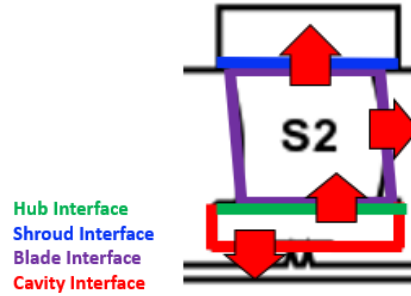
Figure A.4. Heat path for S2 based on experimental data and heat transfer coefficient from computational simulation in CFX.

Table A.4. Convection coefficient translation from computational simulation in CFX to experiment and corresponding heat rate for each section of S3.

|	S3 Blade	S3 Hub	S3 Shroud (Casing)	S3 Shroud (Stator)	S3 Cavity
Heat Flux (CFX) [BTU/s-ft^2]	0.0266	0.0433	-0.2676	-0.2676	-0.0385
HTC (CFX) [BTU/s-ft^2-°F]	0.3510	0.3383	0.2593	0.2593	0.3369
HTC (Experiment) [BTU/s-ft^2-°F]	0.0027	0.0038	0.0245	0.0144	0.0024
Area [ft^2]	2.479	1.506	2.573	1.278	1.477
Heat Rate [BTU/s]	0.0068	0.0023	-0.4174	-0.0761	0.0153
Heat Rate [kW]	0.0072	0.0025	-0.4403	-0.0803	0.0162

Figure A.5. Heat path for S3 based on experimental data and heat transfer coefficient from computational simulation in CFX.

Table A.5. Convection coefficient translation from computational simulation in CFX to experiment and corresponding heat rate for each endwall location.

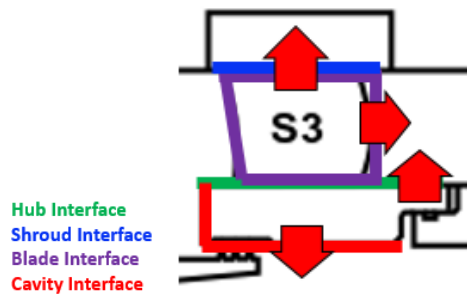|	AIP	FWD Frame	R1	R2	R3	Exhaust
Heat Flux (CFX) [BTU/s-ft^2]	0.0073	0.0073	0.1981	-0.3535	-1.0863	-0.2676
HTC (CFX) [BTU/s-ft^2-°F]	0.2705	0.2705	0.1757	0.1831	0.1906	0.2593
HTC (Experiment) [BTU/s-ft^2-°F]	0.056	0.0011	0.0433	0.0267	0.0486	0.0189
Area [ft^2]	4.729	1.426	1.23	1.23	1.131	3.19
Heat Rate [BTU/s]	0.0505	0.0057	-0.2785	-0.7692	-0.9804	-0.4483
Heat Rate [kW]	0.0532	0.0060	-0.2938	-0.8115	-1.0343	-0.4730

Figure A.6. Heat path for endwalls based on experimental data and heat transfer coefficient from computational simulation in CFX.

Table A.6. Convection coefficient translation from computational simulation in CFX to experiment and corresponding heat rate for each external wall of the casing.

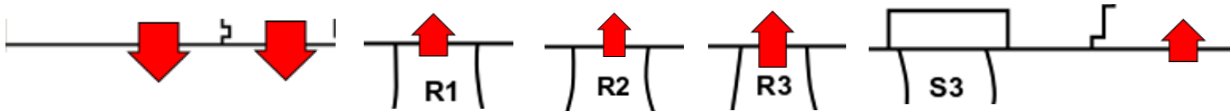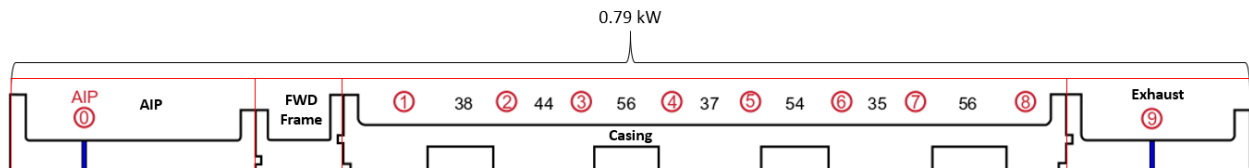|	AIP Outer Wall	FWD Frame Outer Wall	Casing Outer Wall	Exhaust Outer Wall
Heat Flux (CFX) [BTU/s-ft^2]	0.0068	0.0056	0.0346	0.051
HTC (CFX) [BTU/s-ft^2-°F]	10	10	10	10
Area [ft^2]	4.637	1.645	16.400	3.403
Heat Rate [BTU/s]	0.0032	0.0092	0.5674	0.1736
Heat Rate [kW]	0.0033 (to ambient)	0.0097 (to ambient)	0.5986 (to ambient)	0.1831 (to ambient)

Figure A.7. Heat path for external wall of casing based on experimental data and heat transfer coefficient from computational simulation in CFX.

REFERENCES

Adkins, G.G., Jr. & Smith, LH., Jr., 1982, "Spanwise Mixing in Axial-Flow Turbomachines," ASME. J. Eng. Power. 1982;104(1):97-110. doi:10.1115/1.3227271.

Atkins, N.R., and Ainsworth, R.W. 2012, "Turbine Aerodynamic Performance Measurement Under Nonadiabatic Conditions." ASME. J. Turbomach. November 2012; 134(6): 061001. doi:10.1115/1.4004857

Bayley, F.J., & Childs, P.R.N., "Air Temperature Rises in Compressor and Turbine Stator Wells." Proceedings of the ASME 1994 International Gas Turbine and Aeroengine Congress and Exposition. Volume 4: Heat Transfer; Electric Power; Industrial and Cogeneration. The Hague, Netherlands. June 13–16, 1994. V004T09A034. ASME. doi:10.1115/94-GT-185

Berdanier, R.A., Smith, N.R., Fabian, J.C., Key, N.L., 2015, "Humidity Effects on Experimental Compressor Performance—Corrected Conditions for Real Gases", Journal of Turbomachinery, 137(3), 031011 (10 pages). doi: 10.1115/1.4028356. Errata.

Borgnakke, C., & Sonntag, R. E. (2019). Fundamentals of thermodynamics.

Carter, A.D., and Cohen, E.M., "Preliminary Investigation into the Three-Dimensional Flow Through a Cascade of Aerofoils," Aeronautical Research Council Reports and Memoranda No. 2339, Feb. 1946.

Casey M.V., 2007, "Accounting for losses and definitions of efficiency in turbomachinery stages." Proceedings of the Institution of Mechanical Engineers, Part A: Journal of Power and Energy. 2007;221(6):735-743. doi:10.1243/09576509JPE459

Casey, M.V., and Fesich, T.M. 2010, "The Efficiency of Turbocharger Compressors with Diabatic Flows." ASME. J. Eng. Gas Turbines Power. July 2010; 132(7): 072302. doi:10.1115/1.4000300.

Cozzi, L., Rubechini, F., Giovannini, M., Marconcini, M., Arnone, A., Schneider, A., and Astrua, P., 2019, "Capturing Radial Mixing in Axial Compressors with Computational Fluid Dynamics." ASME. J. Turbomach. March 2019; 141(3): 031012. doi:10.1115/1.4041738

Cozzi, L, Rubechini, F, Arnone, A, Schneider, A, & Astrua, P. "Improving Steady CFD to Capture the Effects of Radial Mixing in Axial Compressors." Proceedings of the ASME Turbo Expo 2019: Turbomachinery Technical Conference and Exposition. Volume 2C: Turbomachinery. Phoenix, Arizona, USA. June 17–21, 2019. V02CT41A016. ASME. doi:10.1115/GT2019-90363

Cumpsty, N. A. 1989. Compressor Aerodynamics. Harlow, Essex, England: Longman Scientific & Technical.

Cumpsty, N. A., 2009, "Some Lessons Learned," ASME. Turbo Expo: Power for Land, Sea, and Air, Volume 7: Turbomachinery, Parts A and B ():785-794. doi:10.1115/GT2009-60368.

De Ruyck, J., & Hirsch, C.H., 1988, "A Radial Mixing Computation Method," ASME. J. Turbomach. 1988; 10.1115/88-GT-68.

Dean, R. C, Jr., "Secondary Flow in Axial Compressors," ScD thesis, Massachusetts Institute of Technology, May 1954.

Demargne, A.A.J, & Longley, J.P., "The Aerodynamic Interaction of Stator Shroud Leakage and Mainstream Flows in Compressors." Proceedings of the ASME Turbo Expo 2000: Power for Land, Sea, and Air. Volume 1: Aircraft Engine; Marine; Turbomachinery; Microturbines and Small Turbomachinery. Munich, Germany. May 8–11, 2000. V001T03A095. ASME. doi:10.1115/2000-GT-0570

Dixon, S.L. (2005). Fluid Mechanics, Thermodynamics of Turbomachinery. Amsterdam: Elsevier-Butterworth-Heinemann.

Dring, RP & Joslyn, David & Hardin, LW., 1979, "Experimental investigation of compressor rotor wakes. Final Report," 1 Sep. 1977 - 30 Sep. 1979., United Technologies Research Center, East Hartford, CT -1.

Dring R.P., 1993, "Radial Transport and Momentum Exchange in an Axial Compressor," ASME. J. Turbomach. 1993;115(3):477-486. doi:10.1115/1.2929278.

Gallimore, S.J. & Cumpsty, N.A., 1986, "Spanwise Mixing in Multistage Axial Flow Compressors: Part I—Experimental Investigation," ASME. J. Turbomach. 1986;108(1):2-9. doi:10.1115/1.3262019.

Gallimore S.J., 1986, "Spanwise Mixing in Multistage Axial Flow Compressors: Part II—Throughflow Calculations Including Mixing," ASME. J. Turbomach. 1986; 108(1):10-16. doi:10.1115/1.3262009.

Giles, M., 1988, "Calculation of Unsteady Wake/Rotor Interaction," AIAA. J. Propulsion, July 1988. 4(4): 356-362. doi: 10.2514/3.23074

Goto, T, Oshio, T, Tani, N, Aotsuka, M, Pallot, G, & Kato, D. "Effect of Turbulence Model on the Prediction of Performance and Span-Wise Mixing in High-Speed Highly-Loaded Multi-Stage Axial-Flow Compressor." Proceedings of the ASME Turbo Expo 2019: Turbomachinery Technical Conference and Exposition. Volume 2A: Turbomachinery. Phoenix, Arizona, USA. June 17–21, 2019. V02AT39A022. ASME. doi:10.1115/GT2019-91141

Hall, D.K., 2011, "Performance Limits of Axial Turbomachine Stages," MS Thesis, Department of Aeronautics and Astronautics, Massachusetts Institute of Technology.

Hawthorne, W.R., "Rotational Flow Through Cascades, Part I, the Components of Vorticity," Quarterly Journal of Mechanics and Applied Mathematics, Vol. 8,1955, pp. 266-279.

Hearsey, R.M., 1975, "A Revised Computer Program for Axial Compressor Design, Vol 1," ARL TR 75-0001, Vol. 1, Aerospace Research Laboratories, Wright Patterson Air Force Base, OH.

Howell, A.R., 1945. "Fluid Dynamics of Axial Compressors," Proc. Imm. Mech. Engrs., 441.

Imanari K.K., 1994, "Theoretical Model of the Spanwise Mixing Caused by Periodic Incoming Wakes." ASME. Turbo Expo: Power for Land, Sea, and Air, Volume 1: Turbomachinery, 1994; V001T01A063. doi:10.1115/94-GT-153.

Jackson, R. W., Luberti, D., Tang, H., Pountney, O. J., Scobie, J. A., Sangan, C. M., Owen, J. M., and Lock, G. D., 2021, "Measurement and Analysis of Buoyancy-Induced Heat Transfer in Aero-Engine Compressor Rotors." ASME. J. Eng. Gas Turbines Power. June 2021; 143(6): 061004. https://doi.org/10.1115/1.4049100

Kiss, A., and Spakovszky, Z., 2018, "Effects of Transient Heat Transfer on Compressor Stability." ASME. J. Turbomach. December 2018; 140(12): 121003. doi:10.1115/1.4041290

Koch C.C., and Smith L.H., Jr., 1976, "Loss Sources and Magnitudes in Axial-Flow Compressors," ASME. J. Eng. Power. 1976;98(3):411-424. doi:10.1115/1.3446202.

Kormanik III, N.J., 2017, "Characterization of Aerodynamic Forcing Functions for Embedded Rotor Resonant Response in a Multistage Compressor," MS Thesis, School of Aeronautics and Astronautics, Purdue University, West Lafayette, IN.

Kormanik III, N.J., Matthews, D.R., Key, N.L., and King, A.J., "Purdue 3-Stage Axial Compressor Research Facility: Through the Years, to Infinity, and Beyond." Presented at the AIAA Propulsion and Energy 2019 Forum. Indianapolis, Indiana, USA. Aug. 19-22, 2019. AIAA. doi:10.2514/6.2019-4000

Kussoy, M.I., and Bachkin, D., 1958, "Comparison of Performance of Two Aerodynamically Similar 14-Inch-Diameter Single Stage Compressor Rotors of Different Chord Length," NACA RM E57I03.

Lemmon, E.W., Huber, M.L., and McLinden, M.O., 2013, NIST Standard Reference Database 23: Reference Fluid Thermodynamic and Transport Properties—REFPROP, Version 9.1, National Institute of Standards and Technology, Standard Reference Data Program, Gaithersburg, MD.

Lewis, L.V., 2002, "In-Engine Measurements of Temperature Rises in Axial Compressor Shrouded Stator Cavities." ASME. Proceedings of the ASME Turbo Expo: Power for Land, Sea, and Air, Volume 3: Turbo Expo 2002, Parts A and B. Amsterdam, The Netherlands, June 3-6, 2002., pp. 781-794. doi:10.1115/GT2002-30245.

Leylek J.H., and Wisler D.C., 1991, "Mixing in Axial-Flow Compressors: Conclusions Drawn from Three-Dimensional Navier–Stokes Analyses and Experiments," ASME. J. Turbomach. 1991;113(2):139-156. doi:10.1115/1.2929069.

Li, S.M., & Chen, M.Z., 1992, "A Simple and Unified Model for Spanwise Mixing in Multistage Axial Flow Compressors," J. of Thermal Science, 1992; 1: 98. doi:10.1007/BF02650845

Liu, L, Li, X, Ren, X, & Gu, C., 2017, "Effect of Cooling on the Aerodynamic Performance in the Intercooled Compressor Vanes." Proceedings of the ASME Turbo Expo 2017: Turbomachinery Technical Conference and Exposition. Volume 5B: Heat Transfer. Charlotte, North Carolina, USA. June 26–30, 2017. V05BT22A008. ASME. doi:10.1115/GT2017-63875

Lüddecke, B., Filsinger, D., Ehrhard, J., Steinacher, B., Seene, C., and Bargende, M., 2013, "Contactless Shaft Torque Detection for Wide Range Performance Measurement of Exhaust Gas Turbocharger Turbines." ASME. J. Turbomach. June 2014; 136(6): 061022. doi:10.1115/1.4025824

Maesschalck, C.D., Lavagnoli, S., Paniagua, G., and Vinha, N., 2013, "Aerothermodynamics of tight rotor tip clearance flows in high-speed unshrouded turbines." Elsevier. Applied Thermal Engineering. April 2014; 65(1-2), pp. 343-351. doi: 10.1016/j.applthermaleng.2014.01.0145.

Menter, F.R., 1994, "Two-Equation Eddy-Viscosity Turbulence Models for Engineering Applications," AIAA J., vol. 32, no. 8, 1994, doi: 10.2514/3.12149.

Millward, J.A., and Edwards, M.F., 1996, "Windage Heating of Air Passing Through Labyrinth Seals." ASME. J. Turbomach. April 1996; 118(2): 414–419. doi:10.1115/1.2836657

Owen, J.M., Tang, H., and Lock, G.D., 2018, "Buoyancy-Induced Heat Transfer inside Compressor Rotors: Overview of Theoretical Models." Aerospace, 5(1), pp. 1-22. doi:10.3390/aerospace5010032.

Schinnerl, M., Ehrhard, J., Bogner, M., and Seume, J., 2017, "Correcting Turbocharger Performance Measurements for Heat Transfer and Friction." ASME. J. Eng. Gas Turbines Power. February 2018; 140(2): 022301. doi:10.1115/1.4037586.

Sirakov, B., & Casey, M., 2012. "Evaluation of Heat Transfer Effects on Turbocharger Performance." ASME. J. Turbomach. March 2013; 135(2): 021011. doi:10.1115/1.4006608.

Smith, L.H., "Casing Boundary Layers in Multistage Axial-flow Compressors," Brown Boueri Symposium, Flow Research in Blading, Elsevier, 1969.

Smith, N.R., Allison, T.C., Wilkes, J. C., Clarke, C., and Cave, M., 2018, "The Comparison of Aerodynamic Performance Data Acquired from Thermal Measurements and a Torquemeter on a Compressor Impeller." ASME. J. Eng. Gas Turbines Power. April 2019; 141(4): 041011. doi: 10.1115/1.4041740

Standahar, R. M., and Geye, R. P., 1955, "Investigation of a High-Pressure Ratio Eight-Stage Axial Flow-Research Compressor with Two Transonic Inlet Stages, V—Preliminary Analysis of Over-All Performance of Modified Compressor," NACA RM E55A03.

Swan, W.C., 1958, "A Practical Engineering Solution to the Three-Dimensional Flow in Transonic Type Axial Flow Compressors," Technical Report 58-57, Wright Air Development Center, Air Research and Development Command, Wright-Patterson Air Force Base, OH.

Talalayev, A., 2011, "On the Renovation of the Three-Stage Axial Compressor Research Facility for Compressor Performance Research," MS Thesis, Mechanical Engineering, Purdue University, West Lafayette, IN.

Tipton, D. L., 1968, "Improved Techniques for Compressor Loss Calculation," AGARD Conference Proceeding No. 34, Advanced Components for Turbojet Engines, Part I.

Wagner, JH, Dring, RP & Joslyn, HD., 1985, "Inlet Boundary Layer Effects in an Axial Compressor Rotor: Part I—Blade-to-Blade Effects," ASME. J. Eng. Gas Turbines Power. 1985;107(2):374-380. doi:10.1115/1.3239734.

Wennerstrom, A.J., 1990, "Highly Loaded Axial Flow Compressors: History and Current Developments," ASME. J. Turbomach. 1990; 112(4):567-578. doi:10.1115/1.2927695.

Wennerstrom A.J., 1991, "A Review of Predictive Efforts for Transport Phenomena in Axial Flow Compressors," ASME. J. Turbomach. 1991;113(2):175-179. doi:10.1115/1.2929080.

Wisler, D.C., 1998, "The Technical and Economic Relevance of Understanding Boundary Layer Transition in Gas Turbine Engines," Minnowbrook II, 1998 Workshop on Boundary Layer Transition in Turbomachines, NASA/CP- 1998-206958.

Yasa, T., Paniagua, G., & Bussolin, A. 2007. "Performance analysis of a transonic high-pressure turbine." Proceedings of the Institution of Mechanical Engineers, Part A: Journal of Power and Energy, 221(6), 769–778. doi:10.1243/09576509JPE467.

Young, W.H., 1957, "The Experimental Investigation of a Research Transonic Inlet Stage Compressor," Technical Report 57-207, Wright Air Development Center, Air Research and Development Command, Wright-Patterson Air Force Base, OH (AD 118172).

PUBLICATIONS

Technical Papers

1. Lou, F., Matthews, D.R., Kormanik III, N.J, and Key. N.L., "Accounting for Circumferential Flow Nonuniformity in a Multi-Stage Axial Compressor," Presented at ASME Turbo Expo 2021; doi:10.1115/GT2021-59968.

2. Lou, F., Matthews, D.R., Kormanik III, N.J., and Key, N.L., 2020, "Reconstructing Compressor Nonuniform Circumferential Flow Filed from Spatially Undersampled Data – Part 2: Practical Application for Experiments" Presented at ASME Turbo Expo 2020; doi:10.1115/GT2020-15465

3. Kormanik III, N.J., Matthews, D.R., Key, N.L., and King, A.J., 2019, "Purdue 3-Stage Axial Compressor Research Facility: Through the Years, to Infinity, and Beyond" In AIAA Propulsion & Energy 2019 Forum; doi:10.2514/6.2019-4000.

4. Li, J., Aye-Addo, N., Kormanik III, N., Matthews, D., Key, N.L., and Kielb, R.E., 2017, "Mistuned Higher-Order Mode Forced Response of an Embedded Compressor Rotor: Part 1 – Steady and Unsteady Aerodynamics" In the Proceedings of ASME Turbo Expo 2017; doi:10.1115/GT2017-64633.

Patents

1. Key, N.L., Kormanik III, N.J., Leng, Y., Lou, F., and Matthews, D.R., & Purdue University. 2019, Low-Cost, Non-Intrusive, Turbomachinery Blade Vibration Detection and Monitoring System, 2019-KEY-68629 (pending)

Journal Articles

1. Lou, F., Matthews, D.R., Kormanik III, N.J., and Key, N.L., 2021, "Reconstructing Compressor Nonuniform Circumferential Flow Field from Spatially Undersampled Data— Part 2: Practical Application for Experiments." ASME. J. Turbomach. August 2021; 143(8): 081003. doi:10.1115/1.4050434.

2. Lou, F., Matthews, D.R., Kormanik III, N.J, and Key. N.L., 2021, "Understanding the Blade Row Interactions in a Multi-Stage Axial Compressor From the Circumferentially Reconstructed Flow Field," Accepted for publication in ASME J. Turbomach. (pending).